

FACULTY
OF MATHEMATICS
AND PHYSICS
Charles University

DOCTORAL THESIS

Ivo S. Vinklárek

Photodissociation of small polyatomic molecules investigated via molecular beam and velocity map imaging techniques

Department of Chemical Physics and Optics

Supervisor of the doctoral thesis:	doc. Mgr. Michal Fárník Ph.D., DSc.
Study programme:	Biophysics, chemical and macromolecular physics
Study branch:	Physics

Prague 2022

I declare that I carried out this doctoral thesis independently, and only with the cited sources, literature and other professional sources. It has not been used to obtain another or the same degree.

I understand that my work relates to the rights and obligations under the Act No. 121/2000 Sb., the Copyright Act, as amended, in particular the fact that the Charles University has the right to conclude a license agreement on the use of this work as a school work pursuant to Section 60 subsection 1 of the Copyright Act.

In ..... date ....

Author's signature

I cannot express how thankful I am to all my colleagues from the Department of Dynamics of Molecules and Clusters (J. Heyrovský Institut of Physical Chemistry of the CAS) for an amusing three and half years during my Ph.D. studies. My Ph.D. years were full of fun, great discussions and schooling not only in scientific work.

My great thanks and admiration belongs to my colleague Dr. Jozef Rakovský with whom I spent the most time when experimenting on our beloved (and slightly hated) AIM. Thanks to him, I quickly learned all the details in the VMI method, laser techniques, electronics, and many other fields. Similar great thanks and appreciation belong to my supervisor doc. Michal Fárník who had enough courage to enable me to jump into the rich field of molecular beams and was always full of support in all my ideas and occasional struggle. The third colleague I was lucky to meet, Dr. Andriy Pysanenko, introduced me to the mass spectrometric experiments on our CLUB machine. Still, I think that I will remember more our open discussions and friendly (and blunt) jokes. Furthermore, I thank Dr. Ondřej Votava for his beautiful presentations about many exciting points of physics and optics, and Dr. Viktoriya Poterya for her calm and wise attitude in the discussions about the acquired results and many great recommendations of articles to read. Together they formed an advisory board, which got me into the field of molecular beam physics and velocity map imaging.

Thanks to my fellow from the office, Dr. Miloš Rankovič, who introduced me into the SIMION simulations and basics of Arduino programming and joined me in my climbing attempts on the artificial wall. Thanks to Dr. Kateřina Grygoryeva, Mgr. Kamila Moriová for collaboration and discussions over the experimental results. The same is true for Dr. Deb Pratim Mukhopadhyay, who also introduced me to a rich and exotic Indian culture. I also very much appreciate collaboration and discussions with our colleagues from the electron collisions and irradiation chemistry groups, Dr. Pamir Nag, Dr. Thomas F. Luxford, Dr. Leo Sala, Dr. Jaroslav Kočišek, and group leader Dr. Juraj Fedor. Also, many thanks to Juraj for teaching me some basics in quantum physics. And my final and great thanks belong to Ing. Barbora Sedmidubská.

Tuto práci dopisuji v době ruské invaze na Ukrajinu. Přijdou možná dny, kdy mnoho toho co v této práci píši bude překonáno nebo zapomenuto, ale věřím, že se vždy bude připomínat zbytečná ruská brutalita, která je zdrojem hrůz dnešního času.

Title: Photodissociation of small polyatomic molecules investigated via molecular beam and velocity map imaging techniques

Author: Ivo S. Vinklárek

Department: Department of Chemical Physics and Optics

Supervisor: doc. Mgr. Michal Fárník Ph.D., DSc., J. Heyrovský Institute of Physical Chemistry of the CAS, v. v. i.

Abstract: Velocity map imaging (VMI) combined with supersonically expanded molecules provides molecular-level insight into many fundamental natural phenomena. This comprehensive work delivers an introduction to the photodissociation theory and applied VMI and mass spectrometric experimental techniques, followed by an overview of our achievements in the investigation of photodissociation and clustering on the selected molecular systems. Also, new implementations of the centroiding mode and the current status of the apparatus for imaging are commented on for future measurements. The first part of the experimental results focuses on fundamental research of photodissociation of isolated molecules. We demonstrate an efficient coupling between the stretching vibration and ejection of hydrogen radical in pyrrole and, furthermore, describe the impact of singlet-triplet dynamics and molecular frame on energy redistribution during the fragmentation of selected chloroalkanes. The second part revolves around chloroalkane clusters in the perspective of atmospheric chemistry, which is represented by the observations of different dynamics for CH_3 and Cl fragments in $(CH_3Cl)_n$ cluster photodissociation. Finally, the clustering research is extended by our recent pickup experiments with clusters of polyaromatic hydrocarbons used as a model system for mimicking the atmospheric and space heterogeneous chemistry and ice mantle growth.

Keywords: mass spectrometry, clusters, pyrrole, chloroalkanes, polyaromatic hydrocarbons

Contents

1 Theory and Motivation **3**
- 1.1 Photodissociation . . . 5
- 1.2 Potential Energy Surfaces and Representations . . . 7
  - 1.2.1 Adiabatic Representation and Born-Oppenheimer Approximation . . . 8
  - 1.2.2 Diabatic Representation . . . 10
  - 1.2.3 Conical Intersection . . . 11
- 1.3 Singlet-Triplet Transitions . . . 12
  - 1.3.1 Spin-Orbit Coupling . . . 12
  - 1.3.2 Intersystem Crossing . . . 14
- 1.4 Classical Mechanics Models . . . 15
  - 1.4.1 Hard Sphere Model . . . 15
  - 1.4.2 Spectator Model (Pure Impulsive) . . . 15
- 1.5 Clusters . . . 17
  - 1.5.1 Effects of Environment on Photodissociation: Clusters as Environment Model . . . 18

2 Methods and Experiments **21**
- 2.1 Introduction to Molecular Beams . . . 21
  - 2.1.1 Molecular Beams by Supersonic Expansion . . . 22
  - 2.1.2 Cluster Beams by Supersonic Expansion . . . 24
- 2.2 Mass Spectrometry . . . 26
  - 2.2.1 Time of Flight Mass Spectrometer . . . 27
- 2.3 Velocity Map Imaging . . . 28
  - 2.3.1 Kinetic Energy Distribution . . . 31
  - 2.3.2 Anisotropy and Vector Correlations . . . 32
  - 2.3.3 Photoionization: Resonant and Non-Resonant . . . 34
  - 2.3.4 Time-Resolved Pump-Probe VMI Experiments . . . 36
  - 2.3.5 Spatial Resolution and Centroiding . . . 37
- 2.4 Apparatus for Imaging . . . 40
  - 2.4.1 Control of AIM and Data Acquisition . . . 41
  - 2.4.2 Apparatus Synchronization . . . 42
  - 2.4.3 VMI Calibration by HBr . . . 45
- 2.5 Cluster Beam Apparatus . . . 47
- 2.6 Pickup Experiments . . . 48
  - 2.6.1 Poisson Distribution in Pickup Experiments . . . 48

3 Results **51**
- 3.1 Pyrrole . . . 52
- 3.2 Ã-band Induced Photofragmentation of Selected Haloalkanes as Isolated Molecules and Clusters . . . 55
  - 3.2.1 Photodissociation of Isolated Higher Chloroalkanes . . . 59
  - 3.2.2 Photodissociation of CH_3Cl clusters . . . 66
  - 3.2.3 Comparison of Multiphoton Effects and Clustering . . . 68

3.3 Pickup Experiments in Molecular Beams 74
3.3.1 Pickup on Polyaromatic Hydrocarbons Clusters 74
3.3.2 Pickup of Hydrogen Bonding Molecules on Benzene Clusters 83
3.3.3 Pickup Experiments with Adamantane Clusters 86
3.4 Future Prospects 90

Conclusion **93**

Bibliography **95**

List of Figures **109**

List of Tables **113**

List of Abbreviations **115**

List of publications **117**

A Attachments **119**
A.1 Applied Lasers 119
A.2 Nozzle and Tube Circuit Diagram 121
A.3 NT230 UV OPO Laser LabView Controller 122
A.4 Delay Generators LabView Controller 123
A.5 Delay Generators Settings 124

B Reprints of Author's Publication **125**
B.1 Publication I 126
B.2 Publication II 134
B.3 Publication III 146
B.4 Publication IV 163
B.5 Publication V 176

1. Theory and Motivation

> "What Mach calls a thought experiment is of course not an experiment at all. At bottom it is a grammatical investigation."
>
> *Ernst Mach*

Absorption of the photon(s) by molecule initiates an interplay of various relaxation pathways to dissipate the gained energy. Many experimental techniques were developed to probe these photodynamical processes and elucidate the energy flow on the multi-dimensional potential energy surfaces (PES).[1] Typically, the absorbed energy can be emitted through quanta of energy known as fluorescence or phosphorescence, or it can be distributed across different internal modes of the molecule, which can be probed by infrared (IR) spectroscopic methods.[1, 2] If the molecule is incorporated into the environment, the excitation can be collisionally quenched or transferred by non-radiative energy transfer, similar to pigments in light-harvesting complexes.[3, 4] Sometimes, the gained energy exceeds bond energy, which leads to a bond cleavage process called *photodissociation* (also found in literature as "photofragmentation" or "half-reaction"). In particular, the radiation from the ultraviolet range (UV, $\lambda < 400\,\mathrm{nm}$, $E > 3.1\,\mathrm{eV}$) of spectra has enough energy to surpass the bond energy of weaker covalent bonds and thus induce the molecular fragmentation. The present thesis investigates the photodissociation from the view of small polyatomic molecules, which enables us to study radiationless transitions between the quantum states[5, 6, 7, 8], internal energy redistribution[8], conical intersections [8], and intersystem crossing[5, 6] on the fragmentation pathway.

The selected molecular systems are probed by *molecular beam* technique combined with laser methods and mass spectrometry. Together, these methods create a robust experimental tool of velocity map imaging,[9] which provides us with molecular-level insight into the photodissociation of single unperturbed particles. This is especially beneficial for a detailed understanding of fragmentation pathways in isolated molecules, as is demonstrated by studies of vibrationally mediated photodissociation of pyrrole[8] and singlet-triplet interplay in four representatives of chloroalkanes.[5, 7, 6]

However, the molecules are barely found isolated. From the dense gas in Earth's atmosphere to the diffuse clouds in the infinite space of the universe, we observe that molecules are exposed to interactions with their immediate environment that cause changes in their physical properties and courses of chemical reactions. The generation of *molecular clusters* by supersonic expansion enables us to simulate specific environmental conditions to investigate various natural phenomena.[10, 11] Specifically, molecular clusters are a promising system for studying the heterogeneous chemistry of atmospheric aerosols and nanoparticles, whose role in global climate, atmospheric chemistry and air pollution should not be underestimated.[12, 10, 11] Our research of chloroalkane clusters[5, 7] is motivated by its relevance in atmospheric chemistry as the impact of chlorine radicals on stratospheric ozone depletion and tropospheric radical chemistry is well

known.[10, 13, 14] Finally, the cluster research is extended by our recent experiments with the molecular pickup on polyaromatic hydrocarbon (PAH) clusters to study cluster growth and coagulation as a prerequisite for the future study of their photochemistry.[15] PAHs are known from atmospheric pollution and mid-IR-observations of interstellar space medium; therefore, they are suggested to play a crucial role in chemical pathways in the Earth's atmosphere and the universe.[16, 17]

Together, the selected systems offer a broad inventory of investigated physical phenomena, which makes this thesis helpful for any student who just started or wants to gain a broader perspective in the field of molecular beams. Simultaneously with the research progress, we invested a considerable effort into the upgrading of our apparatus for imaging, which is commented on explicitly in chapter 2. The following chapters briefly introduce the photodissociation theory and the necessary tools for further discussion.

1.1 Photodissociation

Photodissociation is an irreversible process in which an isolated molecule in a bound state is fragmented due to its interaction with an electromagnetic field represented by photons $N \cdot h\nu$. The simplified description of the whole photodissociation process is as follows[1, 9, 18]

$$ABC(i) \xrightarrow[absorption]{N \cdot h\nu} (ABC)^* \xrightarrow[fragmentation]{} A(\alpha_k) + BC(\beta_k). \tag{1.1}$$

In this example, the quantum state of polyatomic molecule ABC is transferred from the initial bound state i to an excited state $(ABC)^*$ by absorption of photon energy in the first step. Next, the absorbed energy compensates the bond dissociation energy and partly is converted into translational energy of recoiling fragments. Finally, the atomic fragment A and polyatomic fragment BC are produced in their particular electronic α and rovibronic β states, respectively.

Before the absorption, the molecules either occur in the ground state with a very narrow initial rovibrational distribution, which can be further reduced in nozzle expansion,[2] or the initial state is selectively prepared by laser experiments such as in vibrationally mediated photodissociation.[19, 9] Then, the starting point on the excited state PES is determined by the initial quantum state i and the laser radiation.[1] The possibility to tune the laser wavelength is a great advantage in studying fragmentation dynamics by photodissociation experiment. Tuneable solid-state, or dye lasers, can deliver spectrally narrow nanosecond pulses for pumping or probing the investigated system in the state-selective experiments.[1, 20] In contrast, the ultrafast femtosecond laser pulses, which application goes beyond the scope of this work, enable to probe the energy flow during the photodissociation in time-resolved experiments in exchange for the loss of spectral information.[1, 20]

The probability for the fragmentation in particular channel k depends on the initial state i and photon energy $h\nu$, which is expressed as

$$P_k(i, h\nu) = \frac{\sigma_k(\alpha_k, \beta_k; h\nu, i)}{\sum_l \sigma_l}, \tag{1.2}$$

under the assumption that all the relaxation pathways lead to dissociation. The σ_l is used for photodissociation cross-section by the given fragmentation pathway l. The cross-sections are usually presented in their relative differential forms to plot angular distribution $d\sigma/\,d\Omega$ or kinetic energy distribution $d\sigma/\,dE$.[1] Such plots can reveal information about the transition dipole moment, quantum state symmetry, PES topology, coupling interactions among PES and excess energy distribution.[6, 9, 2, 19, 8] For example, the angular distribution of H fragments from HCl dissociation corresponds to the symmetry of the quantum state combined with transition dipole moment (and laser polarization),[19] whereas the analysis of recoil energy of H fragments from H_2O dissociation brings information about the co-fragment rovibrational excitation.[21, 22, 1]

The threshold energy for dissociation varies from IR radiation up to the far UV range.[1] Even few meV can induce evaporation of molecules from weakly bound systems represented by atmospheric aerosols or nanoparticles in the interstellar space.[10, 16, 12] In contrast, the chemical bonds often ask for at least a few eV.[1, 9] The formal division of the photodissociation of chemically bonded systems into

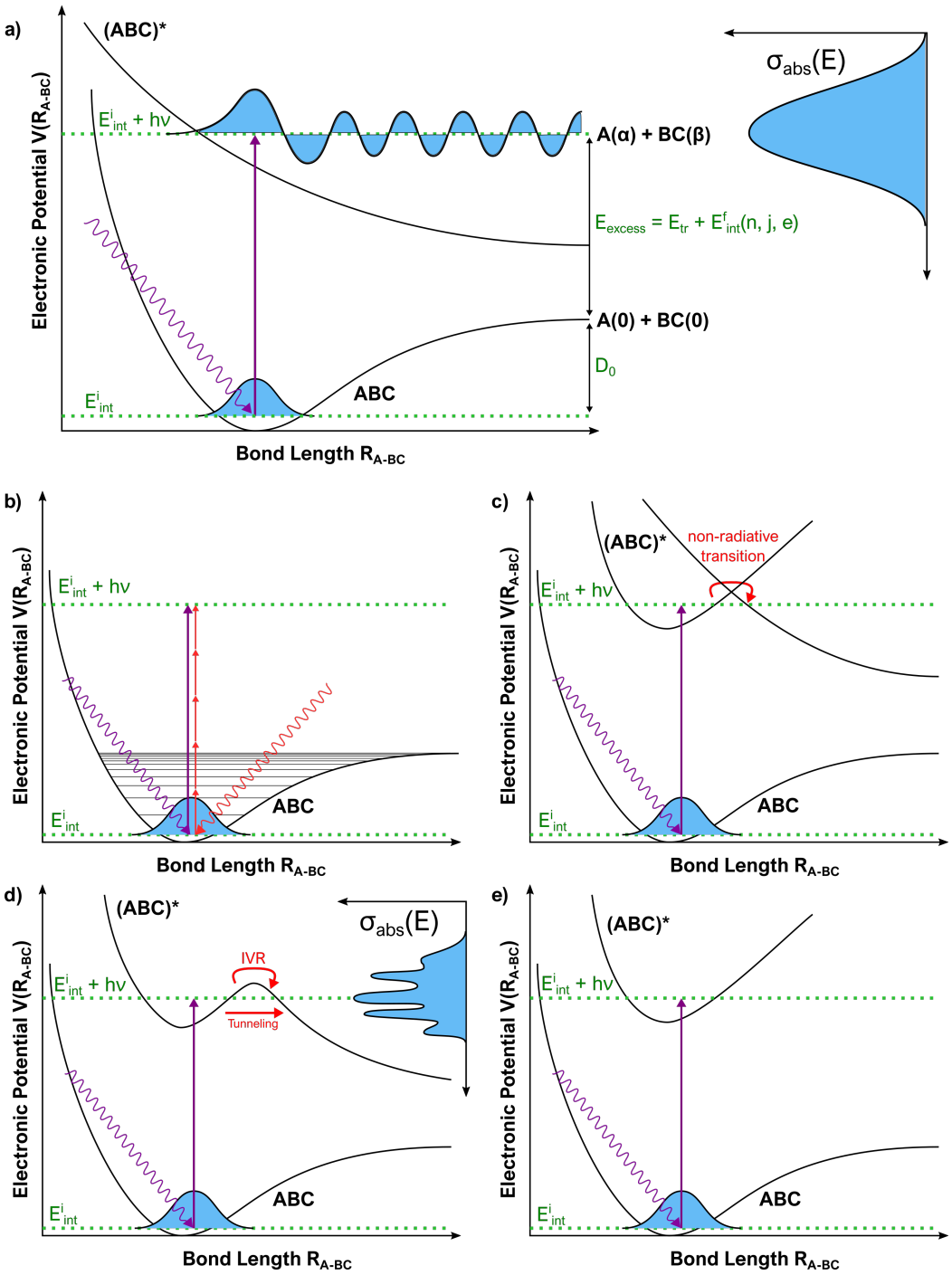


Figure 1.1: Comparison of various types of photodissociation. The illustrations were drawn according to similar schemes from [1] and [18] and modified.

the basic types is shown in figure 1.1. In the first case of direct dissociation shown in subplot a), the molecule is transferred from the bound state to the repulsive excited state. The repulsive potential along the dissociation coordinate leads to the fast fragmentation with the excess energy over the dissociation energy D_0 distributed into translational modes E_{tr} and internal excitation E_{int}^f of departing fragments. The E_{int}^f includes excitation of electronic state e for atomic fragment A, but also rotational j and vibrational n modes for molecular fragment BC. Together, the energy balance during the dissociation must always obey the energy

conservation law

$$E^i_{int} + h\nu - D_0 = E_{excess} = E^f_{int}(n, j, e) + E_{tr}. \tag{1.3}$$

Direct dissociation can also occur by one-photon pumping directly to a highly vibrational overtone to surpass the dissociation energy. However, the probability is usually too small,[23] which opens a way for multiphoton excitation as shown in subplot b). The involvement of only a single dissociative state on the fragmentation pathway is rather exceptional. The indirect photodissociation in subplots c-e) proceeds through the interplay between two or more quantum states, exchanging the excitation due to the mutual couplings. For example, the coupling between the firstly excited bound state and other repulsive states enables the radiationless transition and subsequent decay of the molecule, which is called electronic predissociation (or Herzberg's type I predissociation), see subplot c).[1, 18] The vibrational predissociation (or Herzberg's type II predissociation) results from the avoided crossing of bound and higher electronic state, which builds up the topology of PES with an energy barrier preventing the direct dissociation.[1, 18] The initially excited quasi-bound state then can tunnel through the barrier or, in the case of polyatomic molecules, bypass the barrier by internal vibrational energy redistribution (IVR) on the pathway to fragmentation. The last prototypical indirect decay is shown in subplot e). The first excited bound state non-radiatively decays through internal vibrational relaxation to the highly rovibrationally excited state above the dissociation limit. This pathway usually produces also highly rovibrationally excited molecular fragments. The characteristics of the photodissociation pathway are inscribed into the pattern of total absorption cross-section, as is shown in the insets of subplots a) and d). This can be presented on the dissociation of water H_2O in the first three absorption bands.[22, 1] The fast direct dissociation from $\tilde{A}(^1B_1)$ is represented by broadband coming from the reflection principle of the initial eigenstate on the excited state PES. On the other hand, the peaked structure of the $\tilde{B}(^1A_1)$ and $\tilde{C}(^1B_1)$ bands indicates the indirect fragmentation from the quasi-stable states with lifetime up to the order of several internal vibrations.[22, 1]

Similar to the absorption spectra, information about the fragmentation pathway can also be elucidated from the kinetic energy distribution and angular distributions of fragments, as is discussed in the chapter about the used mass spectrometric methods and techniques 2.3. This approach is based on the application of equation 1.3 in a simplified two-body fragmentation view combined with the classical mechanics models,[6, 8] or the advanced molecular dynamics (MD) simulations,[6] which will help us to investigate the processes in more detail.

Before discussing these phenomena like conical intersection and intersystem crossing, we need first to understand the terms like PES, adiabatic and diabatic (or non-adiabatic) representations, adiabatic separation, etc.

1.2 Potential Energy Surfaces and Representations

Calculating the photodissociation dynamics of even single polyatomic molecule expressed through wavefunction $\Psi(\boldsymbol{R}, \boldsymbol{r}, t)$ directly by solving the Schrödinger

equation 1.4a is far too demanding, usually impractical, and can hinder some of the essential properties of the studied process from the observer. Therefore, several approximations are applied to simplify the description

$$\left[i\hbar\frac{\partial}{\partial t} - \hat{H}_{mol}(\boldsymbol{R},\boldsymbol{r})\right]\Psi\left(\boldsymbol{R},\boldsymbol{r},t\right) = 0 \rightarrow \tag{1.4a}$$

$$\left[\hat{H}_{mol}(\boldsymbol{R},\boldsymbol{r}) - E_i\right]\Psi_i\left(\boldsymbol{R},\boldsymbol{r}\right) = 0, \tag{1.4b}$$

$$\Psi\left(\boldsymbol{R},\boldsymbol{r},t\right) = \sum_i a_i \Psi_i\left(\boldsymbol{R},\boldsymbol{r}\right) e^{-iE_i t/\hbar}. \tag{1.4c}$$

The molecular Hamiltonian $\hat{H}_{mol}(\boldsymbol{R},\boldsymbol{r})$ representing the electrons and nuclei is time-independent when no external perturbation is active. Thus, the Schrödinger equation 1.4a can be expressed in the time-independent form 1.4b, and consequently, the molecular wavefunction $\Psi\left(\boldsymbol{R},\boldsymbol{r},t\right)$ is split into a time-independent part and an exponential time-dependent phase factor. In equation 1.4c, we apply on $\Psi\left(\boldsymbol{R},\boldsymbol{r},t\right)$ the decomposition into the basis of stationary eigenfunctions $\Psi_i\left(\boldsymbol{R},\boldsymbol{r}\right)$ in the Hilbert space of $\hat{H}_{mol}(\boldsymbol{R},\boldsymbol{r})$.[1, 24, 2]

If we would like to describe the photon absorption as the first step in photodissociation, we would need to start with the implementation of perturbation into the equation 1.4b due to the interaction with an electromagnetic field. Under the assumption of weak and long-lasting perturbation due to the spectrally narrow light pulses, we would derive through the first-order time-perturbation theory the formula of Fermi's golden rule for the absorption probability, or transition rate, of the resonant transition between the initial Ψ_i and excited molecular state Ψ_f[1]

$$\sigma(h\nu) = \frac{\pi}{\hbar\epsilon_0 c}\omega_{fi}\delta(E_f - E_i - h\nu)|\langle\Psi_f|\boldsymbol{e}\cdot\hat{\boldsymbol{d}}|\Psi_i\rangle|^2, \tag{1.5}$$

where we applied the electric dipole approximation with $\hat{\boldsymbol{d}}$ as dipole operator and $\boldsymbol{e}$ as unit vector in the direction of electric field.

1.2.1 Adiabatic Representation and Born-Oppenheimer Approximation

To describe the photodissociation pathway on PES, we first apply approach with the Born-Oppenheimer approximation to extract the motion of electrons and nuclei from the molecular wavefunction $\Psi_i\left(\boldsymbol{R},\boldsymbol{r}\right)$. Each of the particles have very different character. The electrons are more than a thousand times lighter than protons and thus acquire velocities approximately three orders of magnitude higher for the same momentum. Therefore, the rapidly moving electrons can almost instantly react to the slowly changing nuclear geometry and as such fulfill the adiabatic theorem.[1] Vice versa, the nuclei "feel" only the mean field generated by the electrons. This leads to adiabatic separation of $\Psi_i\left(\boldsymbol{R},\boldsymbol{r}\right)$ into electronic part $\psi_i^e\left(\boldsymbol{r};\boldsymbol{R}\right)$ and nuclear part $\Theta_i^n\left(\boldsymbol{R}\right)$ for solving the time-independent Schrödinger equation 1.4b. In adiabatic approach, first the nuclear motion is frozen to get a solution $\psi_i^e\left(\boldsymbol{r};\boldsymbol{R}\right)$ for the so-called electronic Hamiltonian $\hat{H}_e(\boldsymbol{r};\boldsymbol{R})$[1]

$$\begin{aligned}\hat{H}_{mol}(\boldsymbol{R},\boldsymbol{r}) &= \hat{T}_n(\boldsymbol{R}) + \hat{T}_e(\boldsymbol{r}) + \hat{V}_{ee}(\boldsymbol{r}) + \hat{V}_{en}(\boldsymbol{r},\boldsymbol{R}) + \hat{V}_{nn}(\boldsymbol{R}) \\ &= \hat{T}_n(\boldsymbol{R}) + \hat{H}_e(\boldsymbol{r};\boldsymbol{R}).\end{aligned} \tag{1.6}$$

Technically, we omit the nuclear motion operator (see eq. 1.6) and calculate the eigenstates $\psi_i^e(\boldsymbol{r};\boldsymbol{R})$ with frozen position of nuclei $\boldsymbol{R}$ corresponding to the the electronic energy $V_i(\boldsymbol{R})$

$$\xrightarrow[Adiab.\ Sep.]{} 1)\left[\hat{H}_e(\boldsymbol{r};\boldsymbol{R}) - V_i(\boldsymbol{R})\right]\psi_i^e(\boldsymbol{r};\boldsymbol{R}) = 0. \tag{1.7}$$

Secondly, we expand the molecular wavefunction into the electronic eigenstates $\psi_i^e(\boldsymbol{r};\boldsymbol{R})$ as

$$\Psi(\boldsymbol{R},\boldsymbol{r}) = \sum_i \Theta_i^n(\boldsymbol{R})\psi_i^e(\boldsymbol{r};\boldsymbol{R}), \tag{1.8}$$

and solve the time-independent Schrödinger's equation 1.4b to find the expression for the expansion coefficients $\Theta_i^n(\boldsymbol{R})$,[24] which are identified with nuclear wavefunctions

$$\begin{aligned}\left[-\sum_I \frac{\hbar^2}{2m_I}\frac{\partial^2}{\partial R_I^2} + V_i(\boldsymbol{R}) - E_i\right]\Theta_i^n \\ -\sum_{j,I}\frac{\hbar^2}{2m_I}\left[\langle\psi_i|\frac{\partial}{\partial R_I}|\psi_j\rangle\frac{\partial}{\partial R_I} + \langle\psi_i|\frac{\partial^2}{\partial R_I^2}|\psi_j\rangle\right]\Theta_j^n = 0.\end{aligned} \tag{1.9}$$

In the Born-Oppenheimer approximation, we can neglect the kinetic coupling between the electrons and nuclei in the second term, which leads to a set of uncoupled equations for the nuclear wavefunction $\Theta_{i\nu}^n(\boldsymbol{R})$ related to particular electronic energies $V_i(\boldsymbol{R})$

$$\xrightarrow[Born.\ Oppen.]{} 2)\left[\hat{T}_n(\boldsymbol{R}) + V_i(\boldsymbol{R}) - E_{i\nu}\right]\Theta_{i\nu}^n(\boldsymbol{R}) = 0. \tag{1.10}$$

The index ν comes for distinct solutions of nuclear wavefunction on the same electronic potential $V_i(\boldsymbol{R})$. The representation of the time-independent molecular wavefunction in equation 1.8 is called adiabatic and the potentials $V_i(\boldsymbol{R})$ are correspondingly called adiabatic potentials. In summary, in case of a weak (and slow in time-domain) kinetic coupling between the electrons and nuclei, the probability for a transition from one to another electronic state is low and thus we can work with the independent set of electronic states belonging to a particular adiabatic potential $V_i(\boldsymbol{R})$. The Born-Oppenheimer approximation is valid if the coupling between the states is much less than the energetic separation between two electronic states

$$\langle\Theta_{i\nu}^n|\left(-\langle\psi_i|\hat{T}_n(\boldsymbol{R})|\psi_j\rangle + \frac{\hbar^2}{2}\sum_I\frac{1}{M_I}\langle\psi_i|\frac{\partial}{\partial R_I}|\psi_j\rangle\frac{\partial}{\partial R_I}\right)|\Theta_{j\mu}^n\rangle \ll |E_{i\nu} - E_{j\mu}|. \tag{1.11}$$

The condition is usually not fulfilled when two distinct electronic states are close to each other in order of vibrational energies.

In the case of a diatomic molecule, the two potentials of the same electronic symmetry are not allowed to cross, which results in the *avoided crossing* as is shown in the figure 1.2 a).[1]

1.2.2 Diabatic Representation

Typically, the states exchange their characters like symmetry or polarity in the region of avoided crossing. This rapid change of the electronic wavefunction behavior on a relatively small space might be a reason for the increase of the coupling elements. In such a case described by adiabatic representation, the motion of electrons and nuclei cannot be further separated and the $\hat{T}_n(\boldsymbol{R})$ operator leads to non-diagonal elements of molecular Hamiltonian, which enables the transition among the different states corresponding to different electronic potentials $V_i(\boldsymbol{R})$

$$\sum_{\nu} \Psi_{i\nu}(\boldsymbol{R}, \boldsymbol{r}) \rightarrow \sum_{j \neq i, \mu} \Psi_{j\mu}(\boldsymbol{R}, \boldsymbol{r}). \tag{1.12}$$

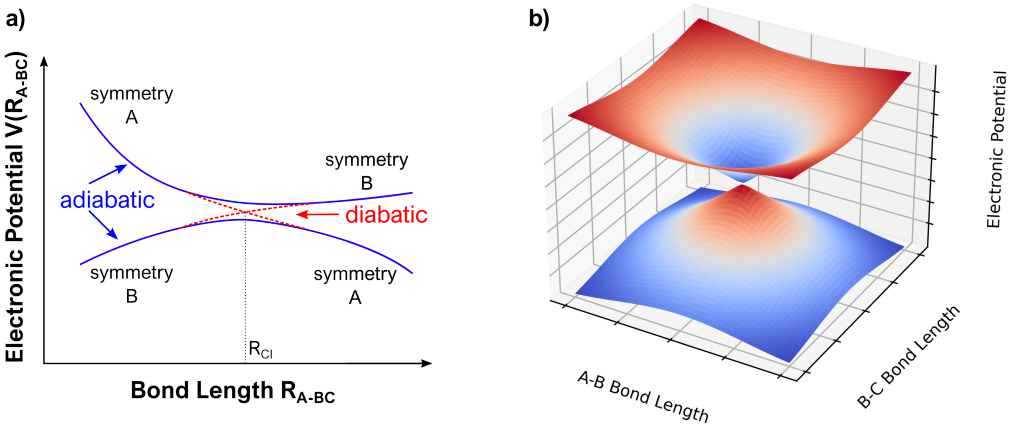


Figure 1.2: Schematic pictures of a) cut through the adiabatic and diabatic potentials and b) conical intersection.

The adiabatic representation is inconvenient for the description of the wavefunction as the coupling between the motions of electrons and nuclei increases, and therefore the diabatic representation is used instead. The task is to find the representation where the second term of equation 1.9 is as small as possible. Contrary to the adiabatic representation, the diabatic representation can be adjusted according to the specific topology of the investigated system. There are several approaches on how to find the best representations.[1, 25, 26] One way is to expand the molecular wavefunction in the electronic basis functions, which are independent of the position of nuclei as

$$\Psi\left(\boldsymbol{R}, \boldsymbol{r}\right) = \sum_{i} \psi_i^e\left(\boldsymbol{r}; \boldsymbol{R_0}\right) \Theta_i^n\left(\boldsymbol{R}\right), \tag{1.13}$$

where the $\psi_i^e\left(\boldsymbol{r}; \boldsymbol{R_0}\right)$ are eigenstates of the electronic Hamiltonian at the nuclear geometry $\boldsymbol{R_0}$. Substituting the diabatic representation into the time-independent Schrödinger equation 1.4b we get corresponding expression to equation 1.9 in diabatic approach

$$\begin{aligned}\left[-\sum_I \frac{\hbar^2}{2m_I}\frac{\partial^2}{\partial R^2} + V_i(\boldsymbol{R_0}) - E_i\right]\Theta_i^n \\ + \left[\langle\psi_i^e|\tilde{V}(\boldsymbol{r}, \boldsymbol{R}) - \tilde{V}(\boldsymbol{r}, \boldsymbol{R_0})|\psi_j^e\rangle\right]\Theta_j^n = 0.\end{aligned} \tag{1.14}$$

The second term marked as $\tilde{V}^d$ covers all the Coulomb interactions. Its diagonal elements $\tilde{V}^d_{ii}$ represent the PESs in diabatic representation, whereas, the coupling among the states are caused by the non-diagonal elements $\tilde{V}^d_{ij}, i \neq j$.[26, 1] The diabatic potentials are marked as the red dashed lines in figure 1.2 a).

1.2.3 Conical Intersection

For a model of diatomic molecules with two PES of the same symmetry,[26, 27] the coupling matrix $\tilde{V}^d$ has 2×2 structure

$$\tilde{V}^d = \begin{pmatrix} \tilde{V}_{11} & \tilde{V}_{12} \\ \tilde{V}_{21} & \tilde{V}_{22} \end{pmatrix} \xrightarrow[N=2]{} \begin{pmatrix} E_c + p_1 & p_2 \\ p_2 & E_c - p_1 \end{pmatrix}. \tag{1.15}$$

We can evaluate the adiabatic PES from diagonalization of the matrix and consequently calculate the energy separation of the two adiabatic states

$$\Delta\tilde{V}^d = \sqrt{\left(\tilde{V}^d_{11} - \tilde{V}^d_{22}\right)^2 + 4|\tilde{V}^d_{12}|^2} \xrightarrow[N=2]{} 2\sqrt{p_1^2 + p_2^2}., \tag{1.16}$$

and therefore, the diatomic states in the crossing point would have to be degenerated but not coupled, which explains why the system with only one free parameter results in the avoided crossing.[26, 1] For polyatomic molecules with $N \geq 2$ free parameters, the condition $\Delta\tilde{V}^d = 0$ can be fulfilled on the $N-2$ dimensional surface. There the states are degenerated for the given nuclear geometries, which is called *conical intersection* (CI).

A simplified example of CI is the case of a two-dimensional system, e.g., two bond distances, described by the second parts of equations 1.15 and 1.16. As a result, the PES surfaces intersect at one point, which is shown in the figure 1.2 b). CIs enable fast relaxation between the electronic states through internal conversion. The radiationless deexcitation is essential for the stability of many biological systems like DNA as they can rapidly relax to the ground state before the fragmentation.[1, 8, 28]

Formally, the same approach can be applied for the time-dependent Hamiltonian to address the adiabatic, or non-adiabatic dynamics. The system described by time-dependent wavefunction $\Psi_i(t)$ will undergo adiabatic dynamics if the perturbation is evolving slowly as described by the adiabatic criterion[29]

$$\langle\Psi_i|\frac{\partial\hat{H}}{\partial t}|\Psi_k\rangle \ll \frac{E_{ik}}{\tau_t}. \tag{1.17}$$

The probability of non-adiabatic transition is dealt by Landau-Zener expression for two diabatic potentials with constant slope $|\gamma|$ as[27]

$$P_{\text{non-adia.}} = 1 - \exp\left(-2\pi\omega_{12}\tau_t\right) = 1 - \exp\left(-2\pi\frac{V_{12}^2}{\hbar|\gamma|}\right), \tag{1.18}$$

where the τ_t is characteristic time for the transition through the crossing region, ω_{12} is Rabi frequency and the V_{12} is coupling element among the two potentials.

1.3 Singlet-Triplet Transitions

The previous paragraphs discuss the molecular electronic states and their mutual interactions without considering their electronic spin character. This chapter will bring a brief theoretical background for spin-altering processes in the photofragmentation of molecules.

The molecular eigenstates of Hamiltonian in non-relativistic approximation can be represented through expansion in Slater determinants, where each electron is assigned to single-electron spin-orbital wavefunction separately dependent on its spatial and spin coordinates $\psi(r_k, s_k) = \phi(r_k)\sigma(s_{z_k})$.[24] The notation of wavefunction in the determinant expression guarantees the fulfillment of the anti-symmetry character requirement coming from the Pauli principle. Most of the molecules in their ground state have the spins of their electrons compensated, which classifies them according to the multiplicity as the singlet states ($S = \sum_i s_{z_i} = 0 \Longrightarrow 2S + 1 = 1$). On the contrary, some excited states have non-compensated electron spins, e.g., a molecule with a pair of non-compensated electron spins yields the triplet state ($S = 1 \Longrightarrow 3$).

In the non-relativistic approximation, the Hamiltonian is commuting with the operators of total electron spin $\hat{\boldsymbol{S}}^{\boldsymbol{2}}$ and spin projection $\hat{\boldsymbol{S}}_{\boldsymbol{z}}$ and therefore share the same set of eigenfunctions. The selection rules can be derived from the expression for the photon transition by Fermi's golden rule (see eq. 1.5) in the Born-Oppenheimer approximation as[24]

$$\langle \Psi_f | \hat{\boldsymbol{\mu}} | \Psi_i \rangle = \int \Theta_f^{n*} \Theta_i \, \boldsymbol{dR_n} \int \psi_i^{e*} \hat{\boldsymbol{\mu}}_{\boldsymbol{e}} \psi_f^e \, \boldsymbol{dr} \int \psi_f^{s*} \psi_i^s \, \boldsymbol{d\tau_s}, \tag{1.19}$$

where the terms are ordered as vibrational, orbital, and spin (sometimes the first two terms are combined to a single vibronic term due to the electron-nuclear coupling). The spin term is equal to zero for the states with different multiplicities due to the orthogonality of spin wavefunctions. Therefore, the transitions between the states with different multiplicity is strictly forbidden. Of course, the expression 1.19 was derived with many approximations. However, the result explains why an absorption probability of spin forbidden transitions is usually lower by many orders of magnitude compared to fully allowed, or orbital forbidden transitions.

The inclusion of relativistic effects through Pauli approximation of molecular Hamiltonian yields two spin coupling terms: a) spin-orbit coupling and b) spin-spin coupling. Although the resulting energy shift is rather low, their impact on the calculation of oscillator strength for singlet-triplet transitions is substantial.[24]

1.3.1 Spin-Orbit Coupling

Spin-orbit coupling (SOC) arises from the interaction between the electron spin magnetic momentum and orbital magnetic momentum.[30, 31] The SOC increases with atomic number (and charge) and contraction of electron orbitals due to the origin of the coupling in magnetic field induced by electron moving in Coulomb potential of atomic nuclei. This is reflected in the approximated expression for

SOC by the semiempirical effective charge Z^{ef} [30]

$$\hat{H}_{SO} = \frac{e^2}{2m^2} \sum_I \sum_i \frac{Z_I^{ef}}{r_{iI}} \hat{\boldsymbol{l}}_{\boldsymbol{i}} \cdot \hat{\boldsymbol{s}}_{\boldsymbol{i}}, \tag{1.20}$$

where we sum over single-electron operators of electron spin $\hat{\boldsymbol{s}}_{\boldsymbol{i}}$ and orbital angular momentum $\hat{\boldsymbol{l}}_{\boldsymbol{i}}$ divided by distances between electrons and nuclei r_{iI} (other two-electron interactions are included in effective charge Z_{ef}). The SOC term enables coupling among the states with the change in total spin angular momentum equal to $\Delta S = 0, \pm 1$, e.g., triplet-singlet transition. Expansion of electronic Hamiltonian with the spin-orbit perturbation term generates a new set of the electronic eigenfunctions, which are further not the eigenfunctions of $\hat{\boldsymbol{S}}^{\boldsymbol{2}}$ and $\hat{\boldsymbol{S}}_{\boldsymbol{z}}$. Therefore, the spin selection rule is not valid and the non-diagonal coupling elements of Hamiltonian can be non-zero for the states with different multiplicity.

The singlet states thus can borrow some of the triplet state character and contrary, the triplet states can borrow the character of singlet states[32, 24, 1]

$$\Psi^S \xrightarrow{SOC} \Psi^S + \gamma_S \Psi^T, \quad \Psi^T \xrightarrow{SOC} \Psi^T + \gamma_T \Psi^S, \tag{1.21}$$

where $\gamma_{S/T}$ are coupling coefficients usually much smaller than one. The resulting oscillator strength among the perturbed singlet $\Psi^{S'}$ and triplet $\Psi^{T'M_s}$ states described by the equation 1.5 is proportional to [33, 24]

$$\begin{aligned} \langle \Psi^{S'} | \hat{\boldsymbol{\mu}}_{\boldsymbol{e}} | \Psi^{T',M_s} \rangle = & \sum_k \frac{\langle \Psi_k^S | \hat{H}_{SO} | \Psi^{T,M_s} \rangle}{E^T - E_k^S} \langle \Psi^S | \hat{\boldsymbol{\mu}}_{\boldsymbol{e}} | \Psi_k^S \rangle \\ & + \sum_l \frac{\langle \Psi_l^{T,M_s} | \hat{H}_{SO} | \Psi^S \rangle}{E^S - E_l^T} \langle \Psi^{T,M_s} | \hat{\boldsymbol{\mu}}_{\boldsymbol{e}} | \Psi_l^{T,M_s} \rangle. \end{aligned} \tag{1.22}$$

Transition energy is thus given by the unperturbed states, whereas the intensity and polarization come from singlet-singlet and triplet-triplet transitions. The spin-orbital Hamiltonian $\hat{H}_{SO}$ is transformed according to the total symmetric irreducible representation of symmetric group belonging to a given molecule. Therefore the direct involvement of spin-orbital interaction enables only transitions among the states with the same symmetry. This can be bypassed when the vibration coupling is included. The previously idealized electronic Hamiltonian for the static geometry of nuclei can be expanded in Taylor series around the equilibrium position of normal coordinates $\boldsymbol{R}$ as[24]

$$\hat{H}^e(\boldsymbol{R}) = \hat{H}_0^e + \hat{H}_{SO} + \sum_I \left(\frac{\partial \hat{H}_0^e}{\partial R_I} \right) R_I + \sum_I \left(\frac{\partial \hat{H}_{SO}}{\partial R_I} \right) R_I, \tag{1.23}$$

which brings a new interaction term SOCv to couple the states with different multiplicity.

If the first order SOC and SOCv are too weak or forbidden by symmetry, the spin-spin coupling (SSC) can cause the multiplicity to change $\Delta S = 0, \pm 2$. SSC arises from the interaction of two electronic spins, and its role is suggested in triplet-triplet annihilation and reverse singlet fission. The SSC interaction couples the molecules in complex with a combined spin state, e.g., molecules in singlet and doublet states yield doublet, and triplet with doublet states yield

quartet or doublet. The perturbation from paramagnetic molecules thus induces the spin-forbidden transitions as it is in the case of the well-known example of molecular oxygen.[24, 34]

Other electron spin coupling terms also come from higher-order perturbation or interaction with the nuclear spin. However, these go far beyond the focus of this thesis.[33]

1.3.2 Intersystem Crossing

The previous paragraphs give theoretical support for observation of singlet-triplet transitions in absorption spectra. In an analogical way, we can derive formally similar expression for the rate of internal conversion and *intersystem crossing* (ISC) for non-adiabatic spin-conserving and -altering izoenergetic transitions, respectively. In Condon approximation of small change of the electronic coupling upon the nuclear distortion, the formula can be written as [33, 24]

$$k_{ISC} = \frac{2\pi}{\hbar}|\langle\psi_i^S|\hat{H}_{SO}|\psi_f^T\rangle|^2 \sum_{\nu} |\langle\Theta_{i\nu_0}|\Theta_{f\nu}\rangle|^2 \delta(E_{i\nu_0} - E_{f\nu}). \tag{1.24}$$

This expression fails for the strong coupling of electronic states or ultrafast non-adiabatic transitions through CIs,[33] where non-adiabatic nuclear dynamics simulations must be applied to solve this issue. The generalized El-Sayed rules for ISC can be derived through investigation of the coupling term $\langle\psi_i^S|\hat{H}_{SO}|\psi_f^T\rangle$. [33, 24] A simplified version says that the ISC is efficient only between the singlet and triplet states with different single excited configurations localized on the same center.[32, 35, 33]

The relaxation trough ISC is especially common for the molecules containing atoms with a high atomic number like halogens. Usually, a molecule relaxes to the first excited singlet state by vibrational or internal conversion, where it undergoes ISC to a closely lying triplet state. There are well-known examples of metal-containing tetrapyrrole molecules[3, 4] with a high quantum yield of phosphorescence, or halogenated molecules with iodine, bromine and chlorine ($I \gg Br > Cl$), where the relaxation pathway through ISC is competitive to other radiative or non-radiative relaxation processes as is illustrated on one of our model systems in chapter 3.2.1. The heavy atom effect can also externally affect the ISC rate, as is known from the halogen-containing environment.[36]

The discussion of our experimental results in chapter 3 requires basic knowledge of the wavefunction representations, PES, and internal conversion or ISC transitions delivered in the above chapters. Nevertheless, to better understand investigated systems, we had to employ advanced MD simulations through collaborations with theoretical physicists.[6, 37] The simulations offer a deep insight into the photodynamics of PES thanks to the high computing power of computer technology. However, there are still simple classical mechanics models, which cannot deliver the complete picture of investigated processes but can be helpful for experimental physicists to describe the redistribution of the excess energy among the recoiling fragments.

1.4 Classical Mechanics Models

Interpretation of the fragmentation through the approximative classical mechanics is based on conservation laws. The fragmentation models must obey the energy conservation described with equation 1.3 supplemented by the conservation laws of linear momentum and angular momentum.[38, 39, 40] In the inertial frame of center-of-mass, the excess energy E_{excess} originated from the internal energy of parent molecule E^i_{int} and photon $h\nu$ is partitioned among the translational energy E_{tr} and internal excitation E^f_{int} of recoiling fragments. The velocity-resolved experiments enable us to detect the translational energy distribution, which might come not only from the excess energy redistribution but also from the initial distribution of parent internal energy $P(E^i_{int})$. Therefore, the supersonic expansion will be introduced in chapter 2.1.1 for efficient cooling of the parent molecules together with unification of their velocities. Here we discuss only the idealistic case of $E^i_{int} = 0$. On the product side of equation 1.3, the fragment internal energy E^f_{int} is partitioned into the vibrational E_{vib}, rotational E_{rot} or electronic excitation E_e. The precise assignment of E^f_{int} to the particular modes requires the application of various spectroscopic methods or advanced *ab initio* calculations.[1, 9]

Alternative estimation can be obtained from statistical models.[40] The necessary assumption is that the excitation lifetime is long enough to randomize excess energy among the internal modes. The statistical assumption can be used before or after fragmentation. The former case is related to the R.R.K.M. theory for unimolecular dissociation.[41, 38] Whereas the latter case weighs all possible fragmentation channels with restrictions given by conservation laws.[42, 43, 38] For the rapid fragmentation without the possibility of evolving into equilibrium, there are direct models that can describe the limit situations of no- and maximal-energy partitioned into the internal modes of recoiling fragments.

1.4.1 Hard Sphere Model

An idealistic picture of fast direct dissociation can be treated with the two-body model of hard spheres. The situation is illustrated in figure 1.3 a).[9] In this model, all the excess energy is departed into the produced fragments' kinetic energy, and the internal modes are neglected. The fragment velocities must be equal to the reverse ratio of their masses $v_A/v_B = m_B/m_A$ to fulfill the conservation of linear momentum. If we measure the velocity of one type of fragments, we can easily calculate the velocity of co-fragments or total kinetic energy as

$$E_{tr} = \frac{1}{2}m_A v_A^2 + \frac{1}{2}m_B v_B^2 = \frac{1}{2}m_1 v_A^2 \left(1 + \frac{m_A}{m_B}\right) = E^A_{tr}\left(1 + \frac{m_A}{m_B}\right), \qquad (1.25)$$

where we just combined the conservation of energy with the conservation of linear momentum. Reversely, the knowledge of dissociation energy and photon energy enables us to evaluate the maximal limit of the velocity for the two-body dissociation.

1.4.2 Spectator Model (Pure Impulsive)

For the model situation of dissociating three atomic molecule, e.g., A-BC molecule from equation 1.1, the repulsive force and bending torque can induce rotational

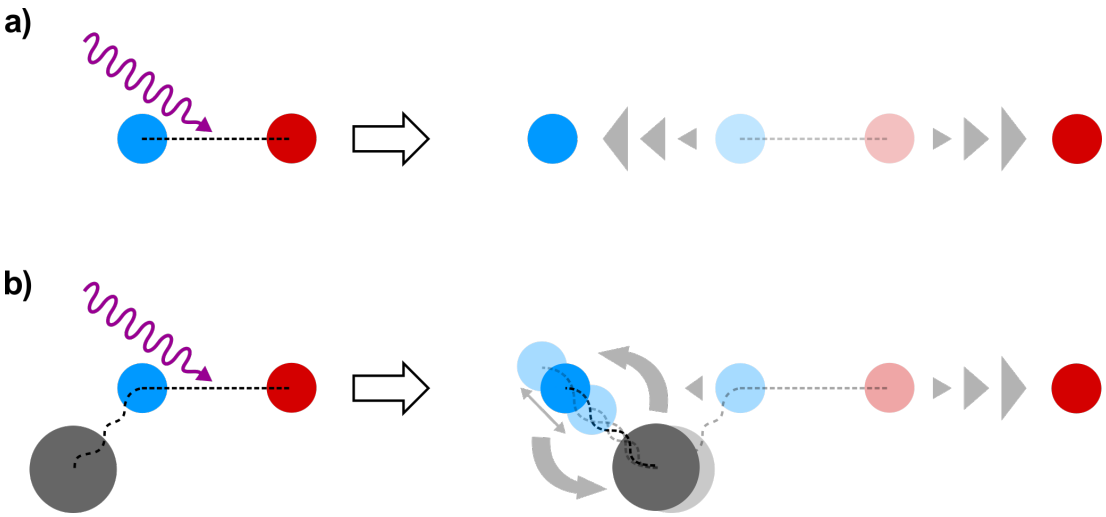


Figure 1.3: Schematic illustrations of a) hard-sphere and b) spectator models derived from classical mechanics.

and vibrational excitation in the BC fragment, see figure 1.3 b).[1] The idea behind the spectator model in case of sharp dissociation is that the impulse is firstly distributed between the A and B atoms and atom C is only a spectator.[38] In the second step, the linear momentum of B atom is shared with the atom C to obey the conservation of linear momentum $\boldsymbol{p_A} + \boldsymbol{p_{BC}} = 0$. It can be easily derived that the resulting translational energy is

$$E_{tr} = \left(\frac{\mu_0}{\mu_{A-BC}}\right) E_{excess} \Longrightarrow E_{int}^{BC} = \left(1 - \frac{\mu_0}{\mu_{A-BC}}\right) E_{excess} \tag{1.26}$$

where the μ_0 is the reduced mass of the A and B atoms, and μ_{A-BC} is the reduced mass of the A and BC fragments. Correspondingly, the energy imparted into the rotational and vibrational modes E_{int}^{BC} is equal to the difference between the excess energy and translational energy. As a consequence of the conservation of angular momentum, we can further estimate the branching between the vibrational and rotational energy as [40, 38]

$$\frac{E_{vib}^{BC}}{E_{rot}^{BC}} = \frac{\cos^2\theta}{\sin^2\theta}, \tag{1.27}$$

where θ is an angle $\angle ABC$. The spectator model fits the situations where a heavy atom recoils from a flexible molecular chain like in the case of iodoalkanes.[38] However, this model is not reasonable for molecules with stiffly bonded heavy atoms, e.g., NO_2 dissociation.[40] There, we can assume that all the excess energy will be distributed into rotational and translational energies according to the formulas for the rigid rotor model described in [40, 38].

The above models can be further upgraded to fit the observed data, e.g., by incorporating the equilibrium geometry of the dissociating molecule in the initial and excited state. However, such models risk over-interpretation, and their connection to real dissociation dynamics is disputable.

We can learn about the fundamental laws of physics and chemistry through research of isolated molecules, however, the molecules even in the interstellar space medium are barely isolated.

1.5 Clusters

Molecules situated in the environment are exposed to the mutual interaction with other molecules, significantly influencing their structure, phase, and chemistry. Clusters formed by two to thousands of molecules represent a model system for a detailed investigation of the role of the environment in bulk. Moreover, the clusters in the form of aerosols and nanoparticles seem to have a non-negligible impact on atmospheric and space chemistry and physics, and thus research focused directly on cluster-induced heterogeneous chemistry is of our great interest. Cluster role in the depletion of ozone, global radiation budget linked with global warming, greenhouse gas chemistry, precipitation, and industrial and traffic pollution is already known, although in many aspects still not well understood.[12, 10, 18]

Supersonic expansion in vacuum chambers (see chapter 2.1.2 for details) enables us to produce isolated clusters to mimic the aerosols and apply the mass spectrometric and single-molecule laser techniques. This is especially beneficial for the detailed study of small clusters, which are difficult to probe directly in the Earth's atmosphere or the atmospheric simulation chambers. [12] Furthermore, the cluster beam generation can be followed by the uptake of other molecules, scattering experiments, and interaction with electrons or photons to trigger particular processes.[12]

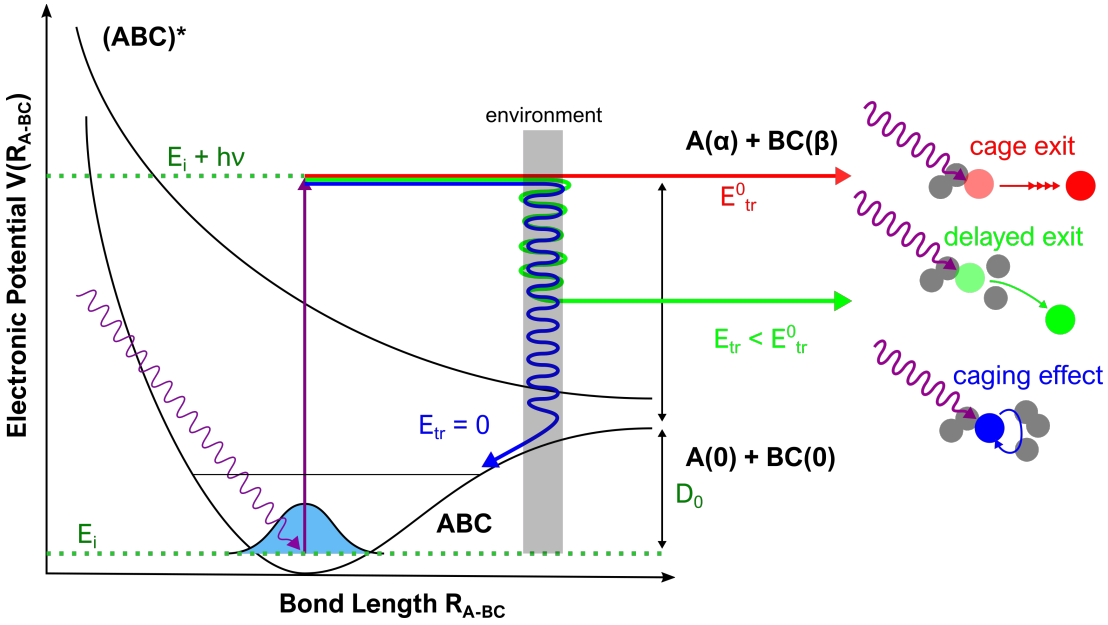


Figure 1.4: Photodissociation in environment. Three basic scenarios of cage exit (red), delayed exit (green) and caging effect (blue) are illustrated on the right side. The picture was taken and redrawn from [18].

Photodissociation outcomes in the cluster environment can be substantially stirred in various ways. The molecule embedded within the cluster is interacting with surrounding molecules, which leads to significant changes in its geometry, shifts in absorption spectra, and even new orchestrated photochemistry.[44, 45] Moreover, the rate of relaxation from highly vibrationally and rotationally excited states of the parent molecule is enhanced by environmental perturbation.

From the detection view, the ejected fragments must first get out of the cluster

to be detected, as is illustrated in the figure 1.4.[45] The environment is schematically drawn as a grey barrier in the PES scheme. Some of the fragments marked by the red arrow (cage exit) can be detected without any change compared to the isolated molecules. Others marked with the green arrow (delayed exit) are slowed down by inelastic collisions, which also makes their angular distribution more isotropic. If there is not enough kinetic energy to leave the cluster, the radicals can react with other molecules or recombine with co-fragment to the parent molecule's highly vibrationally excited state, which is marked with the blue arrow (caging effect).

1.5.1 Effects of Environment on Photodissociation: Clusters as Environment Model

Most of the atmospheric aerosols are built from water molecules incorporated with other atmospherically relevant molecules, e.g., nitric (HNO_3) or sulfuric (H_2SO_4) acids and halogen-containing molecules. A typical example are polar stratospheric clouds (PSCs), which play an important role in damaging the stratospheric ozone layer. There are two types of PSCs divided according to their composition. The rare pure water clusters are called PSCs type II,[46, 47] whereas most clouds in the stratosphere are formed in liquid super-cooled phase with an admixture of H_2SO_4 and HNO_3 (PSCs Ib).[12, 48, 47, 46] Other types marked as Ia and Ic consist of a mixture of water with nitric acid trihydrate and metastable water-rich HNO_3 in the solid-state, respectively.[12, 48] The acids play a crucial role in the life of aerosols as they were proposed as a growth nucleus for cloud formation in the troposphere.[10, 49, 50]

The ozone depletion process above Antarctica is linked to the interplay of PSCs and halogen-containing molecules, e.g., freon CF_2Cl_2.[51, 12] Their high stability allows them to reach stratospheric altitudes, where they are stripped of Cl radicals by solar UV radiation.[12] The highly reactive Cl radicals react with surrounding ozone in several cycles until they undergo a reaction pathway producing the so-called reservoir species like HCl, ClO, or $ClONO_2$.[52] The heterogeneous chemistry of these compounds on PSCs produces the photolyzable Cl_2 molecules, which are released into the atmosphere during the Antarctic spring and again take part in ozone depletion.[12] PSCs also enhance the efficiency of ozone depletion through uptake of nitrogen-containing molecules, which can deactivate the ClO compounds from further involvement in ozone depletion.

The clusters are not only connected to Earth's atmosphere, but they are well known from the astronomical observations of interstellar space medium (ISM).[16, 53] The ISM is stuffed with a broad inventory of rather complex species, which require some rich and specific chemistry. The ISM molecules meet with harsh conditions of low temperatures combined with a low density of reaction partners, which eminently lowers the chance for the necessary chemistry.[16] The clusters in the form of interstellar dust particles were proposed as a possible source of the complex molecules through the combination of heterogeneous chemistry and ion-molecule reactions.[16, 10] The up-taken molecules are exposed to the cosmic radiation that generates secondary species like radicals and ions, which can react with surrounding molecules in close vicinity. The ISM molecules might also be used as probes for the distant parts of our galaxy to reveal the chemical evolution

of the universe.[16]

The mid-IR spectroscopic observations estimate that around 15% of carbon in ISM is stored in polyaromatic hydrocarbons (PAHs).[16, 53] The spectra reveal strong bands of vibrational modes identified as the stretching of C-H and C-C bonds and bending motions of the PAH species.[16] Also, there are spectroscopic signs of PAH clusters represented by broad plateaus in mid-IR spectra. PAHs are often abundant in the same areas as fullerenes.[16] This indicates that there might be similar chemistry behind their synthesis. The research of ISM PAHs is currently a hot topic in space chemistry research as the James Webb Space Telescope (NASA), designed for the observations in IR spectral range, was successfully launched into Earth's orbit at the beginning of 2022.[54] However, PAHs are also common as environmentally harmful pollutants due to the incomplete combustion of coal, tar, and biofuels, which make them also relevant for our Earth's atmospheric chemistry research.[17] We can generate the isolated or clustered PAHs with supersonic expansion and probe them with lasers and electrons in conditions similar to ISM. The vacuum chamber conditions also allow us to investigate the pickup of other molecules, their coagulation, and electron- or photon-induced reactions.[12, 15]

All the above mentioned molecular systems are noted in a broader perspective as a motivation for the chapter 3, where we discuss the results of our investigation on vibrational mediated dissociation of pyrrole, UV dissociation of selected chloroalkanes as isolated molecules and clusters, and the elementary steps in cluster growth on aromatic hydrocarbons.

2. Methods and Experiments

"He who wishes to be obeyed
must know how to command."

Machiavelli
The Prince

The old desire for a complete knowledge of the reactants and their reactions pathways and the ability to drive the reactions to the intended products sounds almost feasible due to the current technological advancements in laser techniques, electronics, and detection systems. Here we present mass spectrometry (MS) techniques, which we applied primarily to investigate photodissociation, clustering, or molecular uptake in selected molecular systems. First, the supersonic beam expansion, which is crucial in the preparation of the isolated particles for the next step of precisely tuned photon- or electron-induced processes, is discussed in the next chapter 2.1. Then, the applied MS for detection of the reaction products is introduced in chapter 2.2 linked to chapter 2.3 about the velocity map imaging (VMI) technique, which provides the kinetic energy and angular distributions of recoiling fragments. The other chapters are dedicated to the description of the design and application of MS experimental methods in our two apparatuses, AIM ("Apparatus for IMaging") and CLUB ("CLUster Beam apparatus").

2.1 Introduction to Molecular Beams

Kinetic gas theory gives us a great tool to calculate all mean properties, or at least their good estimation, for gas in equilibrium. The equilibrium is maintained by energy and linear momentum transfer by permanent collisions among the particles.[2, 18] Upon these collisions, the particle energy is redistributed among the translational, vibrational, and rotational modes. The particle velocities follow the Maxwell-Boltzmann distribution, which describes the magnitude of the particle velocity v with mass m at thermodynamic temperature T according to the formula

$$f(v)\,dv = \frac{4}{\sqrt{\pi}}\left(\frac{m}{2k_BT}\right)^{3/2} \cdot v^2 \cdot \exp\left(-\frac{mv^2}{2k_BT}\right) dv, \tag{2.1}$$

where k_B is Boltzmann constant.

Kinetic gas theory can be practically applied for the gas expanded under effusive beam conditions given by Knudsen number $K = \lambda/d \gg 1$, which is equal to the inverse number of collisions in the aperture vicinity. In other words, if the mean free path λ of the molecules colliding with Maxwellian speed distribution is much longer than the characteristic size of the nozzle d. We can estimate the expected flow rate, velocity, and angular distribution of the expanded beam for such conditions,[55, 2] which is well suited for rare and expensive samples [2, 18] or investigation of cluster nucleation.[56, 57, 58]

Unfortunately, the beautiful and absolute world of "equilibrium" gives some fundamental disadvantages in experiments with isolated molecules and clusters.

In the figure 2.1, we can see that the Maxwellian distribution $f(v)$ (blue) has a broad full width at half maximum (FWHM). This can be illustrated on argon gas with the most probable speed equal to $353\,\mathrm{m\,s^{-1}}$ at room temperature. However, around $\sim 5\%$ of Ar atoms are present with speed two times higher. Such a big variance may appear as a blurring due to the initial velocities, which lowers the resolution of the measured VMI images or mass spectra. Another bottleneck are the collisions after expansion, which can quench the laser-prepared states and rule out the experiments with isolated molecules. Finally, the excitation in rotational modes and bending vibrations can be quite abundant in normal conditions, and this can lower the sensitivity and cause signal interference in spectroscopic experiments, vibrationally mediated experiments, and quantitative measurements. The generation of molecular beams can bypass all the problems mentioned above by a method of supersonic expansion (also known as "free-jet expansion" or "nozzle expansion" in literature).[18, 2, 1]

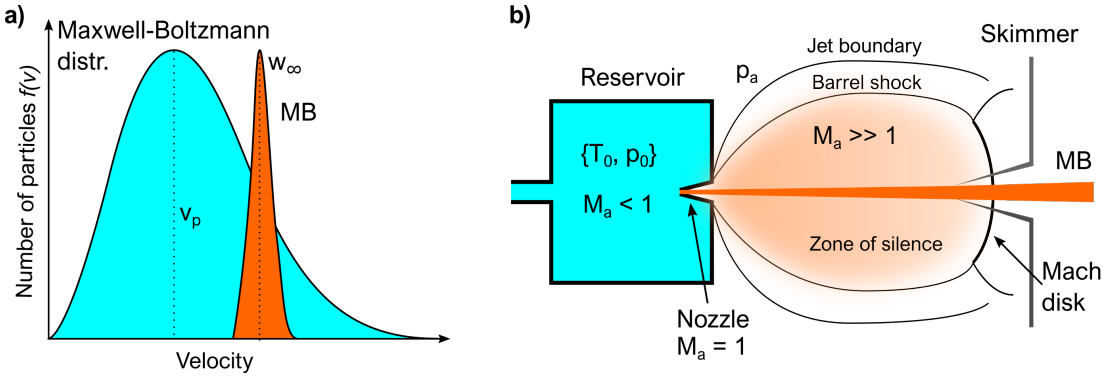


Figure 2.1: a) Velocity distributions of molecules in equilibrium and molecular beam (MB). b) Schematic illustration of supersonic expansion into MB with description. The images were modified from [2, 18].

2.1.1 Molecular Beams by Supersonic Expansion

To perform supersonic expansion, the expanded gas in the reservoir must undergo transfer between the reservoir (T_0, p_0) and source chamber (p_a) with an abrupt pressure change $p_0 \gg p_a$ and a large number of collisions ($K \ll 1$). In conditions of instant interactions among the molecules, the description through the kinetic gas theory must be replaced for flow dynamics and thermodynamic equations.[2, 18] The initial equilibrium is disrupted, and at each point of the pressure gradient, a new local equilibrium is achieved. The pressure gradient accelerates the molecules up to the nozzle throat, where the molecules reach the local sonic speed.[2, 18] Furthermore, the critical condition must be fulfilled for further acceleration. If $p_0/p_a > ((\kappa+1)/2)^{\kappa/(\kappa-1)}$, where κ is the heat specific ratio, then the gas is under-expanded at the nozzle exit and later will further accelerate to supersonic speed. Otherwise, the subsonic expansion will occur. The expansion is illustrated in figure 2.1 b), where M_a is Mach number, which represents the ratio of directional velocity compared to the random thermal motion.

If we neglect the friction, heat exchange, effects of other external forces and assume the time-independent flow, we can consider the supersonic expansion as a

one-dimensional isentropic process and describe the energy exchange during the molecular flow through the energy conservation[2, 18]

$$h_0 = \frac{1}{2}w^2(x) + h(x) = \frac{1}{2}w_\infty^2, \tag{2.2}$$

where we defined h_0 as the enthalpy per mass unit of molecules in reservoir, $h(x)$ and $v(x)$ are enthalpy and velocity in position x, and w_∞ is limit velocity. For ideal gas, the enthalpy change can be expressed through the specific heat $c_p = k_b\frac{\kappa}{\kappa-1}$ in constant pressure as

$$\frac{w^2(x)}{2} = h(x) - h_0 = \int_{T(x)}^{T_0} c_p\, dT = c_p\left(T_0 - T(x)\right). \tag{2.3}$$

If all the thermal energy would be transferred to translational mode $T(x) = T_\infty = 0$, we can derive a formula for maximal molecular beam velocity $v_{MB} = w_\infty$ from above equations as

$$w_\infty = \sqrt{\frac{2k_BT_0}{m}\frac{\kappa}{\kappa-1}}. \tag{2.4}$$

This is an idealistic case. In reality, the molecules are cooling by collisions within the nozzle, but since the nozzle exit, the number of collisions decreases proportionally to the molecular density until the molecules freeze in the current state. The boundary when the collisions are not frequent enough to further change the molecular state is called quitting (or sudden freeze) surface and separates the two expansion regimes, i.e., the isentropic flow of gas medium and free molecules without mutual collisions.[2, 12, 18] The ensemble of expanded molecules therefore attain a non-equilibrium state with narrow velocity distribution, as shown in figure 2.1 a). In turn, we cannot define temperature as we know it from the equilibrium ensemble, and the description of the beam characteristics is far more complicated. For example, the quenching rate of rotational states is roughly $\times 100$ times more efficient than for the vibrational ones, which results in rotational and vibrational excitation corresponding to different temperatures. Similarly, the broadening of transverse and longitudinal velocities is different. The reason is the geometrical "cooling" of transverse velocity along the beam path.

One possibility to characterize the beam is to evaluate the speed ratio S, which is defined as the ratio of the molecular beam velocity v_{MB} and the remaining thermal energy α [18]

$$S = \frac{v_{MB}}{\alpha} \approx 2\sqrt{\ln 2}\frac{v_{MB}}{\Delta v_{MB}}, \tag{2.5}$$

where the second expression is an empiric formula with experimentally determined molecular beam velocity v_{MB} and its FWHM Δv_{MB}. This expression was used to calculate longitudinal speed ratios and temperatures in figure 2.2.

A schematic picture of the supersonic expansion is shown in figure 2.1. The expanded gas forms a gas cloud with three different regions characterized by corresponding Mach numbers. The middle region is the zone of silence, where free molecules are moving with supersonic speed ($M_a \gg 1$). For molecular beam generation, the skimmer must extract the supersonic molecules to another evacuated chamber. Otherwise, the expanded gas will end in a Mach disk shock wave with a discontinuous pressure increase and abrupt flow change.[2, 18] For more information about the shock wave physics see [2].

The supersonic beams offer many advantages compared to the effusive beams, e.g., narrow velocity distribution, small angular divergence, high intensity, and efficient cooling of internal modes,[18, 2] but in exchange for the high demands on the pumping speed to prevent scattering of the expanded gas behind the nozzle. In our experiments, we worked either with steady-state continuous mode or pulse mode. Whereas the pulse mode is not a huge burden for pumping speed in the source chamber, its reproducibility is rather low. Nowadays, there are also commercial pulse sources, which can be run with a high repetition rate up to 1 kHz and pulse width around 20 µs.[59] However, they are still rather expensive, and their use is mainly for isolated molecules and small cluster beams.[60] The reproducibility of the expansion conditions is essential for cluster generation. Therefore, the continuous beams are far more convenient in cluster experiments in exchange for the necessity of multi-stage differential pumping and lower signals.[12]

2.1.2 Cluster Beams by Supersonic Expansion

The path from atomic or molecular beams to cluster beams is straightforward. Usually, the clusters are an unwanted by-product of the supersonic expansion, and their generation is prevented by controlling the properties of an expanded sample, [6, 5] e.g., sample concentration, temperature, or pressure.[12, 10] It did not take long to realize that cluster beams offer by themselves a new opportunity to study the bulk interactions with the same methods, which were previously tested on single molecules and atoms. Moreover, the clusters can be applied to investigate heterogeneous catalytic chemistry or to mimic atmospheric aerosols.[10, 61]

The clustering during the supersonic expansion can be enhanced by conical divergent nozzles with a small sub-millimeter pinhole. Unfortunately, the small characteristic size d of such nozzles significantly complicates direct observation of clustering as most of the collisions during the expansion occur within tenths of the nozzle-skimmer distance.[12, 18] The skimmer position is constrained by the position x_{MD} of the Mach disk, which is described by the empiric formula as

$$x_{MD} = 0.67 \cdot \sqrt{\frac{p_0}{p_a}} \cdot d, \tag{2.6}$$

where the variables p_0 and p_a determine pressure conditions before and after the nozzle, respectively. Usually, the x_{MD} does not exceed 2-3 cm and consequently, the clustering is finished within 2-3 mm from the nozzle exit. Therefore, alternative experiments with expansion through Laval macroscopic nozzles are thus applied to study aerosol nucleation with x-ray, electron or neutron scattering and IR spectroscopy.[12, 58]

In our experiments, we also apply a pulsing jet for cluster generation. However, the pulsing creates unstable conditions during the expansion as shown in figure 2.2 and therefore, it can yield different cluster distributions in the initial, central, and final phases of the opening cycle as is reported in [5]. Therefore, substantial attention must be given to the synchronization of lasers and beam pulses in such an experiment.

Secondly, the selection of buffer gas can also trigger clustering through efficient collision cooling in co-expansion. Therefore, argon or xenon buffer gases are used to enhance the clustering, whereas low concentrations of samples in light helium

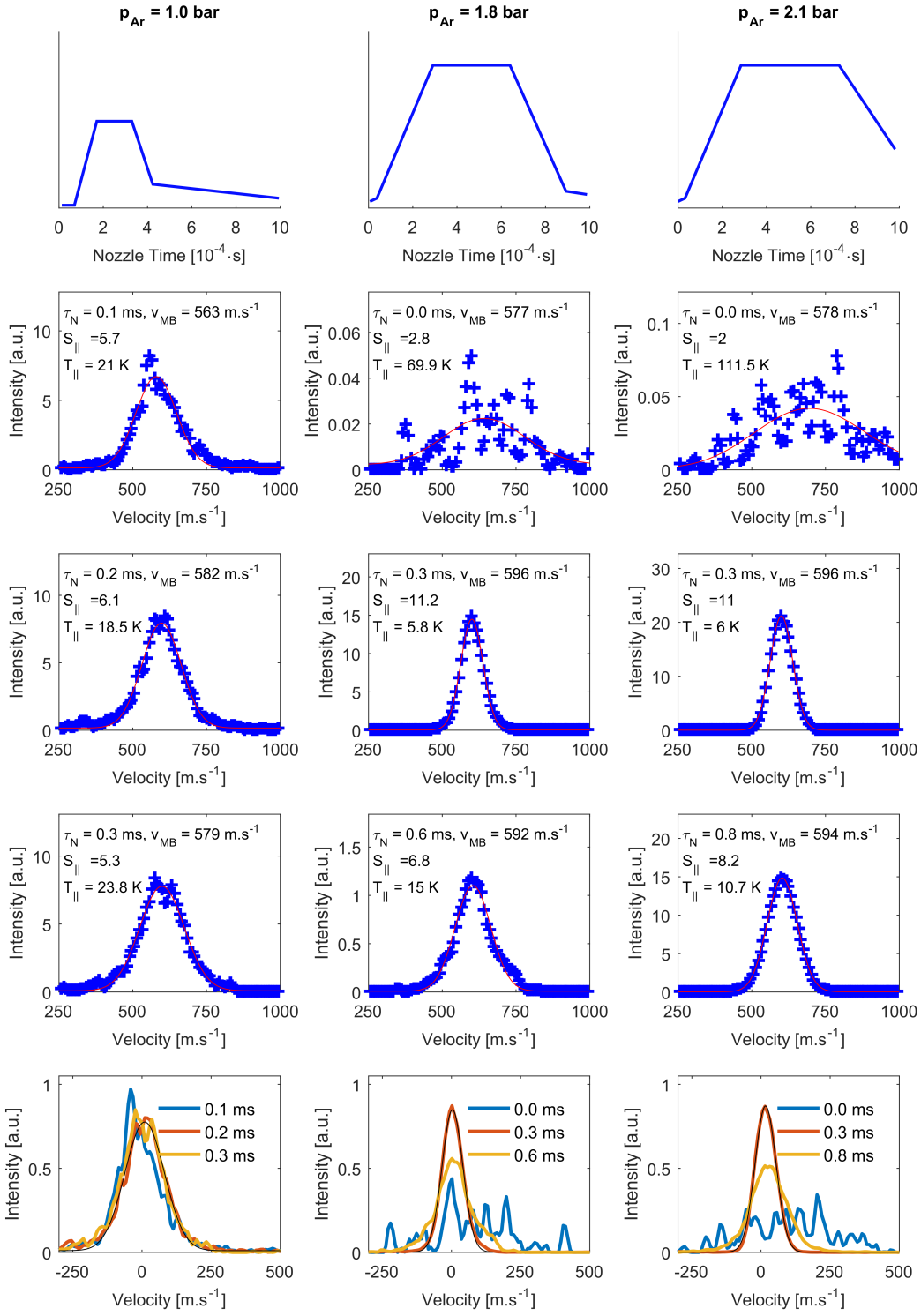


Figure 2.2: The nozzle opening profiles (1^{st} row) and the parent longitudinal ($2^{nd} - 4^{th}$ rows) and transverse (5^{th} row) beam velocity profiles measured for different backing pressures p_{Ar} and nozzle delays τ_N. Signal corresponds to the detected parent ions of pure CO seeded in argon. The longitudinal profiles were fitted by Gaussian to estimate the mean molecular beam velocity v_{MB}, speed ratio S and longitudinal temperature $T_{||}$.

can, on the contrary, suppress the clustering. In reality, the generated clusters usually show the distribution across a large range of different sizes with a mixed character of exponential and log-normal distributions for small and large clusters, respectively, corresponding to different growth mechanisms. Unfortunately, identifying the neutral cluster distributions from mass spectra is non-trivial due to the ionization step in detection. The electron- or photon-induced ionization often causes cluster fragmentation and thus the difference between the actual and observed distributions. Therefore, the so-called pickup method was used to study cluster growth based on a pickup experiment, see chapter 2.6.1.

An alternative approach is to select only a specified size of neutral clusters and then perform the intended experiments. One possibility is to use an elastic scattering of cluster beam on crossing helium beam and select the required size by rotation of the apparatus. Another possibility is to apply an electrostatic field to deflect the clusters according to their dipole moment/mass. This purification method was recently used on small hetero-aggregates of pyrrole.water and indole.water to study their stereodynamics and cluster temperature.[60, 62, 63] On the other side, the mentioned size-selecting method is applicable only for clusters containing up to ten molecules.[12]

In subsequent chapters, we will go through two main experimental methods, i.e., mass spectrometry and velocity map imaging, which are incorporated in our experimental setups and use the advantages of supersonic beams to study isolated molecules and clusters.

2.2 Mass Spectrometry

A particle with mass m, velocity v and charge q in an electromagnetic field is exposed to Lorentz force

$$\mathbf{F} = m\mathbf{a} = q\left(\mathbf{E} + \mathbf{v} \times \mathbf{B}\right), \tag{2.7}$$

where $\mathbf{E}$ and $\mathbf{B}$ are the electric and magnetic fields, respectively. The force field drives the particle's trajectory and velocity, which was first applied at the turn of the 19^{th} and 20^{th} century to separate particles with different mass-to-charge m/q ratio [2] and laid the foundations for nowadays the vast field of mass spectrometry (MS). The development of MS led to different techniques designed according to sample phase and particle sizes. These techniques are, in general, different in the three crucial steps, which describe the whole process of MS experiments and mass spectra analysis: 1) ionization, 2) mass separation, 3) detection, and mass spectra analysis.

To make particles visible for MS methods, they must be first charged by the ionization process selected according to the sample phase. Typically, electron ionization is applied in experiments with molecular beams, where an electron is detached from a cluster or molecule by another electron with high kinetic energy

$$P + e^-(70\,\mathrm{eV}) \longrightarrow P^+ + 2e^-. \tag{2.8}$$

The ionization step may induce a chemical reaction or cause particle fragmentation, making it impossible to detect parent molecules or original clusters.

This can be prevented by soft ionization techniques, e.g., sodium doping with subsequent photodetachment of electrons.[10] However, even the fragmentation pattern might characterize observed particles by comparison with the mass spectra databases.

The crucial step of MS is mass separation by the m/q ratio. Depending on the applied magnetic or electric field, we can separate the particles according to their trajectory curvature or velocity. An example of the MS based on velocity is the time-of-flight (ToF) technique, where the static electric field is applied to accelerate the charged particles and separate them according to the time necessary to drift through the field-free tube. Compared to the previous examples, there are other MS techniques that apply dynamic driving fields, e.g., the quadrupole mass filter, where the particles go through a radio frequency field, which stabilizes the paths only for particles of the selected m/q ratio.

Finally, the ions are recorded by current induction, charge accumulation, or ion splat at the detector. The conventional ToF method uses electron multipliers called microchannel plates (MCP) for the detection of ion splats.[9]

In our experimental setups, there are implemented ToF and quadrupole MS techniques to study molecular beams.

2.2.1 Time of Flight Mass Spectrometer

Electrons or short laser pulses generate ions, which are extracted from the interaction region by extraction pulse and accelerated by electric field U_{ToF} to the same kinetic energy ($q = 1$) in the direction of the free-field drift tube of length l. Particles are flying through a field-free drift tube to the detector with different velocity v, which is dependent on their mass m, and are detected at the time of arrival $\tau_{arrival}$ to the detector

$$\tau_{arrival} - \tau_0 = \tau_{ToF} = \frac{l}{\sqrt{2U_{ToF}}}\sqrt{\frac{m}{q}}, \tag{2.9}$$

where t_0 is the instrumental constant gained from calibration of mass spectra. Mass spectra are then plotted as current or counts versus time of arrival.

An indisputable advantage of ToF MS is that mass resolution $R = \Delta M/M$ is not mass-dependent, and thus this MS technique is suitable for detecting large and heavy clusters.[2] The spectrometer resolution is mainly given by the length of ionization time inducing time broadening, size of the interaction volume inducing spatial broadening, and initial velocity distribution.[2, 18] The last effect can be divided into both spatial and time broadening. Therefore, the molecular beams with very narrow velocity distributions bring an intrinsic advantage to the ToF-MS experiments. Another problem can be caused by ionizing dissociation when the ionized fragment is kicked out from the rest of the molecule/cluster. The interaction time is given by ionizing electron pulse (µs) or laser pulse (ns), which is constant for a given experiment, and therefore its impact can be diminished by prolongation of the free-field drifting tube. On the contrary, the spatial defocusing, which is caused by the various starting positions of the ions in the accelerating field, is a linear function of time of flight τ_{ToF}.[2] The particles ionized further away from the detector are accelerated for a longer time to higher drifting velocities, and thus, they have shorter drifting times and *vice versa*. The

task to diminish the broadening due to ionization position is thus to find space focusing conditions when both effects would compensate each other. This can be expressed by the first-order[1] space focusing condition in the differential formula as

$$0 = \frac{\delta t_{arrival}}{\delta z}. \tag{2.10}$$

A crucial step to overcome the spatial broadening was Wiley & McLaren's two-stage design of mass spectrometer,[65, 2] where the particles are ionized in the first stage between repeller and extractor lenses and then accelerated through the second stage in the direction of the field-free drifting tube. The focusing conditions can be found by tuning the potentials on the repeller U_{Rep} and extractor U_{Extr}. It can be derived from the simple kinematics equations discussed, for example, in [2] that the crucial parameter is the ratio of the repeller and extractor potentials U_{Ext}/U_{Rep}, which is characteristic for the position of the detector given by experimental design. In reality, we tune the voltage on the extractor and look at the FWHM of the peak for a given mass. Unfortunately, the length of the drifting tube is not a free parameter any longer for a given U_{Ext}/U_{Rep} ratio and, therefore, cannot be used to diminish broadening due to the different initial velocities of the ions with the same mass.[2, 18] Moreover, the alternative solution through the higher potentials would increase the spatial broadening in exchange.[2] A reflectron ToF (rToF) architecture can effectively solve this issue by mirroring the spatial focus of the ion source on the ion detector and simultanously compensate the various initial kinetic energies. Moreover, rToF prolongs the drifting time and thus increase even more the resolution of mass spectra.[2]

The MS techniques are a powerful tool when connected to the molecular beams for probing the products after electron- and photon-induced reactions and for investigation of clustering and coagulation of molecules after the pickup experiments. However, the information about the internal energy distribution, or the recoil energy and direction after the process is usually wasted. The next chapter discusses a method derived from the MS techniques, which significantly extends the possible application in chemical physics by graphic insight into the dynamics of molecules and clusters.

2.3 Velocity Map Imaging

Velocity map imaging (VMI) is a quickly advancing experimental method with a blooming scientific community, which brought revolutionary applications and improvements of VMI to the vast directions of physics and chemistry during the last two decades. Combination of the VMI detection with molecular beams and laser techniques offers some extra information compared to the other methods on the path to a complete understanding of the physical and chemical processes like chemical reactions, inelastic scattering, photoionization, photofragmentation, excited state relaxation dynamics, quantum state coherences, cluster structure, and many others.[9, 66] In our context, the VMI method is introduced as a

[1] More complicated designs of the mass spectrometer with additional electrodes, non-linear field, and electrode design can also solve the second and higher-order of space focusing, which is described in [64].

technique for ion imaging after photon-induced fragmentation of molecules seeded in the molecular beam as it was first presented by D. Chandler and P. Houston in the late '80s[67] and later improved A. Eppink and D. Parker in the late '90s.[68] The general idea behind VMI is that the particles of a given mass are detected at the velocity frame. In other words, the measurement of product velocity, which magnitude and direction are intrinsically connected to the studied processes, provides insight into the geometry and character of PES, arrangement of quantum states, and relaxation pathways.

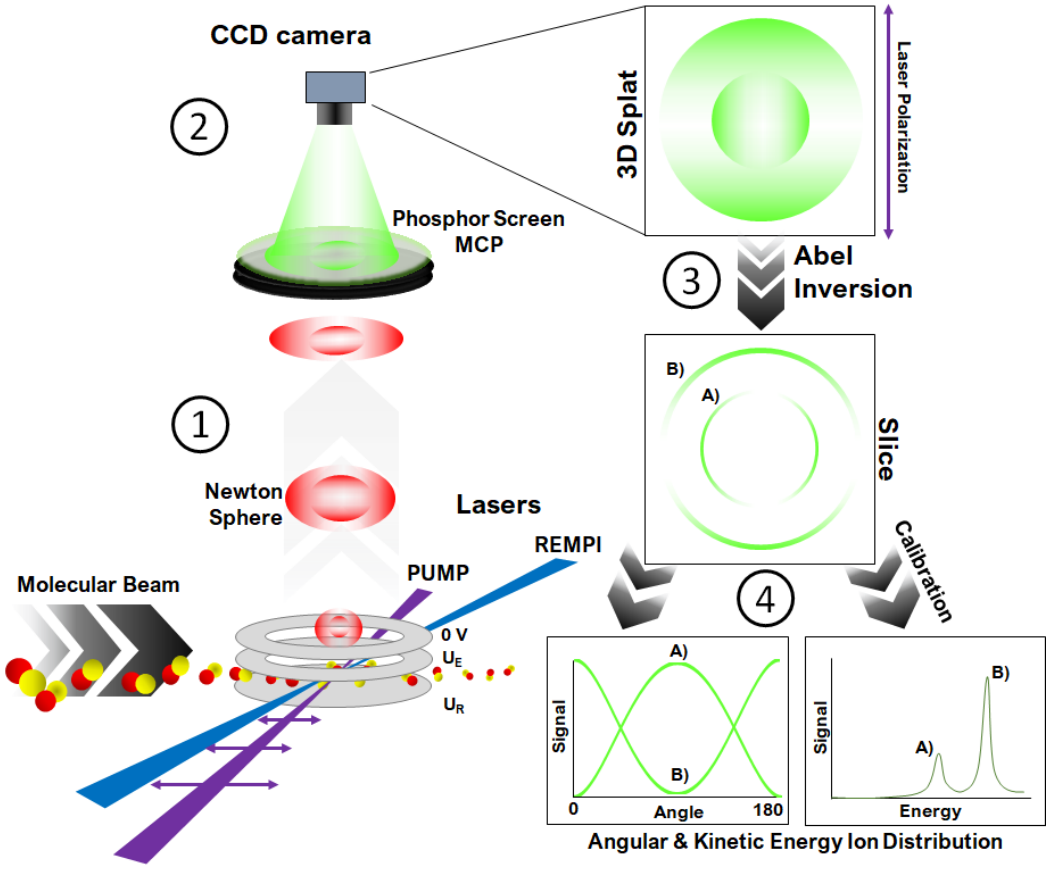


Figure 2.3: The crucial steps in velocity map imaging technique according to A. Eppink and D. Parker architecture.[9, 68]

Photofragment translational spectrometry and Doppler spectroscopy offer alternative routes to VMI.[66] Both methods yield one-dimensional projections of the particle velocity distributions, which can lead to interpretation ambiguities. On the contrary, VMI yields a two-dimensional projection by detecting the particles with a position sensitive detector at the coordinates unambiguously connected (or through transformation) to their velocity vector $\boldsymbol{v_P}$.[9] This approach, in principle, not only simplifies the experiment but also offers a detailed insight into molecular dynamics by experiments with the vector correlations or the molecular alignment.[69, 70, 9, 71]

The investigated molecular system is introduced to VMI after supersonic expansion, which prevents image blurring due to narrow velocity distribution. The following example of the two-body fragmentation triggered by single-photon excitation will serve as a model for presenting the VMI technique. The isolated

molecule is firstly excited with pump laser pulse when flying through the interaction region between the repeller and extractor lenses. The gained energy is then dissipated into the fragmentation pathway resulting in two neutral fragments A and B ($m_A \neq m_B$). These two atomic fragments recoiling in the center-of-mass frame must conserve the initial linear momentum $m_A\mathbf{v_A} = -m_B\mathbf{v_B}$, where $\mathbf{v_A}$ and $\mathbf{v_B}$ are fragment recoil velocities. The repeating of the same dissociation process forms an ensemble of fragments expanding into the so-called Newton spheres, which 1) extraction, 2) detection, 3) reconstruction, and 4) analysis are crucial steps in the VMI method, see figure 2.3.

The neutral fragments must be first ionized to be extracted in the direction of the detector. The most extended ionization technique combined with VMI is photoionization by lasers. Then the ionized fragments are repelled by the electrostatic field gradient between repeller and extractor into the free-field drifting tube. During the drifting, the fragments can further expand into the Newton sphere until their splat[2] at the detector. This is sometimes combined with the Newton sphere contraction in the direction of flight called "pancaking", which improves mass resolution and prevents mass interference. The spread of time of arrival is proportional to the recoil velocity $\sim \sqrt{E_{tr}}$ and repeller voltage U_R as $\Delta t \propto \sqrt{E_{tr}}/U_R$ with values in tenths of nanoseconds. [66] However, Wiley & McLaren's condition cannot be achieved by the simple three electrode architecture as the VMI goal is the projection of initial velocities, which, as was discussed in chapter 2.2, goes against the high mass resolution.

The direct observation of the whole Newton sphere directly in three dimensions is at the edge of the current detection capabilities. The more conservative way of detecting is a projection of the entire Newton sphere on the position sensitive detector and reconstruction of its center slice by inverse Abel transformation. This bijection between the 3D object and its 2D projection requires the cylindrical symmetry of the experiment. The orientation of the molecules in supersonic expansion is usually isotropic, and therefore the experiment symmetry is determined by the polarization of the pumping laser, which must be parallel to the plane of the detector.

The same experimental approach was used by A. Eppink and D. Parker [68] in their revolutionary exchange of the thin wire meshes for the Einzel lenses, which focus the ions without any distortion and almost completely wipe out the blurring due to the different space origin.[9] The lower constraints on the size of the interaction region are critical as the high density of ions can induce repulsive blurring due to the space charge. The conventional VMI brings a relatively simple experimental technique in exchange for high demands on the image post-processing. The inverse Abel transformation between 2D projection and Newton sphere is given by prescription[9]

$$s(r) = \frac{1}{\pi}\int_r^{+\infty} \frac{df/dx}{\sqrt{x^2 - r^2}} dx, \tag{2.11}$$

which shows two sources of noise in the directly transformed images, i.e., the singularity $x^2 = y^2$ and the derivative df/dx around the symmetry axis.[9] There are various methods to calculate inverse Abel transformation, which are all incorporated in the Python module *pyabel*, see [72, 73]. Except for the direct calculation

[2]The word "splat" comes from the terminology used in the SIMION simulation software.

of equation 2.11, the methods are, for example, based on a decomposition of the 2D image into a linear base of convenient functions or onion pealing of the image layers.

An experimental way to bypass the pitfalls of image post-processing lies in direct imaging of the central slice of the Newton sphere in so-called "slicing methods". Several approaches were developed according to the application and technical possibilities.[66] For example, one of the methods uses fast gating of the detector combined with the stretching of Newton sphere provided by sequential electrostatic field or extraction pulse. On the other hand, the optical slicing method uses spatial-selective ionization based on the spatial and temporal delay between the pumping and ionization steps.[66] A new generation of fast cameras enables to detect temporal information of the ion arrival for each event with up to $\sim$1 ns resolution.[74, 75] Moreover, the high rate of these cameras and short pixel dead-time enables detection of all the ionized particles independently of their mass in one cycle. In such an experiment, the MCP detector is loaded with high voltages, and all the events are stored for future analysis.[75] The bottleneck of these detection systems is the high demand for computational capacity and, of course, the price.

The true wealth of the VMI method lies in the image analysis. First, the images provide an angular distribution of recoiling fragments, enabling vector-correlation or alignment experiments to study excited state PES and energy redistribution after fragmentation. Secondly, the time-resolved imaging, especially in sub ps timescale, combined with ion-electron or ion-ion coincidence measurements, offer unprecedented insight into photodynamics and the energy flow during the relaxation pathways of isolated molecules and clusters.[76, 75] The analysis of the images will be shortly discussed in the following paragraphs about kinetic energy distribution (KED) and surface patterns of Newton spheres.

2.3.1 Kinetic Energy Distribution

Although the name "velocity map imaging" suggests that the direct information gained from the VMI images is the velocity of recoiling fragments, this is not exactly true. As was discussed in previous paragraphs, the Newton sphere (or its "pancake") is linearly expanding in the plane of the detector throughout the drifting to the detector. The radius of the image r_{splat} is proportional to the projection of the recoil velocity into the detector plane v_p times the time-of-flight τ_{ToF}. Therefore, to evaluate the variable of our interest - v_p - we have to divide the measured r_{splat} by the τ_{ToF}, which depends on repeller voltage U_{Rep}, length of the drifting tube l and the fragment mass-to-charge m/q ratio ($q = 1$)

$$\begin{aligned} r_{splat} = m_{VMI} \cdot v_p \cdot \tau_{ToF} &= m_{VMI} \cdot v_p \cdot l \sqrt{\frac{m}{2U_{Rep}}} \\ &= \frac{k_{cal}}{\sqrt{2}} \cdot v_p \cdot \sqrt{m} = k_{cal} \cdot \sqrt{E_{tr}}, \end{aligned} \tag{2.12}$$

where m_{VMI} is the VMI spectrometer magnification and k_{cal} is calibration factor. This leads to a conclusion that the VMI images give us direct knowledge about square root of kinetic energy. Furthermore, two fragments with different masses and the same kinetic energy will be detected at the same radius r_{splat} from the

image center. This is an important result that enables us to use images from HBr dissociation for energetic calibration of all the other VMI images independently on fragments mass, see chapter 2.4.3. Beware that the image center is shifted for different masses in the case of VMI apparatus with perpendicular geometry.

Kinetic energy distribution (KED), which is connected to an image's radial pattern, can be obtained by an integration of the Newton sphere layers. This cannot be done directly through a simple summation over the values $I(\theta, r_{splat})$ as each point must be multiplied by a factor $2\pi r_{splat} \sin\theta$ corresponding to the circumference around the axis of cylindrical symmetry

$$\mathrm{KED_{px}}(r_{splat}[\mathrm{px}])\, dr_{splat} = dr_{splat} \int_0^{\pi} I\,(\theta, r_{splat}) \cdot (2\pi r_{splat} \sin\theta) \cdot r_{splat}\, d\theta, \quad (2.13)$$

where the term $dr_{splat} r_{splat}\, d\theta$ is an area element in polar coordinates. Next, the dependency on radius $\mathrm{KED_{px}}(r_{splat}[\mathrm{px}])$ can be changed to the energetic dependency $\mathrm{KED_E}(E_{tr}[\mathrm{eV}])$ by application of the calibration 2.12 as

$$N = \int_0^{+\infty} \mathrm{KED_{px}}(r_{splat}[\mathrm{px}]) \cdot dr_{splat} = \left\| \begin{array}{l} r_{splat} = k_{cal}\sqrt{E_{tr}} \\ dr_{splat} = k_{cal} \frac{dE_{tr}}{2\sqrt{E_{tr}}} \end{array} \right\| \quad (2.14a)$$

$$= \int_0^{+\infty} \mathrm{KED_{px}}(k_{cal}\sqrt{E_{tr}}) \cdot \frac{k_{cal}}{2\sqrt{E_{tr}}} \cdot dE_{tr} \quad (2.14b)$$

$$= \int_0^{+\infty} \mathrm{KED_E}(E_{tr}[\mathrm{eV}]) \cdot dE_{tr}[\mathrm{eV}]. \quad (2.14c)$$

The equation 2.14b give us a prescription, which shows that the unit change demands renormalization of the KED function by a term inversely proportional to the fragment velocity $1/\sqrt{E_{tr}} \sim 1/v_p$. The obtained KED can be further analyzed to find the precise peak positions or integrate different peaks to discuss the relaxation pathway efficiency.

The energy of a molecule and cluster after a photon absorption consists of a kinetic term (in center-of-mass frame $E_{tr}^{CM} = 0$) and internal term E_{int}^{i} raised by an energy quanta $h\nu$. During the whole relaxation process, the system must obey the conservation of energy expressed in equation 1.3. For two-body fragmentation, we can rewrite the formula into

$$E_{excess} = E_A^i + E_B^i + \frac{1}{2} m_A v_A^2 + \frac{1}{2} m_B v_B^2 \quad (2.15)$$

with two kinetic terms and two terms corresponding to the internal energy of generated fragments. An image of one type of fragment gives us knowledge of the total kinetic energy and internal energy when considering the conservation of linear momentum. This is especially beneficial when combined with the selective ionization technique. If we know the quantum state of the detected fragments, we can also determine the precise internal energy of its counter-partner. On the other hand, the non-selective ionization combined with coincidence detection by ultrafast detectors provides us valuable insights for more complex multi-fragment processes in case of instant or sequential fragmentation.[75, 74]

2.3.2 Anisotropy and Vector Correlations

The angular layout of the VMI images is directly connected to the Newton sphere surface pattern. In the case of an isotropically oriented ensemble of molecules,

the cylindrical symmetry is determined by the laser polarization due to the probability for absorption proportional to the squared dot product $\propto |\boldsymbol{\mu} \cdot \mathbf{E}|^2 = (\mu E)^2 \cos\theta^2$ of electric field vector $\mathbf{E}$ and transition dipole moment $\boldsymbol{\mu}$. This phenomenon is called photoselection and defines an ensemble of excited molecules that undergo fragmentation.[77, 9] In the next paragraphs, we will discuss the fragment angular distribution after axial recoil, which is typical for most UV-fragmentations. All the considerations below are under the assumption of prompt dissociation of a diatomic molecule in timescales below 100 fs. Otherwise, the anisotropy would be blurred due to the molecular rotation.

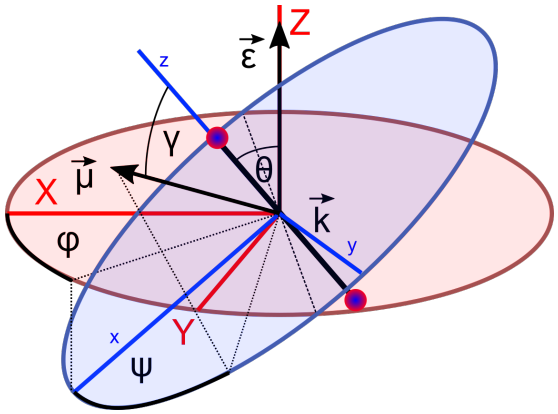


Figure 2.4: Euler angles and coordinates corresponding to molecular (blue) and laser polarization (red) frames.

The orientation of dipole moment $\boldsymbol{\mu}$ in the molecular framework (x, y, z) with the bond axis $\boldsymbol{k}$ oriented along z can be expressed as

$$\boldsymbol{\mu} = \mu \left(\sin\gamma\cos\psi \boldsymbol{e_x} + \sin\gamma\sin\psi \boldsymbol{e_y} + \cos\gamma \boldsymbol{e_z}\right), \tag{2.16a}$$

$$\overset{(\boldsymbol{k}\parallel\boldsymbol{\mu})}{=} \mu \boldsymbol{e_z}, \tag{2.16b}$$

$$\overset{(\boldsymbol{k}\perp\boldsymbol{\mu})}{=} \mu(\cos\psi \boldsymbol{e_x} + \sin\psi \boldsymbol{e_y}), \tag{2.16c}$$

where the meaning of the angles (γ, ψ) is shown in figure 2.4. For evaluation of fragment flux $I(\theta, \phi)$, we have to find the excitation probability of molecules which are pointing into the oriented solid angle $\sin\theta\, d\theta\, d\phi$. That means to express the excitation probability of a given molecule transformed to laboratory framework ($\Phi_{Ii} : x, y, z \longrightarrow X, Y, Z$) and then do the averaging through the azimuthal angle ψ with the assumption that the probability of molecular orientations (and thus the orientation of dipole momentum $\boldsymbol{\mu}$) is isotropic, for details see [77]. In the case of simple diatomic molecules, molecules whose excitation is linked to a specific bond, or symmetrical polyatomic molecules, there are only two cases of transition dipole moment orientation: a) parallel ($\gamma = 0$), prescribed by eq. 2.16b and b) perpendicular ($\gamma = \pi/2$), prescribed by eq. 2.16c. Finally, if the polarization of the incident light $\boldsymbol{\epsilon} = \epsilon \boldsymbol{e_Z}$ is identical with the Z axis of the laboratory frame,

then the formula for angle distribution is[77]

$$I(\theta,\phi) = \sum_i \frac{1}{2\pi}\int_0^{2\pi} \Phi_{Zi}^2(\theta,\phi,\psi)\,d\psi, \tag{2.17a}$$

$$\overset{(\boldsymbol{k}\parallel\boldsymbol{\mu})}{=} \frac{1}{2\pi}\int_0^{2\pi} \Phi_{Zz}^2(\theta,\phi,\psi)\,d\psi \qquad = \sin^2\theta, \tag{2.17b}$$

$$\overset{(\boldsymbol{k}\perp\boldsymbol{\mu})}{=} \frac{1}{2\pi}\int_0^{2\pi} \Phi_{Zx}^2(\theta,\phi,\psi)\,d\psi + \frac{1}{2\pi}\int_0^{2\pi} \Phi_{Zy}^2(\theta,\phi,\psi)\,d\psi \qquad = \cos^2\theta. \tag{2.17c}$$

The general expression in eq. 2.17a turns to eq. 2.17b and 2.17c for parralel and perpendicular symmetry, respectively. When $\gamma \neq \{0, \pi/2\}$, the first step is to decompose the dipole moment into axial and perpendicular projections $\boldsymbol{\mu} = \boldsymbol{\mu}_\parallel + \boldsymbol{\mu}_\perp$. The angle distribution $I_\gamma(\theta,\phi)$ is then equal to the summation of the parallel and perpendicular components[3]

$$I_\gamma(\theta,\phi) = A_\gamma \cdot I_\parallel(\theta,\phi) + B_\gamma \cdot I_\perp(\theta,\phi) = A_\gamma \cdot \cos^2\theta + B_\gamma \cdot \sin^2\theta. \tag{2.18}$$

This prescription has a form of a dipole radiation[77, 9], which distribution is given by a formula

$$I_\gamma(\theta,\phi) \overset{\text{cyl.sym.}}{=} I_\gamma(\theta) = \frac{1}{4\pi}\left[1 + \beta_\gamma \mathrm{P}_2(\cos\theta)\right], \tag{2.19}$$

where P_2 is the second-order Legender polynomial $3\cos^2\theta - 1/2$ and β_γ is called an anisotropy parameter. The comparison of the equations 2.18 and 2.19 yields that the $\beta = -1$ indicates perpendicular absorption character, whereas $\beta = 2$ indicates parallel absorption character. The link between the transient dipole moment $\boldsymbol{\mu}$ and the recoil velocity $\boldsymbol{v}$ is called $\boldsymbol{\mu}-\boldsymbol{v}$ vector correlation and provides us with information about the excitation symmetry. In other specific experiments, we can even play with higher-order vector correlations with three and more vector inter-dependencies, which can reveal the geometry of the excited state PES and photodissociation dynamics. A typical example of three-vector correlation is the interlink between the fragment's internal angular momentum $\boldsymbol{j}$, velocity recoil direction $\boldsymbol{v}$ and parent's transition dipole moment $\boldsymbol{\mu}$, which probes the alignment of the produced fragments.[9, 66]

2.3.3 Photoionization: Resonant and Non-Resonant

The VMI method is usually combined with the application of laser pulses for fragment ionization. An indisputable advantage of photoionization is that most of the excess energy is retracted by the ejected electron, which prevents the additional velocity blurring, although the light fragments like hydrogen can still "feel" a small kick (see chapter 2.4.3).

There are different types of photoionization shown in figure 2.5. The fragments can be either probed selectively or non-selectively. In the former case, as is illustrated in figure 2.5 a) and b), the fragments are first resonantly excited to an

[3] All the cross-terms $I_{\mu_\parallel\mu_\perp} \propto \boldsymbol{\mu}_\parallel \cdot \boldsymbol{\mu}_\perp \propto \int_0^{2\pi} \sin\psi\cos\psi\,d\psi = 0$ disappear due to the orthogonality.

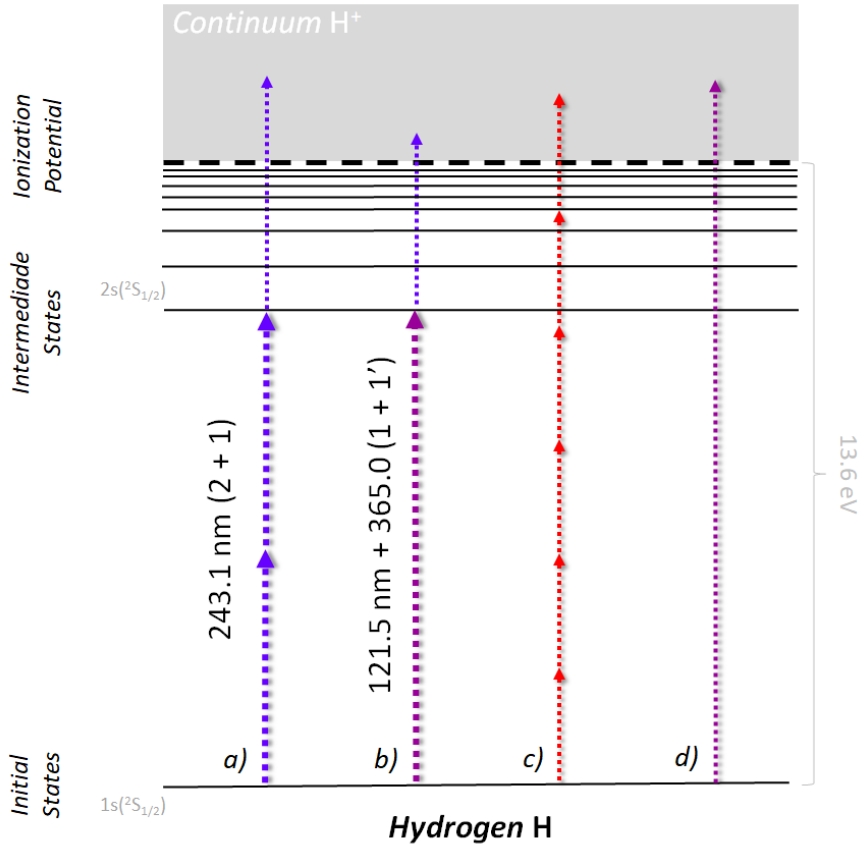


Figure 2.5: Photoionization schemes for hydrogen radical. a) 2+1 REMPI scheme at 243.1 nm. b) 1+1' REMPI scheme at 121.5 nm generated by third-harmonic generation from 365 nm.[78] c) Non-resonant multiphoton ionization. Scheme for strong-field ionization.[63] d) Non-resonant one photon ionization.[79]

intermediate state with a bunch of n photons and then ionized with another bunch of n' photons. This approach is called resonance-enhanced multiphoton ionization (REMPI). The crucial idea of REMPI is that the resonant transition into the intermediate state, often the low-lying Rydberg state, is strongly fragment- and state-specific. Also, the resonant transition magnifies the probability of ionization for selected fragments. The multiphoton step in the REMPI scheme needs high power density, leading to a generation of the non-resonant background signal, which can even interfere with the gated mass. Therefore, there is always necessary to check the origin of the signal.[7]

In the experiment, the characteristic REMPI wavelengths must often be found by scanning the laser over a broad range and simultaneous recording ion signal in so-called action spectra. The action spectra are also helpful when studying rotational or vibrational state distribution in produced fragments.[5, 7]

Although the non-resonant ionization is part of this thesis only marginally in chapter 3.2.3, [7] it should be mentioned as it is a current trend due to the ultrafast time-resolved VMI pump-probe experiments. In principle, there are two approaches currently in use. The first, called strong-field ionization, applies short femtosecond pulses at the near IR region, which leads to multiphoton ($n > 6$) ionization.[63] In my experience during campaign on OCS dissociation, we used

7 fs pulses centered around 790 nm with energy 50 µJ. This yields more than one thousand times more pulse power than in our conventional REMPI pulses generated by UV OPO laser, see Appendix A.1. The second approach is to generate short wavelength (< vacuum UV) pulses, of which one-photon energy is high enough to surpass ionization potential.[79]

Up to now, we have spoken about the mapping of products after the end of fragmentation or reaction. This state-selective approach offers an overview of the channel rates, quantum yields, or state distributions when combined with specific REMPI. The next chapter will briefly discuss the time-resolved VMI experiment, which enables detailed insight into the intermediate states, fragmentation mechanism, or energy flow in conical intersections and ISC.[80]

2.3.4 Time-Resolved Pump-Probe VMI Experiments

When a short laser pulse pumps energy into the investigated system, it initiates the photodynamic, which is left to evolve until the second pulse probes its current state. The particular use of applied laser pulses is mainly given by their temporal width and spectral width, which are constrained by the uncertainty principle. In the case of spectrally narrow nanosecond pulses, the system rises to one exact excited energy level.[37] This is especially useful for studies of vibrationally mediated photodissociation and internal vibrational energy redistribution. On the other hand, the ultrashort femtosecond pulses are intrinsically spectrally broad, and thus the pump pulse creates the wave packet, which then evolves on the PES. Subsequently, the probing is usually arranged by non-resonant ionization techniques discussed in the previous chapter.[37]

In this thesis, we use the pump-probe approach to investigate vibrational redistribution within the isolated pyrrole. Here the molecules are first pre-excited with 5 ns IR laser pulse tuned to excite N-H stretch vibration and then dissociated with delayed 5 ns UV pulse in the range from −20 ns to 150 ns. The UV pulse not only induces fragmentation but also ionizes the ejected H fragments. Unfortunately, the right-angle geometry of our experiment offers only a qualitative comparison of images measured for different delays due to the motion of pre-excited molecules out of UV focus ($\approx 50\,\mu m$) with molecular beam velocity ($\approx 1.7\,km\,s^{-1}$). This is not a problem for sub-nanosecond experiments, where the shift of the pumped particles is negligible.

A special case of a time-resolved experiment is Coulomb explosion pump-probe imaging, where a strong femtosecond pulse causes non-resonant ionization of both co-fragments or multi-charge dissociative-ionization.[81] In such a case, a new Coulomb term $\sim Q_1 \cdot Q_2/r_{12}$ must be added to the equation 2.15, which expresses the dependence of the recoil velocity on the initial radius of the repulsive fragments. Application of the Coulomb explosion for probing the photoinduced processes opens an opportunity for real-time monitoring of molecular motion by VMI.[81] These types of experiments called "molecular movies" are currently a "hot topic" in the VMI community.[82, 81]

2.3.5 Spatial Resolution and Centroiding

The application of an inhomogeneous electric field by Parker and Eppink to find the VMI condition was an elegant solution that almost diminished the blurring from the spread of initial fragment positions and unprecedentedly enhanced the spatial resolution of the ion imaging.[83, 9] The remaining sources of blurring are connected to the velocity spread of the molecular beam, probing step, and ion detection, which set the limit for the VMI resolution.[9]

As is illustrated in figure 2.2, the longitudinal velocity spread is usually broader than the transverse one, which suggests that the imaging detector should be in the path of the molecular beam to reach the best resolution. However, the axial geometry of the apparatus can cause other problems with the residual gas and detector damage.

The probing step can cause electron recoil and space charge. The electron recoil comes from the excess energy after ionization divided among an ejected electron and ion, which will be discussed in chapter 2.4.3 together with the HBr images used for the VMI calibration. On the other hand, the space charge disrupts the VMI images through the Coulomb repulsion among the ions, which should always be tested and prevented, e.g., by acquiring the images for different probing laser intensities.

On the detection side, the detector assembly determines the blurring of ion splat. Each ion hits MCP at a given position and raises an avalanche of secondary electrons through the MCP channels, resulting in the phosphorscreen (PS) flash. The size and intensity of the spot detected by a camera depend on the ion kinetic energy and the bias voltage across the MCP/PS. Furthermore, the splat intensity distribution is driven by a stochastic process of electron generation, which can be further affected by inhomogeneity among the PS areas. The solution for these issues is the real-time analysis of each event during the measurement. The processing is called ion counting (IC, or centroiding mode), and its task is to locate the coordinates of each splat and use them to create a new map with assigned values of 1 to each event, which can effectively solve the problem of the image inhomogeneity and splat blurring. Another advantage of centroiding is the possibility to set a threshold parameter so that all the signal coming from noise events or hot pixels can be discriminated. Several algorithms can be applied to recover the central splat position, e.g., 2-D Gaussian fit, intensity-weighted center of mass approach, spath algorithm, and others.[84] Each algorithm has different demands on the computing power proportional to its precision. Nevertheless, the current processors' computing power usually exceeds the demands for 2D detection, and a bottleneck is usually connected to the readout speed from CCD/CMOS cameras.[85] The situation might differ for the new cameras with spatial and temporal detection.[86] In any case, the necessary condition for IC is the low rate of the ions per laser pulse, otherwise, the analysis might lead to data loss and false image intensities.

To enhance VMI resolution, we introduced the centroiding mode to our AIM apparatus, see chapter 2.4.1. In our case, the centroiding algorithm is implemented through the LabView library (IMAQ, Particle Analysis Report) by the post-processing of the acquired image after each laser cycle: 1) each pixel belonging to one event is assigned by an intensity of 1, and 2) central pixel is found by the calculation of the center-of-mass. Thus, the resolution of our CCD camera

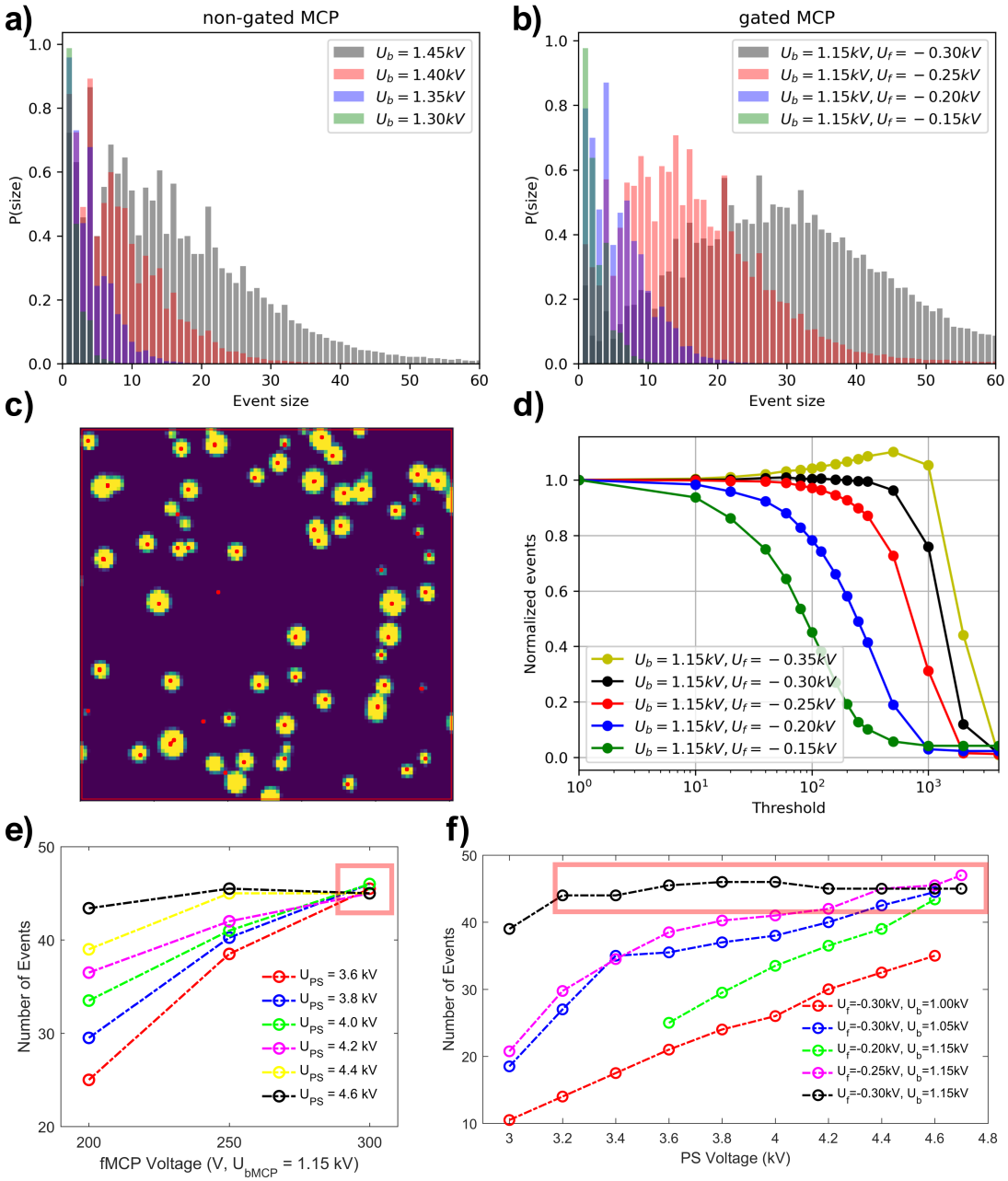


Figure 2.6: Ion counting mode and saturation settings of the MCP/PS for ion detection.

limits the spatial resolution of the acquired images. Also, from the above, it follows that we do not apply the weighting by pixel intensity, which could improve the result a little bit in exchange for higher computational demands. However, the detected blobs are symmetrical, as is illustrated in figure 2.6 c), and we were more concerned about the speed of the centroiding algorithm.

We have done several testing measurements to find the best MCP/PS assembly and IC threshold settings. Firstly, there is a significant difference when the IC is applied in MCP's gating and non-gating regimes. For each case, there is a plot of splat size distributions for different MCP/PS bias voltages in figures 2.6. In the non-gated regime, all ions/photon-stray are detected, which yields a broad distribution between 1-pixel up to 50-pixel sized splats for the

$U_{bMCP} = 1.45\,\mathrm{kV}$, see figure 2.6 a). Increasing the voltage between front MCP (fMCP) and back MCP (bMCP) broadens the size distribution. Nevertheless, the small splats due to the photon stray are still detected, which can be effectively solved by the IC threshold. However, the IC is usually incompatible with the non-gated regime due to too high ion signal. On the contrary, the gated regime shows close to Gaussian distributions for saturated conditions with higher voltages, e.g., $U_{fMCP} = -0.25\,\mathrm{kV} + U_{bMCP} = 1.15\,\mathrm{kV}$, see figure 2.6 b). Moreover, gating enables only the detection of ions with selected mass. The crucial setting for the detection and usage of IC is whether the detector is in the non-saturated regime with reduced sensitivity and irregular spot shape or if the detector is in the saturated regime when each event results in a homogeneous Gaussian-like spot, as is shown in figure 2.6 c) (10 sweeps, $U_{fMCP} = -0.30\,\mathrm{kV} + U_{bMCP} = 1.15\,\mathrm{kV}$).

In figure 2.6 d), there are dependencies of the number of events on threshold values for different detector settings. The yellow line shows a slight signal increase for the threshold above 100 due to an overlap between the event splats, which are again separated by higher thresholds. Apparently, the number of events was too high for IC in this case of detector settings, and lower voltage or pumping laser intensity is necessary for the image acquisition.

The automatic plotting of splat size histogram and threshold curves was implemented into the acquisition mode to always check if 1) the detector is in saturation mode and 2) the number of events is appropriate for IC.

In figures 2.6 d) and e), there are shown event counts as functions of the MCP and PS bias voltage with a gated MCP detector. The state of the detector, when all events are detected, is reached when the sum voltage across the front MCP and back MCP plates is together between the 1.4-1.5 kV as is marked in the figures by red rectangles. These settings were also applied during all measurements on our AIM reported in the experimental chapter 3.

2.4 Apparatus for Imaging

The scheme of the apparatus is shown in figure 2.7. The apparatus is built in the right-angled geometry[68] with three functional parts: a) source chamber, b) VMI chamber, and newly equipped c) quadrupole mass spectrometer chamber with dump.

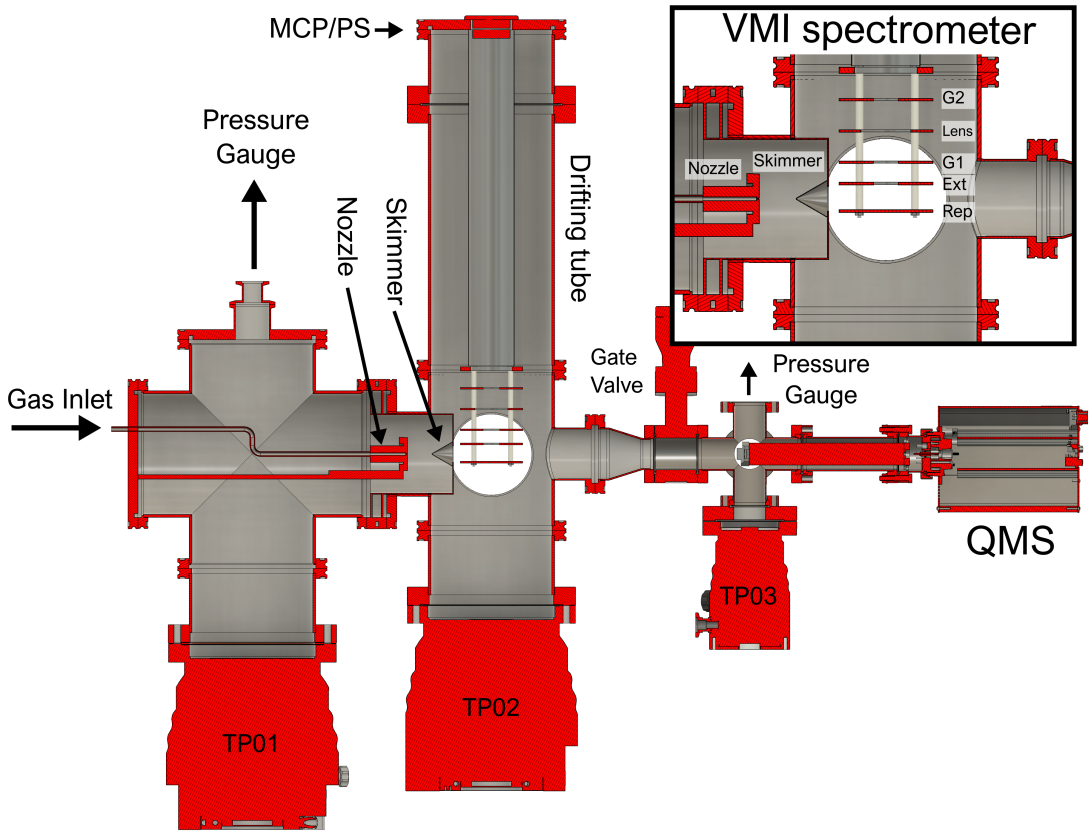


Figure 2.7: Slice through 3D model of Apparatus for Imaging (AIM). The apparatus is equipped with the VMI spectrometer (detail in inset with description), quadrupole mass spectrometer (QMS) and three turbomolecular pumps (TP).

The sample seeded in buffer gas is guided through Swagelok tubes into the pulse valve (General Valves) inside the source chamber (2×10^{-7} mbar). The pulse valve opens with 10 Hz repetition rate for approximately several hundred microseconds. Each pulse builds up supersonic expansion into the source chamber, where a skimmer (pinhole 0.55 mm, opening angle 30°, nozzle-skimmer distance within 1.5-2.5 cm) extracts the molecular beam into the VMI chamber (9×10^{-8} mbar). The molecular beam flies through the space between the repeller and extractor electrodes, where it crosses laser beams used for triggering photoinduced dynamics and ionization. For the VMI experiments, the repeller and extractor are loaded with a high voltage in ratio to meet the VMI focusing conditions[4]. The voltages were adjusted to change the size of the taken images,

[4]Spatial imaging conditions are $U_{Rep}/U_{Ext} = 2.2\,\text{kV}/2.3\,\text{kV}$. Beware that the spatial imaging causes the inversion of the image, which is especially important to realize for experiment adjustment.

e.g., $U_{Rep}/U_{Ext} = 3.7\,\mathrm{kV}/2.9\,\mathrm{kV}$ was typically used for CH_3 and Cl ions and $U_{Rep}/U_{Ext} = 3.0\,\mathrm{kV}/2.3\,\mathrm{kV}$ for H ions.

The electric field accelerates the ionized fragments in the direction of the shielded drifting tube, which goes from the grounded lens to the detector. During the drifting, the ions are simultaneously expanded in the plane of the detector and contracted in the direction of flight until they hit the detector. The detector consists of MCP coupled with a phosphorescence layer (PS, P43) and a CCD camera (Unibrain). The MCP front can be gated with $U_{fMCP} \approx -0.3\,\mathrm{kV}$ by 30 ns pulses to detect only the selected ions at a given mass. Each splat of ion generates the electrons, which are accelerated and amplified in MCP channels assembled in a chevron stack until they are ejected from the back MCP (gated regime $U_{bMCP} = 1.15\,\mathrm{kV}$, non-gated $U_{bMCP} = 1.45\,\mathrm{kV}$) in the direction of the phosphorscreen, where it generates photon flash recorded by the CCD camera (exposure 3 ms, gain $0-50$). In case of a low rate of events, the images were processed with the centroiding. Further processing of the taken images is discussed in chapters 2.3.1 and 2.3.2. The synchronization of the experiment is provided by two delay generators (BNC575, Berkley Nucleonics).

The AIM apparatus is newly equipped with the quadrupole mass spectrometer working in the range $0 - 300$ m/q situated in the last chamber (5×10^{-8} mbar), which also serves as a molecular beam dump.

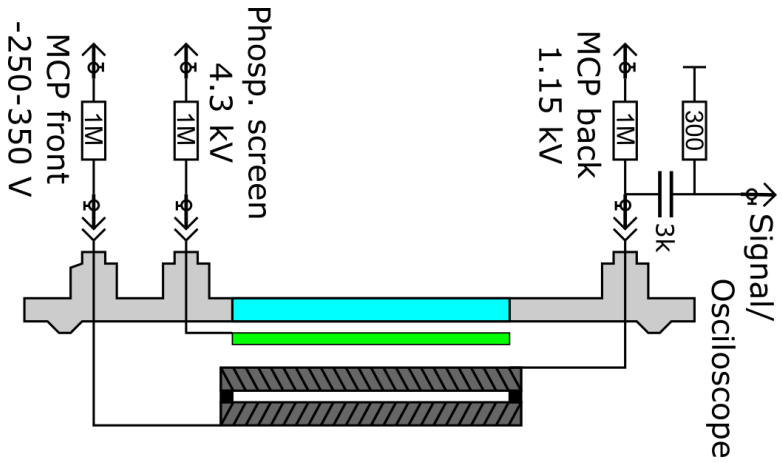


Figure 2.8: Wiring of the new MCP/PS detector.

2.4.1 Control of AIM and Data Acquisition

During the last three years, the control of AIM was changed hand to hand with the implementation of the centroiding mode for ion detection, sorting of images for background detection, heating of the nozzle valve (Appendix A.2), remote control of delay generators (DGs, Appendix A.4), a new UV optical parametric oscillator (OPO) laser (Appendix A.3), and installation of a new MCP detector.

The main driving program was developed in LabView (v2015) by Dr. J. Rakovský. The program task is to initialize the CCD camera through the Arduino kit (Ard01) and set its gain and exposition length. For the measurement itself, the program starts/stops the data acquisition by enabling to trigger camera's electronic shutter, which precise timing is further discussed in chapter 2.4.2.

Also, the program is responsible for the acquisition, sorting, and saving of data. Furthermore, we recently upgraded the program with new tabs for ToF measurements, VMI focusing, and IC analysis.

The strong inhomogeneity of the images, even with active centroiding, persuaded us to install a new detector, see figure 2.8 a) for wiring. The images currently show perfect symmetry, and thus we can use all four quadrants for the data analysis. Moreover, the signal processed with centroiding yields unambiguous physical meaning of signal as the number of detected ions, which allows us to estimate the signal ratios for different types of fragments and image layouts.

2.4.2 Apparatus Synchronization

The block diagrams of connections for synchronization of the AIM apparatus are shown in the figures 2.9 a) and b).

In the case of IR+UV experiments shown in a), we used three different lasers with pumping by Q-switched Nd:YAG lasers, i.e., UV OPO, UV Dye, and IR OPO, see Appendix A.1 for details. The Q-switch enables us to precisely drive the synchronization of the experiment by delay generator (DG01), which externally triggers the laser flashlamps/diodes and, subsequently, with the given delay, opens the Q-switches to build up the laser pulses. The timeline for synchronization of the IR+UV experiment is shown in 2.9 c). The newly equipped UV OPO requires the 20 Hz repetition rate, which sets the fundamental frequency for the DG01.[5] The maximal CCD frame rate is 10 Hz, and thus, the divider coefficients must be used for other channels driving the IR laser, nozzle, CCD camera, and MCP gating. The first must be triggered the valve opening so that the molecular beam can meet the laser pulses in the interaction region.

The acquisition task in IR+UV experiments is to record the IR+UV and UV images separately to subtract the background signal coming from UV-only dissociation/ionization. Therefore, the channel F (Ch F) triggering the IR laser Q-switch runs at 5 Hz and is also connected with the LED through the Arduino kit (Ard02). LED is installed next to the phosphor screen in the focus plane of the CCD camera, which detects the LED flashes when the IR laser is triggered. The LED marking of the IR+UV images enables us to separate them from UV-only images, as is illustrated at the bottom of figure 2.9 c). The ions are detected only when they reach the detector during the gate window driven by Ch G, which delay is synchronized with the Q-switch of the ionizing UV laser. Finally, the CCD camera is triggered through milliseconds, and thus the precise synchronization with MCP gating is not crucial for our experiments.

The block diagram in figure 2.9 b) is meant for UV_{193nm}+UV experiments, where the UV_{193nm} excimer pulse causes photodissociation and the second UV OPO pulse ionizes the generated fragments. The diagram is vastly different from the previous one because of the excimer laser, which cannot be precisely triggered due to its intrinsic laser properties. Therefore, the excimer laser, OPO UV diodes, and nozzle are triggered by DG01. However, the delay of the other devices and UV Q-switch must be driven by the excimer laser pulse. The excimer laser provides an OUT sync signal to trigger another delay generator (DG02). Unfortunately, the delay between the pulse and OUT sync is strongly dependent on the voltage

[5] Beware! The UV OPO has to be set to 21 Hz for external triggering.

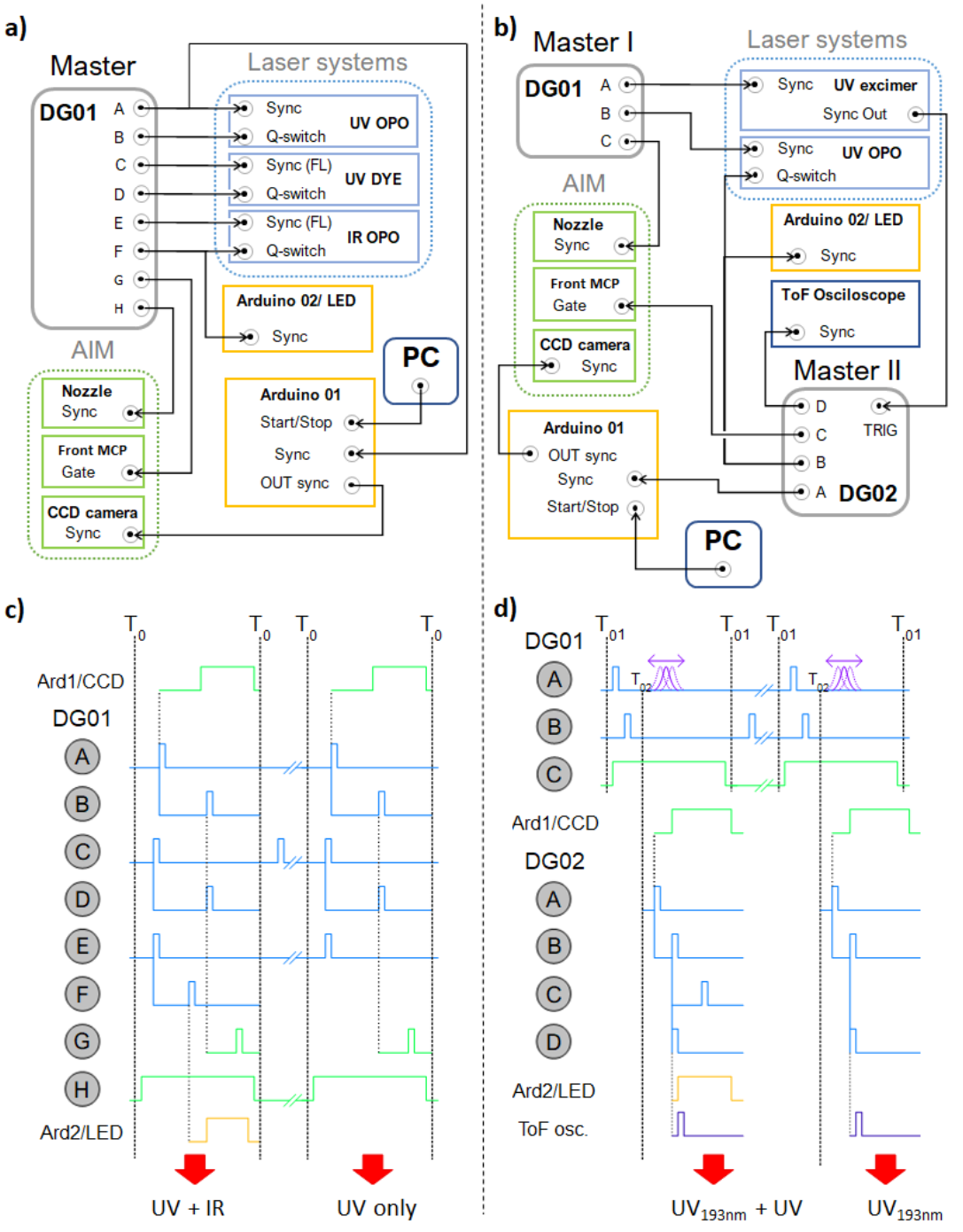


Figure 2.9: Block diagrams and timeline for synchronization of AIM apparatus in IR+UV and UV_{193nm}+UV experiments.

of excimer flashlamps and aging of the ArF premix, and therefore the precise delays in DG02 must always be tuned according to the cross-correlation signal on a photodiode. The pulse jitter is usually within 20 ns, which is good enough for our experiments. The excimer laser has enough energy per pulse for efficient non-resonant ionization, which requires to recorded background signal coming from the excimer ionization. Therefore, the UV OPO laser Q-switch is pulsed with 5 Hz repetition rate and connected to an LED for signal sorting. On the contrary, the non-resonant ionization can be used for recording ToF mass spectra with the

combination of non-gated MCP and oscilloscope, which is triggered according to the UV OPO Q-switch.

The DG settings for IR+UV and UV_{193nm}+UV experiments are listed in tables A.1 and A.2 in Appendix.

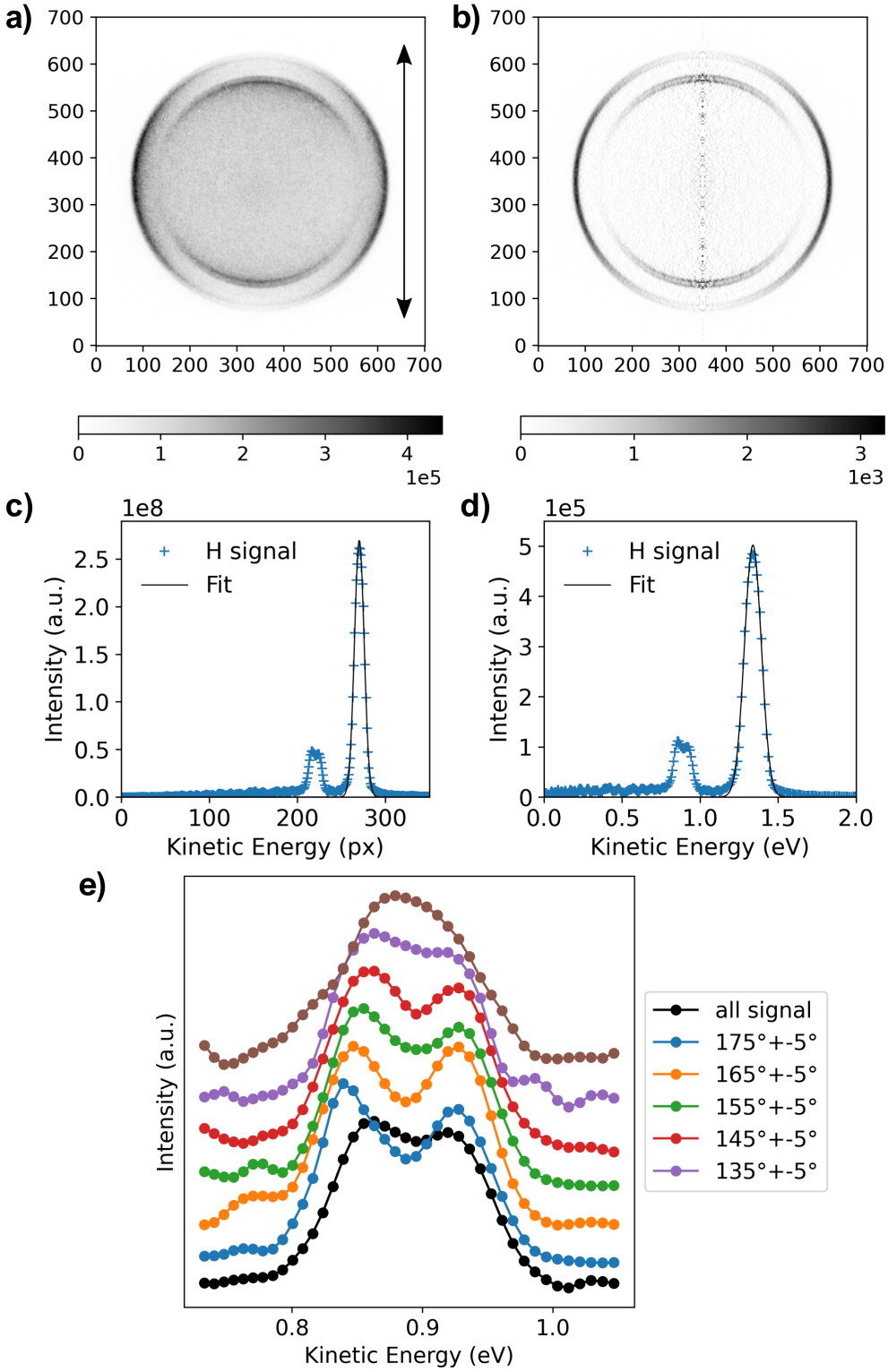


Figure 2.10: a) Raw image of H fragments from HBr dissotiation at 243 nm. b) Transformed image by inverse Abel trasnformation. c) KED[px] d) KED[eV] e) Detailed view of the slow peak.

2.4.3 VMI Calibration by HBr

Equation 2.12 enables us to calibrate all acquired VMI images by application of one VMI image with known kinetic energy distribution. In our group, we use as a benchmark photodissociation of HBr at 243.1 nm, which is also REMPI wavelength for H radical. In figure 2.10, there are shown a) raw image of H fragments and b) its slice after inverse Abel transformation.[87] The two concentric rings have origin in two dissociative pathways of HBr

$$\begin{aligned} \mathrm{HBr} + h\nu &\longrightarrow \mathrm{H}(^2\mathrm{S}) + \mathrm{Br}(^2\mathrm{P}_{3/2}), \\ &\longrightarrow \mathrm{H}(^2\mathrm{S}) + \mathrm{Br}^*(^2\mathrm{P}_{1/2}), \end{aligned} \tag{2.20}$$

which are different from each other in the resulting electronic state of Br radical. Also, the absorption character is different for each channel. The bigger ring has perpendicular anisotropy, whereas the smaller ring with intensified poles has a parallel absorption character.

The integration of radial distribution yields KED[px] shown in figure 2.10 c) with fitting of the the faster peak position r_{cal}. From literature [87], we know that the peak should be centered at 1.337 eV, which we used to calculate the calibration constant k_{cal} from equation 2.12 as $k_{cal} = \sqrt{1.337}/r_{cal}$. The calibrated KED[eV] is shown in figure 2.10 d).

Both images seem to be somehow more blurred in the poles, which is illustrated on the slower peak shown in detail in figure 2.10 e). The reason for this blurring is the electron recoil after photoionization. A hydrogen atom is around $\times 1800$ heavier than an electron, which takes out most of the excess energy after ionization, but still, part of the energy stays with the hydrogen. In the case of (2+1) REMPI at 243.1 nm, the excess energy is equal to 1.7 eV and imparted momentum into the H fragment change the velocity by $423\,\mathrm{m\,s^{-1}}$ along the laser polarization. The H fragments velocity before the ionization is around $13\,\mathrm{km\,s^{-1}}$ and the additional velocity should split the peak by 0.11 eV, which nicely corresponds to the blue line (175°) in figure 2.10 e). The energy splitting decreases for the signal further from the poles proportionally to $\propto \cos\theta$. The last curve where it is possible to distinguish the splitting is the red curve corresponding to the angle 145°, which suggests that the resolution of this VMI image is around 0.09 eV. In general, the energetic resolution of the VMI imaging differs for each experimental campaign mainly due to the FWHM of the longitudinal molecular beam velocity.

Doppler Effect in Ions Detection

It is unnecessary to tune the wavelength for photodissociation over the doppler bandwidth due to supersonic beams' relatively narrow transverse velocity distribution. However, the situation is different after the photodissociation, when all available energy might be imparted into the translational energy of the created fragments. Especially, the light particles, e.g., hydrogen and deuterium, can reach velocities of several kilometers per second, which can cause selective detection of ejected fragments according to their velocity projection into the laser beam direction due to the Doppler effect.

Two lasers, see Appendix A.1, were used for REMPI detection: a) dye laser with bandwidth $0.5\,\mathrm{cm^{-1}}$ at 243 nm and b) UV OPO laser with bandwidth $4\,\mathrm{cm^{-1}}$

Fragment	Mass mu	E_{tr} eV	Velocity $m\,s^{-1}$	REMPI ν cm^{-1}	$2 \times \Delta\nu$ cm^{-1}
H	1	1.4	16436	41152	4.6
Cl	35	0.8	2100	42553	0.58
CH_3	15	2.0	5072	30030	1.0

Table 2.1: Doppler effect in detection of the three selected fragments from our experiments in chapter 3.

at 235 nm − 333 nm. The three different fragments detected in our VMI experiments H, Cl, and CH_3 are listed in the table 2.1 with their masses, maximal kinetic energies and corresponding velocities, REMPI frequency ν and maximal frequency shift $\Delta\nu$ due to the Doppler effect.

Comparing the values from the last column and lasers' bandwidth reveals that the dye laser, which was mainly used to detect H fragments, must be tuned to acquire a true image. On the contrary, the UV OPO laser, which was applied to photoionize Cl, CH_3 and H fragments, does not require frequency tuning. Its bandwidth $4\,cm^{-1}$ is approximately 7× the Doppler spread for Cl radical and around 4× for CH_3 detection. The situation for H is just on edge. However, HBr was merely used for the energy calibration, where the precise band intensity and anisotropy are unimportant. Just for our curiosity, the published β anisotropy parameters of H fragments from photodissociation of HBr at 243 nm are -0.96(0.1) and 1.9(0.2), respectively.[88, 89] Our calibration images yield the β values equal to -0.81 and 1.7, which is caused except for the Doppler effect by admixture of vertical polarization (∼8%) in UV OPO laser.

2.5 Cluster Beam Apparatus

The experiments with large clusters were all performed on our unique versatile CLUster Beam apparatus (CLUB), which detailed description with currently outgoing experiments is reported in [10, 12]. The main advantage of this setup is a continuous molecular beam, which significantly increases the reproducibility of the experiments. However, the massive volume of the expanded gas per second requires differential pumping of the whole apparatus, which consists of six chambers shown in figure 2.11. Inside the first chamber, there is a sample reservoir with a buffer gas supply connected to a conical nozzle source (50-130 µm, opening angle 30°, length 2 mm). Next, the vapor is expanded and skimmed (1 mm, opening angle 30°) into the second and third chambers, which are used for molecular pickup. The first three chambers are pumped by diffusion oil pumps backed by Roots and rotary pumps to persist high vacuum. The next three chambers are held in ultra-high vacuum (1×10^{-9} mbar) by turbomolecular pumps to provide conditions for photo- or electron-induced experiments and product detection. The apparatus is equipped with a VMI spectrometer in the fourth chamber and MS techniques in the last two chambers. Special attention deserves the reflectron Time-of-Flight spectrometer (rToF), which is in right-angled geometry and designed for cluster experiments with high resolution and sensitivity over five orders of signal intensity. rToF can be combined with electron- or photon-ionization and enables experimenting in a negative field, e.g., ion detection after electron attachment.[90] The molecular beam ends in a quadrupole mass spectrometer (QMS) with continuous electron ionization, which can also be used for tuning the nozzle position and monitoring of the molecular beam. Also, the velocity of the molecular beam can be estimated by QMS if combined with a pseudorandom chopper.

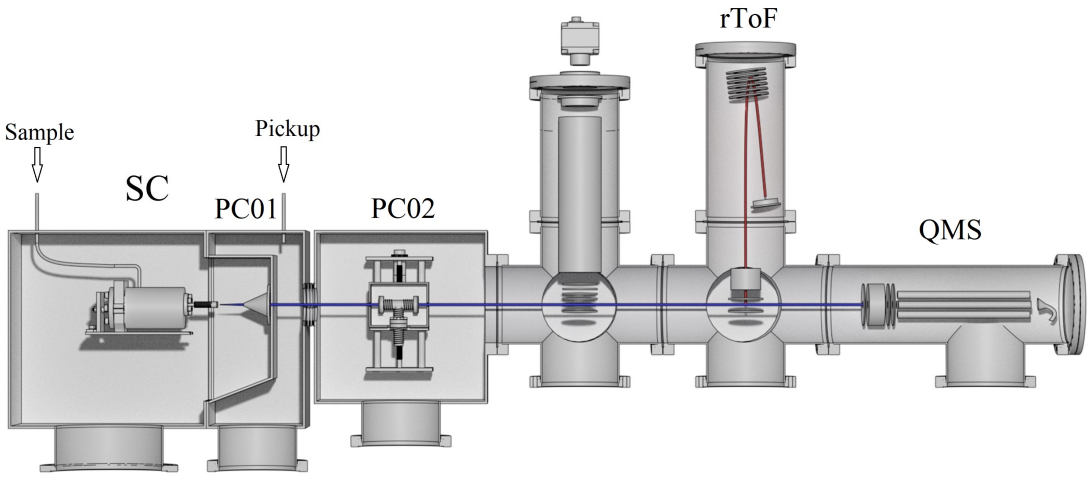


Figure 2.11: Schematic picture of the CLUB apparatus with source chamber (SC), 1^{st} pickup chamber (PC01), 2^{nd} pickup chamber (PC02), reflective time-of-flight spectrometer (rToF) and quadrupole mass spectrometer (QMS).

One of the CLUB's advantages is that multiple experiments can probe the same molecular beam and provide complementary information. On the other hand, the whole path of the molecular beam is long ≈ 2 m to rToF and 1.6 m to

the VMI spectrometer, which significantly reduces the molecular beam density compared to AIM. This is the reason why our VMI experiments on isolated molecules are measured on the AIM, which signal intensity is far more favorable.

2.6 Pickup Experiments

The doping of molecules on clusters in molecular beam offers a unique way to study photoinduced processes on molecules perturbed by an environment or mimic heterogeneous chemistry of the atmosphere and interstellar space medium. In this technique, the clusters generated in nozzle beam expansion are doped by other molecules upon sticking collisions during the flight through the pickup chamber with low vapor pressure. As a result, part of the molecular beam is scattered, which can be observed on the signal decrease proportionally to the vapor pressure, but the others stay on the path to the detector chamber. Our description of the whole pickup process must consider several situations. For example, some clusters can fly without collisions, and some collide without picking up the molecule. The property characterizing the collision of two particles is collision cross-section σ_c, and this must be extended with the sticking probability γ to get a pickup cross-section σ_p. The simplistic view on collision is through geometrical cross-section $\sigma_c^g = \pi \left(R_C + r_M\right)^2$ derived from characteristic radii of the cluster R_C and molecule r_M. However, the attractive interactions often enlarge the real cross-section, which can virtually increase the estimated cluster radius. On the contrary, the sticking coefficient γ ranges between 0 and 1 and thus reduces the estimated cluster radius.

Apparently, estimating cluster size through the pickup experiments is challenging and must be usually combined with the MD calculations to get the proper cluster radius. On the other hand, it offers an alternative route to threshold photoionization, high energy electron collisions, elastic scattering, and sodium doping, which are applicable only to specific cases.[12, 10] One way to estimate the cluster size through pickup experiments is to measure the molecular beam velocity due to the linear momentum transfer during the collisions of clusters and molecules.

2.6.1 Poisson Distribution in Pickup Experiments

Another approach is to apply Poisson statistics to study the cluster size distribution. The Poisson statistics is a discrete probability distribution, which expresses the probability that a given number of events (the pickup collisions) occurs during the given interval (the length of the pickup chamber) if the events are independent and have a constant mean rate. Both of these conditions are fulfilled in our pickup experiments. Furthermore, we have to assume that the picked up molecules M stick ($\gamma = 1$) with the cluster and coagulate to $\mathrm{M_k}$ clusters, which is not fragmented upon 70 eV electron ionization. If all the conditions are met, then the cluster ion abundances in mass spectra series of $\mathrm{C_i} \cdot \mathrm{M_k}|_{i=const.}$ should follow the probability mass function

$$P\left(k;\lambda\right) = \frac{\left(\lambda\right)^k}{k!} \cdot \exp\left(\lambda\right), \quad \lambda = p\frac{\sigma_p L}{k_B T}, \tag{2.21}$$

where p is pressure of vapour in pickup chamber, L =17 cm is the length of the pickup chamber, k_B is Boltzmann constant, T is termodynamic temperature and σ_p is pickup cross-section.

We can evaluate the mean pickup cross-section or effective radius by fitting the function 2.21. An important step is always to check the consistency of the results for different mass series $\mathrm{C_i} \cdot \mathrm{M_k}|_{i=const.}$ and correspondence between the data and Poisson distribution, which can be used as an argument against the ionization-induced fragmentation. The same data processing is also valid when $\gamma < 1$, which on the other hand, might significantly complicate the discussion.

3. Results

> "Knowledge and error flow from the same mental sources; only success can tell one from the other."
>
> *Ernst Mach*

The following chapters give a brief overview of the achieved results during the past four years. The results are ordered as follows: 1) the experimental outcomes from the VMI method and 2) the experimental outcomes of the pickup experiments on the CLUB apparatus. Chapters below delivers an introduction and summary to the five papers,[8, 5, 7, 6, 15] which are attached in Appendix B. The chapters also describe a significant part of unpublished results, which might be used for future publication and as a source of inspiration for further investigation. The story of my research is not straightforward, as many turning points forced me to change the course of the investigation, which is commented below.

My contribution: I performed all the experiments below, data analysis, interpretation, visualization and discussion. Of course, all the work above was done in collaboration with my colleagues. The *ab initio* dynamical simulations in higher chloroalkanes[6] and PAHs[15] comes from our collaboration with theoretical departments.

My other articles published during my PhD study listed in the "List of publications" are not added. Either my contribution was merely data acquisition and analysis,[90, 91, 92, 93] or the article topic is connected to other fields of physical chemistry [4, 3, 94].

3.1 Pyrrole

Pyrrole (C_4H_5N) is a symmetric heterocyclic compound that is a biosynthetic precursor to many naturally occurring species, e.g., heme, vitamin B_{12} and plant pigments. Besides, its five-membered aromatic ring induces absorption in the UV range, making it a desirable system for investigating photostability and energy flow during fragmentation. The complexity of the pyrrole opens alternative routes for energy dissipation through the excitation of vibrational modes competing with the direct fragmentation and photon emission. Firstly, the gained energy constrains the possible relaxation outcomes. Furthermore, the dynamic is driven by the energy redistribution due to mutual vibrational couplings and the excited state topologies. In addition, the laser techniques provide an additional way to tune the fragmentation pattern by state-selective sample preparation.[95, 96]

In molecular beam experiments, pyrrole photodynamics was broadly investigated as a prototypical system of $\pi\sigma^*$ excited state in the perspective of N-H bond fragmentation.[97, 98, 99, 100, 101] The first excited state $^1A_2\,(\pi\sigma^*)$ has a repulsive character with a shallow dwell in the Franck-Condon region separated by a small barrier. Upon N-H bond prolongation, the $^1A_2\,(\pi\sigma^*)$ state crosses the ground state (S_0) in conical intersection (CI). Hence the relaxation can proceed either through quick diabatic fragmentation leading to the fast H-fragments, or slow internal conversion into the vibrationally hot S_0 state. The latter case is then followed by unimolecular dissociation leading to vibrationally excited pyrrolyl fragments and slow H-fragments with a broad statistical kinetic energy distribution.[98, 99] The slow H-fragments might also originate from alternative routes, including CIs induced by out-of-plane deformations of the aromatic ring or multiphoton effects.[99, 100, 101]

Our study[8] was focused on vibrationally mediated photodissociation of pyrrole induced by IR excitation at $\nu_{IR} = 3532\,\mathrm{cm}^{-1}$ (0.44 eV) corresponding to N-H stretching vibration, $\nu_1 = 1$, followed by UV-photon fragmentation at 243.1 nm (5.1 eV). The UV wavelength is not chosen randomly as it is also the REMPI wavelength for H-fragment ionization. The acquired images were transformed through direct inverse Abel transformation, calibrated according to HBr images, and proceeded by standard procedure to obtain KED and angular distributions, see chapters 2.4.3, 2.3.1 and 2.3.2.

The VMI images show qualitatively the same features for IR+UV and UV-only experiments. A broad isotropic blob in the middle assigned to slow H-fragments is surrounded by a ring of perpendicular anisotropy assigned to H-fragments. The IR+UV image shows a more profound H-fragment yield in both channels due to the favorable Franck-Condon overlap between the initial vibrationally excited wavefunction and final state. The same observations are shown in KED spectra.[8]

The KED difference of both measurements corresponding to the pure IR+UV signal reveals that the maximum of the fast peak is centered at 1.04 eV and shifted by 0.23 eV to higher energy compared to the UV-only signal. From the equations 1.3 and 1.25, we can evaluate that 47 % of additional IR energy stays within the pyrrolyl vibrational modes, and the rest is released into the fragments' recoil.

The IR+UV results were also compared to an isoenergetic, single-photon UV-only experiment at 224 nm (5.54 eV) to investigate the impact of energy allocation on the energy flow.[22] The KED for isoenergetic UV-only photodissociation was

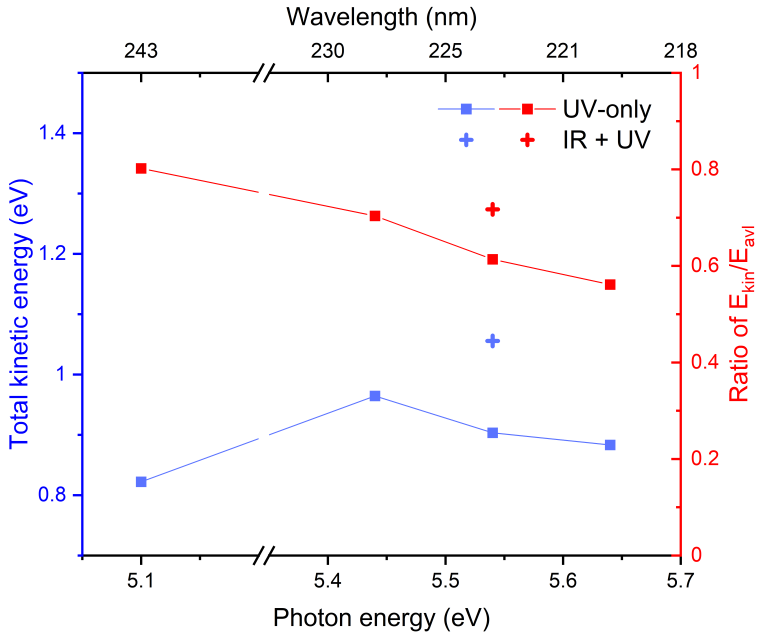


Figure 3.1: Comparison of the fast H-fragment kinetic energy between the UV-only and IR+UV experiments. The blue plots belong to the left axis, which describes the dependence of released total kinetic energy on the photon energy. The red plots belong to the right axis, which describes the dependence of the ratio of the total kinetic energy over the maximum available energy. The values for the IR+UV experiment are marked with crosses. The UV-only results are marked with squares. The extra values at 220 and 228 nm were taken from Cronin et al.[99]

obtained after the subtraction of the UV-only signal at 243.1 nm. The fast fragment peak is broader than in the previous spectra and with maximum shifted to lower energy by 0.15 eV compared to the IR+UV spectra. Assuming no initial internal excitation and dissociation energy of N-H bond equal to 4.07 eV,[8] we can estimate that 72 % and 61 % is deposited to fragment kinetic energy in the IR+UV and isoenergetic UV-only experiments, respectively. Interestingly, the available energy is converted more efficiently into the translational mode in the case of the IR+UV experiment. It illustrates that the allocated energy into N-H vibration couples efficiently with the released fragment kinetic energy.

Finally, the internal vibrational redistribution in pyrrole was studied by the time-resolved nanosecond pump-probe experiment up to 150 ns. All the acquired KED spectra share qualitatively the same bimodal character, enhancing the faster H-fragments independently on the delay between IR and UV pulse. The observation suggests only a weak coupling of the N-H bond stretching vibration to other vibrational modes.

One of the unsolved questions of our pyrrole campaign is the origin of the slow H-fragments.[99, 100, 101] The ratios of the slow and fast H-fragments shown in figure 3.2 are strongly dependent on the UV and IR laser intensity which suggest the origin of slow-H fragments in multiphoton effects. Another interesting scenario might be the perturbation of CI crossing induced by an external UV laser. However, our time resolution prevents us from providing any further proof.

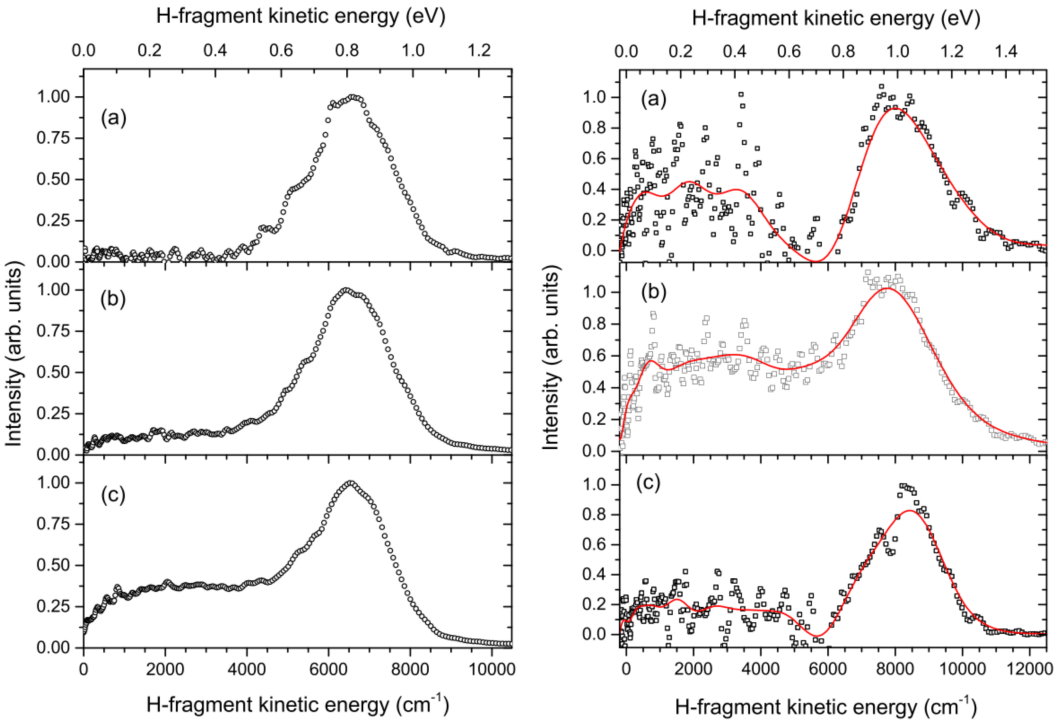


Figure 3.2: (Left) The H-fragment KED spectra dependence on UV energy per pulse: (a) 200 µJ/pulse, (b) 600 µJ/pulse and (c) 1200 µJ/pulse. (Right) The H-fragment KED spectra obtained by the difference of IR+UV and UV-only signal acquired with different IR and UV pulse intensities: (a) IR ∼ 3 mJ/pulse, UV ∼ 390 µJ/pulse, (b) IR ∼ 12 mJ/pulse, UV ∼ 390 µJ/pulse and (c) IR ∼ 12 mJ/pulse, UV ∼ 150 µJ/pulse. [8]

Much effort was also given to the investigation of pyrrole clustering. The photodissociation experiments with pyrrole clusters were performed previously with the CLUB apparatus using rTOF technique to analyze the fragment kinetic energy.[102, 103] Unfortunately, none of the performed experiments on the AIM apparatus reliably confirmed the cluster observation, partly due to the interference with the signal of the slow H-fragments.[62, 104]

These results have been published in [8], which is added as attachment B.1 to this thesis.

3.2 Ã-band Induced Photofragmentation of Selected Haloalkanes as Isolated Molecules and Clusters

Small haloalkanes are among the most abundant atmospheric species originating from natural and anthropogenic emissions with an extensive application as chemical solvents and intermediates in the petrochemical industry, agriculture, and chemical synthesis.[105, 106] Their involvement in radical, catalytic, and heterogeneous chemistry is a substantial driving force of chemistry in the Earth's atmosphere. A well-known example is the depletion of the stratospheric ozone layer due to the radical reaction between the ozone and halogen radicals, see chapter 1.5.1. Consequently, the selected halogenated compounds were banned by the Montreal Protocol (MP, 1983), and since then, they have been carefully monitored.[51, 12, 105, 52] Simultaneously with the phasing-out of the monitored haloalkanes, others overtake their role in ozone depletion. Currently, the methyl chloride CH_3Cl is responsible for about 16% of all ozone depletion, and its importance will increase during the next 10-30 years.[105]

CH_3Cl is the most abundant carrier of Cl atoms in the atmosphere.[105] Although its origin is predominantly natural from sources like the tropical rainforests, marine emissions, and biomass burning, there is considerable uncertainty about the origin of the 20% of its atmospheric contain.[107] The recent observations nearby industrial areas of 24h cycles in CH_3Cl concentration superimposed on the seasonal changes point out the non-negligible impact of the anthropogenic activity.[105] The monitoring of atmospheric CH_3Cl and understanding of its photodynamics is thus of high importance for the global community, especially when the compound is not included in MP.

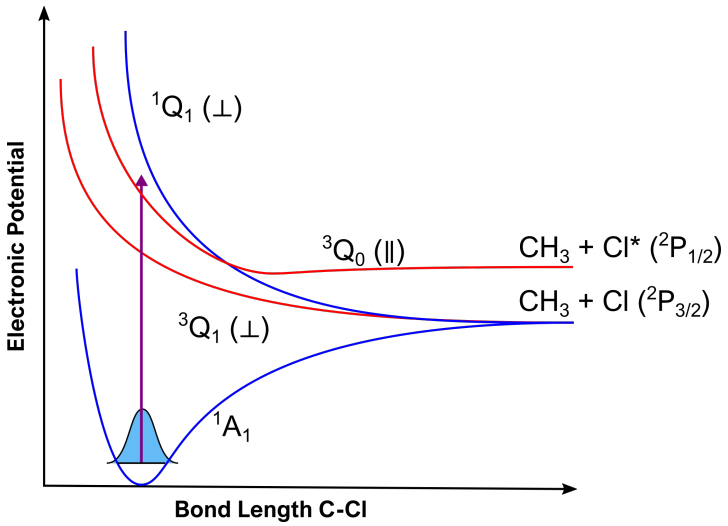


Figure 3.3: Schematic picture of the cut through the PES of the ground and three lowest excited states of small chloroalkanes in perspective of C-Cl bond.

We investigated photofragmentation of CH_3Cl upon excitation into the first Ã-band induced by laser pulses at 193 nm (6.41 eV). The Ã-band corresponds to electron transfer from the non-bonding orbital localized on the Cl atom to

the antibonding σ^* orbital along with the C-Cl bond. Moreover, we extend the investigation to selected higher chloroalkanes to study the impact of the alkyl chain length and Cl-group position on the involvement of triplet states, which were recently proposed as a viable pathway for atmospheric photochemistry.[6, 108]

The photodynamics in the first absorption band is driven by an interplay of three excited states ordered bottom-up in the Frank-Condon region as $^3Q_1$, $^3Q_0$, and $^1Q_1$.[109] Their schematic picture in perspective of C-Cl bond elongation is shown in figure 3.3, which will be later applied also for the higher chloroalkanes. All the excited states have a repulsive character with the $^3Q_1$, $^1Q_1$ states correlating to the bond-cleavage with Cl in the ground state and the $^3Q_0$ correlating to the bond-cleavage with Cl* in the excited state. The spin-orbit splitting of Cl fragments is 0.109 eV. The $^1Q_1$ and $^3Q_0$ states are crossing upon C-Cl bond prolongation, which opens the route driven by intersystem crossing dynamics. The $^3Q_0$ and $^1Q_1$ states were reported to have also different absorption symmetry. Whereas the transition into $^3Q_0$ state has a parallel character, the transition into $^1Q_1$ has a perpendicular character.[6] The lowest triplet state $^3Q_1$ is considered as a dark state with approximately two orders of magnitude lower absorption cross-section compared to the $^3Q_0$ and $^1Q_1$ states. Due to a steep repulsive character, the fragmentation should occur within several tenths of femtoseconds.

We followed the previous VMI study [109] of Towsend et al. on isolated CH_3Cl and further extended it with new images of CH_3 fragments in the ground vibrational state $\nu = 0$. The (2+1) REMPI schemes were applied for state-selective ionization of Cl fragments[110, 109, 5]

$$\mathrm{Cl}\left(3\mathrm{p}\ ^2\mathrm{P}_{3/2}\right) \xrightarrow{2\times 235.31\,\mathrm{nm}} \mathrm{Cl}\left(4\mathrm{p}\ ^2\mathrm{D}_{3/2}\right) \xrightarrow{235.31\,\mathrm{nm}} \mathrm{Cl}^+, \tag{3.1a}$$

$$\mathrm{Cl}^*\left(3\mathrm{p}\ ^2\mathrm{P}_{1/2}\right) \xrightarrow{2\times 235.17\,\mathrm{nm}} \mathrm{Cl}\left(4\mathrm{p}\ ^2\mathrm{P}_{1/2}\right) \xrightarrow{235.17\,\mathrm{nm}} \mathrm{Cl}^+, \tag{3.1b}$$

and CH_3 fragments[111]

$$\mathrm{CH}_3\left(\nu = 0, 2\mathrm{p}^2\right) \xrightarrow{2\times 333.5\,\mathrm{nm}} \mathrm{CH}_3\left(3\mathrm{p}^2\right) \xrightarrow{333.5\,\mathrm{nm}} \mathrm{CH}_3^+. \tag{3.2}$$

The recorded VMI images with extracted KEDs and angular distributions of (a,b,c) Cl, Cl* and (d,e,f) CH_3 fragments are shown in figure 3.4. The polarization of the pumping laser is indicated in the first image by the white arrow. All images have a single ring structure with apparent perpendicular anisotropy, which supports the assumption of rapid fragmentation.

The KEDs of Cl and Cl* fragments show single peaks centered at 0.79 and 0.78 eV, respectively. The estimated peak positions reveal a substantial internal excitation of recoiled CH_3 fragments. The energy shift compared to the maximal possible kinetic energy value of 0.86 eV and 0.82 eV estimated from hard sphere model, see chapter 1.4.1, fits to the excitation of CH_3 umbrella mode, $\nu_2 = 2 - 3$ (606 cm^{-1}).

Therefore, $CH_3(\nu = 0)$ image represents only a fraction of all ejected CH_3 fragments. The corresponding KED spectrum in e) shows the peak centered around 1.95 eV with indicated theoretical maximal value of 1.99 eV also exposing rotational excitation of the CH_3 fragments. This is also supported by our search for vibrationally excited CH_3 fragments by scanning action spectra, which

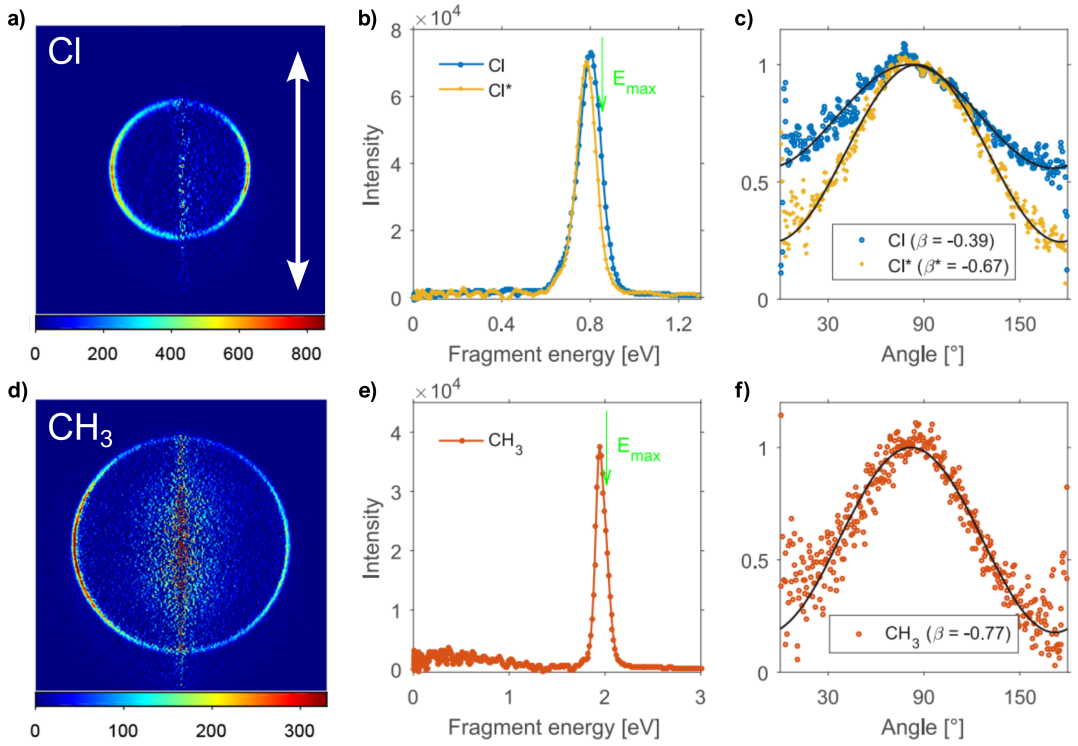


Figure 3.4: Comparison of the VMI images with extracted KED spectra and angular distributions assigned to (a,b,c) Cl, Cl* and (d,e,f) CH_3 fragments. The figures were taken from [5] and modified.

revealed a very broad peak corresponding to excitation of umbrella mode $\nu_2 = 1$ of CH_3, see [5] for details.

The mutual peak positions of Cl and CH_3 fragments illustrate that most of the energy is departed into the translational mode during abrupt fragmentation, and therefore, we can look at the CH_3Cl fragmentation through the view of the simplified pseudo-diatomic hard sphere model.

The Cl fragment angular distributions plotted in figure 3.4 c) show perpendicular character independently on the Cl state. The significantly higher values of anisotropy parameter β than -1 comes from a significant absorption into $^3Q_0$ state with a parallel transition character. Moreover, even more perpendicular value of anisotropic parameter $\beta^* = -0.67(8)$ corresponding to the excited Cl* compared to $\beta = -0.39(7)$ of the ground Cl fragments has an origin in efficient ISC in both directions between $^3Q_0$ and $^1Q_1$ states. Combining the anisotropic parameters with the signal ratio of excited and ground Cl fragments equal to $[Cl^*]/[Cl] = 0.86$, we can evaluate the probability of the ISC transitions as $P_{ISC}(^3Q_0 \rightarrow {}^1Q_1) = 0.61$ and $P_{ISC}(^1Q_1 \rightarrow {}^3Q_0) = 0.49$, and ratio of absorption into triplet compared to singlet state as $P_{abs}(^3Q_0)/P_{abs}(^1Q_1) = 0.16/0.84$.

The angular distribution of $CH_3(\nu = 0)$ fragments also shows the perpendicular character with slightly higher value of $\beta_{CH_3} = -0.77(10)$. An even higher value was observed for $CH_3(\nu_2 = 1)$ fragments, which is consistent with the predictions of Townsend et al.[109] However, it also indicates that the vast majority of the CH_3 fragments, probably with high internal excitation, is not detected.

Our results are in good agreement with the previous investigation of isolated

CH_3Cl.[109]

3.2.1 Photodissociation of Isolated Higher Chloroalkanes

We further investigated the surprisingly extensive involvement of the triplet states in the photodynamics of CH_3Cl by series of the VMI experiments combined with direct *ab initio* dynamical simulations on selected higher chloroalkanes. The ball structures of CH_3Cl and the higher chloroalkanes are shown in figure 3.5.

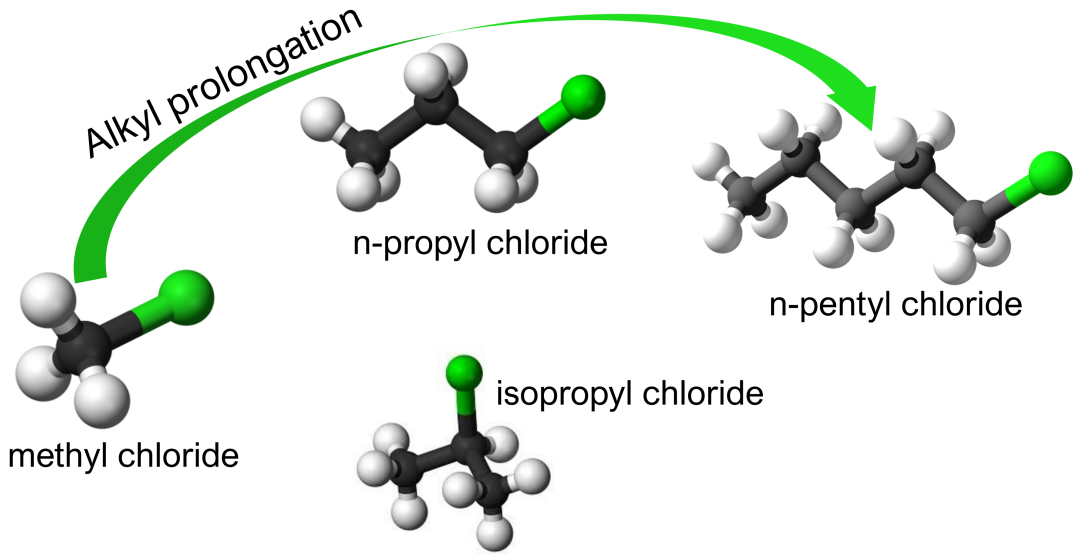


Figure 3.5: The structures of investigated chloroalkanes. The models were taken from [112] and modified.

First, we were interested in the impact of alkyl chain prolongation on the probability of the ISC and direct singlet-triplet absorption by experiments with n-propyl chloride (n-C_3H_7Cl) and n-pentyl chloride (n-$C_5H_{11}Cl$). Secondly, we also probed the impact of the Cl-group position in experiments with isopropyl chloride (i-C_3H_7Cl). Previous studies were merely focused on the iodo- and bromoalkanes due to the stronger spin-orbit effects caused by a heavier halogen atom. Nevertheless, our previous experience with CH_3Cl shows that the spin-orbit coupling also drives the photodynamics in chlorinated species, which is further demonstrated in the paragraphs below.

The previous case of CH_3Cl could be treated in a pseudo-diatomic manner. On the other hand, the higher chloroalkanes offer far more possibilities to distribute the excess energy among the internal modes of the alkyl (R) fragment. Moreover, the alkyl chain's distortion of the linear C-Cl frame can reduce the coupling between the orientation of the transition moment and the C-Cl bond, which further complicates the analysis of the experimental results. Therefore, the theoretical anisotropy parameters of -1 and 2 for absorption into $^1Q_1$ and $^3Q_0$ states, respectively, were recalculated, including the distortion effect. Furthermore, we also applied the non-adiabatic *ab initio* calculations, see [6, 37] for technical details, to analyze the acquired KEDs and compared them to the classical mechanic approach discussed in chapter 1.4.

All three VMI images of higher chloroalkanes independently on the Cl state exhibit the one ring structure similar to CH_3Cl. The weak i-C_3H_7Cl image also shows an additional signal in the image center, most likely originating from the clustering. The obtained KED spectra were fitted with a Gaussian function to

Molecule	$E_{tr}^{Cl}/\Delta E_{tr}$	f_I^{exp}	f_I^{spec}	f_I^{CASSCF}	f_I^{rigid}
CH_3Cl	0.79/0.12	0.08	0.15	0.01	0.00
n-C_3H_7Cl	0.82/0.26	0.47	0.54	0.36	0.22
n-$C_5H_{11}Cl$	0.81/0.26	0.56	0.62	0.47	0.22
i-C_3H_7Cl	0.87/0.35	0.43	0.54	0.33	0.21

Table 3.1: Fitted kinetic energies of ground Cl fragments and corresponding experimental fractions, $f_I^{exp} = 1 - E_{tr}/E_{excess}$, and model estimations of internal excitation energy f_I^x after dissociation of the selected higher chloroalkanes.

extract the peak positions. The calculated excess energy E_{excess} from photon energy and experimental dissociation energies does not allow fragmentation of other alkyl bonds, and therefore, we could assume two-body R-Cl dissociation. This we applied to evaluate the excess energy redistribution among the translational E_{tr} and internal degrees of freedom from conservation of linear momentum, see table 3.1. Although the KED spectra exhibit similar peak positions, the mean total kinetic energy is vastly different among the investigated compounds. Contrary to the previous example of the CH_3Cl ($\sim 10\%$), around half of the excess energy is distributed into rotational and vibrational excitation of R-fragment. Also, we observed systematic 5-10% lower internal excitation of the R-fragments recoiling from the excited Cl* fragment.

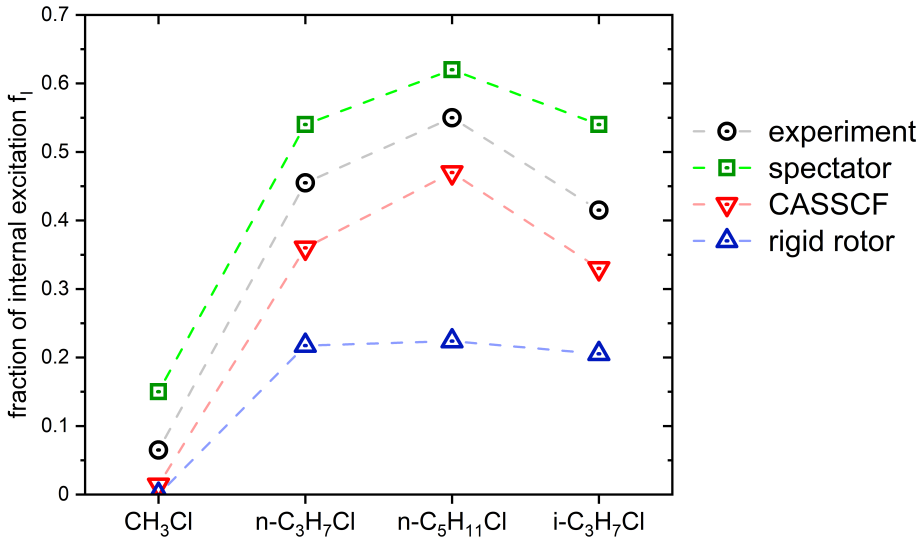


Figure 3.6: Comparison of fraction of internal excitation f_I^x obtained from experiment, classical models and *ab initio* CASSCF simulations.

The classical models enable us to compare our experimental results with the two extreme situations of no internal energy excitation represented by the hard sphere model and maximal possible internal excitation represented by the spectator model. Apparently, the hard sphere model cannot capture the substantial alkyl internal excitation, and thus the calculated Cl fragment kinetic energy vastly

overestimates the experimental values.

The spectator model treats the process as dissociation of chlorine against the closely binding carbon, which is expressed in linear momentum conservation and resulting kinetic energy of Cl fragment equal to $E_{sp} = E_{excess} \cdot m_C/(m_C + m_{Cl})$. The rest of the excess energy is then distributed among the alkyl internal excitation and recoil, fullfiling the conservation of momentum $\boldsymbol{p_{Cl}} = \boldsymbol{p_{alkyl}}$.

A comparison between the experimental values and calculated kinetic energies is shown in figure 3.7. However, it should be stressed that the calculated values do not correspond to the mean peak energies but represent the limits for Cl fragment kinetic energy. In fact, the calculated values show that the spectator model (green squares) overestimates the experimentally estimated internal excitation (black circles). There is also another blue line corresponding to the rigid rotor model taken from [113, 38], which assumes no vibrational excitation. From the above, we can say that the alkyl chain is a relatively soft, energy-absorbing unit, representing an intermediate situation between both limits given by the classical mechanics approaches.

Apparently, none of the models can capture the complete picture of the dynamics during dissociation, and thus we applied *ab initio* CASSCF simulations to further elucidate the energy transfer among different modes. In simulations, all four compounds exhibit fast fragmentation effectively completed within 25 fs, which agrees with the classical photodissociation model, [114] assuming the similar PES steepness and effective reduced mass of the R-Cl system. Unfortunately, the CASSCF lacks the dynamical correlation, and thus, the energy scale of the calculated Cl fragment distributions is somehow shifted toward the higher energies. Nevertheless, the comparison of the simulated Cl fragment KEDs can offer a qualitative picture of the impact of the alkyl chain elongation and the Cl-group position.

The simulations could not fully catch the mutual change between the almost pseudo-diatomic dissociation of CH_3Cl and the balance between the stiffness and rigidity of the alkyl chains in other chloroalkanes but still, illustrate high consistency with the experimental spectra. The Cl fragments corresponding to CH_3Cl show narrow distribution and, similar to the experiment, depart almost all the available energy into the recoil of Cl and CH_3. On the contrary, the other chloroalkanes exhibit far broader distribution shifted to the higher energies. Also, we were able to reproduce the unambiguously slightly higher energy of Cl fragments for i-C_3H_7Cl compared to the other two, n-C_3H_7Cl and n-$C_5H_{11}Cl$, chloroalkanes. Again, we recalculated the fraction f_I^{CASSCF} of excess energy deposited in the alkyl internal energy, which is shown in figure 3.6. Somehow lower values compared to the experimental ones correlate with the 0.8 correction for the Hartree-Fock method proportional to the square of the known scaling factor for vibrational frequencies, which seems to have a non-negligible impact even in such an abrupt fragmentation.[115]

In the second part, we focused on investigating the direct singlet-triplet absorption and ISC hidden in the angular distribution of the acquired images. The angular distributions were processed by standard procedure and fitted to estimate the anisotropy parameters. Same as in the case of CH_3Cl, the images of higher chloroalkanes show swapped characters of the Cl and Cl* angular distributions towards the diabatically correlating $^1Q_1$ and $^3Q_0$ states, respectively. The Cl

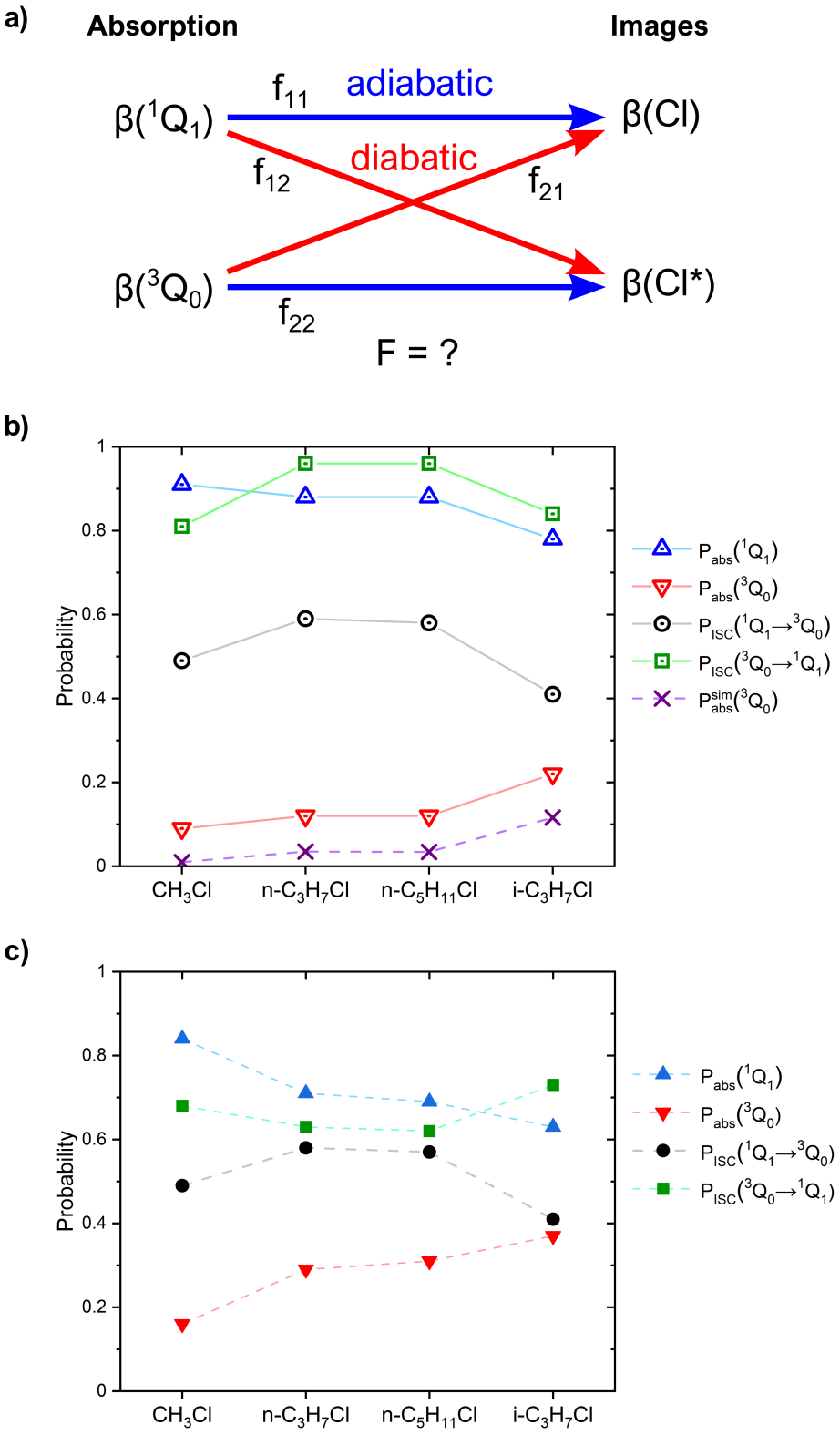


Figure 3.7: (a) Scheme of model for calculation of ISC and singlet-triplet absorption probabilities. (b) Estimated probabilities of ISC and singlet-triplet absorption with the simulated β^{sim}-parameters. (c) Estimated probabilities of ISC and singlet-triplet absorption with the maximal theoretical values of β-parameters.

fragments exhibit the β-values above zero $\sim 0.1 - 0.3$ indicating slightly parallel anisotropy in contrary to the asymptotically correlating $^1Q_1$ state with perpendicular absorption character and *vice versa* for the Cl* fragments. The distributions indicate substantial direct singlet-triplet absorption and ISC transition enabled by the strong spin-orbit coupling.

For quantitative parameterization of the spin-orbit effect, we calculated the relative probabilities for the absorption into $^1Q_1$ and $^3Q_0$ states and probability for ISC in both directions according to a simple model found in literature [109]. The model estimates suitable probabilities (P) from the comparison of the theoretical β-parameters for absorption and the experimental fitted β-parameters, which is schematically illustrated in figure 3.7 a).

We assumed two sets of theoretical absorption β-parameters: 1) Similar to Townsend et al.[109], the $\beta = -1$ and $\beta^* = 2$ for the perpendicular and parallel transitions to the $^1Q_1$ and $^3Q_0$ states, respectively. 2) A new set of simulated β^{sim}-parameters with the implemented effect of a non-linear alkyl frame, which causes disruption in absorption character and thus makes the theoretical values more isotropic. The new β^{sim}-parameters were fitted from the angular distributions between the C-Cl bond and the transient moment with included photoselection.

The estimated values for the absorption and ISC transition probabilities are shown in figure 3.7 b) calculated from the simulated β^{sim}-parameters. As was assumed, the radiation at 193 nm induces preferential absorption into $^1Q_1$ with a relative probability above 0.8 represented by the blue line. Whereas the alkyl prolongation leads to only a slight increase in the singlet-triplet absorption to $^3Q_0$, the Cl-group position seems to induce a two times higher probability of direct singlet-triplet absorption for i-C_3H_7Cl compared to n-C_3H_7Cl. The ISC probabilities are generally high for all investigated chloroalkanes, between 0.4-0.6 for $^1Q_1 \rightarrow {}^3Q_0$ transition and above 0.8 for $^3Q_0 \rightarrow {}^1Q_1$ transition. A small but consistent effect of alkyl prolongation from CH_3Cl to n-C_3H_7Cl and n-$C_5H_{11}Cl$ is shown in 0.1-0.2 increase for ISC in both directions. Interestingly, the Cl-group position seems to have an opposite effect in i-C_3H_7Cl, resulting in ISC probability comparable to CH_3Cl. In figure 3.7 c), there are also shown the estimated values calculated with the maximal absorption β-parameters (-1 and 2) to illustrate the importance of the recalculated β^{sim}-parameters.

The high probability of the direct excitation into the triplet state was also confirmed by the simulations of the UV absorption spectra. The radiation at 193 nm is at the red edge of the singlet-singlet absorption band, which is centered ~ 180 nm and sharply decreases towards the longer wavelengths. Oppositely, the center of the singlet-triplet band is shifted above ~ 190 nm close to the laser radiation and thus becomes competitive even to the singlet-singlet absorption.

The results above indicate a surprisingly high impact of the spin-orbit effects for an organic molecule with a chlorine group. Our analysis neglected the involvement of the $^3Q_1$ state due to its low absorption cross-section. However, the alkyl extension and Cl-group positions might open this route, which would be effectively incorporated in a slight overestimation of the probability for $^1Q_1$ absorption and $^1Q_1 \rightarrow {}^3Q_0$ ISC transition. Nevertheless, at the moment, it is still an open question for future investigation.

These results have been published in [6], which is added as attachment B.4 to this thesis.

The previous experiments were focused on isolated molecules to investigate the fundamental photochemistry of selected chloroalkanes. Our long-term goal is to move from the VMI experiments on single molecules to the clusters mimicking the atmospheric aerosols. The following three chapters are about our first step towards the chloroalkanes in clusters.

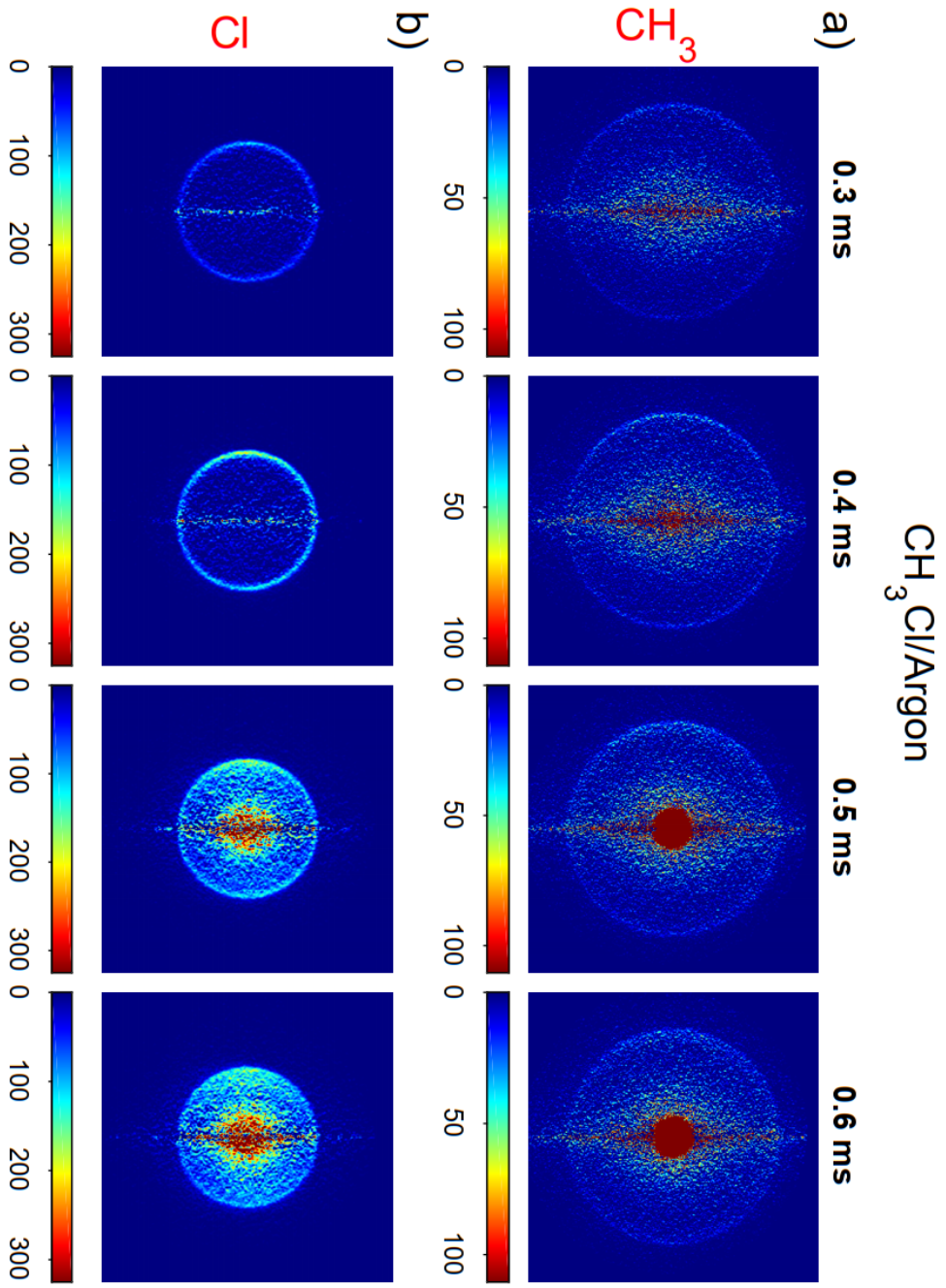


Figure 3.8: VMI images of CH_3 and Cl fragments after 193 nm photofragmentation of CH_3Cl seeded in argon. The images were taken in different delays of beam profile.[5]

3.2.2 Photodissociation of CH_3Cl clusters

Contrary to the previous experiments, we seeded the sample in argon buffer gas to induce clustering. The VMI images shown in figure 3.8 were taken in different clustering conditions by scanning the delay between the nozzle opening and the laser pulses. The images detected at 0.3 and 0.4 ms share the one-ring structure similar to the images from the isolated molecules. The next two sets of images detected at 0.5 and 0.6 ms are dominated by the strong central blobs surrounded by weaker ring structures. The corresponding KED spectra are shown in figure 3.9. The fast fragments forming the narrow peaks were assigned to the molecular signal. This was confirmed by the narrow peak positions and anisotropy parameters $\beta(\mathrm{Cl}) = -0.35(4)$, $\beta^*(\mathrm{Cl}^*) = -0.61(7)$ and $\beta(\mathrm{CH_3}) = -0.67(18)$ nicely fitting to the values shown in figure 3.5. Slightly lower values of $\beta(\mathrm{Cl})$ and $\beta^*(\mathrm{Cl}^*)$ were justified by the interference with the signal from clusters.

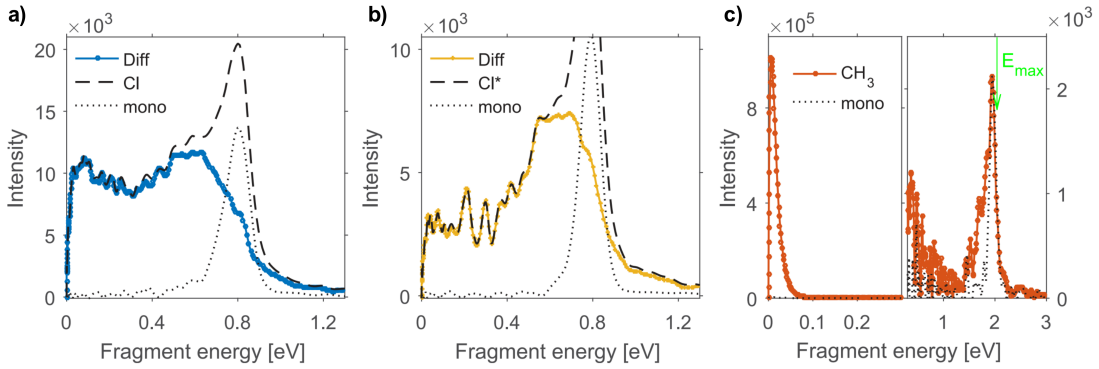


Figure 3.9: Obtained KED spectra corresponding to a) Cl, b) Cl* and c) CH_3 fragments. The dashed lines are raw spectra. The dotted lines are monomer signal. The plots were taken and modified from [5].

The central blobs are a characteristic effect of clustering caused by fragment caging. The ejection of fragments is accompanied by collisions with the surrounding environment resulting in a reduction of kinetic energy. Nevertheless, the inspection of the central features indicates the vast difference among the $CH_3(\nu = 0)$ and Cl (or Cl*) fragments. The CH_3 fragments exhibit strong caging with a narrow peak close to zero. Contrary, the Cl and Cl* fragment spectra with subtracted monomer signals are formed by qualitatively identical broad bimodal distribution with the first peak maximum close to zero kinetic energy and the second peaking around ~ 0.6 eV. Some of the Cl fragments even surpass the kinetic energy of fragments ejected from monomers, which was already observed in ICl clusters due to recoil against the mass of the whole cluster.[116]

The KEDs spectra illustrate distinct dynamics of Cl and CH_3 fragments. Whereas the $CH_3(\nu = 0)$ fragments are caged in a cluster environment, losing almost all the kinetic energy, the Cl fragments are only slowed down, which corresponds to the delayed exit mechanism shown in figure 1.4.

The second observation in the case of clustering was the change in intensity ratios between $CH_3(\nu = 0)$ versus Cl fragments and Cl* versus Cl fragments compared to the experiments with monomers. The ratio of $[CH_3(\nu = 0)]/[Cl]$ exhibits ten times increase from ≈ 0.25 to ≈ 2.15. The ratio of Cl fragments in the ground and excited states, on the contrary, decreased from ≈ 0.86 to ≈ 0.55.

The same results were obtained in several control measurements with a different delay between pump and probe laser pulses. A possible experimental artifact caused by more efficient detection of the slowed CH_3 fragments was also excluded by simple simulations.

We explained the apparent increase in CH_3 signal or Cl signal decrease[1], upon clustering conditions through several combined mechanisms. One of the mechanisms is the quenching of rovibrationally excited CH_3 fragments. The Cl KED spectra of single molecules suggest that the departed CH_3 fragments should have approximately $2-3$ quanta in umbrella stretching mode. The quenching of CH_3 to $\nu = 0$ state would thus yield a higher $CH_3(\nu = 0)$ signal. This was confirmed by measuring the action spectrum, which shows no fragments at the vibrationally excited $\nu_2 = 1$ state. However, this cannot explain the entire increase of the $[CH_3(\nu = 0)]]/[Cl]$ ratio. The second mechanism is taken from the published experiments with $(CH_3I)_n$ clusters, where I_2 generation was reported.[117, 118] Similarly, we suggest the same mechanism leading to Cl signal decrease due to the generation of Cl_2 molecules.

The experiments on $(CH_3I)_n$ clusters also reported the decrease in the [I*]/[I] ratios, which was explained by preferential participation of the excited I* fragments in the same intracluster reaction producing I_2.[117, 118] An analogical pathway would also work for our results. However, we cannot exclude the electron excited state Cl* quenching and the changes in probabilities of direct triplet absorption and ISC induced by the environment. Unfortunately, the signal of faster ions is interfering with the monomer signal, and the central blob shows isotropic distribution β_{Cl/Cl^*} due to the cluster caging. Therefore, it is not possible to estimate the transition probabilities.

We also performed another series of experiments with different concentrations of the CH_3Cl/Ar mixture to investigate the composition of the observed clusters. Even the expansion with pure CH_3Cl revealed qualitatively identical bimodal distribution, suggesting that we generate the pure $(CH_3Cl)_n$ clusters in expansion with argon. The reported calculations of the pure $(CH_3Cl)_2$ dimers revealed two hydrogen-bonded structures with parallel and antiparallel orientations of the CH_3Cl frames.[119, 120, 121] In both arrangements, the Cl and CH_3 endings have free space for ballistic recoil and thus cannot explain the observed caging effect. Therefore, we concluded that our observations suggest the large cluster arrangement with CH_3Cl molecules oriented by their Cl-group outside of the cluster. A similar structure was also proposed for $(HCl)_n$ clusters.[122] Nevertheless, the comparison should be taken with caution, and our data ask for structure and dynamic simulations to elucidate the observed phenomena.

These results have been published in [5], which is added as attachment B.2 to this thesis.

[1] We calculated relative signals, and thus we cannot distinguish between these two scenarios.

3.2.3 Comparison of Multiphoton Effects and Clustering

The VMI method is usually applied for studying photochemical processes on single molecules. The reason lies in the problematic interpretation of the features appearing in the image center due to the clustering effect (fragment caging), which is sometimes confused with multiphoton effects or statistical dissociation. Therefore, we also performed a study of the multiphoton effects on CH_3Cl.

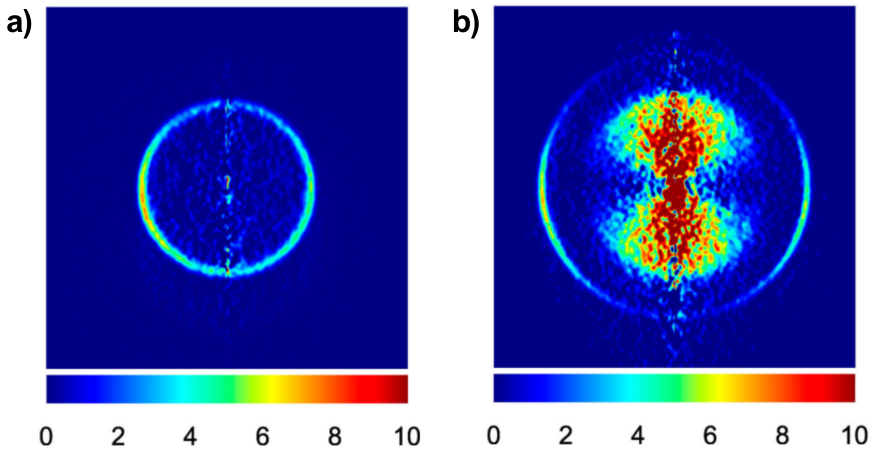


Figure 3.10: The VMI images of a) Cl and b) CH_3 in high irradiation conditions, $I_{193} = 16 \times 10^{25}$ photons/cm^2/s. [7]

We acquired VMI images of CH_3Cl dissociation induced by 193 nm laser pulse followed by REMPI detection with different photon fluxes.[7] In low laser intensities ($I_{193} = 4 \times 10^{25}$ photons/cm^2/s), we get the images shown in figure 3.5. The situation is dramatically changed when the flux is increased to $I_{193} = 16 \times 10^{25}$ photons/cm^2/s, which is illustrated in image 3.10. The Cl image preserves the simple one ring structure, whereas the CH_3 image shows a strong anisotropic feature with an "hour-glass" shape in the image center. The squared dependence of the signal on the 193 nm photon flux indicated the double photon process behind the central feature. The anisotropy of the "hour-glass" effect is connected to the polarization of the REMPI laser, not the 193 nm laser. However, the signal is independent of the precise wavelength of the probing laser, and we can detect a similar signal even at non-resonant 333.0 nm. Therefore, the "hour-glass" effect corresponds to the non-state-selective signal of CH_3. In the case of the 193 nm-only experiment, the acquired mass spectra show intensive peaks at m/z = 50 and 52 corresponding to CH_3Cl^+ signal, which is depleted when the REMPI laser is on. This leads to an interpretation that the central signal has origin in [123]

$$CH_3Cl \xrightarrow{2\times 193\,\mathrm{nm}} CH_3Cl^+ \xrightarrow{\sim 330\,\mathrm{nm}} CH_3^+ + Cl^{\cdot}. \tag{3.3}$$

The corresponding total kinetic energy release (TKER) spectra show broad band between 0 and 2 eV with maximum at 1.1 eV. The anisotropy was analyzed in 0.14 eV slices of the broad band. The fitted formula 2.19 yields the β in range from 1.3 to 2.0 proportional to the TKER.

The schematic picture of the CH_3Cl^+ ionic states with indicated excitation is shown in figure 3.11. The double photon (193 nm) excitation brings 12.82 eV to

the system, which is enough for excitation to ion bound ground X^2E state. Another ~ 333.0 nm photon thus can induce further transition to B^2E or A^2A_1 state. According to the parallel absorption symmetry and strong oscillator strength, we assigned the observed signal to the B^2E excitation. The B^2E is a bound state, and the dissociation thus was reported to proceed through internal conversion into a highly vibrationally excited X^2E state and following asymptotic fragmentation into $CH_3^+(1^1A_1') + Cl(^2P_{3/2})$ with threshold energy of 13.41 eV. Therefore, the plotted TKER distribution reflects the convolution of vibrational excitations in $CH_3Cl^+(X^2E)$ parent ion and produced $CH_3^+(1^1A_1')$ ions.

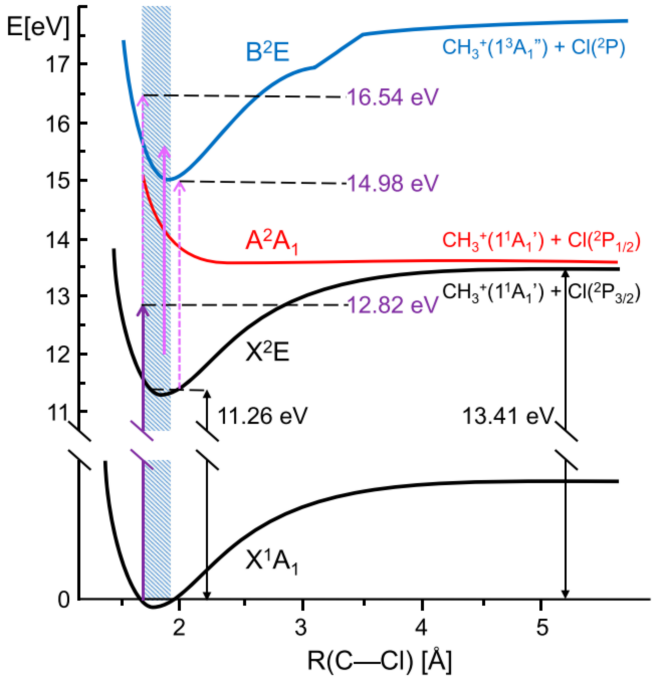


Figure 3.11: Schematic representation of the PES that play a role in CH_3Cl^+ dissociation along the C-Cl coordinate. The violet and pink arrows mark the excitations into the ionic states. The scheme was taken from [7].

The maximum of 1.1 eV corresponds to $5-6$ vibrational quanta distributed in CH_3^+ umbrella or in-plane modes, which is in good agreement with the experiments on CH_3Br^+.[124, 125] The previous experiment with CH_3Cl^+ photodissociation at 357 nm studied by mass-analyzed ion kinetic energy spectrometry revealed a signal with similar parallel character, but substantially lower anisotropy $\beta \approx 1.2$ and kinetic energy peaking around 0.9 eV. However, the difference might be explained by different production of parent ion CH_3Cl^+ by electron ionization instead of multiphoton excitation.

These results have been published in [7], which is added as attachment B.3 to this thesis.

Photodissociation of Higher Chloroalkanes in Clusters

Recently, we also performed photodissociation experiments with clusters of the selected higher chloroalkanes induced by 193 nm radiation. The sample temperature was controlled according to the backup pressure to guarantee a 10 % sample mixture seeded in an argon buffer gas. The temperature was calculated according to the Antonine equations reported in [126, 127, 128]. We tested different pressure conditions between $1 - 3.6$ bar. The clustering was reached above the 2 bar without exception. The delay scanning between the nozzle opening and pump-probe pulses shows a similar evolution to the CH_3Cl clusters. Again, we see the close to monomer mode in the initial and final phase of the nozzle opening and the clustering in between. The monomer signal exhibits the one ring structure with the anisotropy β-parameters equal to the experiments in [6] within the errorbars. The laser settings were similar to the experiments with CH_3Cl, see [5, 7].

The acquired images of Cl and Cl* ions in clustering conditions are shown in figure 3.12. The experiments were repeated several times as the clustering seems to be highly affected by the state of the pulsing puppet. Here I present the images without monomer signal, which is sometimes present in lower backup pressures < 3 bar and can be removed by subtraction of the signal from co-expansion with helium. However, then it is difficult to analyze the angular distribution for kinetic energies above 0.6 eV. The results for iso-Cl-propane are shown only for illustration as the weak and noisy signal makes any deeper analysis impossible. The corresponding KEDs and angular distributions are shown in figure 3.13.

KEDs were renormalized on the branching ratio of [Cl*]/[Cl] equal to 0.86 published in the [109] for dissociation of isolated CH_3Cl. The spectra show similar broad bimodal distribution as in the case of the CH_3Cl clusters with one peak close to zero energy and the other one around 0.6 eV for Cl and around 0.7 eV for Cl* fragments.

The angular distributions were analyzed separately for the slow and fast bands. Due to the low signal, the noise along the axis of inversion caused by Abel inversion can induce some discrepancy in the fitting. Therefore, we also checked the angular distribution of non-inverted images to confirm the fitted character. The slow bands show isotropic angular distribution with an average anisotropy parameter equal to 0.03(10), which is expected for the caging of the ejected fragments. Surprisingly, the fast peak exhibits slightly negative anisotropy with values of $\beta(\mathrm{Cl}) = -0.12(10)$ and $\beta^*(\mathrm{Cl}^*) = -0.35(12)$.

The value of $\beta^*(\mathrm{Cl}^*)$ can be explained by the admixture of the monomer signal, which also has a perpendicular character with $\beta < -0.3$. However, the ground state Cl fragments coming from monomers have parallel characters with a slightly positive anisotropy parameter, $\beta > 0.15$. Therefore, we cannot justify the change in the anisotropy only by collisional quenching.

We also performed a series of control measurements with dissociation laser polarization perpendicular to the detector plane. These experiments were done to prevent possible artifacts in the angular distribution analysis and see how sensitive our setup is for the image anisotropy. The acquired images thus lack cylindrical symmetry and cannot be transformed by inverse Abel transformation. Nevertheless, on the other hand, they should provide isotropic angular distribution. This was confirmed by the values around 0.03(8).

In summary, although the slightly negative value of $\beta = -0.12(10)$ for the Cl

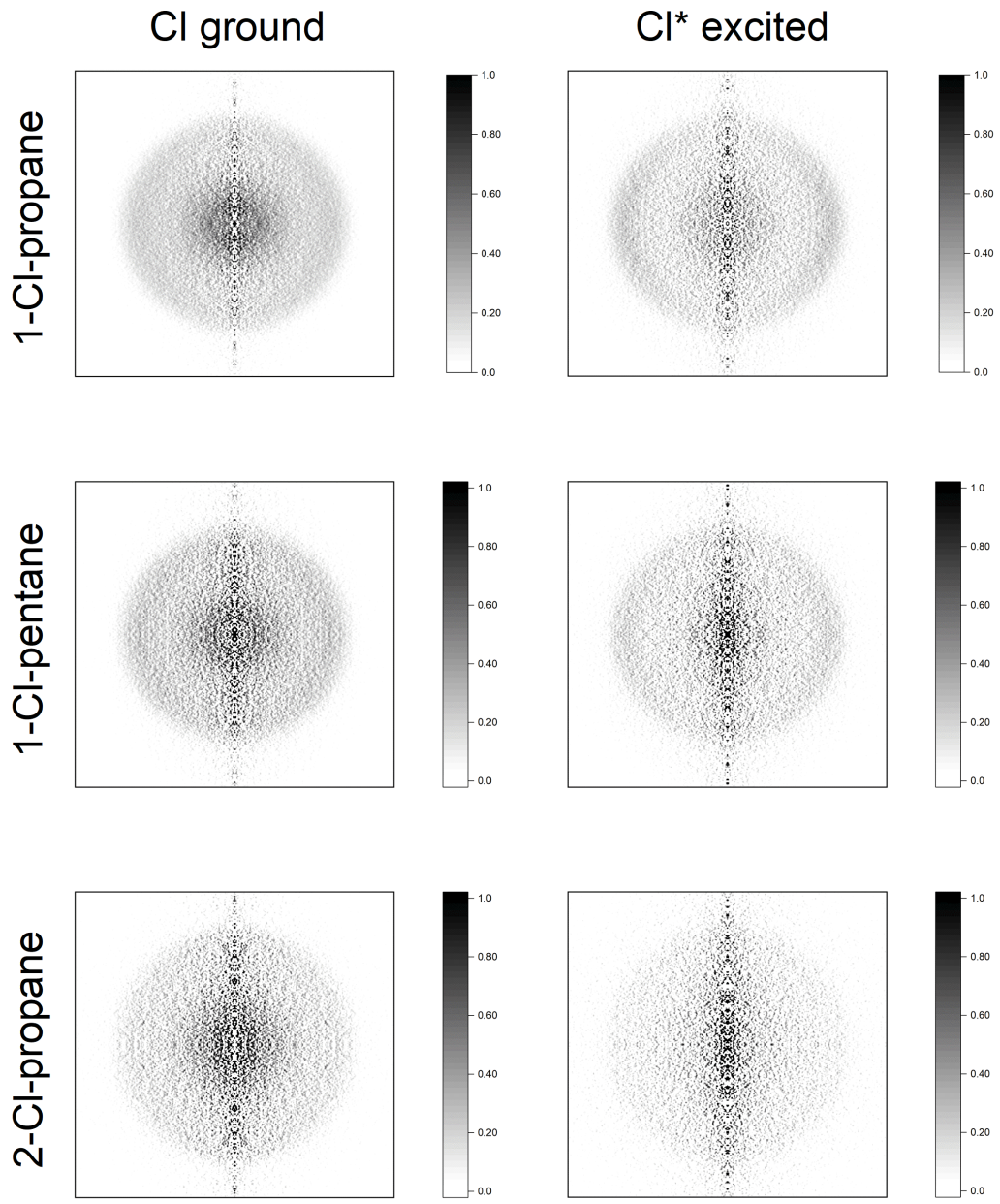


Figure 3.12: Transformed VMI images from photodissociation at 193 nm of selected higher chloroalkanes, i.e., of 1-Cl-propane, 1-Cl-pentane and iso-Cl-propane, in clustering conditions.

ground state channel is at the edge of our sensitivity, we put it forward as a very interesting preliminary result. A tempting interpretation is the cluster enhanced absorption into singlet $^1Q_1$ state caused by the excimer effect and change in probability for non-adiabatic transitions due to the cluster environment, which asks for the molecular dynamics simulations of the big chloroalkane clusters. Another explanation might be the cluster-induced cooperative effect, which is discussed below.

The estimated branching ratios of the Cl* and Cl channels for the 1-Cl-

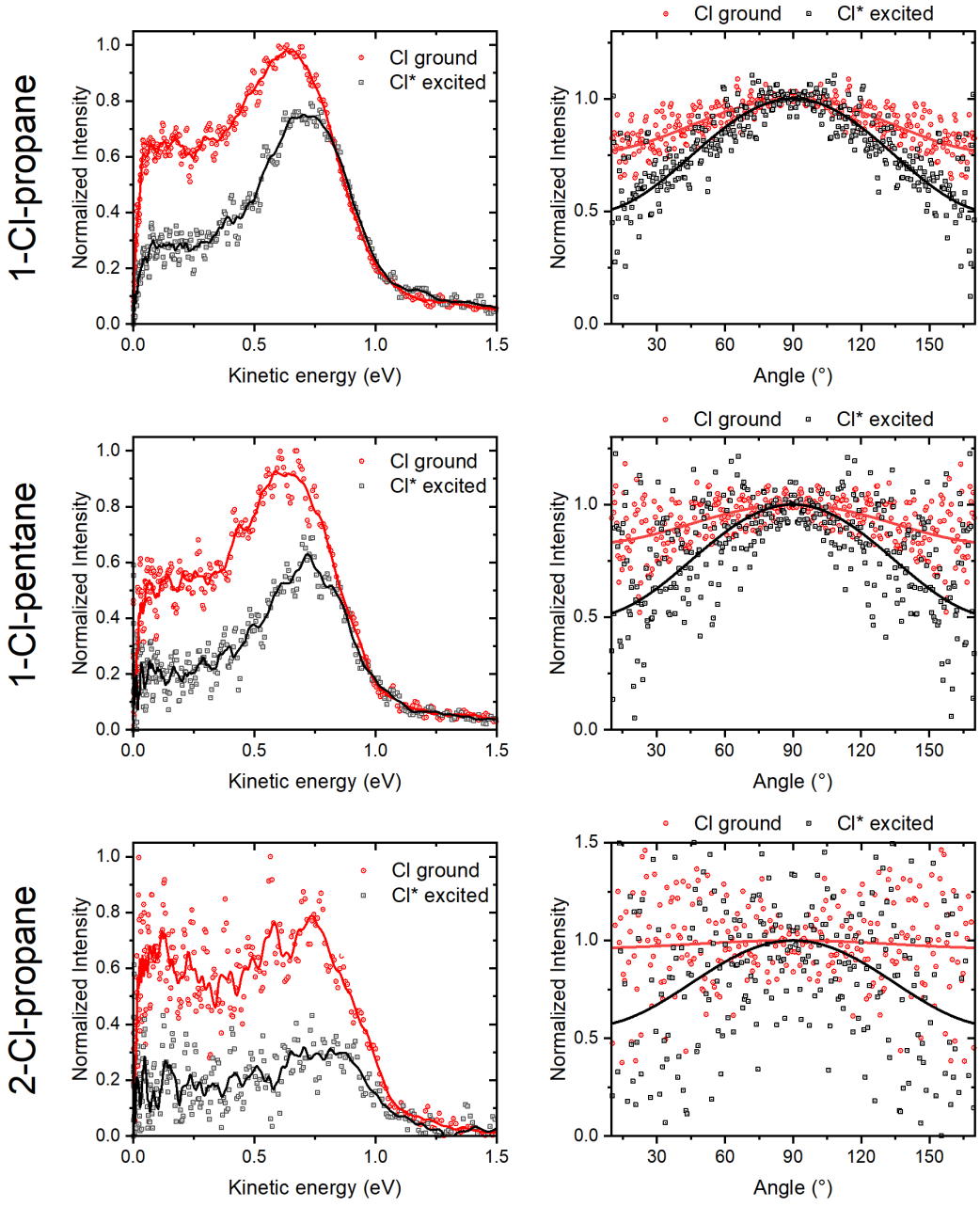


Figure 3.13: Kinetic energy distributions and angular distributions acquired from the analysis of images shown in figure 3.12.

propane and 1-Cl-pentane are equal to 0.60(15) and for iso-Cl-propane equals to 0.35(20), which is in good agreement with the branching ratio of 0.55 for CH_3Cl clusters published in [5]. This might be explained by collisional electronic quenching of the excited Cl* fragments into the ground electronic state. Also, a similar decrease in [I*]/[I] ratio was reported in [117, 118] and justified by preferential involvement of I* in the cooperative rearrangement into I_2. Unfortunately, our mass spectra in the same conditions as in the VMI experiments did not show any peaks corresponding to Cl_2 at 70 or 72 m/q. Recently, we changed the skimmer and repeated the mass spectra measurement in high fluxes of the excimer laser, inducing strong non-selective ionization. The newly acquired mass spec-

trum on 1-Cl-propane shows weak peaks assigned to the Cl_2 signal. However, this result should be taken cautiously as the current conditions vastly differ from the previous experiment. Especially, if the Cl_2 ($D_0 = 2.508\,\mathrm{eV}$) would be produced and then fragmented by another photon(s), we should observe a fraction of Cl fragments with energy above 1.3 eV ($h\nu - D_0 = 5.27 - 2.508$),[129] which is not the case. On the other hand, the additional quenching in a cluster environment or autodissociation of highly vibrationally excited Cl_2 might result in the slowed Cl fragments shown in our KED spectra.

Apparently, the results ask for a supportive experimental campaign focused on combining clustering and multiphoton effects, which might be enhanced in the clusters contrary to the monomers.[44] Another obvious course is pickup experiments with the selected chloroalkanes on argon/water clusters in stable continuous molecular beams produced in the CLUB apparatus, as an additional step toward the heterogeneous atmospheric chemistry. The argon clusters can help us understand the pure mechanistic effects, which are present in such an inert solvent, before we will focus on the photochemistry of the stratospheric ice nanoparticles containing the chloroalkanes. The preliminary results with 1-Cl-propane and 1-Cl-pentane co-expanded with argon buffer gas show extensive clustering but no Cl_2 generation upon ionization with 70 eV electrons.

3.3 Pickup Experiments in Molecular Beams

The following series of experiments were performed on the CLUB apparatus. The experiments investigate cluster growth and coagulation in the perspective of the collisional complexes in the atmosphere and interstellar space medium (ISM). The general advantages of the CLUB apparatus for cluster experiments are described in chapter 2.5. The clusters were either generated in co-expansion with argon buffer gas or through molecular uptake (pickup). The chapters below investigate selected hydrocarbon systems by applying the electron ionization and rToF technique. The other campaign oriented on a generation of pure hydrogen peroxide clusters is only cited here as another example of the pickup experiments where I was involved [92, 93].

3.3.1 Pickup on Polyaromatic Hydrocarbons Clusters

Astronomical spectroscopy detected a broad spectrum of chemical compounds in ISM, some of them surprisingly complex for harsh conditions of the ISM due to the cosmic radiation, low particle densities, and low temperatures.[53, 16, 130] The gas-phase chemistry driven by collisions and ion-molecule reactions cannot explain all the observations, and therefore, heterogeneous chemistry on the abundant dust nanoparticles was proposed as a possible source of the detected species. The ISM clusters and nanoparticles are often formed as carbonaceous grains coated by ice mantles containing various molecules,[131, 132, 133] e.g., H_2O, CO_2, CO, CH_3OH, smaller admixtures of CH_4 or NH_3 and other up-taken molecules, which are in close vicinity prepared for the reaction triggered by the ionizing cosmic radiation. Our pickup experiments can mimic the isolated nanoparticles in ISM and simultaneously investigate the heterogeneous chemistry of clusters and nanoparticles induced by UV photons and electrons ($0 - 100\,\mathrm{eV}$).[12, 10]

Up to $\sim 15\,\%$ of the galactic carbon is stored in gaseous and clustered aromatic hydrocarbon compounds, which fingerprint is detected in astronomical mid-IR spectroscopy as sharp peaks assigned to characteristic vibrational frequencies and broad plateaus.[16, 53] Various chemical pathways were proposed for their generation and fragmentation, like bottom-up and top-down chemistry in the ISM, including the transformation into well-known fullerenes.[16] The PAHs clusters in the role of substrate combined with ice mantles are also promising systems for investigation of the heterogeneous catalytic chemistry leading to the synthesis of various complex molecules in the ISM. Simultaneously, the PAHs are also known from the Earth's atmosphere as by-products of incomplete combustion of organic compounds.[16] In the atmosphere, they can be incorporated into the atmospheric aerosols, which are known to have a substantial impact on global climate through heterogeneous chemistry and global radiation budget.[10, 12] Unfortunately, the stability of the aromatic rings makes PAHs major air pollutants with possible affection to human health.[17]

In our experiments, we generated different neutral PAH clusters in a molecular beam and exposed them to the vapor of atmospheric and ISM relevant species. The clusters with pickup were then probed by mass spectrometric technique after 70 eV electron ionization. The experiments mimic the initial step in the growth of the ice mantle on the ISM PAH clusters or the atmospheric PAH aerosols. The

selected aromatic hydrocarbons are benzene (Bz), PAHs containing 6-membered rings, i.e., naphthalene (Np), phenanthrene (Ph), anthracene (An), pyrene (Py) and PAHs containing 5-membered ring, i.e., indene (In) and fluoranthene (Fl).

The following chapters are ordered as follows: First, I give an overview of the pure PAH clusters and their fragmentation. Secondly, I discuss the performed pickup experiments and preliminary results for estimated relative pickup probabilities for hydrogen bonding molecules. Finally, the following two chapters give a detailed overview of the pickup experiments on clusters of benzene and adamantane (Ad). The experiment with Ad clusters was added to have a comparison with non-aromatic hydrocarbon compounds with a 3D structure.

PAH clusters and fragmentation

Mass spectra of the PAH clusters generated by supersonic expansion are dominated by $(\mathrm{PAH})_n^+$ series surrounded by weak peaks assigned to dehydrogenated and protonated ions. The dehydrogenated ions on the smaller mass side have approximately $5-10\times$ smaller intensities. On the higher mass side, there are also significant peaks, which mainly correspond to the occurrence of isotope $^{13}\mathrm{C}$ with a possible small contribution of protonated ions for $(\mathrm{PAH})_n^+$, $n \leq 3$.

PAH clusters							
PAH	Benzene	Naphthalene	Anthracene	Phenanthrene	Pyrene	Indene	Fluoranthene
$\frac{T_N}{T_R}$ (°C)	60 27	96 86	240 235	210 200	250 245	114 74	240 235
$\overline{n}_{clu}(\mathrm{PAH})_n^+$	3.3	2.5	2.4	2.5	2.3	3.4	2.3
$n_{max}(\mathrm{PAH})_n^{2+}$	47	25	15	17	13	25	15
fragmentation pattern Δm	+16,+38, +68	weak -34	-11	-11	weak -11	-13,-22, -26,-35, +18,+58	-10, -21
$(\mathrm{PAH})_n.\mathrm{Ar}_k^+$ $\delta_{rel} \approx \frac{I(\mathrm{PAH}_n.\mathrm{Ar}_k^+)}{I(\mathrm{PAH}_n^+)}$	X	10^{-2}	10^{-4}	10^{-4}	10^{-5}	X	10^{-3}

Table 3.2: Comparison of the apparent PAH cluster sizes, fragmentation and relative intensity of $(\mathrm{PAH})_n.\mathrm{Ar}_k^+$ mixed clusters.

The size of generated clusters cannot be revealed directly from our mass spectra measurements due to the fragmentation caused by electron ionization and perpendicular geometry of rToF ($\mathrm{m/z} < 2000$). The cluster generation is strongly dependent on the backup pressure, nozzle geometry and PAH concentration. The results here are presented for the backup pressure of $p_{Ar} = 3\,\mathrm{bar}$. The temperatures of reservoir T_R and nozzle T_N are shown in table 3.2 for each PAH experiment. Still, we can make a relative comparison among the different PAHs from the observed mass series of double charged $(\mathrm{PAH})_n^{2+}$ clusters and the mean size of the detected clusters $\overline{n}_{clu}(\mathrm{PAH})_n^+$. The values are also reported in table 3.2. The

comparison indicates that the clusters have roughly comparable physical sizes, e.g., the Bz clusters have putative mean size of 3.3 and $n_{max}^{Bz} = 47$, whereas the Np clusters have putative mean size of 2.48 and $n_{max}^{Np} = 25$. The more precise estimation of the cluster size will be derived from the pickup experiments combined with the theoretical calculations, which will be presented in 3.3.2.[15]

We can also study PAH cluster fragmentation from the mass spectra without the pickup. Generally, the peaks assigned to fragmentation are at least three orders lower than the primary $(PAH)_n^+$ ion series. Whereas the Bz and In clusters have rather complex fragmentation patterns, the more complex PAHs, i.e., An, Ph and Py, exhibit only a weak series with a displacement of $\Delta m = -11$ corresponding to loss of C-atom and protonation. Fluoranthene exhibit two additional series with $\Delta m = -10, -21$. Unlike, the Np clusters exhibit essentially no fragmentation.

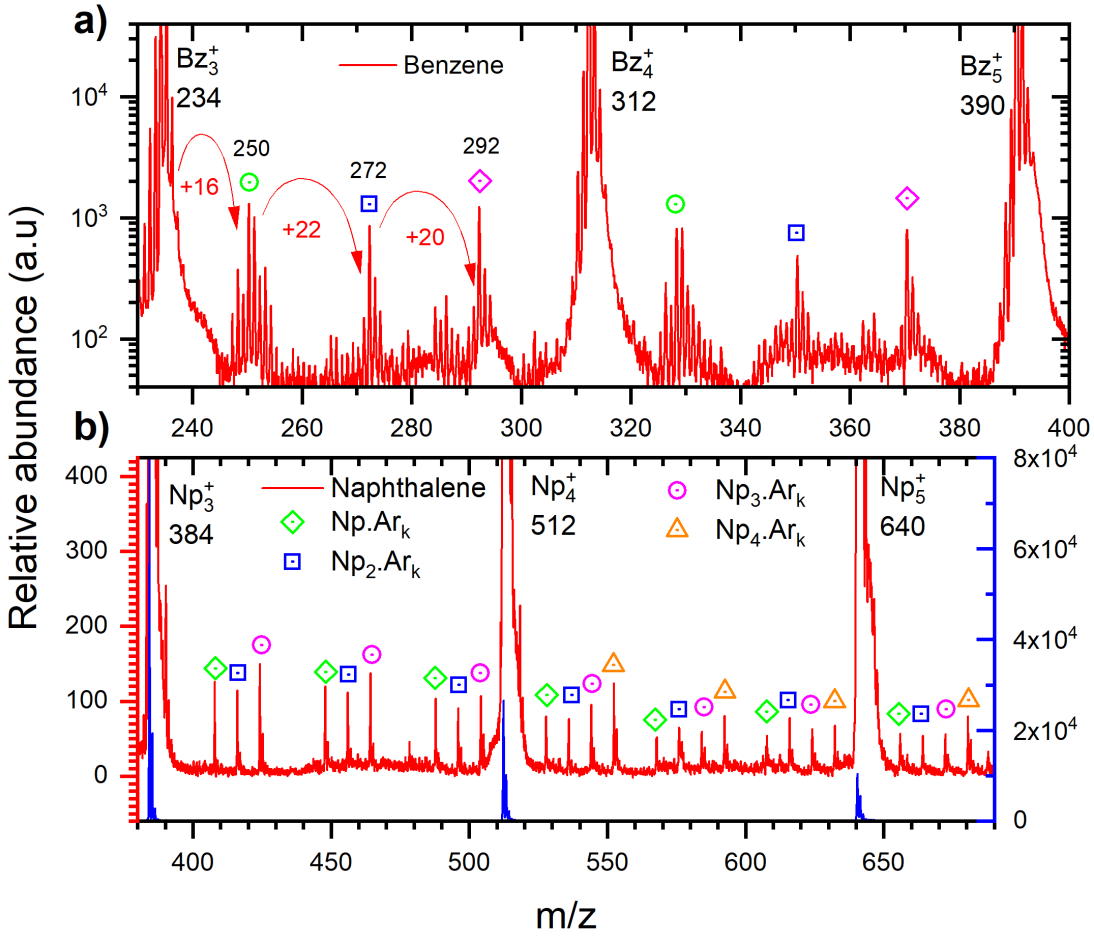


Figure 3.14: Mass spectra of a) the benzene clusters with the major $(Bz)_n^+$ ion series accompanied by series assigned to cluster fragmentation and b) the naphthalene clusters with marked series of mixed $(Np)_n.Ar_k^+$ clusters.

The same spectra also show weak peaks assigned to the mixed $(PAH)_n.Ar_k^+$ clusters, which relative contribution to the spectra compared to the major $(PAH)_n^+$ series is listed in the last row of table 3.2. The spectra of Np and Fl clusters exhibit a series of $(PAH)_n.Ar_k^+$ clusters with relative intensity of $\approx 10^{-2} - 10^{-3}$ compared to the closest $(PAH)_n^+$ peaks. The same argon mixed series are also present in

spectra of Ph, An, and Py with a factor below $\approx 10^{-4}$. On the contrary, there is no indication of the mixed series for Bz and In clusters. The example spectra for cluster fragmentation and mixed $(PAH)_n.Ar_k^+$ series are shown in figure 3.14.

No observation of the $(PAH)_n.Ar_k^+$ peaks in the case of Bz and In spectra do not mean that there are no such clusters. Firstly, the weak peak can overlap with their complex fragmentation structure. Secondly, the weakly bound argon atoms can easily evaporate from the cluster surface upon electron ionization. The matter of cluster coating by argon layer was specially investigated in measurements of ion yield thresholds of $(PAH)_n^+$ and $(PAH)_n.Ar_k^+$ clusters by scanning electron energy from 5 to 18 eV in the case of naphthalene. The threshold for Ar^+ is around ≈ 15 eV, whereas our $(PAH)_n^+$ and $(PAH)_n.Ar_k^+$ signals exhibit lower ion threshold close to ≈ 11 eV. This value is in good agreement with the ion threshold for Np^+ ions, which suggests that even the ionization of the mixed clusters is initiated with Np ionization. Apparently, our clusters are not argon-coated, contrary to our previous experiments with water clusters.[134, 135] We assume that our $(PAH)_n$ clusters, which exhibit the mixed $(PAH)_n.Ar_k^+$ fragments have more like an Ar-decorated structure with the argon clusters residing on the top of the aromatic rings, which asks for MD simulations to support our results.

PAH clusters and pickup

The characterized $(PAH)_n$ clusters were applied in the experiments to pickup atmospherically and ISM relevant molecules. They are listed in the first column of table 3.3. The molecules were evaporated into the pickup cell ($l = 17$ cm), where the $(PAH)_n$ clusters pick them up on the way to the detector. The pickup molecules have then approximately 3 ms to coagulate or mix with the PAH substrate before they reach the interaction center in the rToF spectrometer. The vapor pressure was set in several values between $5 \times 10^{-5} - 8 \times 10^{-4}$ mbar to check different pickup conditions.

The pickup is observed by detecting new mass series with characteristic Δm corresponding to the parent or its fragments. The tables 3.3 and 3.4 show the observed series assigned to the pickup. The pickup on benzene clusters will be discussed in detail separately in chapter 3.3.2. The example spectra for the Np and Ph clusters are shown in figure 3.15. Here we will focus mainly on the general pattern of mass spectra after pickup of molecules with hydrogen bonding, i.e., methanol, ethanol, and water at the vapor pressure was 1.0×10^{-4} mbar. For the comparison, there are in the tables also the observed series after pickup of other molecules[2], which usually exhibit only weak but unambiguous peaks accompanying the main series.

Mass spectrum of the Np clusters with the pickup of water exhibits new ion series assigned to mixed Np/water clusters (squares) as is shown in figure 3.15 b). The right scale belongs to the mass spectrum without a pickup (grey) drawn for the comparison. We also observed weak protonated pure water clusters $(H_2O)_kH^+$ for $k \leq 4$. The maxima of the mixed cluster series are assigned to $(Np)_n.(OH)^+$ and protonated $Np_n.(H_2O)_kH^+$ for $k > 2$. Similar behavior with prevailing dehydrogenated clusters for the first two peaks in mass series was also

[2]The necessary vapor pressure for other series of other compounds differ, because of the much weaker signal.

Pickup experiments 1/2			
PAH Uptaken molecule	Benzene	Naphthalene	Anthracene (Phenanthrene)
Methanol CH_3OH	$(Me)_k.H^+$ $Bz_n.(Me)_k.H^+$ $Bz_n.(Me)_k^+$ $(Bz_n.(Me)_k\text{-}H)^+$	$(Me)_k.H^+$ $Np_n.(Me)_k.H^+$ $Np_n.(Me)_k^+$ $(Np_n.(Me)_k\text{-}H)^+$	$An_n.(Me)_kH^+$ $k = 1, 2, 3$
Ethanol CH_3CH_2OH	$(Et)_k.H^+$ $Bz_n.(Et)_k.H^+$ $Bz_n.(Et)_k^+$ $(Bz_n.(Et)_k\text{-}H)^+$	$(Et)_k.H^+$ $Np_n.(Et)_k.H^+$ $Np_n.(Et)_k^+$	$An_n.(Et)_k.H^+$ $k = 1, 2, 3$
Water H_2O	$(H_2O)_kH^+$ $Bz_n.(H_2O)_k.H^+$ $Bz_n.(H_2O)_k^+$ $Bz_n.(OH)_k^+$	$(H_2O)_kH^+$ $Np_n.(H_2O)_k.H^+$ $Np_n.(H_2O)_k^+$ $Np_n.(OH)^+$	$An_n.(H_2O)_2.H^+$ $An_n.(OH)^+$
Methane CH_4	X	? $(Np_n.CH_4\text{-}2H/H)^+$	X
Amoniak NH_3	$(NH_3)_k.H^+$ $Bz_n.(NH_3)_k^+$ $Bz_n.(NH_3)_k.H^+$	$Np_n.(NH_3)_k.H^+$	$An_n.(NH_3)_k.H^+$ $n > 2$
Oxygen O_2	$Bz_n.O_2^+$ $Bz_n.O^+$	$Np_n.O_2^+$	weak $An_n.O^+$
Carbon dioxide CO_2	X	weak $Np_n.CO_2^+$ $Np_n.O^+$	weak $An_n.O^+$
Benzene C_6H_6	–	weak $(Np.Bz\text{-}H)^+$ $Np_n.Bz^+$, $n > 2$	weak $(An.Bz\text{-}H)^+$ $An_n.Bz^+$, $n > 2$
Toluen C_7H_8	$Bz_n.Tol_k^+$	weak $(Np.Tol\text{-}H)^+$ $Np_n.Tol^+$, $n > 2$	weak $(An_n.Tol\text{-}H)^+$ $n = 1, 2$
α-Pinene $C_{10}H_{16}$	αPin_k^+ $Bz_n.\alpha Pin_k^+$	weak $Np.\alpha Pin^+$	weak $(An_n.\alpha Pin\text{-}H)^+$ $n = 1, 2$

Table 3.3: Table of performed pickup experiments with PAH clusters and molecular pickup. (1^{st} part)

observed for water pickup on Bz and In clusters.

The methanol and ethanol show somehow stronger pickup than the pickup of water. The example spectrum is shown in figure 3.15 a). There are clear series with protonated pure ethanol (green circles) and mixed Np/ethanol clusters

Pickup experiments 2/2			
PAH Uptaken molecule	Pyrene	Indene	Fluoranthene
Methanol CH_3OH	$Pyr_n.(Me)_k.H^+$	$In_n.(Me)_k.H^+$ $(In_n.(Me)_k.H^+$ -CH)	$Fl_n.(Me)_kH^+$ $k = 1, 2, 3$
Ethanol CH_3CH_2OH	$Pyr_n.(Et)_k.H^+$	$In_n.(Et)_k.H^+$ $(In_n.(Et)_k.H^+$ -CH)	$Fl_n.(Et)_k.H^+$ $k = 1, 2, 3$
Water H_2O	$Pyr_n.(H_2O)_k.H^+$ $Pyr_n.(H_2O)_k^+$ $Pyr_n.(OH)^+$	$In_n.(H_2O)_k.H^+$ $In_n.(OH)^+$	weak $Fl_n.(H_2O)_k.H^+$ $Fl_n.(H_2O)_k^+$ $Fl_n.(OH)_k^+$ $k = 1, 2$
Methane CH_4	X	? $(In_n.CH_4\text{-}2H/H)^+$	? $(Fl_n.CH_4\text{-}2H)^+$
Amoniak NH_3	$Pyr_n.(NH_3)_k.H^+$	$In_n.(NH_3)_k.H^+$	$Fl_n.(NH_3)_k.H^+$ $k = 1, 2$
Oxygen O_2	weak $Pyr_n.O_2^+$ $Pyr_n.O^+$	$In_n.O_2^+$ $In_n.O^+$	weak $Fl_n.O_2^+$ $Fl_n.O^+$
Carbon dioxide CO_2	weak $Pyr_n.O^+$	$In_n.O^+$	weak $Fl_n.O^+$
Benzene C_6H_6	weak $(Pyr_n.Ben\text{-}H)^+$ $n = 1, 2, 3$	weak $(In_n.Bz\text{-}H)^+$	weak $(Fl_n.Bz\text{-}H)^+$
Toluen C_7H_8	weak $(Pyr_n.Tol\text{-}H)^+$ $n = 1, 2, 3$	weak $(In_n.Tol\text{-}H)^+$	weak $(Fl_n.Tol\text{-}H)^+$ $n = 1, 2, 3$
α-Pinene $C_{10}H_{16}$	weak $(Pyr_n.\alpha Pin\text{-}H)^+$ $n = 1, 2, 3$	$In_n.\alpha Pin^+$	weak $(Fl_n.\alpha Pin\text{-}H)^+$ $n = 1, 2$

Table 3.4: Table of performed pickup experiments with PAH clusters and molecular pickup. (2^{nd} part)

(squares). The first two main peaks of the series are non-protonated and from $n > 2$ the protonated clusters $Np_n(EtOH)_kH^+$ prevail. A similar pattern seems to have also spectrum with methanol, however, the analysis is disturbed by peak overlap between mixed Np/methanol (32) and pure naphthalene ($128 = 4 \times 32$) clusters.

The more complex PAHs show significantly weaker signals ($\approx 1 \times 10^{-5}$) in comparison to their spectra without a pickup. The example spectra for water and ethanol pickup on the An clusters are shown in figure 3.15 c) and d). The same

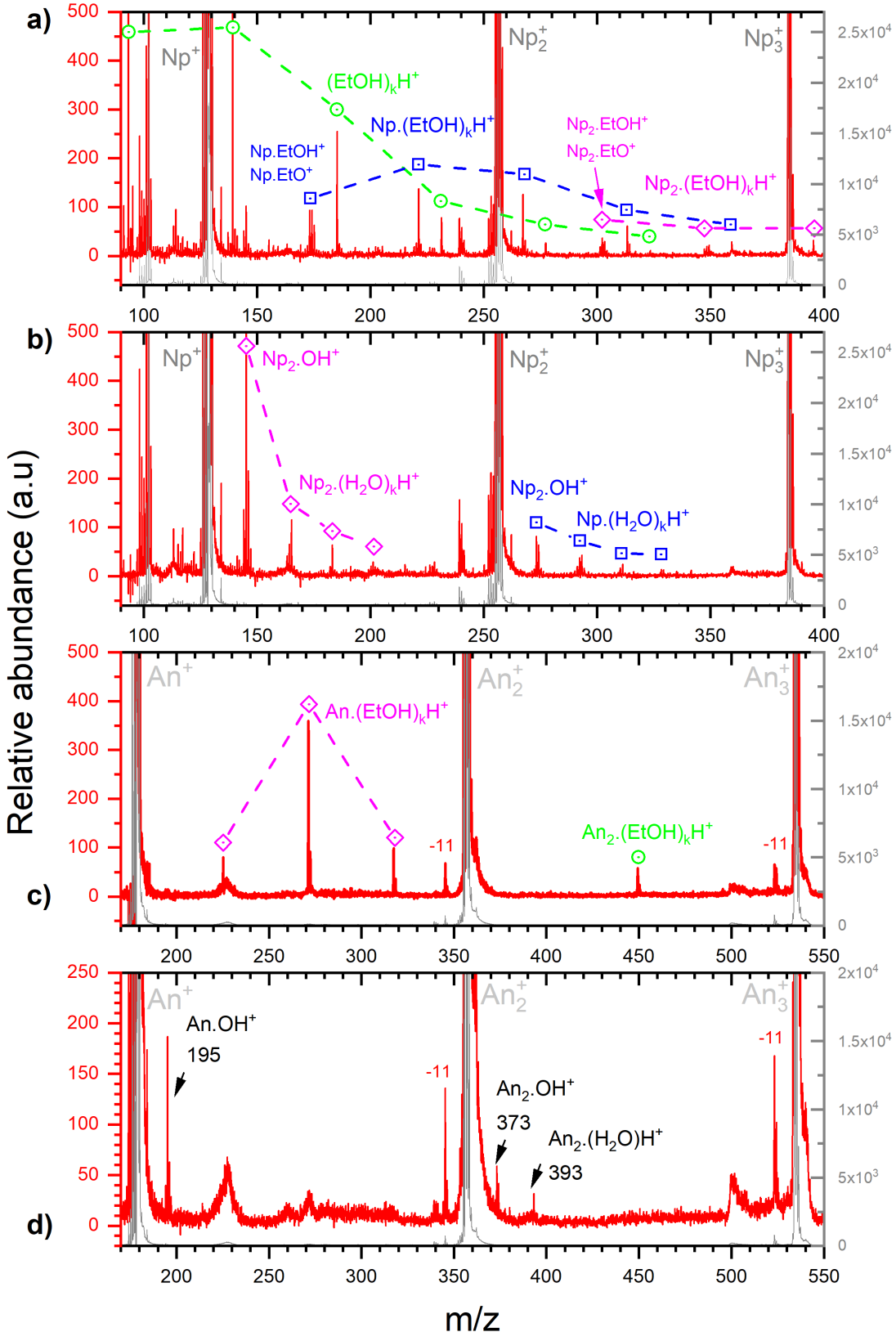


Figure 3.15: Example of mass spectra corresponding to pickup of (a,c) ethanol and (b,d) water on (a,b) naphthalene and (c,d) anthracene.

patterns were discernible also for the other complex PAHs, i.e., phenanthrene,

pyrene, and fluoranthene.

Only the weak peaks assigned to $(An)_nOH^+$ and $(An)_n(H_2O)_2H^+$ cluster ions are visible. On the contrary, the pickup of methanol and ethanol is more efficient with discernible three peaks in series with maxima assigned to the protonated $(An)_n(XOH)_kH^+$, $k \leq 3$, clusters.

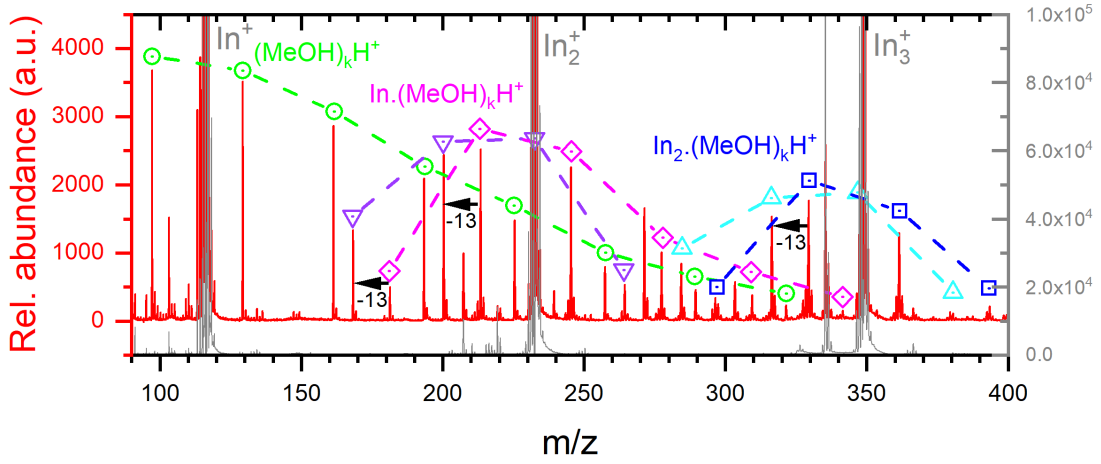


Figure 3.16: Mass spectrum of indene clusters with pickup of methanol.

The situation is slightly different for indene containing a 5-membered ring. In the case of water pickup, we again observed only a small pickup with weak but unambiguous peaks corresponding to the protonated $(In)_n(H_2O)_kH^+$ ion series. The pickup of methanol is shown in figure 3.16 with marked series corresponding to protonated $(MeOH)H^+$ (green circles) and mixed $(In)_n(MeOH)_kH^+$ (squares) clusters. Moreover, there are different series (triangles), which also correspond to methanol pickup due to their regular spacing with $\Delta m = 32$. The series start at $m/z = 168$ and 284 and are spaced by $\Delta m = 52$ from the closest pure indene clusters, which do not correspond to any indene fragments. A similar pattern was also observed in spectra with the pickup of ethanol. Here the new series start at $m/z = 196$ and 312, which is displaced by $\Delta m = 80$ from the closest pure indene clusters. This suggests that the additional series do not correspond to any indene fragments, but on the contrary, it comes from the elimination of CH(13) upon electron ionization. It should be noted that this fragmentation channel was not observed for any other complex PAHs or benzene.

All the tested hydrogen bonding molecules have higher ionization energy ($> 10.5\,\text{eV}$) than the PAHs ($< 9.3\,\text{eV}$), which prevents a possible ionization of the pickup through charge transfer from PAH cluster constituents.[136] Therefore, the observed series after molecular pickup (M) results from direct molecular ionization, or the molecules stick to the PAH ion fragment. Nevertheless, the observed pure protonated series M_kH^+ cannot result from the latter mechanism. On the contrary, the proton affinity of the hydrogen bonding molecules ($< 8.08\,\text{eV}$) is lower than for the PAHs ($> 8.29\,\text{eV}$).[136] Therefore, we assume that the proton transfer from the up-taken molecules to PAH is feasible, which means that the PAH constituents are rather protonated than a molecule in the $(PAH)_n.M_kH^+$ series. Also, we can conclude that the M_kH^+ series cannot be ionized through proton transfer from PAH.

Several measurements of ionization threshold for the clusters of $(EtOH)_kH^+$

and $(Np)_n.(EtOH)_kH^+$ were performed to elucidate the origin of the ion series. Whereas the ionization of pure $(Np)_n^+$ and mixed $(Np)_n.(EtOH)_kH^+$ clusters show threshold around 9 eV, the signal assigned to pure ethanol $(EtOH)_kH^+$ clusters arise with electron energy around 10.5 eV. Therefore, we can conclude that M_kH^+ and $(PAH)_n.M_kH^+$ series originate from different ionization pathways, i.e., direct M ionization and protonation of PAH constituents after PAH ionization, respectively.

A question arises if the pickup for the larger PAH clusters is weaker because of the lower sticking efficiency or smaller geometrical size of generated clusters. In the previous chapter, we proposed several arguments why we think that our clusters should be comparable in size, however, this should be taken very cautiously. Nevertheless, we can compare relative uptake for the different molecules on the same type of PAH clusters. The vapor pressure was measured by ion gauge and corrected with the correction factors of 1.1, 1, 8 and 3.6 for water, methanol and ethanol, respectively. In the table 3.5, there are values of relative uptake ratios R_{up} calculated by integrating the signal corresponding to the pickup peaks and divided by the total signal. The necessary assumptions for this comparison are broadly discussed in [15]. The values were calculated only for the benzene, naphthalene and indene as the other more complex PAHs exhibit rather weak pickup series. The estimated values show that the pickup of methanol and ethanol is generally more efficient than the pickup of water, which was also evident from the mass spectra analysis.

Pickup probabilities			
PAH Molecule	Benzene	Naphthalene	Indene
CH_3OH	0.30	0.05	0.12
CH_3CH_2OH	0.29	0.13	0.11
H_2O	0.21	0.02	0.07

Table 3.5: Comparison of the relative pickup probabilities for hydrogen bonding molecules on benzene, naphthalene and indene.

After a brief overview of the performed experiments with PAH clusters, we can focus on the first case of pickup experiments with hydrogen bonding molecules on benzene clusters.

3.3.2 Pickup of Hydrogen Bonding Molecules on Benzene Clusters

The pickup on benzene clusters is a complementary approach in preparing the mixed benzene-water/methanol/ethanol clusters in contrast to the previous experiments with clusters generated by co-expansion, which were used to investigate the van der Waals interaction between the aromatic ring and water.[137, 138] Also, IR spectroscopy and ion-mobility experiments were applied to study the hydration and proton transfer in cationic clusters.[139, 140] These measurements combined with theoretical simulations can provide relevant information about cluster structure and energetics for atmospheric chemistry and IR benchmark spectra for astrochemical observations.[141, 142] Our experiments, on the other hand, mimic the initial step in cluster growth and ice mantle coating by pickup of selected hydrogen bonding molecules M.[10]

The benzene clusters were generated by supersonic expansion of 5% mixture with argon buffer gas ($p_{Ar} = 3.0\,\mathrm{bar}$). The skimmed molecular beam was transferred into the pickup chamber, where it was exposed to the vapor ($1 \times 10^{-4}\,\mathrm{mbar}$) of the three hydrogen bonding molecules. The clusters with pickup were then detected in the rToF spectrometer after 70 eV electron ionization.

Mass spectrum of benzene clusters without a pickup, see figure 3.14 a), exhibits a main ion series of $(\mathrm{Bz})_n^+$ accompanied by smaller peaks on both sides of mass spectra with significantly lower intensities, which origin was already discussed in chapter 3.3.1.

Mass spectra in figure 3.17 show the benzene clusters after pickup of a) water, b) methanol and c) ethanol with indicated mass series. The first spectrum exhibits several new ion series coming from the pickup of water on $(\mathrm{Bz})_n^+$ clusters. There are series assigned to the protonated pure water clusters $(\mathrm{H_2O})_k\mathrm{H}^+$ and mixed non-protonated $\mathrm{Bz}_n.(\mathrm{H_2O})_k^+$ clusters. Although, the first three members of the second series are dominated by dehydrogenated species $\mathrm{Bz}_n.(\mathrm{H_2O})_k\mathrm{OH}^+$, $k \leq 3$. The other two spectra show a similar pickup pattern with methanol and ethanol pickup propagating as $(\mathrm{MeOH/EtOH})_k\mathrm{H}^+$ and $\mathrm{Bz}_n.(\mathrm{MeOH/EtOH})_k^+$ mass series. In this project, we were interested in the process of pickup, and thus, the observation of the peaks corresponding to protonated, non-protonated and dehydrogenated ions are left for future theoretical investigations. The acquired mass spectra prove that all the tested molecules can be picked up by the $(\mathrm{Bz})_n$ clusters. Furthermore, we observe that the up-taken molecules are highly mobile on PAH substrate as they can coagulate into clusters within 3 ms between pickup and ionization. Similar behavior was observed for pickup of various molecules on argon clusters $(\mathrm{Ar})_N$,[143, 144, 92, 92] whereas the molecules adsorbed on $(\mathrm{H_2O})_N$ clusters was reported to be less mobile.[145, 146]

The similarity with the argon clusters can be justified by comparing the binding energies between the hydrogen bonding molecules and benzene. The binding energy between heterodimer (M-Bz) is weaker approximately by $8-9\,\mathrm{kJ/mol}$ compared to the binding energy between the homodimers (M-M).[15] Furthermore, the M_k coagulation is also favored due to the chain or cycle structures attached to the benzene with double hydrogen bonds contrary to the single hydrogen bond in the heterodimer.[15]

We also quantified the difference in pickup probabilities between the tested

molecules M. The relative uptake ratios R_{up} were calculated as $R_{up} = \frac{I_M}{I_M+I_C}$, where I_M is summed up signal assigned to benzene clusters which picked up at least one molecule and I_C is signal of pure $(\mathrm{Bz})_n^+(+\Delta m = \pm 1, 2)$ clusters. This estimation requires assumptions of the ionization probability, detection probability and fragmentation independent of the picked-up molecules, which are reasonably fulfilled for the investigated systems, see [15] or attachment B.5. The calculated values R_{up} are shown in the second column of table 3.5. We proposed several reasons, which follow the observed trend. Firstly, the binding energy of water to benzene is slightly lower than for the alcohols. Also, another correction might be added due to the lower water geometrical cross-section by approximately 10% compared to methanol and ethanol. Although, we presume that the pickup cross-section should be dominated by the radius of $(\mathrm{Bz})_n$ cluster. Nevertheless, none of the factors can fully explain the observed $\sim 30\%$ decrease in relative uptake ratio.

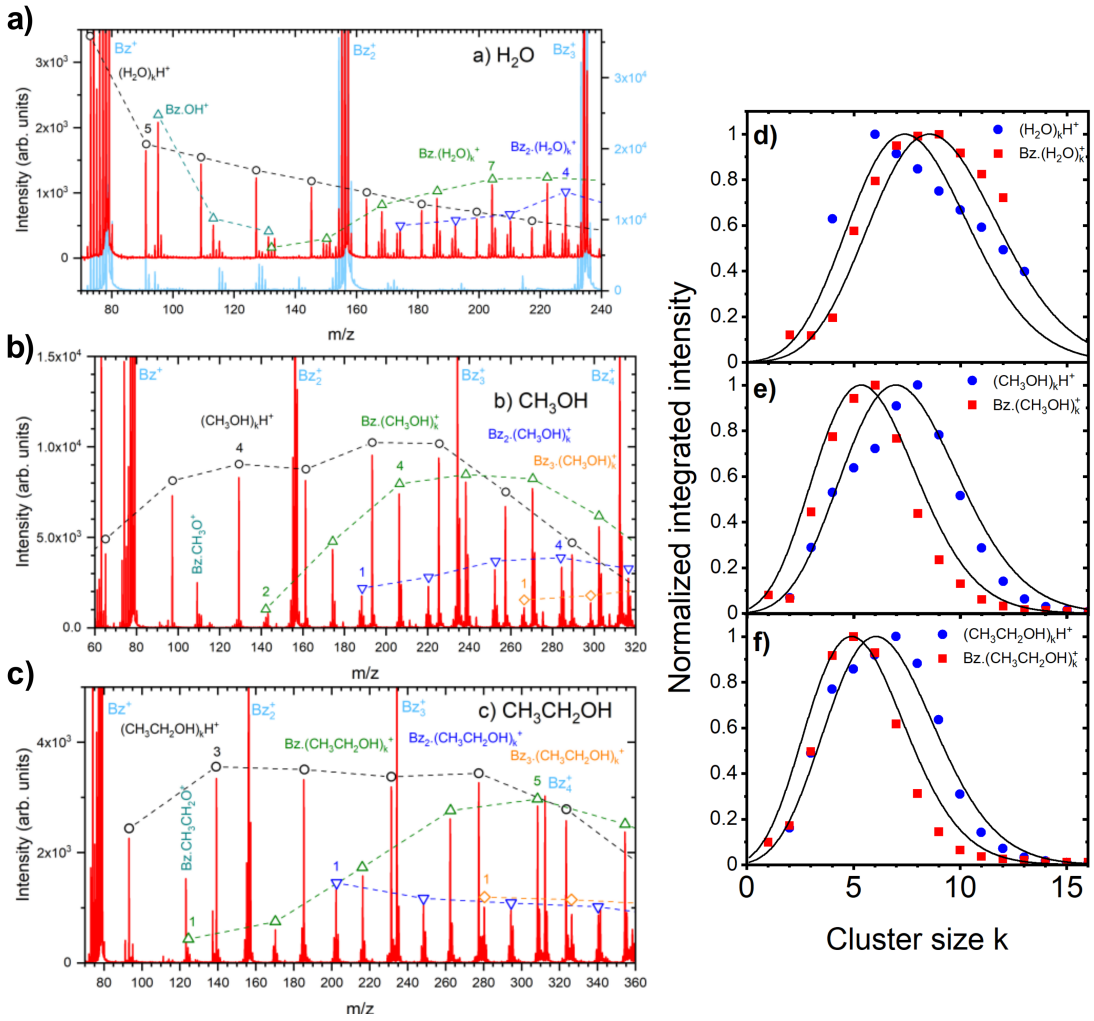


Figure 3.17: Mass spectra of benzene clusters with molecular pickup of a) water, b) methanol and c) ethanol. The corresponding integrated intensities of selected mass series $\mathrm{M}_k\mathrm{H}^+$ and $\mathrm{Bz.M}_k^+$ from pickup of d) water, e) methanol and f) ethanol. The graphs were taken and modified from [15].

We also estimated the $(\mathrm{Bz})_n$ cluster size to characterize the investigated pickup. The putative mean cluster size of $\overline{n}_{clu}(\mathrm{Bz}_n^+) = 3.3$ is far from reality due

to the intense fragmentation and mass discrimination. Therefore, we estimated the mean cluster size from our pickup experiments by application of Poisson distribution described in 2.6.1. The plotted integrated intensities of peaks assigned to M_kH^+ and $Bz.M_k^+$ series fitted by Poisson distribution (eq. 2.21) are shown in figure 3.17. Several strong assumptions had to be made that the ionization did not induce M_k^+ fragmentation and molecules coagulate into one cluster, which is supported by a nice correspondence between plotted data and fit.[15] In the case of pure water clusters $(H_2O)_nH^+$, the distribution does not follow the Poisson distribution, which indicates that the assumption is not fulfilled. However, the good agreement between the mixed clusters and pure $(MeOH/EtOH)_nH^+$ clusters enables us to estimate the mean pickup cross-section around $\overline{\sigma}_p = 1.5 \times 10^{-13}\,\mathrm{cm}^{-2}$ and cluster radius around $\overline{R} = 2.2(2)\,\mathrm{nm}$.

The mean cluster size calculated from the pickup experiments corresponds to the $(Bz)_n$ clusters built of 300 Bz molecules. This number greatly exceeds the largest detected $(PAH)_n^{+2}$ cluster, $n = 47$. The cluster size can be overestimated due to the interactions between polar and polarizable molecules, however, it should not be crucial for the non-polar benzene clusters. On the other hand, the sticking coefficient γ lower than one can cause a discrepancy between geometrical and pickup cross-sections and, therefore, underestimate the cluster size.

The experiments were done in the perspective of cluster growth and coagulation. Therefore, the state and temperature of generated $(Bz)_n$ clusters are also essential for its description. The temperature upper limit of $T_{clu}^{Bz} = 160\,\mathrm{K}$ was estimated by the model presented by Klot et al.[147, 148] This is in good agreement with the reported cluster vibrational temperature around $100 - 150\,\mathrm{K}$.[149] Our simulated clusters show a non-crystalline disordered structure similar to the liquid-like state observed by IR spectroscopy. This is supported by the rapid coagulation of clusters detected in pickup experiments. The molecules after pickup are embedded into $(Bz)_n$ clusters with the liquid surface, which enables the molecular high mobility and hydrogen bonded cluster coagulation within a few milliseconds.

In summary, our pickup experiments give the first experimental quantified comparison between water and methanol condensation on the clusters formed by aromatic hydrocarbons. Therefore, our results might be interesting for describing ice mantle growth on nanoparticles in the atmosphere and ISM.

These results have been published in [15], which is added as attachment B.5 to this thesis.

3.3.3 Pickup Experiments with Adamantane Clusters

Experiments with Ad clusters provide us a comparison to the pickup on PAH clusters interacting through the π electron framework of aromatic rings. Adamantane and its derivatives have a broad application in the polymer chemical industry and drug delivery in medicine.[150, 151] Therefore, a detailed description of its interaction with other molecules is highly interesting for many scientific fields.

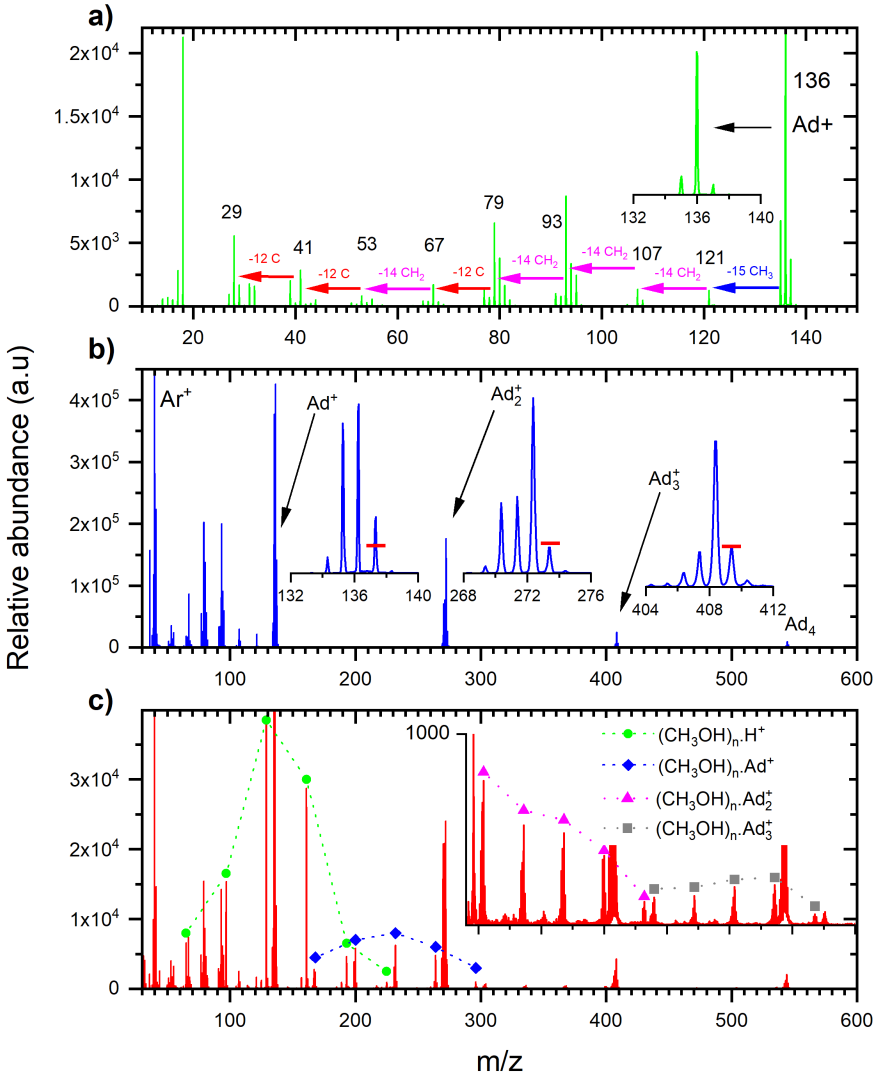


Figure 3.18: Mass spectra of adamantane seeded in a) helium, b) argon and after pickup of c) methanol.

The acquired mass spectra of adamantane co-expanded in a) helium (T_N/T_R = 146 °C/130 °C, p_{He} = 2 bar), b) argon (T_N/T_R = 150 °C/130 °C, p_{Ar} = 2 bar) and c) after methanol pickup are shown in the figure 3.18. The first spectrum is in agreement with the spectrum reported in the NIST database[152] with the main fragments at 29, 41, 56, 67, 79, 93, 107 and 121 masses, which corresponds to the sequential elimination of CH_k groups. The two major fragments at 79 and 93 correspond to loss of linear chain with three and four carbons, respectively. A similar fragmentation pattern exhibit the ionized $(Ad)_n^+$ clusters with three accompanying ion series with Δm = 14, 80 and 94. However, the peaks are two

to three orders of magnitude lower and thus are not discernible in the linear scale of figure 3.18 b). The insets in figure 3.18 a) and b) show a detailed view of the main ion series after ionization of isolated and clustered adamantane, respectively. The isotopic contribution ^{13}C is marked with red lines. Only a small part of the peak at 137 can be attributed to protonated ions. Otherwise, the spectrum is dominated by non-protonated $(Ad)_n^+$ clusters and dehydrogenated species.

In pickup experiments, we tested the pickup of methanol primarily. The $(Ad)_n$ clusters were exposed to the methanol vapor pressure of 2.5×10^{-4} mbar and the resulting spectrum is shown in figure 3.18 c). The dashed lines indicate the ion series arisen from methanol pickup. The green circles correspond to protonated pure methanol clusters $(CH_3OH)_kH^+$, whereas the other lines correspond to the protonated mixed $(CH_3OH).(Ad)_n^+$ ion series. Similar to benzene clusters, we observe protonated pure methanol clusters accompanied by practically no signal around ($< 1\%$ of the corresponding $(CH_3OH)_nH^+$ intensity), which is a typical pattern for direct electron ionization of hydrogen bonded clusters. This is interesting in comparison to methanol pickup on argon clusters $(Ar)_n^+$, where we can see that the accompanying peaks ($\Delta m = \pm 1, 2$) have non-negligible intensities, see figure 3.21.

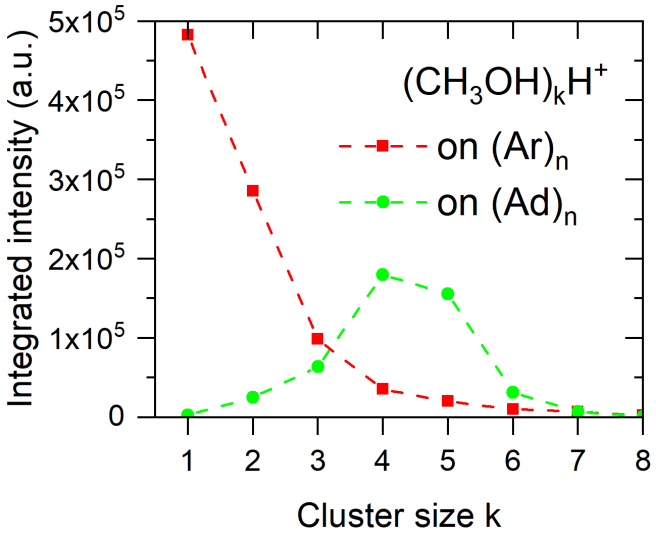


Figure 3.19: Integrated intensities of selected mass series from adamantane clusters with pickup of methanol.

Similar to PAH clusters, we also observe the Poisson-like distribution for $(CH_3OH)_nH^+$ clusters, which should be stressed is not a typical distribution for Ar_n clusters. Independently on the methanol vapor pressures, we observed an exponential character for the distribution of coagulated methanol clusters on Ar_n clusters. This is shown in figure 3.19. The same Poisson distribution can also be seen in mixed $(CH_3OH)_k.(Ad)_n^+$ ion series with some irregularities for $n > 2$.

We also investigated the pickup of other molecules, i.e., ethanol, methylamine, carbon monoxide, acetone, formic acid and methane, in similar conditions to methanol pickup or higher pickup pressures. The last four molecules did not show any discernible peaks, which could be assigned to the pickup (sensitivity $\approx 1 \times 10^{-5}$). Therefore, we assume these molecules do not stick or coagulate on $(Ad)_n$ clusters. Figure 3.20 a) show the mass spectrum acquired after pickup

of ethanol. Although the analysis of ethanol pickup is complicated due to the coincidences with other adamantane fragments, we can also observe a pattern similar to the methanol pickup and coagulation. In fact, there is a small difference in the mixed $(CH_3CH_2OH)_k.(Ad)_n^+$ series, where the first two members prevail as dehydrogenated ions. For the interest, we also add the mass spectrum after pickup of methylamine in 3.20 b) with quite different exponential character of $(CH_3NH_2)_k.(Ad)_n^+$ ion series.

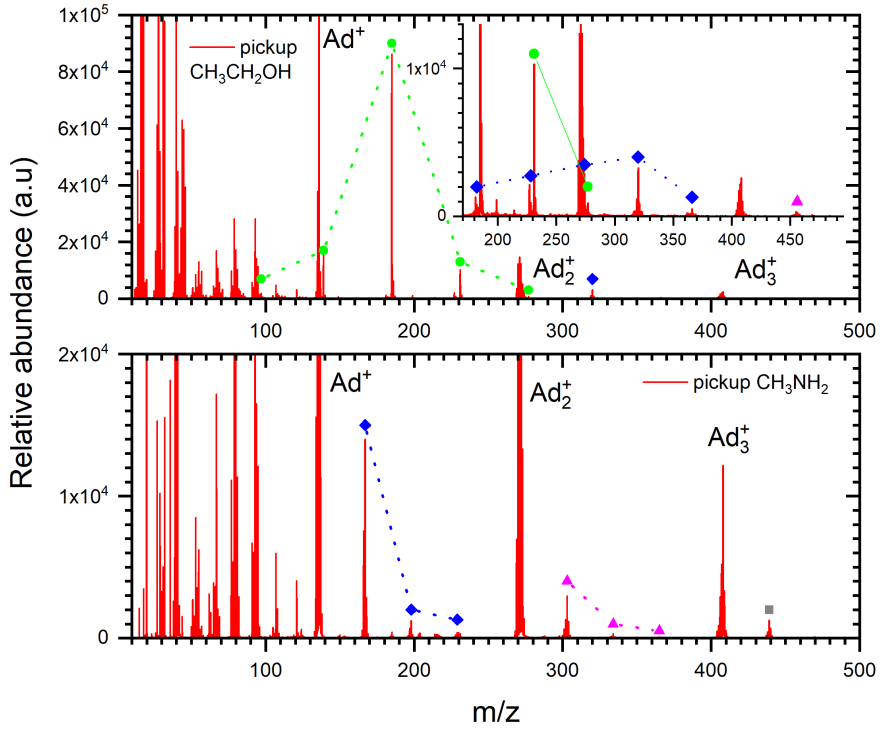


Figure 3.20: Mass spectra of adamantane clusters with pickup of a) ethanol and b) methylamine.

Proton transfer in methanol clusters

A question arose about the proton transfer in methanol clusters after the electron ionization. Whether, the protonation comes from the CH_3, or OH group. The first one is energetically more favorable, whereas the latter makes sense regarding hydrogen bonding interaction. This question was previously addressed during an investigation of the pickup of methanol on ammonia and argon clusters,[153, 154] which were supported by calculations suggesting that the proton transfer from CH_3 is energetically more favorable. However, the supportive experiments with deuterated methanol did not confirm the calculations for the case of ammonia clusters, whereas, in the case of argon clusters, both protonation pathways were observed.[10] Here we have tested the pickup of deuterated methanol CH_3OD and CD_3OH to tackle the question about the protonation pathway on $(Ad)_n$ clusters and re-measured the case of argon clusters $(Ar)_n$.

Figure 3.21 presents a detailed view of the first three members of the pure methanol ion series after pickup. Here the plots are presented from the measurement of argon clusters $(Ar)_n$ as the spectra from $(Ad)_n$ experiments are

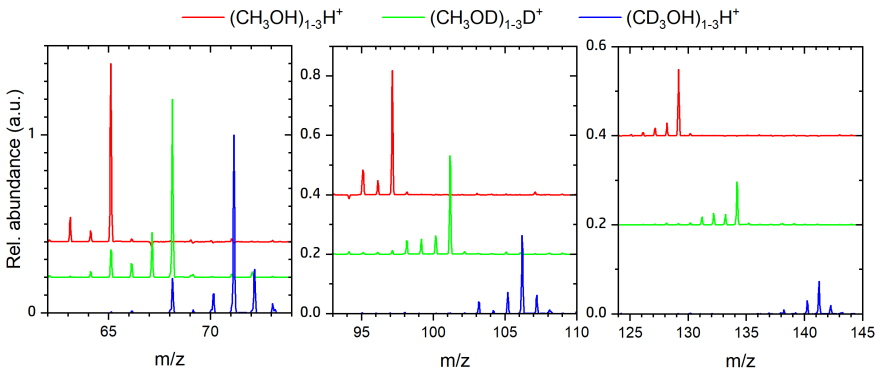


Figure 3.21: Detailed view on the the first three members of a) $(CH_3OH)_{1-3}H^+$, b) $(CH_3OD)_{1-3}D^+$ and c) $(CD_3OH)_{1-3}H^+$ mass series.

more complicated due to adamantane fragmentation. In each subplot, there is a comparison of the spectra after pickup of CH_3OH (red), CH_3OD (green) and CD_3OH (blue). The spectra are shown with offsets and normalized on the most intense peaks in the series for a better comparison. The major peaks in the series correspond to $(CH_3OD)_kD^+$ in the case of CH_3OD and $(CD_3OH)_kH^+$ in the case of CD_3OH. Both spectra suggest that the main channel for proton transfer is from OH, respectively OD, group. Nevertheless, the spectra also show strong peaks assigned $(CH_3OD)_kH^+$ and $(CD_3OH)_kD^+$ ions. An intensity ratio of $(CD_3OH)_kD^+$ to $(CD_3OH)_kH^+$ is around 1:4[3]. Assuming the abundance of hydrogens in methyl group CH_3, we can estimate that the proton transfer from the OH group is $\times 12$ times more probable than the transfer of hydrogen bonded to carbon. The same observations were made for methanol pickup by adamantane clusters.

In conclusion, both pathways are feasible after ionization with 70 eV electrons, but the proton transfer from the hydroxyl group is preferred.

[3]An intensity ratio of $(CH_3OD)_kH^+$ to $(CH_3OD)_kD^+$ seems to be a comparable. However, a coincidence with cluster fragment ions makes the estimation inaccurate.

3.4 Future Prospects

Following the reported results in the previous chapters, I can propose several future paths for our investigation of polyatomic molecules from the perspective of atmospheric and ISC physical chemistry, which might be helpful for the students that will follow my steps and further extend the investigation.

The described evolution of the AIM apparatus in chapter 2 significantly simplified the data acquisition and accuracy of the VMI experiment. The tedious problems with the installation and aging of the new UV OPO laser were solved by a change of repetition rate to 20 Hz. This opens a possibility to increase the repetition rate of data acquisition from 10 Hz to 20 Hz. Recently, we bought a new camera and short-focal objective, which was meant for the VMI detection on the CLUB apparatus. However, the camera could be used for the AIM due to the one-year delay in the MCP/PS detector delivery. The critical upgrade of the AIM apparatus asks for an exchange of the ISO-KF parts (detector assembly and central cross) for the CF system to maintain ultrahigh vacuum and the installation of a gate valve between the skimmer and the VMI spectrometer, which would significantly simplify the exchange of the nozzle valve puppet. Recently, the AIM apparatus was extended by a new chamber with a quadrupole mass spectrometer, whose application for complementary measurement of MS with electron ionization should bring complementary data for our VMI images.

The pyrrole experiments showed the coupling between the vibrational mode and fragment recoil. But unfortunately, the clustering experiments were not successful. Therefore, before any further experiments in clusters, I would focus on the multiphoton effects in the photodissociation of isolated pyrrole and their role in the generation of the slow H fragments, which might be underestimated, see figure 3.2. Another approach is a collaboration with the group of prof. J. Küpper (University of Hamburg, DESY), who recently reported the generation of purified molecular beams with pyrrole.H_2O dimers, and their focus is rather on ultrafast dynamics.[62] The pyrrole.H_2O dimers system would thus be highly interesting for our state-resolved experiments.

The installation of the new tuneable UV OPO laser enabled us to extend our investigation on selected haloalkanes as isolated molecules and pure clusters. The last chapter devoted to clusters of higher haloalkanes, see chapter 3.2.3 based on the acquired data from the AIM apparatus, lays a foundation for further investigation of photodynamics in clusters. As was written above, the VMI experiments on CLUB apparatus with halohydrocarbons are also planned (summer/autumn 2022) after installing a new detector system. This will enable us first to perform the experiments with haloalkane co-expansion with argon to confirm the observations from the AIM measurement. Secondly, perform the next step in the investigation of weakly bound systems by mimicking the atmospheric aerosols through the pickup of haloalkanes on argon/water clusters.

In the above mentioned pickup experiments, I can also use my acquired experiences from the campaigns with the pickup on $(PAH)_n$ clusters. Now when we analysed the data from the benzene and adamantane, we would like to further focus on the results from larger PAH with preliminary results reported in chapter 3.3.1. Simultaneously, the next campaign will follow with MS in negative mode to study charge stabilization in $(PAH)_n$ clusters after electron attachment per-

turbed by a molecular pickup. We have already performed several experiments in negative mode with benzene and naphthalene clusters with the pickup of hydrogen bonding molecules, ammonia, and oxygen. The preliminary mass spectra exhibit significant changes corresponding to the molecular pickup, which might be highly interesting for astro- and atmospheric chemistry.

Conclusion

The thesis presents a comprehensive experimental study of photodynamics and cluster growth on selected small polyatomic molecules. The topic came out of our long-term goal to investigate molecular systems with atmospheric and astrochemical relevance by molecular beam techniques, which enable us to apply advanced laser and MS methods. The necessary prerequisites for a basic theoretical understanding of the studied phenomena were delivered in chapter 1, which is followed by a brief introduction into the molecular beam and MS techniques with a particular focus on the VMI method in chapter 2. During the course of the investigation, the system of AIM was upgraded in system remote control, implementation of ion counting, signal/background data acquisition, and adjustments of AIM chambers, which will be appreciated in future experimental campaigns.

On one side, the molecular systems were investigated to elucidate their photodynamical pathways for the purpose of fundamental physical chemistry, which is mainly represented by studies of vibrationally mediated photodissociation of isolated pyrrole and singlet-triplet interplay in higher haloalkanes. On the other hand, the selected systems were chosen for their role in various natural processes. This is demonstrated by the research on haloalkanes in clusters as the initial step for mimicking the atmospheric aerosols. Their heterogeneous chemistry also motivated the next campaign with molecular pickup on PAH clusters to investigate water condensation and ice mantle growth.

Our conclusions indicate several novel observations, which can practically provide input for future MD simulations. First, we observed an efficient coupling of N-H bond stretching mode in pyrrole to H fragment recoil in contrast to the expected IVR process. Secondly, we described the impact of the spin-orbit effect during C-Cl fragmentation after $\tilde{A}$-band excitation in higher chloroalkanes of different alkyl lengths and Cl group position. Furthermore, we reported on different photodynamics of CH_3 and Cl fragments in pure chloromethyl clusters. This was again supported by our preliminary results on clusters of higher haloalkanes. Also, we discussed the origin of the "central blobs" in cluster caging and multiphoton effects, which might be helpful for many VMI experimentalists. The PAH clusters are a new field for our group, and therefore, a broad overview of tested systems was presented as a motivation for the ensuing investigation. Lastly, the uptake of the hydrogen bonding molecules on the benzene clusters provides an observation of fast cluster coagulation and the very first relative quantification of pickup efficiency, which might be relevant for astro- or atmospherical simulations of molecular condensation.

Finally, I described our outlook for future experiments in the previous chapter. The present results offer various paths to follow in investigating the photodynamics of isolated molecules and clusters from the perspective of atmospheric chemistry and physics, which, I hope, will attract the attention of the scientific community and students of chemical physics.

Bibliography

[1] Reinhard Schinke. *Photodissociation Dynamics: Spectroscopy and Fragmentation of Small Polyatomic Molecules*. Cambridge Monographs on Atomic, Molecular and Chemical Physics. Cambridge University Press, 1993.

[2] Hans Pauly. *Atom, Molecule, and Cluster Beams I: Basic Theory, Production and Detection of Thermal Energy Beams*, volume 1. Springer Science & Business Media, 2000.

[3] Ivo S. Vinklárek, David Bína, Tomáš Malina, Aaron M. Collins, Radek Litvín, Jan Alster, and Jakub Pšenčík. Triplet state quenching of bacteriochlorophyll c aggregates in a protein-free environment of a chlorosome interior. *Chem. Phys.*, 529:110542, 2020.

[4] Ivo S. Vinklárek, Till L. V. Bornemann, Heiko Lokstein, Eckhard Hofmann, Jan Alster, and Jakub Pšenčík. Temperature dependence of chlorophyll triplet quenching in two photosynthetic light-harvesting complexes from higher plants and dinoflagellates. *J. Phys. Chem. B*, 122(38):8834–8845, 2018.

[5] Ivo S. Vinklárek, Jozef Rakovský, Viktoriya Poterya, and Michal Fárník. Different dynamics of CH_3 and Cl fragments from photodissociation of CH_3Cl in clusters. *J. Phys. Chem. A*, 124(38):7633–7643, 2020.

[6] Ivo S. Vinklárek, Jiří Suchan, Jozef Rakovský, Kamila Moriová, Viktoriya Poterya, Petr Slavíček, and Michal Fárník. Energy partitioning and spin–orbit effects in the photodissociation of higher chloroalkanes. *Phys. Chem. Chem. Phys.*, 23:14340–14351, 2021.

[7] Ivo S. Vinklárek, Jozef Rakovský, Viktoryia Poterya, and Michal Fárník. Clustering and multiphoton effects in velocity map imaging of methyl chloride. *Mol. Phys.*, 119(1-2):e1823507, 2021.

[8] Kateryna Grygoryeva, Jozef Rakovský, Ivo S. Vinklárek, Ondřej Votava, Michal Fárník, and Viktoriya Poterya. Vibrationally mediated photodissociation dynamics of pyrrole. *AIP Adv.*, 9(3):035151, 2019.

[9] Benjamin J. Whitaker. *Imaging in molecular dynamics: technology and applications*. Cambridge University Press, 2003.

[10] Michal Fárník, Juraj Fedor, Jaroslav Kočišek, Jozef Lengyel, Eva Pluhařová, Viktoriya Poterya, and Andriy Pysanenko. Pickup and reactions of molecules on clusters relevant for atmospheric and interstellar processes. *Phys. Chem. Chem. Phys.*, 23:3195–3213, 2021.

[11] Olivier Boucher. Atmospheric aerosols. In *Atmospheric Aerosols*, pages 9–24. Springer, 2015.

[12] Michal Fárník and Jozef Lengyel. Mass spectrometry of aerosol particle analogues in molecular beam experiments. *Mass Spectrom. Rev.*, 37(5):630–651, 2018.

[13] Jin Liao, L. Gregory Huey, Zhen Liu, David J. Tanner, Chris A. Cantrell, John J. Orlando, Frank M. Flocke, Paul B. Shepson, Andrew J. Weinheimer, Samuel R. Hall, et al. High levels of molecular chlorine in the arctic atmosphere. *Nat. Geosci.*, 7(2):91–94, 2014.

[14] Richard P. Wayne, Gilles Poulet, Peter Biggs, John P. Burrows, Richard A. Cox, Paul J. Crutzen, Garry D. Hayman, Michael E. Jenkin, Georges Le Bras, Geert K. Moortgat, Ulrich F. Platt, and Ralph N. Schindler. Halogen oxides: Radicals, sources and reservoirs in the laboratory and in the atmosphere. *Atmos. Environ.*, 29(20):2677–2881, 1995.

[15] Ivo S. Vinklárek, Andriy Pysanenko, Eva Pluhařová, and Michal Fárník. Uptake of Hydrogen Bonding Molecules by Benzene Nanoparticles. *J. Phys. Chem. Lett.*, 2022. Drafted and Accepted, DOI: 10.1021/acs.jpclett.2c00835.

[16] Alessandra Candian, Junfeng Zhen, and Alexander G. G. M. Tielens. The aromatic universe. *Phys. Today*, 71:11–38, 2018.

[17] Mike Howsam and Kevin C. Jones. Sources of PAHs in the environment. In *PAHs and related compounds*, pages 137–174. Springer, 1998.

[18] Michal Fárník. *Molecular dynamics in free clusters and nanoparticles studied in molecular beams*. ICT Prague Press, Institute of Chemical Technology Prague, 2011.

[19] Kateryna Grygoryeva, Jozef Rakovský, Ondřej Votava, and Michal Fárník. Imaging of rotational wave-function in photodissociation of rovibrationally excited HCl molecules. *J. Chem. Phys.*, 147(1):013901, 2017.

[20] Helmut H. Telle, Angel González Ureņa, and Robert J. Donovan. *Laser chemistry: spectroscopy, dynamics and applications*. John Wiley & Sons, 2007.

[21] Blithe E. Rocher-Casterline, Lee C. Ch'ng, Andrew K. Mollner, and Hanna Reisler. Communication: Determination of the bond dissociation energy (D_0) of the water dimer, $(H_2O)_2$, by velocity map imaging. *J. Chem. Phys.*, 134(21):211101, 2011.

[22] Salman Rosenwaks. *Vibrationally Mediated Photodissociation*. The Royal Society of Chemistry, 2009.

[23] Joseph R. Lane and Henrik G. Kjaergaard. Fluorosulfonic acid and chlorosulfonic acid: Possible candidates for OH-stretching overtone-induced photodissociation. *J. Phys. Chem. A*, 111(39):9707–9713, 2007.

[24] Miloš Nepraš and Miloš Titz. *Základy teorie elektronových spekter: Absorpční a luminiscenční spektra organických sloučenin v ultrafialové a viditelné oblasti světla*. SNTL, 1983.

[25] Horst Köppel. Diabatic representation: Methods for the construction of diabatic electronic states. In *Conical Intersections: Electronic Structure, Dynamics and Spectroscopy*, pages 175–204. World Scientific, 2004.

[26] Gerhard Herzberg and H. Christopher Longuet-Higgins. Intersection of potential energy surfaces in polyatomic molecules. *Discuss. Faraday Soc.*, 35:77–82, 1963.

[27] Adiabatic and diabatic representations, study text. `https://ethz.ch/content/dam/ethz/special-interest/chab/physical-chemistry/ultrafast-spectroscopy-dam/documents/lectures/advancedkineticsFS16/Exdef/advkin_exercise06.pdf`. Accessed: 2022-03-05.

[28] Jean-Marc L. Pecourt, Jorge Peon, and Bern Kohler. Ultrafast internal conversion of electronically excited RNA and DNA nucleosides in water. *J. Am. Chem. Soc.*, 122(38):9348–9349, 2000.

[29] Andrei Tokmakoff. Time dependent quantum mechanics and spectroscopy. `https://chem.libretexts.org/Bookshelves/Physical_and_Theoretical_Chemistry_Textbook_Maps/Time_Dependent_Quantum_Mechanics_and_Spectroscopy_(Tokmakoff)`. Accessed: 2022-01-30.

[30] Donald S. McClure. Spin-orbit interaction in aromatic molecules. *J. Chem. Phys.*, 20(4):682–686, 1952.

[31] Dmitri G. Fedorov, Shiro Koseki, Michael W. Schmidt, and Mark S. Gordon. Spin-orbit coupling in molecules: Chemistry beyond the adiabatic approximation. *Int. Rev. Phys. Chem.*, 22(3):551–592, 2003.

[32] Mostafa A. El-Sayed. Spin-orbit coupling and the radiationless processes in nitrogen heterocyclics. *J. Chem. Phys.*, 38(12):2834–2838, 1963.

[33] Christel M. Marian. Understanding and Controlling Intersystem Crossing in Molecules. *Ann. Rev. Phys. Chem.*, 72(1):617–640, 2021.

[34] Ivo S. Vinklárek, Marek Scholz, Roman Dědic, and Jan Hála. Singlet oxygen feedback delayed fluorescence of protoporphyrin IX in organic solutions. *Photochem. Photobiol. Sci.*, 16:507–518, 2017.

[35] Pavel Pokhilko and Anna I. Krylov. Quantitative El-Sayed Rules for Many-Body Wave Functions from Spinless Transition Density Matrices. *J. Phys. Chem. Lett.*, 10(17):4857–4862, 2019.

[36] Michael Kasha. Collisional Perturbation of Spin-Orbital Coupling and the Mechanism of Fluorescence Quenching. A Visual Demonstration of the Perturbation. *J. Chem. Phys.*, 20(1):71–74, 1952.

[37] Jiří Suchan, Daniel Hollas, Basile F. E. Curchod, and Petr Slavíček. On the importance of initial conditions for excited-state dynamics. *Faraday Discuss.*, 212:307–330, 2018.

[38] Stephen J. Riley and Kent R. Wilson. Excited fragments from excited molecules: energy partitioning in the photodissociation of alkyl iodides. *Faraday Discuss.*, 53:132–146, 1972.

[39] Masahiro Kawasaki, Kazuo Kasatani, Hiroyasu Sato, Hisanori Shinohara, and Nobuyuki Nishi. Photodissociation of molecular beams of halogenated hydrocarbons at 193 nm. *Chem. Phys.*, 88(1):135–142, 1984.

[40] George E. Busch and Kent R. Wilson. Triatomic photofragment spectra. I. Energy partitioning in NO_2 photodissociation. *J. Chem. Phys.*, 56(7):3626–3638, 1972.

[41] Francesco Di Giacomo. A short account of RRKM theory of unimolecular reactions and of Marcus theory of electron transfer in a historical perspective. *J. Chem. Educ.*, 92(3):476–481, 2015.

[42] Philip Pechukas, John C. Light, and Charles Rankin. Statistical Theory of Chemical Kinetics: Application to Neutral-Atom-Molecule Reactions. *J. Chem. Phys.*, 44(2):794–805, 1966.

[43] Christoph Schlier. *Molecular Beams and Reaction Kinetics.* Academic Press, 1970.

[44] Alexey V. Baklanov and David H. Parker. Weakly bound environment of molecular oxygen as a catalyst of photooxidation. *Kinet. Catal.*, 61(2):174–197, 2020.

[45] Rebeca de Nalda, José Durá, Jesús González-Vázquez, V. Loriot, and Luis Bañares. The primary step in the ultrafast photodissociation of the methyl iodide dimer. *Phys. Chem. Chem. Phys.*, 13(29):13295–13304, 2011.

[46] Susan Solomon. Stratospheric ozone depletion: A review of concepts and history. *Rev. Geophys.*, 37(3):275–316, 1999.

[47] Thomas Peter. Microphysics and heterogeneous chemistry of polar stratospheric clouds. *Ann. Rev. Phys. Chem.*, 48(1):785–822, 1997.

[48] Mario J. Molina, Ruijia Zhang, Paul J. Wooldridge, John R. McMahon, Jung E. Kim, Hsun-Yun Chang, and Keith D. Beyer. Physical chemistry of the $H_2SO_4/HNO_3/H_2O$ system: Implications for polar stratospheric clouds. *Science*, 261(5127):1418–1423, 1993.

[49] Jack G. Calvert, Allan Lazrus, Gregory L. Kok, Brian G. Heikes, James G. Walega, John Lind, and Christopher A. Cantrell. Chemical mechanisms of acid generation in the troposphere. *Nature*, 317(6032):27–35, 1985.

[50] Karl D. Froyd, Daniel M. Murphy, Todd J. Sanford, David S. Thomson, John C. Wilson, Leonhard Pfister, and Leslie Lait. Aerosol composition of the tropical upper troposphere. *Adv. Chem. Phys.*, 9(13):4363–4385, 2009.

[51] Richard L. McKenzie, Pieter J. Aucamp, Alkiviades F. Bais, Lars O. Björn, Mohamad Ilyas, and Sasha Madronich. Ozone depletion and climate change: impacts on UV radiation. *Photochem. Photobiol. Sci*, 10(2):182–198, 2011.

[52] Gaëlle Dufour, Ray Nassar, Christopher D. Boone, Robert L. Skelton, Kaley A. Walker, Peter F. Bernath, Curtis P. Rinsland, Kirill Semeniuk, et al. Partitioning between the inorganic chlorine reservoirs HCl and $ClONO_2$ during the Arctic winter 2005 from the ACE-FTS. *Adv. Chem. Phys.*, 6(8):2355–2366, 2006.

[53] Alexander G. G. M. Tielens. *The physics and chemistry of the interstellar medium*. Cambridge University Press, 2005.

[54] Ling Xin. Webb telescope goes into space. *The Innovation*, 3(1), 2022.

[55] David M. Lubman, Charles T. Rettner, and Richard N. Zare. How isolated are molecules in a molecular beam? *J. Phys. Chem.*, 86(7):1129–1135, 1982.

[56] Jorge J. Ferreiro, Satrajit Chakrabarty, Bernhard Schläppi, and Ruth Signorell. Observation of propane cluster size distributions during nucleation and growth in a laval expansion. *J. Chem. Phys.*, 145(21):211907, 2016.

[57] Satrajit Chakrabarty, Jorge J. Ferreiro, Martina Lippe, and Ruth Signorell. Toluene cluster formation in laval expansions: Nucleation and growth. *J. Phys. Chem. A*, 121(20):3991–4001, 2017.

[58] Chenxi Li and Ruth Signorell. Understanding vapor nucleation on the molecular level: A review. *J. Aerosol Sci.*, 153:105676, 2021.

[59] Uzi Even. The Even-Lavie valve as a source for high intensity supersonic beam. *EPJ tech. instrum.*, 2:1–22, 2015.

[60] Sebastian Trippel, Yuan-Pin Chang, Stephan Stern, Terry Mullins, Lotte Holmegaard, and Jochen Küpper. Spatial separation of state-and size-selected neutral clusters. *Phys. Rev. A*, 86(3):033202, 2012.

[61] Musahid Ahmed and Oleg Kostko. From atoms to aerosols: probing clusters and nanoparticles with synchrotron based mass spectrometry and X-ray spectroscopy. *Phys. Chem. Chem. Phys.*, 22(5):2713–2737, 2020.

[62] Melby Johny, Jolijn Onvlee, Thomas Kierspel, Helen Bieker, Sebastian Trippel, and Jochen Küpper. Spatial separation of pyrrole and pyrrole-water clusters. *Chem. Phys. Lett.*, 721:149–152, 2019.

[63] Joss Wiese, Jolijn Onvlee, Sebastian Trippel, and Jochen Küpper. Strong-field ionization of complex molecules. *Phys. Rev. Res.*, 3(1):013089, 2021.

[64] T. Bergmann, Thomas P. Martin, and Helmut Schaber. High-resolution time-of-flight mass spectrometer. *Rev. Sci. Instrum.*, 60(4):792–793, 1989.

[65] W. C. Wiley and I. H. McLaren. Time-of-flight mass spectrometer with improved resolution. *Rev. Sci. Instrum.*, 26(12):1150–1157, 1955.

[66] Michael N. R. Ashfold, N. Hendrik Nahler, Andrew J. Orr-Ewing, Olivier P. J. Vieuxmaire, Rachel L. Toomes, Theofanis N. Kitsopoulos, Ivan Anton Garcia, Dmitri A. Chestakov, Shiou-Min Wu, and David H. Parker. Imaging

the dynamics of gas phase reactions. *Phys. Chem. Chem. Phys.*, 8:26–53, 2006.

[67] David W. Chandler and Paul L. Houston. Two-dimensional imaging of state-selected photodissociation products detected by multiphoton ionization. *J. Chem. Phys.*, 87(2):1445–1447, 1987.

[68] André T. J. B. Eppink and David H. Parker. Velocity map imaging of ions and electrons using electrostatic lenses: Application in photoelectron and photofragment ion imaging of molecular oxygen. *Rev. Sci. Instrum.*, 68(9):3477–3484, 1997.

[69] Florentina Rosca-Pruna and Marc J. J. Vrakking. Experimental observation of revival structures in picosecond laser-induced alignment of I_2. *Phys. Rev. Lett.*, 87(15):153902, 2001.

[70] Lotte Holmegaard, Jens H. Nielsen, Iftach Nevo, Henrik Stapelfeldt, Frank Filsinger, Jochen Küpper, and Gerard Meijer. Laser-induced alignment and orientation of quantum-state-selected large molecules. *Phys. Rev. Lett.*, 102(2):023001, 2009.

[71] Linda V. Thesing, Andrey Yachmenev, Rosario González-Férez, and Jochen Küpper. Laser-induced alignment of weakly bound molecular aggregates. *Phys. Rev. A*, 98(5):053412, 2018.

[72] Stephen Gibson, Daniel D. Hickstein, Roman Yurchak, Mikhail Ryazanov, Dhrubajyoti Das, and Gilbert Shih. PyAbel/PyAbel: v0.8.4. `https://doi.org/10.5281/zenodo.4690660`, 2021. Accessed: 2021-04-30.

[73] Daniel D. Hickstein, Stephen T. Gibson, Roman Yurchak, Dhrubajyoti D. Das, and Mikhail Ryazanov. A direct comparison of high-speed methods for the numerical Abel transform. *Rev. Sci. Instrum.*, 90(6):065115, 2019.

[74] Anton S. Tremsin and John V. Vallerga. Unique capabilities and applications of Microchannel Plate (MCP) detectors with Medipix/Timepix readout. *Radiat. Meas.*, 130:106228, 2020.

[75] Claire Vallance, Mark Brouard, Alexandra Lauer, Craig S Slater, Edward Halford, Benjamin Winter, Simon J. King, Jason W. L. Lee, Daniel E. Pooley, Iain Sedgwick, et al. Fast sensors for time-of-flight imaging applications. *Phys. Chem. Chem. Phys.*, 16(2):383–395, 2014.

[76] Xiang Li, Ludger Inhester, Timur Osipov, Rebecca Boll, Ryan Coffee, James Cryan, Ave Gatton, Tais Gorkhover, Gregor Hartman, Markus Ilchen, et al. Electron-ion coincidence measurements of molecular dynamics with intense X-ray pulses. *Sci. Rep.*, 11(1):1–12, 2021.

[77] Richard N. Zare. Photoejection dynamics. *Mol. Photochem.*, 4(1):1–37, 1972.

[78] Christian T. Matthaei, Deb Pratim Mukhopadhyay, and Ingo Fischer. Photodissociation of Benzoyl Chloride: A Velocity Map Imaging Study Using

VUV Detection of Chlorine Atoms. *J. Phys. Chem. A*, 125(14):2816–2825, 2021.

[79] Benjamin Erk, Daniel Rolles, Lutz Foucar, Benedikt Rudek, Sascha W. Epp, Max Cryle, Christoph Bostedt, Sebastian Schorb, John Bozek, Arnaud Rouzee, et al. Inner-shell multiple ionization of polyatomic molecules with an intense X-ray free-electron laser studied by coincident ion momentum imaging. *J. Phys. B: At. Mol. Opt. Phys.*, 46(16):164031, 2013.

[80] Nikoleta Kotsina and Dave Townsend. Improved insights in time-resolved photoelectron imaging. *Phys. Chem. Chem. Phys.*, 23:10736–10755, 2021.

[81] Felix Allum, Michael Burt, Kasra Amini, Rebecca Boll, Hansjochen Köckert, Pavel K. Olshin, Sadia Bari, et al. Coulomb explosion imaging of CH_3I and CH_2ClI photodissociation dynamics. *J. Chem. Phys.*, 149(20):204313, 2018.

[82] Evangelos T. Karamatskos, Sebastian Raabe, Terry Mullins, Andrea Trabattoni, Philipp Stammer, Gildas Goldsztejn, Rasmus R. Johansen, Karol Długołecki, Henrik Stapelfeldt, Marc J. J. Vrakking, Sebastian Trippel, Arnaud Rouzée, and Jochen Küpper. Molecular movie of ultrafast coherent rotational dynamics of OCS. *Faraday Discuss.*, 10:3364, 2018.

[83] André T. J. B. Eppink and David H. Parker. Velocity map imaging of ions and electrons using electrostatic lenses: Application in photoelectron and photofragment ion imaging of molecular oxygen. *Rev. Sci. Instrum.*, 68(9):3477–3484, 1997.

[84] Bor-Yu Chang, Rama C. Hoetzlein, Julie A. Mueller, Joseph D. Geiser, and Paul L. Houston. Improved two-dimensional product imaging: The real-time ion-counting method. *Rev. Sci. Instrum.*, 69(4):1665–1670, 1998.

[85] Nick Waltham. CCD and CMOS sensors. In *Observing photons in space*, pages 423–442. Springer, 2013.

[86] Rafael Ballabriga, Michael Campbell, and Xavier Llopart. Asic developments for radiation imaging applications: The medipix and timepix family. *Nucl. Instrum. Methods Phys. Res. A*, 878:10–23, 2018.

[87] Juraj Fedor, Jaroslav Kočišek, Viktoryia Poterya, Ondřej Votava, Andriy Pysanenko, M. Laura Lipciuc, Theofanis N. Kitsopoulos, and Michal Fárník. Velocity map imaging of HBr photodissociation in large rare gas clusters. *J. Chem. Phys.*, 134(15):154303, 2011.

[88] Reinhard Baumfalk, Udo Buck, Christian Frischkorn, Nils H. Nahler, and Lutz Hüwel. Photodissociation of HBr molecules and clusters: Anisotropy parameters, branching ratios, and kinetic energy distributions. *J. Chem. Phys.*, 111(6):2595–2605, 1999.

[89] Paul M. Regan, Stephen R. Langford, Andrew J. Orr-Ewing, and Michael N. R. Ashfold. The ultraviolet photodissociation dynamics of hydrogen bromide. *J. Chem. Phys.*, 110(1):281–288, 1999.

[90] Leo Sala, Barbora Sedmidubská, Ivo Vinklárek, Michal Fárník, Robin Schürmann, Ilko Bald, Jakub Med, Petr Slavíček, and Jaroslav Kočišek. Electron attachment to microhydrated 4-nitro- and 4-bromo-thiophenol. *Phys. Chem. Chem. Phys.*, 23:18173–18181, 2021.

[91] Robin Schürmann, Thomas F. M. Luxford, Ivo S. Vinklárek, Jaroslav Kočišek, Mateusz Zawadzki, and Ilko Bald. Interaction of 4-nitrothiophenol with low energy electrons: Implications for plasmon mediated reactions. *J. Chem. Phys.*, 153(10):104303, 2020.

[92] Andriy Pysanenko, Eva Pluhařová, Ivo S. Vinklárek, Jozef Rakovský, Viktoriya Poterya, Jaroslav Kočišek, and Michal Fárník. Ion and radical chemistry in $(H_2O_2)_N$ clusters. *Phys. Chem. Chem. Phys.*, 22:15312–15320, 2020.

[93] Andriy Pysanenko, Ivo S. Vinklárek, Michal Fárník, and Viktoriya Poterya. Generation of $(H_2O_2)_N$ clusters on argon and ice nanoparticles. *Int. J. Mass Spectrom.*, 461:116514, 2021.

[94] Ivo S. Vinklárek, Lukáš Vel'as, Petra Riegerová, Kristián Skála, Ilya Mikhalyov, Natalia Gretskaya, Martin Hof, and Radek Šachl. Experimental Evidence of the Existence of Interleaflet Coupled Nanodomains: An MC-FRET Study. *J. Phys. Chem. Lett.*, 10(9):2024–2030, 2019.

[95] Frank Filsinger, Gerard Meijer, Henrik Stapelfeldt, Henry N. Chapman, and Jochen Küpper. State- and conformer-selected beams of aligned and oriented molecules for ultrafast diffraction studies. *Phys. Chem. Chem. Phys.*, 13(6):2076–2087, 2011.

[96] Xinhua Xie, Stefan Roither, Markus Schöffler, Erik Lötstedt, Daniil Kartashov, Li Zhang, Gerhard G Paulus, Atsushi Iwasaki, Andrius Baltuška, Kaoru Yamanouchi, et al. Electronic predetermination of ethylene fragmentation dynamics. *Phys. Rev. X.*, 4(2):021005, 2014.

[97] Gareth M. Roberts and Vasilios G. Stavros. The role of states in the photochemistry of heteroaromatic biomolecules and their subunits: insights from gas-phase femtosecond spectroscopy. *Chem. Sci.*, 5(5):1698–1722, 2014.

[98] Michael N. R. Ashfold, Graeme A. King, Daniel Murdock, Michael G. D. Nix, Thomas A. A. Oliver, and Alan G. Sage. $\pi\sigma^*$ excited states in molecular photochemistry. *Phys. Chem. Chem. Phys.*, 12(6):1218–1238, 2010.

[99] Bríd Cronin, Michael G. D. Nix, Rafay H. Qadiri, and Michael N. R. Ashfold. High resolution photofragment translational spectroscopy studies of the near ultraviolet photolysis of pyrrole. *Phys. Chem. Chem. Phys.*, 6(21):5031–5041, 2004.

[100] J. Wei, J. Riedel, A. Kuczmann, F. Renth, and F. Temps. Photodissociation dynamics of pyrrole: Evidence for mode specific dynamics from conical intersections. *Faraday Discuss.*, 127:267–282, 2004.

[101] Valérie Vallet, Zhenggang Lan, Susanta Mahapatra, Andrzej L. Sobolewski, and Wolfgang Domcke. Photochemistry of pyrrole: Time-dependent quantum wave-packet description of the dynamics at the π 1 σ^*-S_0 conical intersections. *J. Chem. Phys.*, 123(14):144307, 2005.

[102] Václav Profant, Viktoriya Poterya, Michal Fárník, Petr Slavíček, and Udo Buck. Fragmentation dynamics of size-selected pyrrole clusters prepared by electron impact ionization: forming a solvated dimer ion core. *J. Phys. Chem. A*, 111(49):12477–12486, 2007.

[103] Viktoriya Poterya, Václav Profant, Michal Fárník, Petr Slavíček, and Udo Buck. Experimental and theoretical study of the pyrrole cluster photochemistry: Closing the π σ^* dissociation pathway by complexation. *J. Chem. Phys.*, 127(6):064307, 2007.

[104] Irmgard Frank and Konstantina Damianos. Excited state dynamics in pyrrole–water clusters: First-principles simulation. *Chem. Phys.*, 343(2):347–352, 2008.

[105] Paolo Cristofanelli, Jgor Arduini, Francescopiero Calzolari, Umberto Giostra, Paolo Bonasoni, and Michela Maione. First Evidences of Methyl Chloride (CH_3Cl) Transport from the Northern Italy Boundary Layer during Summer 2017. *Atmosphere*, 11(3), 2020.

[106] Alena Habartová, Anthony Obisesan, Babak Minofar, and Martina Roeselová. Partial hydration of n-alkyl halides at the water–vapor interface: a molecular simulation study with atmospheric implications. *Theor. Chem. Acc.*, 133(3):1–15, 2014.

[107] Enno Bahlmann, Frank Keppler, Julian Wittmer, Markus Greule, Heinz F. Schöler, Reinhard Seifert, and Cornelius Zetzsch. Evidence for a major missing source in the global chloromethane budget from stable carbon isotopes. *Atmos. Chem. Phys.*, 19(3):1703–1719, 2019.

[108] Ondřej Svoboda and Petr Slavíček. Is Nitrate Anion Photodissociation Mediated by Singlet–Triplet Absorption? *J. Phys. Chem. Lett.*, 5(11):1958–1962, 2014.

[109] Dave Townsend, Suk Kyoung Lee, and Arthur G. Suits. DC slice Imaging of CH_3Cl photolysis at 193.3 nm. *J. Phys. Chem. A*, 108(39):8106–8114, 2004.

[110] Detection of cl atoms and hcl molecules by resonantly enhanced multiphoton ionization.

[111] Ursula Meier and Katharina Kohse-Höinghaus. REMPI detection of CH_3 in low-pressure flames. *Chem. Phys. Lett.*, 142(6):498–502, 1987.

[112] Ball structures of selected haloalkanes. `https://en.wikipedia.org/wiki/Chloromethane`. Accessed: 2021-12-30.

[113] George E. Busch and Kent R. Wilson. Triatomic photofragment spectra. II. Angular distributions from NO_2 photodissociation. *J. Chem. Phys.*, 56(7):3638–3654, 1972.

[114] Qianli Liu and Ahmed H. Zewail. Femtosecond real-time probing of reactions. 10. Reaction times and model potentials. *J. Phys. Chem.*, 97(10):2209–2220, 1993.

[115] CCCBDB Vibrational frequency scaling factors. `https://cccbdb.nist.gov/vibnotes.asp`. Accessed: 2022-02-27.

[116] Pavle Glodic, Andreas Kartakoullis, Michal Fárník, Peter C. Samartzis, and Theofanis N. Kitsopoulos. Driving photochemistry by clustering: The ICl-Xe case. *J. Chem. Phys.*, 137(15):154306, 2012.

[117] Jack A. Syage. State specific, angle velocity resolved measurements of photodissociation in clusters: I atom escape from $(CH_3I)_n$ (n= 1, 2, 3). *Chem. Phys.*, 207(2-3):411–426, 1996.

[118] Yu-Bo Fan and D. J. Donaldson. Cluster-induced photochemistry of CH_3I at 248 nm. *J. Chem. Phys.*, 97(1):189–196, 1992.

[119] Ponnadurai Ramasami and Thomas A. Ford. The structures and vibrational spectra of the methyl halide dimers. An *ab initio* study. *J. Mol. Struct.*, 1126:2–10, 2016.

[120] Yoshisuke Futami, Satoshi Kudoh, Fumiyuki Ito, Taisuke Nakanaga, and Munetaka Nakata. Structures of methyl halide dimers in supersonic jets by matrix-isolation infrared spectroscopy and quantum chemical calculations. *J. Mol. Struct.*, 690(1-3):9–16, 2004.

[121] Jarle Harnes, Mahmoud Abu-Samha, Michael Winkler, Henrik Bergersen, Leif J. Sæthre, and Knut J. Børve. Neutral CH_3Cl and CH_3Br clusters studied by X-ray photoelectron spectroscopy and modeling: Insight to intermolecular interactions and structure. *J. Electron Spectrosc. Relat. Phenom.*, 166:53–64, 2008.

[122] Dmitry Skvortsov, Myong Yong Choi, and Andrey F. Vilesov. Study of HCl clusters in helium nanodroplets: Experiments and ab initio calculations as stepping stones from gas phase to bulk. *J. Phys. Chem. A*, 111(49):12711–12716, 2007.

[123] Robert C. Dunbar. Photodissociation of the methyl chloride (CH_3Cl^+) and nitrous oxide (N_2O^+) cations. *J. Am. Chem. Soc.*, 93(18):4354–4358, 1971.

[124] Fengyan Wang, M. Laura Lipciuc, Xueming Yang, and Theofanis N. Kitsopoulos. Multiphoton dissociation dynamics of CH_3Br. *Phys. Chem. Chem. Phys.*, 11(13):2234–2240, 2009.

[125] Valérie Blanchet, Peter C. Samartzis, and Alec M Wodtke. UV photodissociation of methyl bromide and methyl bromide cation studied by velocity map imaging. *J. Chem. Phys.*, 130(3):034304, 2009.

[126] Antoine Equation Parameters iso-Cl-propane. https://webbook.nist.gov/cgi/cbook.cgi?ID=C75296&Mask=4#Thermo-Phase. Accessed: 2022-02-27.

[127] Antoine Equation Parameters 1-Cl-propane. https://webbook.nist.gov/cgi/cbook.cgi?ID=C540545&Mask=4#Thermo-Phase. Accessed: 2022-02-27.

[128] Antoine Equation Parameters 1-Cl-pentane. https://user.eng.umd.edu/~nsw/chbe250/antoine.dat. Accessed: 2022-02-27.

[129] Dave Townsend, Michael P. Minitti, and Arthur G. Suits. Direct current slice imaging. *Rev. Sci. Instrum.*, 74(4):2530–2539, 2003.

[130] Olivier Berné and Alexander G. G. M. Tielens. Formation of buckminsterfullerene (C60) in interstellar space. *Proc. Natl. Acad. Sci. U.S.A.*, 109(2):401–406, 2012.

[131] Theodore P. Snow and Benjamin J. McCall. Diffuse atomic and molecular clouds. *Annu. Rev. Astron. Astrophys.*, 44:367–414, 2006.

[132] Yvonne J. Pendleton and Louis J. Allamandola. The organic refractory material in the diffuse interstellar medium: Mid-infrared spectroscopic constraints. *Astrophys. J., Suppl. Ser.*, 138(1):75, 2002.

[133] Karin I. Oberg. Photochemistry and astrochemistry: Photochemical pathways to interstellar complex organic molecules. *Chem. Rev.*, 116(17):9631–9663, 2016.

[134] Jozef Lengyel, Jaroslav Kočišek, Victoryia Poterya, Andreyi Pysanenko, Pavla Svrčková, Michal Fárník, D. K. Zaouris, and Juraj Fedor. Uptake of atmospheric molecules by ice nanoparticles: Pickup cross sections. *J. Chem. Phys.*, 137(3):034304, 2012.

[135] Jozef Lengyel, Andreyi Pysanenko, Viktoriya Poterya, Petr Slavíček, Michal Fárník, Jaroslav Kočišek, and Juraj Fedor. Irregular shapes of water clusters generated in supersonic expansions. *Phys. Rev. Lett.*, 112(11):113401, 2014.

[136] NIST database, Ion Energies. https://webbook.nist.gov/cgi/cbook.cgi?ID=C91203&Mask=20#Ion-Energetics. Accessed: 2022-03-05.

[137] Michel Mons, Iliana Dimicoli, and François Piuzzi. Gas phase hydrogen-bonded complexes of aromatic molecules: photoionization and energetics. *Int. Rev. Phys. Chem.*, 21(1):101–135, 2002.

[138] Masurekar Prakash, K. Gopal Samy, and Venkatraman Subramanian. Benzene-Water (BZW_n (n=1-10)) Clusters. *J. Phys. Chem. A*, 113(50):13845–13852, 2009.

[139] Mitsuhiko Miyazaki, Asuka Fujii, Takayuki Ebata, and Naohiko Mikami. Infrared Spectroscopy of Size-Selected Benzene- Water Cluster Cations $[C_6H_6\text{-}(H_2O)_n]^+$(n = 1 - 23): Hydrogen Bond Network Evolution and Microscopic Hydrophobicity. *J. Phys. Chem. A*, 108(48):10656–10660, 2004.

[140] Yehia M. Ibrahim, Michael Meot-Ner, Edreese H. Alshraeh, M. Samy El-Shall, and Steve Scheiner. Stepwise hydration of ionized aromatics. Energies, structures of the hydrated benzene cation, and the mechanism of deprotonation reactions. *J. Am. Chem. Soc.*, 127(19):7053–7064, 2005.

[141] Clement Dubosq, F. Calvo, Mathias Rapacioli, E. Dartois, T. Pino, C. Falvo, and Aude Simon. Quantum modeling of the optical spectra of carbon cluster structural families and relation to the interstellar extinction UV bump. *Astron. Astrophys.*, 634:A62, 2020.

[142] Giuliano Malloci, C. Joblin, and G. Mulas. Theoretical evaluation of PAH dication properties. *Astron. Astrophys.*, 462(2):627–635, 2007.

[143] Jozef Lengyel, Andriy Pysanenko, Viktoriya Poterya, Jaroslav Kočišek, and Michal Fárník. Extensive water cluster fragmentation after low energy electron ionization. *Chem. Phys. Lett.*, 612:256–261, 2014.

[144] Andriy Pysanenko, Alena Habartová, Pavla Svrčková, Jozef Lengyel, Viktoriya Poterya, Martina Roeselová, Juraj Fedor, and Michal Fárník. Lack of aggregation of molecules on ice nanoparticles. *J. Phys. Chem. A*, 119(34):8991–8999, 2015.

[145] Andriy Pysanenko, Jaroslav Kočišek, Dana Nachtigallová, Viktoriya Poterya, and Michal Fární. Clustering of Uracil Molecules on Ice Nanoparticles. *J. Phys. Chem. A*, 121(5):1069–1077, 2017.

[146] Peter Rubovič, Andriy Pysanenko, Jozef Lengyel, Dana Nachtigallová, and Michal Farnik. Biomolecule analogues 2-hydroxypyridine and 2-pyridone base pairing on ice nanoparticles. *J. Phys. Chem. A*, 120(27):4720–4730, 2016.

[147] Cornelius E. Klots. Temperatures of evaporating clusters. *Nature*, 327(6119):222–223, 1987.

[148] Cornelius E. Klots. Evaporation from small particles. *J. Phys. Chem.*, 92(21):5864–5868, 1988.

[149] Christof Steinbach, Michal Fárník, Ingo Ettischer, Jörg-Gerald Siebers, and Udo Buck. Isomeric transitions in size-selected methanol hexamers probed by OH-stretch spectroscopy. *Phys. Chem. Chem. Phys.*, 8(23):2752–2758, 2006.

[150] Guy Lamoureux and Graciela Artavia. Use of the adamantane structure in medicinal chemistry. *Curr. Med. Chem.*, 17(26):2967–2978, 2010.

[151] Hartmut Schwertfeger, Andrey A. Fokin, and Peter R. Schreiner. Diamonds are a chemist's best friend: diamondoid chemistry beyond adamantane. *Angew. Chem. Int. Ed.*, 47(6):1022–1036, 2008.

[152] NIST database, mass spectrum of adamantane. `https://webbook.nist.gov/cgi/cbook.cgi?ID=C281232&Mask=200#Mass-Spec`. Accessed: 2022-03-05.

[153] Michal Fárník, Andriy Pysanenko, Kamila Moriová, Lorenz Ballauf, Paul Scheier, Jan Chalabala, and Petr Slavíček. Ionization of ammonia nanoices with adsorbed methanol molecules. *J. Phys. Chem. A*, 122(43):8458–8468, 2018.

[154] Andriy Pysanenko, Francisco Gámez, Karolína Fárníková, Eva Pluhařová, and Michal Fárník. Proton Transfer Reactions between Methanol and Formic Acid Deposited on Free Ar_N Nanoparticles. *J. Phys. Chem. A*, 123(33):7201–7209, 2019.

List of Figures

1.1 Comparison of various types of photodissociation. The illustrations were drawn according to similar schemes from [1] and [18] and modified. 6

1.2 Schematic pictures of a) cut through the adiabatic and diabatic potentials and b) conical intersection. 10

1.3 Schematic illustrations of a) hard-sphere and b) spectator models derived from classical mechanics. 16

1.4 Photodissociation in environment. Three basic scenarios of cage exit (red), delayed exit (green) and caging effect (blue) are illustrated on the right side. The picture was taken and redrawn from [18]. 17

2.1 a) Velocity distributions of molecules in equilibrium and molecular beam (MB). b) Schematic illustration of supersonic expansion into MB with description. The images were modified from [2, 18]. . . . 22

2.2 The nozzle opening profiles (1^{st} row) and the parent longitudinal ($2^{nd} - 4^{th}$ rows) and transverse (5^{th} row) beam velocity profiles measured for different backing pressures p_{Ar} and nozzle delays τ_N. Signal corresponds to the detected parent ions of pure CO seeded in argon. The longitudinal profiles were fitted by Gaussian to estimate the mean molecular beam velocity v_{MB}, speed ratio S and longitudinal temperature $T_{||}$. 25

2.3 The crucial steps in velocity map imaging technique according to A. Eppink and D. Parker architecture.[9, 68] 29

2.4 Euler angles and coordinates corresponding to molecular (blue) and laser polarization (red) frames. 33

2.5 Photoionization schemes for hydrogen radical. a) 2+1 REMPI scheme at 243.1 nm. b) 1+1' REMPI scheme at 121.5 nm generated by third-harmonic generation from 365 nm.[78] c) Non-resonant multiphoton ionization. Scheme for strong-field ionization.[63] d) Non-resonant one photon ionization.[79] 35

2.6 Ion counting mode and saturation settings of the MCP/PS for ion detection. 38

2.7 Slice through 3D model of Apparatus for Imaging (AIM). The apparatus is equipped with the VMI spectrometer (detail in inset with description), quadrupole mass spectrometer (QMS) and three turbomolecular pumps (TP). 40

2.8 Wiring of the new MCP/PS detector. 41

2.9 Block diagrams and timeline for synchronization of AIM apparatus in IR+UV and UV_{193nm}+UV experiments. 43

2.10 a) Raw image of H fragments from HBr dissotiation at 243 nm. b) Transformed image by inverse Abel trasnformation. c) KED[px] d) KED[eV] e) Detailed view of the slow peak. 44

2.11 Schematic picture of the CLUB apparatus with source chamber (SC), 1^{st} pickup chamber (PC01), 2^{nd} pickup chamber (PC02), reflective time-of-flight spectrometer (rToF) and quadrupole mass spectrometer (QMS). 47

3.1 Comparison of the fast H-fragment kinetic energy between the UV-only and IR+UV experiments. The blue plots belong to the left axis, which describes the dependence of released total kinetic energy on the photon energy. The red plots belong to the right axis, which describes the dependence of the ratio of the total kinetic energy over the maximum available energy. The values for the IR+UV experiment are marked with crosses. The UV-only results are marked with squares. The extra values at 220 and 228 nm were taken from Cronin et al.[99] 53
3.2 (Left) The H-fragment KED spectra dependence on UV energy per pulse: (a) 200 µJ/pulse, (b) 600 µJ/pulse and (c) 1200 µJ/pulse. (Right) The H-fragment KED spectra obtained by the difference of IR+UV and UV-only signal acquired with different IR and UV pulse intensities: (a) IR $\sim$ 3 mJ/pulse, UV $\sim$ 390 µJ/pulse, (b) IR $\sim$ 12 mJ/pulse, UV $\sim$ 390 µJ/pulse and (c) IR $\sim$ 12 mJ/pulse, UV $\sim$ 150 µJ/pulse. [8] 54
3.3 Schematic picture of the cut through the PES of the ground and three lowest excited states of small chloroalkanes in perspective of C-Cl bond. 55
3.4 Comparison of the VMI images with extracted KED spectra and angular distributions assigned to (a,b,c) Cl, Cl* and (d,e,f) CH_3 fragments. The figures were taken from [5] and modified. 57
3.5 The structures of investigated chloroalkanes. The models were taken from [112] and modified. 59
3.6 Comparison of fraction of internal excitation f_I^x obtained from experiment, classical models and *ab initio* CASSCF simulations. . . 60
3.7 (a) Scheme of model for calculation of ISC and singlet-triplet absorption probabilities. (b) Estimated probabilities of ISC and singlet-triplet absorption with the simulated β^{sim}-parameters. (c) Estimated probabilities of ISC and singlet-triplet absorption with the maximal theoretical values of β-parameters. 62
3.8 VMI images of CH_3 and Cl fragments after 193 nm photofragmentation of CH_3Cl seeded in argon. The images were taken in different delays of beam profile.[5] 65
3.9 Obtained KED spectra corresponding to a) Cl, b) Cl* and c) CH_3 fragments. The dashed lines are raw spectra. The dotted lines are monomer signal. The plots were taken and modified from [5]. . . . 66
3.10 The VMI images of a) Cl and b) CH_3 in high irradiation conditions, $I_{193} = 16 \times 10^{25}$ photons/cm^2/s. [7] 68
3.11 Schematic representation of the PES that play a role in CH_3Cl^+ dissociation along the C-Cl coordinate. The violet and pink arrows mark the excitations into the ionic states. The scheme was taken from [7]. 69

3.12 Transformed VMI images from photodissociation at 193 nm of selected higher chloroalkanes, i.e., of 1-Cl-propane, 1-Cl-pentane and iso-Cl-propane, in clustering conditions. 71
3.13 Kinetic energy distributions and angular distributions acquired from the analysis of images shown in figure 3.12. 72
3.14 Mass spectra of a) the benzene clusters with the major $(Bz)_n^+$ ion series accompanied by series assigned to cluster fragmentation and b) the naphthalene clusters with marked series of mixed $(Np)_n.Ar_k^+$ clusters. 76
3.15 Example of mass spectra corresponding to pickup of (a,c) ethanol and (b,d) water on (a,b) naphthalene and (c,d) anthracene. 80
3.16 Mass spectrum of indene clusters with pickup of methanol. 81
3.17 Mass spectra of benzene clusters with molecular pickup of a) water, b) methanol and c) ethanol. The corresponding integrated intensities of selected mass series M_kH^+ and $Bz.M_k^+$ from pickup of d) water, e) methanol and f) ethanol. The graphs were taken and modified from [15]. 84
3.18 Mass spectra of adamantane seeded in a) helium, b) argon and after pickup of c) methanol. 86
3.19 Integrated intensities of selected mass series from adamantane clusters with pickup of methanol. 87
3.20 Mass spectra of adamantane clusters with pickup of a) ethanol and b) methylamine. 88
3.21 Detailed view on the the first three members of a) $(CH_3OH)_{1-3}H^+$, b) $(CH_3OD)_{1-3}D^+$ and c) $(CD_3OH)_{1-3}H^+$ mass series. 89

A.1 Scheme of regulated circuit for heating of nozzle and inline tube with Pt100 thermosensors and PID controllers. 121
A.2 A new system for remote control of NT230 UV OPO laser with automatic acquisition of action spectra. 122
A.3 A new system for remote control of NT230 UV OPO laser. The second tab with write and response terminals. Repetition rate must be set with +1 for external triggering. 122
A.4 A new full remote control over the DG generators. 123

List of Tables

2.1 Doppler effect in detection of the three selected fragments from our experiments in chapter 3. 46

3.1 Fitted kinetic energies of ground Cl fragments and corresponding experimental fractions, $f_I^{exp} = 1 - E_{tr}/E_{excess}$, and model estimations of internal excitation energy f_I^x after dissociation of the selected higher chloroalkanes. 60
3.2 Comparison of the apparent PAH cluster sizes, fragmentation and relative intensity of $(PAH)_n.Ar_k^+$ mixed clusters. 75
3.3 Table of performed pickup experiments with PAH clusters and molecular pickup. (1^{st} part) 78
3.4 Table of performed pickup experiments with PAH clusters and molecular pickup. (2^{nd} part) 79
3.5 Comparison of the relative pickup probabilities for hydrogen bonding molecules on benzene, naphthalene and indene. 82

A.1 Settings of DG01 for UV+IR experiments. 124
A.2 Settings of DG01 and DG02 for UV_{193}+UV experiments. 124

List of Abbreviations

- AIM: Apparatus for Imaging
- Ad: adamantane
- An: anthracene
- bMCP: back microchannel plate
- CI: conical intersection
- CLUB: Cluster Beam apparatus
- DG01/02: delay generator 01/02
- fMCP: front microchannel plate
- Ch: channel
- IC: ion counting
- i-C_3H_7Cl: isopropyl chloride
- In: indene
- IR: infrared
- ISC: intersystem crossing
- ISM: interstellar space medium
- IVR: internal vibrational energy redistribution
- Fl: fluoranthene
- fMCP: front microchannel plate
- FWHM: full width at half maximum
- KED: kinetic energy distribution
- M: molecular pickup
- MB: molecular beam
- MCP: microchannel plates
- MD: molecular dynamics
- MP: Montreal protocol
- MS: mass spectrometry
- n-C_3H_7Cl: n-propyl chloride

- n-$C_5H_{11}Cl$: n-pentyl chloride
- Np: naphthalene
- PAH(s): polyaromatic hydrocarbon(s)
- PC: pickup chamber
- PES(s): potential energy surface(s)
- Ph: phenanthrene
- PS: phosphor screen
- PSC(s): polar stratospheric cloud(s)
- Py: pyrene
- OPO: optical parametric oscillator
- R: alkyl fragment
- REMPI: resonance-enhanced multiphoton ionization
- rToF: reflectron time-of-flight spectrometer
- QMS: quadrupole mass spectrometer
- S_0: the ground state
- SC: source chamber
- SOC: spin-orbit coupling
- SOCv: vibrational-spin-orbit coupling
- SSC: spin-spin coupling
- ToF: time-of-flight
- TKER: total kinetic energy release
- TP: turbomolecular pump
- UV: ultraviolet
- VMI: velocity map imaging

List of publications

Molecular and cluster beams

1. Kateryna Grygoryeva, Jozef Rakovský, Ivo S. Vinklárek, Ondřej Votava, Michal Fárník, and Viktoriya Poterya. Vibrationally mediated photodissociation dynamics of pyrrole. *AIP Adv.*, 9(3):035151, 2019.

2. Ivo S. Vinklárek, Jozef Rakovský, Viktoriya Poterya, and Michal Fárník. Different dynamics of CH_3 and Cl fragments from photodissociation of CH_3Cl in clusters. *J. Phys. Chem. A*, 124(38):7633-7643, 2020.

3. Ivo S. Vinklárek, Jozef Rakovský, Viktoriya Poterya, and Michal Fárník. Clustering and multiphoton effects in velocity map imaging of methyl chloride. *Mol. Phys.*, 119(1-2):e1823507, 2021.

4. Ivo S. Vinklárek, Jiří Suchan, Jozef Rakovský, Kamila Moriová, Viktoriya Poterya, Petr Slavíček, and Michal Fárník. Energy partitioning and spin-orbit effects in the photodissociation of higher chloroalkanes. *Phys. Chem. Chem. Phys.*, 23:14340–14351, 2021.

5. Ivo S. Vinklárek, Andriy Pysanenko, Eva Pluhařová and Michal Fárník. Uptake of Hydrogen Bonding Molecules by Benzene Nanoparticles. Drafted and accepted: *J. Phys. Chem. Lett.*, 2022.

6. Andriy Pysanenko, Eva Pluhařová, Ivo S. Vinklárek, Jozef Rakovský, Viktoriya Poterya, Jaroslav Kočišek, and Michal Fárník. Ion and radical chemistry in $(H_2O_2)_n$ clusters. *Phys. Chem. Chem. Phys.*, 22:15312–15320, 2020.

7. Andriy Pysanenko, Ivo S. Vinklárek, Michal Fárník, and Viktoriya Poterya. Generation of $(H_2O_2)_n$ clusters on argon and ice nanoparticles. *Int. J. Mass Spectrom.*, 461:116514, 2021.

8. Robin Schürmann, Thomas F. M. Luxford, Ivo S. Vinklárek, Jaroslav Kočišek, Mateusz Zawadzki, and Ilko Bald. Interaction of 4-nitrothiophenol with low energy electrons: Implications for plasmon mediated reactions. *J. Chem. Phys.*, 153(10):104303, 2020.

9. Leo Sala, Barbora Sedmidubská, Ivo S. Vinklárek, Michal Fárník, Robin Schürmann, Ilko Bald, Jakub Med, Petr Slavíček, and Jaroslav Kočišek. Electron attachment to microhydrated 4-nitro- and 4-bromo-thiophenol. *Phys. Chem. Chem. Phys.*, 23:18173–18181, 2021.

Nanodomains in lipid membranes

1. Ivo S. Vinklárek, Lukáš Veĺas, Petra Riegerová, Kristián Skála, Ilya Mikhalyov, Natalia Gretskaya, Martin Hof, and Radek Šachl. Experimental evidence of the existence of interleaflet coupled nanodomains: An MC-FRET study. *J. Phys. Chem.*, 10(9):2024–2030, 2019.

Photophysics of tetrapyrrole molecules and light harvesting complexes

1. Ivo S. Vinklárek, Marek Scholz, Roman Dědic, and Jan Hála. Singlet oxygen feedback delayed fluorescence of protoporphyrin IX in organic solutions. *Photochem. Photobiol. Sci.*, 16:507–518, 2017.

2. Ivo S. Vinklárek, Till L. V. Bornemann, Heiko Lokstein, Eckhard Hofmann, Jan Alster, and Jakub Pšenčík. Temperature dependence of chlorophyll triplet quenching in two photosynthetic light-harvesting complexes from higher plants and dinoflagellates. *J. Phys. Chem. B*, 122(38):8834–8845, 2018.

3. Ivo S. Vinklárek, David Bína, Tomáš Malina, Aaron M. Collins, Radek Litvín, Jan Alster, and Jakub Pšenčík. Triplet state quenching of bacteriochlorophyllc aggregates in a protein-free environment of a chlorosome interior. *Chem. Phys.*, 529:110542, 2020.

A. Attachments

A.1 Applied Lasers

Four different lasers were operated in the VMI experiments. The UV photons from the excimer, UV OPO, and dye laser were applied for dissociation and photoionization. On the contrary, the radiation from the IR OPO laser was applied for vibrational excitation. In the following paragraphs, there are descriptions of the laser systems.

Dye Laser

Pulsed tunable dye laser (PULSARE, Fine Adjustment) is pumped by Q-switched Nd:YAG laser (SpitLight 1500, InnoLas Laser), which generates pulses at 1064 nm with repetition rate 10 Hz. The radiation at 1064 nm is used for the second harmonic generation of 532 nm, and both beams are guided into the dye laser. The 532 nm beam excites the DCM dye ($\sim$ 630 nm) in the oscillator (and preamplifier) cell, which is situated in the resonator build of the output coupler and the Litrow grating. The adjustment of the grating sets the precise lasing wavelength. The pulse from the dye resonator passes to the amplifier quartz cell, which is again pumped by 532 nm. The amplified beam is first doubled and then mixed with fundamental 1064 nm to generate the required wavelength around 243 nm. All the other wavelengths are filtered out by four Pellin–Broca prisms. The usual energy per pulse is between $1.0 - 3.0$ mJ and temporal FWHM is approximately 3 ns. The dye laser produces narrowband ($0.5\,\mathrm{cm}^{-1}$) radiation, which opens the discussion about the Doppler effect in chapter 2.4.3.

UV OPO Nd:YAG Laser

The UV optical parametric oscillator laser (UV OPO, NT230, Ekspla) tunable between 210 nm-2600 nm is pumped by the Q-switched Nd:YAG laser. The external trigger opens the Q-switch to generate a short and powerful pulse at a wavelength of 1064 nm, which is used for the generation of the second 532 nm and the third 355 nm harmonic. The 355 nm beam is used for pumping the optical parametric oscillator (OPO), which is possible to rotate to tune the wavelength in the range of 405 nm-2600 nm. The OPO output can also be used for second harmonic generation in the range of 210 nm-300 nm with energies per pulse between 0.5 mJ-1.5 mJ. The laser is remotely controlled by a LabView program (see A.3), enabling us to change the wavelength to acquire action spectra automatically. The UV OPO must be Q-switched. If no trigger comes within 5 µs after optimal timing of the the sync trigger at 1061 µs, the laser automatically emits a pulse.

Excimer Laser

The excimer laser (Coherent) is used for photodissociation and non-resonant ionization by pulses at 193 nm, which are generated by ArF mixture pumped by discharge running with the frequency up to 400 Hz. The energy per pulse at the

laser output of the non-polarized beam is around 9.5 mJ. In the case of VMI experiments, the laser beam is polarized by a thin-film polarizer with a compensator oriented in Brewster angle designed for the wavelength of 193 nm. The excimer laser cannot be precisely triggered, contrary to the two previously Q-switched lasers, and therefore, its sync output must be used as a trigger for the other lasers.

IR OPO Nd:YAG Laser

The tunable IR OPO laser is pumped by the second harmonic 532 nm from seeded Q-switched Nd:YAG laser running with a repetition rate up to 10 Hz. The radiation is further amplified in the OPA crystal pumped by the Nd:YAG laser fundamental at 1064 nm. Either idler or signal from OPA is selected by rotation of two silica wafers under Brewster angle. The laser output can be tuned in range of $4300 - 7400\,\mathrm{cm}^{-1}$ (OPA signal) and $2000 - 5100\,\mathrm{cm}^{-1}$ (OPA idler), and its bandwidth is around $< 4\,\mathrm{cm}^{-1}$. The OPO output is calibrated by characteristic lines of neon lamp.

A.2 Nozzle and Tube Circuit Diagram

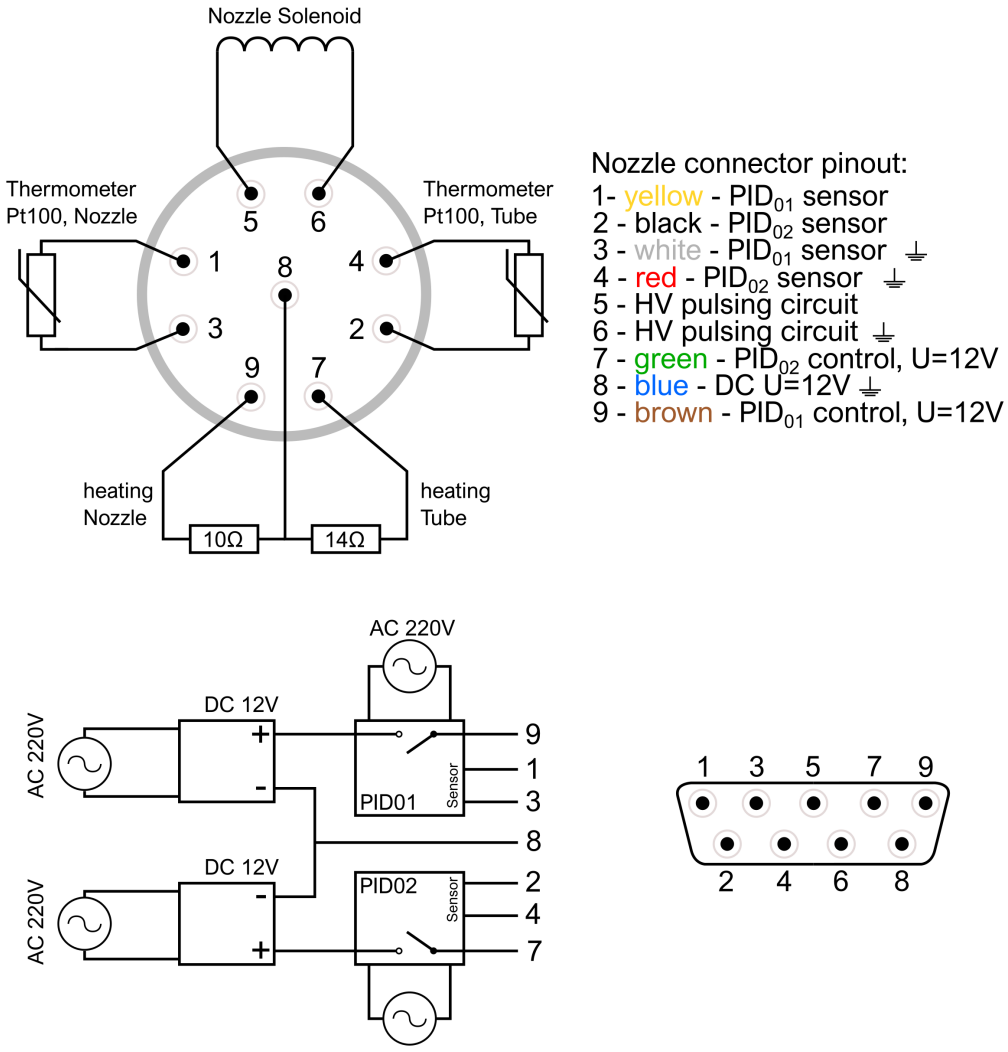


Figure A.1: Scheme of regulated circuit for heating of nozzle and inline tube with Pt100 thermosensors and PID controllers.

A.3 NT230 UV OPO Laser LabView Controller

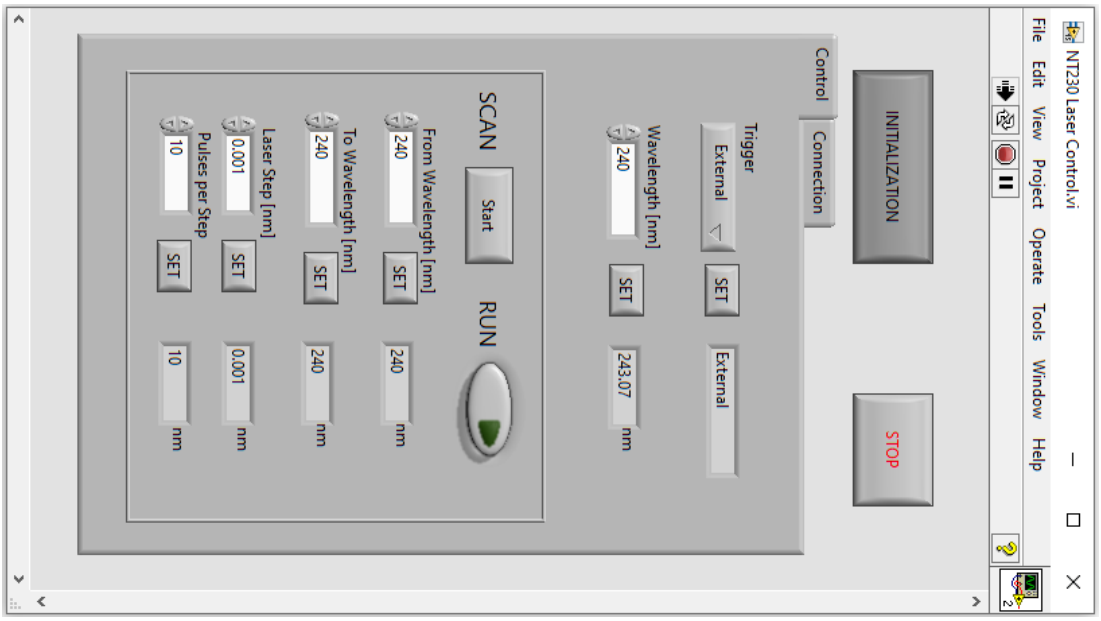


Figure A.2: A new system for remote control of NT230 UV OPO laser with automatic acquisition of action spectra.

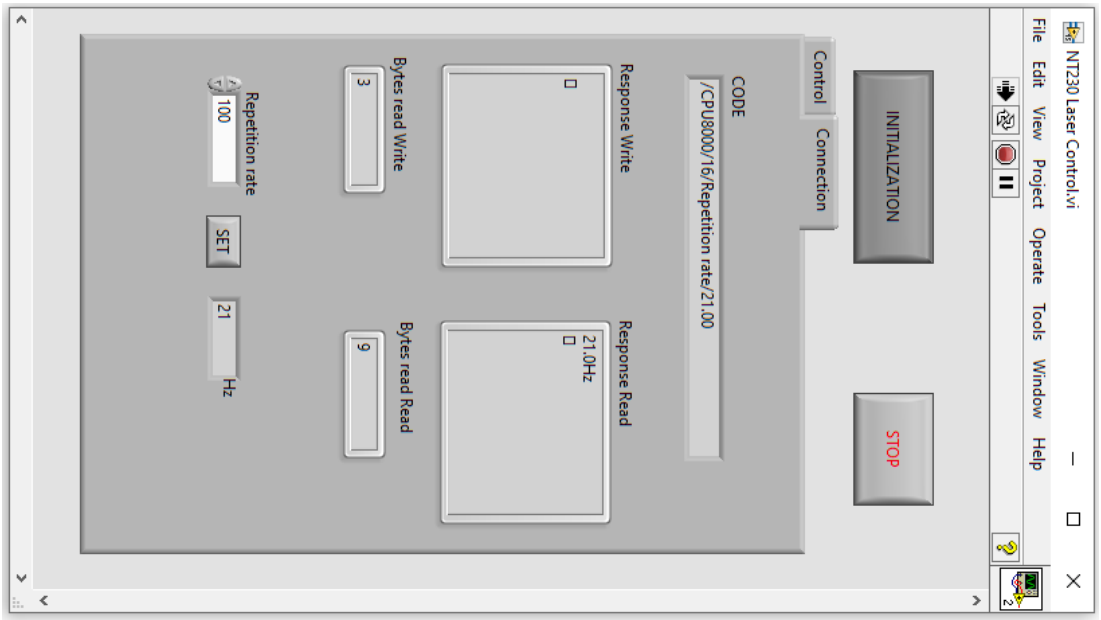


Figure A.3: A new system for remote control of NT230 UV OPO laser. The second tab with write and response terminals. Repetition rate must be set with +1 for external triggering.

A.4 Delay Generators LabView Controller

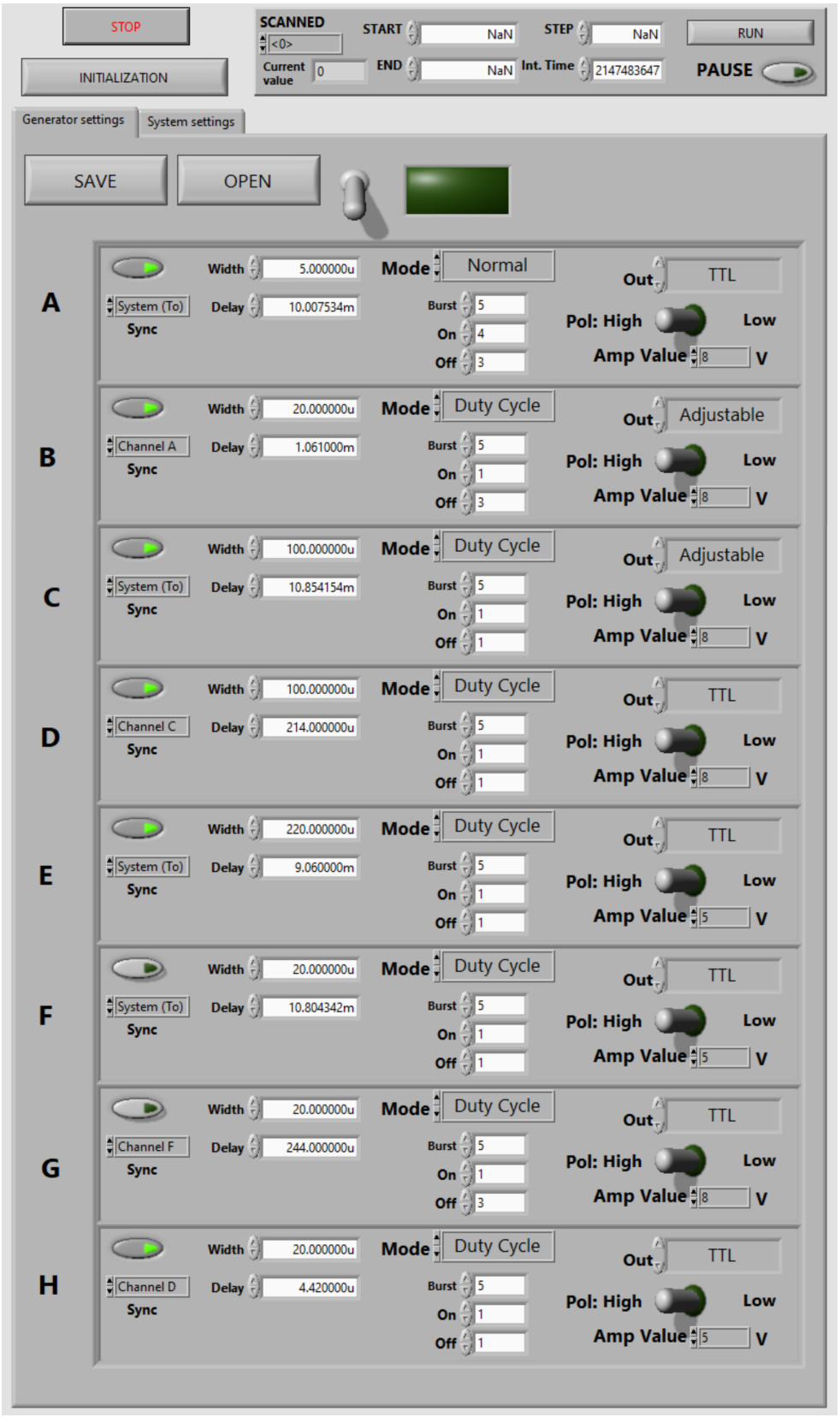


Figure A.4: A new full remote control over the DG generators.

A.5 Delay Generators Settings

Delay Generators **01** Settings						
Channel	sync	Width µs	Delay ns	Output	Mode	Connectors
A	T0	5	10 007 534	TTL Act. High	Normal	UV OPO sync
B	ChA	1	1 061 000	TTL Act. High	DC 1:1	UV OPO Q-switch LED
C	T0	100	10 854 134	Adjustable Act. High 8 V	DC 1:1	Dye sync PC
D	ChC	100	214 000	TTL Act. High	DC 1:1	Dye Q-switch
E	T0	220	99 000 000	TTL Act. High	DC 1:1	Nozzle
F	T0	20	10 804 350	TTL Act. High	DC 1:1	IR OPO sync
G	ChF	20	244 000	Adjustable Act. High 8 V	DC 1:3	IR OPO Q-switch PC
H	ChB	20	622	TTL Act. High	DC 1:1	Gate

Table A.1: Settings of DG01 for UV+IR experiments.

Delay Generators **02** Settings, Triggered by UV excimer						
Channel	sync	Width µs	Delay ns	Output	Mode	Connectors
A	T0	80	2485	TTL Act. High	Normal	UV OPO sync
B	ChA	5	135	Adjustable Act. High 8 V	Normal	UV OPO Q-switch LED
C	ChB	20	4032	TTL Act. High	Normal	Gate
D	ChB	100	214 000	TTL Act. High	DC 1:1	TOF osc.
Delay Generators **01** Settings						
H	T0	20	93 000 034	TTL Act. High	DC 1:1	UV exc.

Table A.2: Settings of DG01 and DG02 for UV_{193}+UV experiments.

B. Reprints of Author's Publication

Publication III. and V. are attached as manuscripts due to copyright policy of the journals.

B.1 Publication I

Title: **Vibrationally mediated photodissociation dynamics of pyrrole**

Journal: *AIP Advances*
DOI: `https://doi.org/10.1063/1.5091974`

Supporting Information

Note: Published in *AIP Advances* with open access.

AIP Advances ARTICLE scitation.org/journal/adv

Vibrationally mediated photodissociation dynamics of pyrrole

Cite as: AIP Advances 9, 035151 (2019); doi: 10.1063/1.5091974
Submitted: 7 February 2019 • Accepted: 12 March 2019 •
Published Online: 28 March 2019

View Online Export Citation CrossMark

Kateryna Grygoryeva,[a] Jozef Rakovský, Ivo S. Vinklárek,[b] Ondřej Votava, Michal Fárník,[c] and Viktoriya Poterya[c]

AFFILIATIONS

J. Heyrovský Institute of Physical Chemistry v.v.i., Academy of Sciences of the Czech Republic, Dolejškova 3, 18223 Prague, Czech Republic

[a]**Also at:** Department of Physical Chemistry, University of Chemistry and Technology, Technická 5, Prague 6, Czech Republic
[b]**Also at:** Faculty of Mathematics and Physics, Charles University, Ke Karlovu 3, 121 16 Prague 2, Czech Republic
[c]**Corresponding authors. E-mail:** michal.farnik@jh-inst.cas.cz and viktoriya.poterya@jh-inst.cas.cz

ABSTRACT

We investigate photodissociation of vibrationally excited pyrrole molecules in a velocity map imaging experiment with IR excitation of N–H bond stretching vibration $v_1 = 1$, ν_{IR}= 3532 cm^{-1}, and UV photodissociation at λ_{UV}= 243 nm. In the IR+UV experiment, the H-fragment signal is enhanced with respect to the 243 nm UV-only photodissociation due to a more favorable Franck-Condon factor for the vibrationally excited molecule. In the measured H-fragment kinetic energy distribution, the maximum of the fast peak in the IR+UV experiment is shifted by 0.23 eV compared to the UV-only photodissociation which corresponds to 53 % of the vibrational energy deposited into the fragment kinetic energy. We compare our results with an isoenergetic UV-only photodissociation at λ_{UV}= 224 nm. About 72 % of the total available energy, is released into the fragment kinetic energy in the IR+UV experiment, while it is only 61 % in the UV-only photodissociation. This can be substantiated by the coupling of the N–H bond stretching vibration into the kinetic energy of the departing H-fragment. We also probe the time-dependent dynamics by a nanosecond pump-probe experiment. The IR excitation enhances the N–H bond dissociation even when the UV photodissociation is delayed by 150 ns. This enhancement increases also the yield of the fast fragments at the position of the peak corresponding to the IR+UV excitation, i.e. even 150 ns after the IR vibrational excitation, the same amount of the IR excitation energy can be converted into the H-fragment velocity as immediately after the excitation.

© 2019 Author(s). All article content, except where otherwise noted, is licensed under a Creative Commons Attribution (CC BY) license (http://creativecommons.org/licenses/by/4.0/). https://doi.org/10.1063/1.5091974

I. INTRODUCTION

Pyrrole C_4H_5N is a simple five-membered ring heteroaromatic molecule, representing an example of UV-active chromophore in such biomolecules as hemes and chlorophylls. Thus investigation of the excited electronic state dynamics of pyrrole provides the first step in a molecular level understanding of deactivation processes and photostability in more complex biomolecules. Besides, pyrrole represents a paradigm system for studying the role of $\pi\sigma^*$ excited states in molecular photochemistry.[1–4] Therefore, it has attracted large attention of both experimentalists and theoreticians over the past decades: a significant number of UV-photodissociation experiments[2,3,5–17] was complemented by theoretical calculations of the excited electronic states.[18–23] Most of the above investigations dealt with the N–H bond photodissociation in pyrrole, which is the topic of our present work as well.

From these investigations, the following picture of the potential energy landscape emerged: the first excited $\pi\sigma^*$ state, $^1A_2$, lying about 5 eV (λ ~250 nm) above the ground state, has a repulsive character along the N–H coordinate. A shallow minimum in the Franck-Condon region of this state is separated by a small barrier from the repulsive part of the potential.[17,18] The second singlet state $^1B_1$ lies about 1 eV higher (at λ ~200 nm) and exhibits a similar $\pi\sigma^*$ character.[17,18,24] Both $\pi\sigma^*$ states are dark states with small absorption cross sections of ~10^{-20} cm^2. A bright $\pi\pi^*$ state at about 6.6 eV (~188 nm)[25] is bound along the N–H coordinate. An important feature of all these states are conical intersections (CI) on the multidimensional potential hypersurface, which open various routes

for population funneling into the ground electronic state S_0. A cut through the potential energy hypersurface along the N–H coordinate is shown in Fig. 1 for illustration. Our schematic picture is based on published potentials.[26]

The CI between the first dissociative $\pi\sigma^*$ state and S_0 is of prime importance for the N–H bond dissociation dynamics. However, various investigations suggested that further CIs between different states exist along the coordinate corresponding to an out-of-plane deformation of the pyrrole ring.[7,9,13,18,19] These CIs connect the bound excited $\pi\pi^*$ state with the dissociative $\pi\sigma^*$ states and with the ground S_0 state, thus opening different dissociation pathways even from the $\pi\pi^*$ state (see, e.g. Fig. 5 in Ref. 19).

At photon energies relevant to our present investigation, the following N–H bond dissociation dynamics can be drawn from previous studies: Upon the excitation to the first $\pi\sigma^*$ ($^1A_2$) state at $\lambda \approx 240$–236 nm, just above the barrier, the dissociation proceeds along the N–H coordinate to a CI with the ground state S_0 where the reaction routes split. Quick diabatic passage through the CI yields H-fragments with high kinetic energy and pyrrolyl fragments in the ground electronic state. Internal conversion from the $\pi\sigma^*$ state into the ground state and subsequent statistical decay from S_0 leads to slow H-fragments with a broad statistical character of energy distribution. Alternative mechanisms were proposed for the slow H-atoms generation, e.g. adiabatic dissociation on the S_1 state,[27] relaxation in the excited state,[28] or multiphoton dissociation of C–H bonds.[5–7] The timescale for the fast dissociation via the $\pi\sigma^*$ state is 35 fs.[17] At lower photon energies, the process is slowed down by tunneling through the barrier on a timescale longer then ~130 fs.[16,17] At shorter wavelengths, the total kinetic energy release (TKER) spectra show similar bimodal distributions with an increase in the intensity of the slow H-atoms compared to the fast ones. This can be rationalized by the involvement of other excited states and CIs through which the population can be funneled into the ground state. Here, the energy can be randomized and the molecules dissociate statistically.[7,9,13,19]

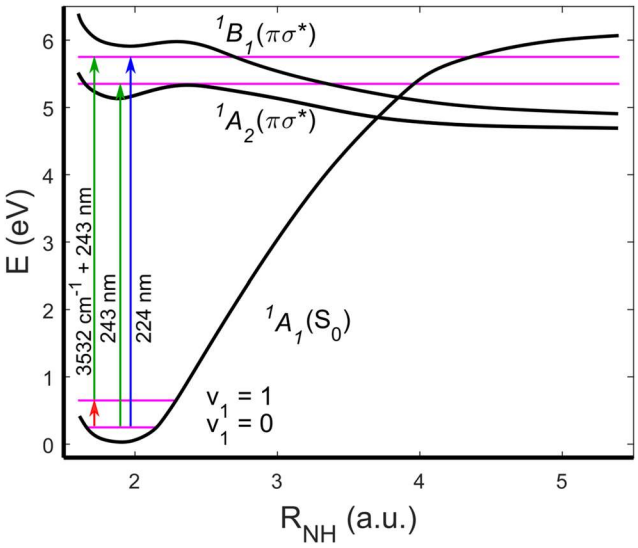


FIG. 1. Schematic picture of the cut through the relevant potential energy surfaces of pyrrole along the N–H coordinate.[26] The arrows correspond to our IR+UV excitation (left, red and green arrows), 243 nm UV-only (center, green arrow), and 224 nm UV excitation isoenergetic with the IR+UV experiment (center, blue arrow).

Vibrationally mediated photodissociation (VMP) represents an useful experimental tool that provides some additional information to the single photon experiments.[29] Fruitful insights can follow from a comparison of two-step IR+UV photodissociation with an isoenergetic, single UV-photon dissociation. The IR vibrational excitation can lead to an increase in the photodissociation cross section by orders of magnitude due to favorable Franc-Condon overlaps of the vibrationally excited states, it also can change the photofragment branching ratios etc.[30–34] VMP of pyrrole at $\lambda = 243$ nm was investigated using stimulated Raman scattering and compared to results of photoacoustic Raman spectroscopy.[35] Pivotal to the VMP processes are the intramolecular vibrational redistribution (IVR) processes.[36]

Recently, we have introduced an IR+UV experiment in our laboratory.[37,38] Here we exploit it to investigate the VMP of pyrrole molecules: we IR-excite the N–H stretch at 3532 cm^{-1} and UV-dissociate the N–H bond at 243 nm; then we detect the H-fragments using velocity map imaging (VMI). The H-fragment kinetic energy distributions from our experiments are compared to previous single UV-photon dissociation experiments at comparable excitation energies.[9] Finally, we introduce a time delay between IR and UV pulses, which provides information about the IVR dynamics.

II. EXPERIMENT

Vibrationally mediated photolysis of pyrrole molecules was studied using an Apparatus for IMaging (AIM) previously described elsewhere.[37–39] Helium buffer gas with an admixture of pyrrole vapor at a reservoir temperature of 5°C was introduced into a vacuum by a supersonic expansion through a pulse valve with a repetition frequency of 10 Hz and a nozzle diameter of 0.6 mm. At 1 bar expansion pressure of helium, the mixture contained about 0.28 % of pyrrole. The skimmed molecular beam entered a reaction chamber where it was intersected at right angles by counter-propagating linearly polarized IR and UV laser beams. The H^+ photoproducts were extracted by ion optics in a configuration by Eppink and Parker[40] for velocity mapping. Ions were detected by a position sensitive channel plate and phosphor screen assembly. Velocity map images were recorded by a CCD camera and further processed with a Labview program which involved a centroiding method. Each image was obtained by scanning the UV laser over a Doppler broadened absorption line of hydrogen. A 3D velocity distribution was reconstructed by applying an inverse Abel transform[41] to the 2D product image. Standard integration procedures[42] were used to obtain kinetic energy distributions (KEDs) and angular distributions, and the energies were calibrated using reference HBr images.

Tunable IR radiation was generated in an OPO/OPA system (Laser Vision). The output IR pulse of energy up to 20 mJ was tuned to the wavelength corresponding to the N-H stretch vibration of pyrrole and focused by a lens with a focal length of 25 cm. The laser polarization was perpendicular to the plane of the detector. UV pulses were generated by a frequency sum of a tunable dye laser (Fine Adjustment) pumped by a Nd:YAG laser (Innolas) with the pump laser fundamental. The output photons of 243 nm were used to dissociate the molecules and also to ionize H fragments in a (2+1)

© Author(s) 2019

resonance-enhanced multiphoton ionization (REMPI) scheme. The UV-pulse energy was kept low below 1 mJ/pulse to avoid multiphoton processes. The laser polarization was parallel to the face of the imaging detector. The beam was focused by a lens with a 35 cm focal length. The lasers were spatially overlapped, and their time delay was varied using a delay generator BNC 575.

The repetition rate of the IR laser was half of the UV laser repetition (10 Hz). This setup allowed measuring alternately the UV and IR+UV photodissociation. An action spectrum of pyrrole was produced by scanning the output of the OPO-OPA laser in the region of 3513–3555 nm at a constant wavelength of the UV laser and by monitoring the total H^+ signal. The observed position of the vibrational excitation for the N–H stretch band center agreed well with the frequency measured previously by vibrationally mediated photodissociation[35] and FTIR spectroscopy.[43] Also dependencies of the H^+ signal intensity on the powers of both UV and IR lasers were measured (see supplementary material.).

The UV-only photodissociation at λ_{UV}= 224 nm was measured with a UV-OPO laser (EKSPLA NT-230). The laser was synchronized with the 243 nm laser for the H-fragment REMPI. The two laser beams were focused and overlapped in the VMI center with the molecular beam as above. The scanning and evaluation procedures were the same as in the case of the IR+UV experiment. A laser energy of 0.5 mJ was used in the present experiment at 224 nm.

III. RESULTS AND DISCUSSION

A. IR+UV excitation of pyrrole

Velocity map images of H-fragments from pyrrole photodissociation are shown in Fig. 2. The part (a) of the left image corresponds to pyrrole photodissociation with UV photons at λ_{UV}= 243 nm. The part (b) shows an image from IR+UV photodissociation at an IR frequency corresponding to the N–H bond excitation, ν_{IR}= 3532 cm^{-1}. The right panel (c) shows an image obtained after subtraction (b)–(a). It is clear, already from these raw images, that the IR vibrational excitation substantially increases the overall yield of H-fragments. Qualitatively, all these images consist of two contributions: an isotropic feature in the middle corresponding to slow statistical H-fragments, and fast fragments originating from transitions of essentially perpendicular character.

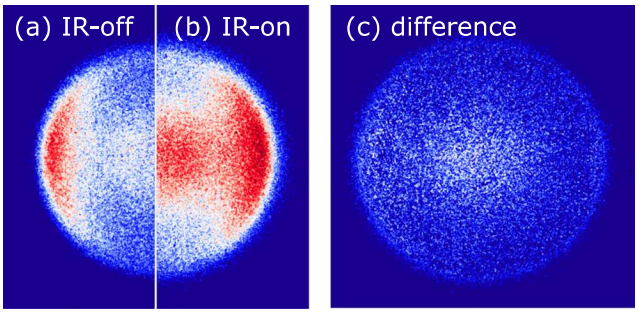


FIG. 2. Hydrogen fragment raw images from pyrrole VMI experiment: (a) UV photodissociation and H-atom REMPI ionization at λ_{UV}= 243 nm; (b) IR vibrational excitation of N–H bond at ν_{IR}= 3532 cm^{-1}. The right image (c) corresponds to the difference [(UV+IR)-(UV-only)].

These two features are clearly separated in the H-fragment KEDs shown in Fig. 3. Top panel (a) corresponds to the UV photodissociation of pyrrole at λ_{UV}= 243 nm. Similar spectra were obtained and discussed in many previous experiments at the same and similar UV wavelengths.[6–9,12,13,16] Only the first $\pi\sigma^*$ state $^1A_2$ can be reached at λ_{UV}= 243 nm. The major peak in KED with a maximum at 0.81 eV (6533 cm^{-1}) corresponds to the direct dissociation along the diabatic passage on the dissociative $\pi\sigma^*$ surface. There is a small contribution of relatively slow H-fragments which was previously assigned to various possible processes described in the introduction: internal conversion at CI from the $\pi\sigma^*$ state into the ground state and subsequent statistical decay from S_0; adiabatic dissociation on the S_1 state;[27] relaxation in the excited state;[28] or multiphoton dissociation including also C–H bond dissociations.[5–7] No matter what the origin of these slow H-fragments is, their contribution is very small under our experimental conditions (e.g., we were careful to avoid UV multiphoton processes (supplementary material)).

Panel (b) of Fig. 3 shows a KED of H-fragments from IR+UV photodissociation of pyrrole at ν_{IR}= 3532 cm^{-1} (v_1 = 1). It exhibits essentially the same features as panel (a), only the fast peak is

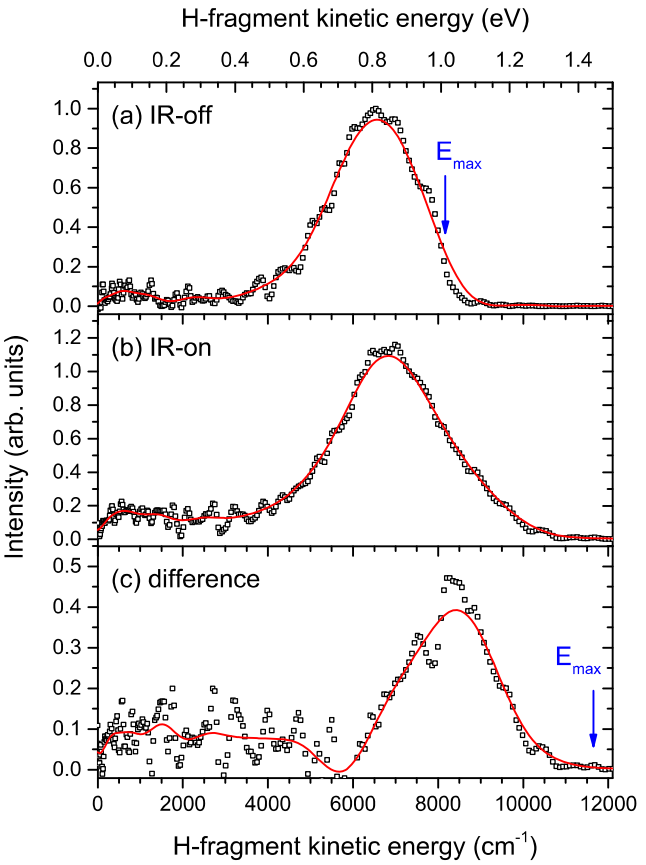


FIG. 3. The H-fragment kinetic energy distributions from VMI experiment presented in Fig. 2. Top panel (a) corresponds to UV photodissociation of pyrrole at λ_{UV} = 243 nm; (b) IR+UV photodissociation at ν_{IR}= 3532 cm^{-1}; (c) difference [(UV+IR)-(UV-only)]. Blue arrows denote the maximum available energy (see text for details).

© Author(s) 2019

broader, and there is a somewhat higher contribution of slow fragments. This is quantitatively documented in panel (c) where the difference between the two spectra (b)–(a) is shown. The spectrum exhibits the bimodal character of fast and slow H-fragments. A notable difference is the substantially higher mean energy of the fast fragments – the maximum is shifted to 1.04 eV (8420 cm^{-1}).

The total energy available for the kinetic energy of the fragments in the photodissociation process can be calculated as

$$E_{avl} = E_\lambda + E_i - D_0 - E_i', \quad (1)$$

where E_λ is the exciting photon energy, D_0 is the N–H bond dissociation energy, E_i is the internal excitation of the parent molecule and E_i' is the internal excitation of the pyrrolyl fragment.

The UV photon energy at λ_{UV} = 243 nm corresponds to E_λ = 5.10 eV. The experimentally determined N–H dissociation energy is D_0 = 4.07 eV (32850 cm^{-1}).[9] In supersonically cooled expansions, the rotational temperature is typically very low, and the internal excitation E_i can be identified with the vibrational excitation of the pyrrole molecule. Assuming no internal excitation of pyrrole, E_i = 0 eV, the maximum available energy which can be released into the kinetic energy of photodissociation fragments is $E_{avl}(UV)$ = 1.03 eV (8292 cm^{-1}), provided that pyrrolyl fragment is formed in its ground state with v′ = 0, E'_i = 0 eV. In the case of IR vibrationally excited pyrrole, E_i = 0.44 eV (3532 cm^{-1}), the corresponding total available energy is $E_{avl}(IR + UV)$ = 1.47 eV (11824 cm^{-1}).

The available kinetic energy is distributed between H and pyrrolyl co-fragments in an inverse ratio of their masses; i.e. for H fragments, the maximum kinetic energies are E_{max} = 1.01 eV (8169 cm^{-1}) and 1.44 eV (11648 cm^{-1}) for UV-only and IR+UV photodissociation, respectively. These values represent the expected cut-off of KEDs assuming no internal excitation of the pyrrolyl fragment, and they are marked by blue arrows in the spectra in Fig. 3.

In case of UV-only photodissociation, Fig. 3 (a), the KED cut-off agrees well with E_{max} confirming the assumption of no initial internal pyrrole excitation E_i = 0 eV. The maximum of the fast peak (smoothed curve) of the hydrogen KED gives a value of E_P = 0.81 eV (6533 cm^{-1}). The corresponding total kinetic energy release is calculated by multiplying E_P by the pyrrole to pyrrolyl mass ratio $E_T = E_P \times 67/66$. Thus, the energy deposited into the internal (vibrational and rotational) excitation of pyrrolyl fragment is $E_i' = E_{avl} - E_T$ = 0.21 eV (1662 cm^{-1}). In case of IR+UV photodissociation in Fig. 3 (c) where the UV-only processes were subtracted, the maximum of the fast peak is at 1.04 eV (8421 cm^{-1}). The corresponding internal excitation of pyrrolyl radical is E_i' = 0.41 eV (3276 cm^{-1}). We also can quantify the vibrational energy redistribution after the photodissociation. With the IR excitation, the fast peak position shifts by 0.23 eV in comparison to the UV-only photodissociation. This means that approximately 53 % of the additional IR-photon energy is converted into the fragment kinetic energy, while the rest goes into the internal pyrrolyl excitation.

So far, we have exploited the information about the energetics of the investigated processes. Additionally, the VMI experiment contains information about the angular anisotropy of the fragment distribution. From the images in Fig. 2, angular distributions were obtained (supplementary material) and fitted by a standard procedure,[42] yielding the anisotropy parameter β. For UV-only photodissociation, the fast channel yields $\beta = -0.7 \pm 0.1$, in agreement with predominantly perpendicular transition at 244 nm dissociation showed by Cronin et al.[9,44] In the IR+UV photodissociation, the fast channel anisotropy barely changes within the experimental error, $\beta = -0.6 \pm 0.3$. For the slow fragments, the corresponding signal is very low, thus the β-parameter could not be determined reliably from our data, yet the images in Fig. 2 suggest an isotropic distribution of the slow fragments in agreement with their statistical origin.

A notable feature of our IR+UV images as already mentioned above, is the significantly higher H-fragment yield in comparison with the UV-only photodissociation. The increase of the total H-yield caused by the vibrational excitation of pyrrole was also previously observed by Epshtein et al.[35] Here we can compare the IR induced yield enhancement of the fast and slow statistical fragments, Fig. 3 (c). Both components of the KED spectra are enhanced by the N–H stretch vibration. The enhancement can be qualitatively justified by the schematic picture of potentials in Fig. 1. Upon the UV-only photodissociation, the excitation proceeds from the center of the bottom S_0 potential, where the v_1 = 0 state wavefunction has its maximum. The corresponding Franck-Condon overlap with the final state wavefunctions is not favorable for the transition. Upon the IR excitation, the character of the initial state wavefunction changes, and transition from the compressed N–H bond has better Franck-Condon overlap with the excited state, leading to the higher overall H-fragment yield.

B. Comparison of IR+UV with isoenergetic UV-only experiments

To reveal the mode-specificity of the deposited/released energy, which is inherently connected with the IVR processes, we compare our IR+UV photodissociation with single photon photodissociation at $\lambda_{UV} \approx 224$ nm in Fig. 4. The position of the fast peak maximum in the IR+UV experiment is at 1.04 eV, while it is at 0.89 eV in the 224 nm photodissociation KED. Thus it is clearly shifted by 0.15 eV towards higher energies in the IR+UV excitation compared to the isoenergetic UV-only photodissociation.

The total kinetic energy release E_T derived as outlined above from the fast peak maximum position in the IR+UV experiment can be compared to the total available energy E_{avl}. The ratio $E_T/E_{avl} \approx 0.72$ corresponds to the fraction of available energy deposited into the fragments kinetic energy. The rest, about 28 %, goes into the internal excitation of the pyrrolyl fragment. In the case of UV-only photodissociation at 224 nm, only 61 % of the total available energy goes into the fragment kinetic energy, and 39 % is deposited into the pyrrolyl fragment excitation. Thus, in the IR+UV experiment, the available energy is converted more efficiently into the fragment kinetic energy than in an isoenergetic UV photodissociation. In other words, the excited N–H vibration couples efficiently into the bond dissociation and fragment kinetic energy.

In our experiments, the relative contribution of the slow H-fragments seems to be somewhat higher in the UV-only photodissociation compared to IR+UV. However, a quantitative comparison is difficult due to the low signal-to-noise ratio of the KEDs (note that they correspond to the difference images), different photon fluxes in the experiments, and especially the high sensitivity of the slow contribution to multiphoton processes demonstrated in supplementary material.

© Author(s) 2019

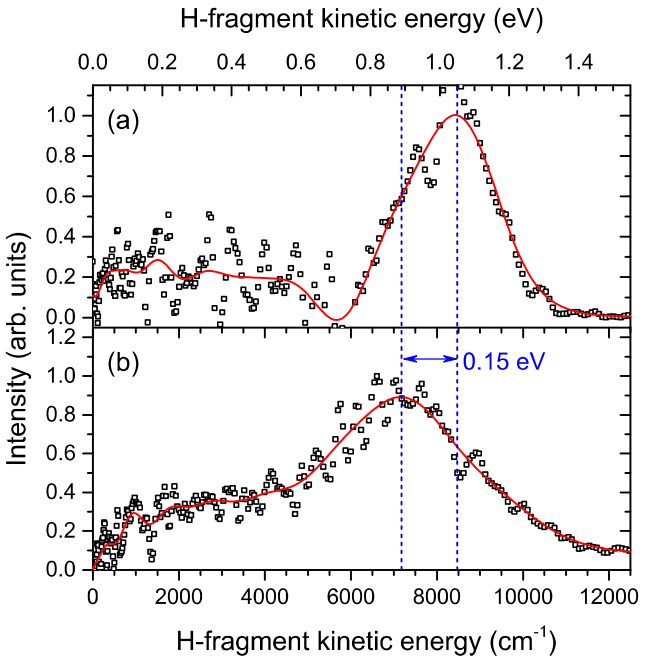


FIG. 4. Comparison of (a) IR+UV photodissociation (λ_{UV}= 243 nm, ν_{IR}= 3532 cm^{-1}), with (b) isoenergetic UV-only photodissociation at λ_{UV}= 224 nm. The spectra correspond to the difference images, where the 243 nm images were subtracted. Vertical lines correspond to the maximum positions displayed by 0.15 eV as indicated.

We can also compare our data to the spectra of Cronin at al.[9] measured at photon wavelengths λ_{UV} = 228 nm and 220 nm, just around 224 nm. They posses resolvable structure in the fast peak, however, for the sake of comparison with our low-resolution spectra, we discuss only the central position of the band corresponding to the fast fragments. At λ_{UV} = 228 nm, E_T corresponds to approximately 7700 cm^{-1} (0.95 eV), and the total available energy E_{avl} = 1.37 eV. Thus about 70 % of E_{avl} goes into the fragment translation. At λ_{UV} = 220 nm, the central position of the fast fragment peak corresponds to $E_T \approx$ 7000 cm^{-1} (0.87 eV) and E_{avl} = 1.56 eV, thus only about 56 % is deposited into the fragment translation. Our value of 61 % at λ_{UV} = 224 nm is in between these values as expected.

The spectra of Cronin et al.[9] also exhibit a higher ratio of slow vs. fast fragments compared to our IR+UV spectrum. This is in agreement with our qualitative scenario suggested above: The excitation from the vibrationally excited v_1 = 1 state proceeds closer to the turning point on the ground state potential, while the UV-only excitation to the same excited state from v_1 = 0 proceeds rather from the minimum position of the ground state potential, Fig. 1. Thus the excitation from v_1 = 1 state lands on the excited state potential surface in a point with a larger gradient towards the N–H dissociation. This can lead to a faster diabatic passage through the conical intersection region yielding the fast H-fragments. At the same time, the internal conversion to the ground state in CI, yielding the slow statistical fragments, is less probable in the IR+UV experiment.

Concerning the slow fragments, it is worth noting that their relative contribution is very sensitive to both IR and UV laser powers, as demonstrated in supplementary material. If the slow peak is caused by an internal conversion to the ground state via conical intersections, an interesting possibility can be considered that this crossing is influenced by external laser fields facilitating the crossing to the ground state. However, we cannot provide any further experimental evidence for this scenario, and it is mentioned here as a possibility for future exploration.

C. Time dynamics

To further investigate the excited state dynamics, we have employed a nanosecond pump-probe experiment in analogy to our previous studies.[37,38] The dependence of the H-fragment KED on the delay between the IR and UV laser pulses is shown in Fig. 5. Each panel shows the difference spectra obtained after the subtraction of UV-only spectra from IR+UV spectra. Note that the spectra in Fig. 5 exhibit a higher contribution of slow statistical fragments compared to Fig. 3 (c). This is due to higher IR photon fluxes. We had to employ higher IR laser intensities in the experiments with the time delay to obtain a better signal-to-noise ratio. It leads to a higher yield of the slow statistical H fragments as demonstrated in

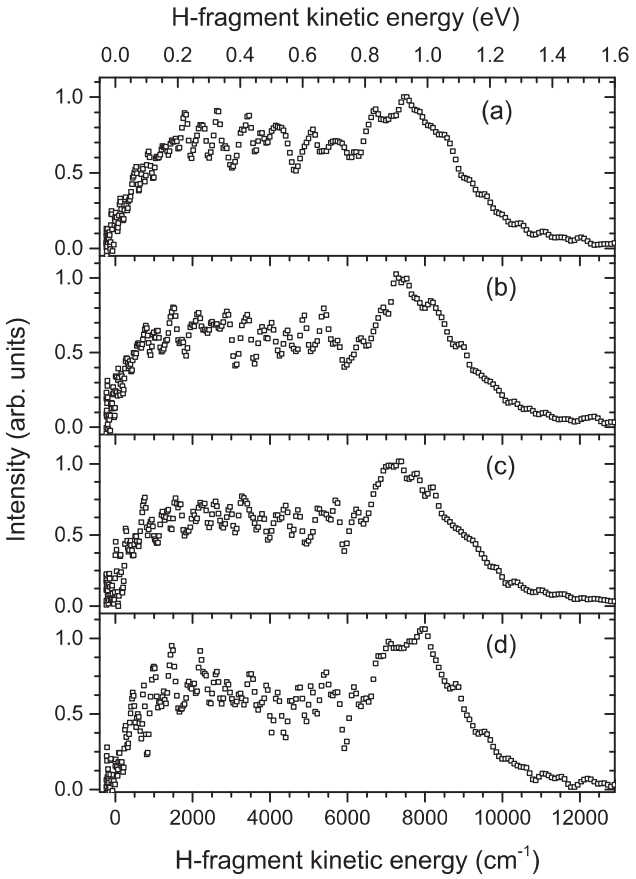


FIG. 5. Delay dependence of the H-fragment KED spectra from IR+UV photodissociation of pyrrole. The delay between IR vibrational excitation and subsequent UV photodissociation was: (a) 0 ns; (b) 50 ns; (c) 100 ns; (d) 150 ns; as determined from detected laser light pulses.

© Author(s) 2019

supplementary material. Nevertheless, the fast H-fragments due to quick diabatic dissociation following the IR+UV excitation as discussed above does not seem to be influenced significantly by the multiphoton processes.

There is no significant qualitative difference (within our experimental error) between the spectra measured with different IR+UV delays up to 150 ns. Indeed, the IVR process within the molecule can be very fast, however, the excitation remains in various degrees of freedom of the molecule for a long time so that it enhances the UV photodissociation of the molecule even after 150 ns. This is consistent with the experimental observations of Epshtein et al., who reported lifetimes of more than 50 ns.[35] We additionally observe that the energy partitioning does not change within the 150 ns, and the same amount of energy is converted into H fragment translations after 150 ns. The IR vibrational excitation can cause an enhancement of the statistical H-fragments in the UV photodissociation following long after the IR excitation, assuming that the original IR excitation has been redistributed over the various degrees of freedom of the molecule via an IVR process. Nevertheless, our experiment demonstrates also an enhancement of the fast H-fragments with kinetic energies, that correspond to the IR+UV experiment where the photodissociation follows the IR excitation immediately. In addition, the shape of the fast peak suggests a non-statistical energy distribution.

IV. CONCLUSIONS

We investigate the photodissociation of vibrationally excited pyrrole in a VMI experiment with IR+UV excitation at ν_{IR}= 3532 cm^{-1} and λ_{UV}= 243 nm (ν_{UV}= 41142 cm^{-1}). The IR excitation corresponds to the N–H bond stretching vibration. We also provide a comparison with UV-only photodissociation at λ_{UV}= 224 nm (44674 cm^{-1}), which corresponds to the sum of our IR+UV photon energy.

In IR+UV experiments, the total H-fragment signal is enhanced with respect to the UV-only photodissociation. This is substantiated by a qualitative picture where excitation from vibrationally excited ground state wavefunction has a more favorable Franck-Condon overlap with the excited state wavefunction.

In terms of energetics, the fast peak in our IR+UV experiment is shifted by 0.23 eV towards higher energies with respect to the fast peak in UV-only 243 nm photodissociation. On average, about 53 % of the energy deposited into the N–H vibration is converted into the fragment kinetic energy (the rest goes into the internal excitation of the pyrrolyl fragment).

Further, we compared our IR+UV experiment with isoenergetic UV-only photodissociation. In the IR+UV experiment, 72 % of the total available energy is deposited into the fragments kinetic energy, while 28 %, goes into the internal excitation of the pyrrolyl fragment. In the UV-only photodissociation the available energy is distributed between the kinetic and internal energy in fractions 61 % and 39 %, respectively. A simple explanation is that the IR excitation of the N–H bond prior to the UV photodissociation couples more efficiently into the kinetic energy of the departing H-fragment compared to the case when the whole energy is deposited into the molecule by a single UV photon.

Finally, we probed the dynamics by a nanosecond pump-probe IR+UV experiment, and observed an enhancement in the N–H bond dissociation even when the UV pulse was delayed by 150 ns. This is consistent with the experimental observations of Epshtein,[35] who reported lifetimes of vibrational excitation longer than 50 ns. Moreover, our experiments provide also information about the kinetic energy of the enhanced H-fragments: the delayed photodissociation yields also the fast H-fragments with kinetic energies, that correspond to the IR+UV experiment where the photodissociation follows the IR excitation immediately. The observed enhancement of the fast fragments is not intuitively obvious. They are faster than in the UV-only experiments, which cannot be explained assuming that the original IR excitation has been redistributed over the various degrees of freedom of the molecule statistically via an IVR process. The above experimental results can provide useful input for future theoretical treatment of the photodissociation dynamics and IVR processes in pyrrole.

SUPPLEMENTARY MATERIAL

See supplementary material for UV and IR flux dependencies, and measured angular distributions of H-fragments.

ACKNOWLEDGMENTS

The authors acknowledge the support of the Czech Science Foundation GACR grant No.: 17-04068S.

REFERENCES

[1] A. Sobolewski, W. Domcke, C. Dedonder-Lardeux, and C. Jouvet, Phys. Chem. Chem. Phys. **4**, 1093 (2002).
[2] M. N. R. Ashfold, G. A. King, D. Murdock, M. G. D. Nix, T. A. A. Oliver, and A. G. Sage, Phys. Chem. Chem. Phys. **12**, 1218 (2010).
[3] G. M. Roberts and V. G. Stavros, Chem. Sci. **5**, 1698 (2014).
[4] B. Marchetti, T. N. V. Karsili, M. N. R. Ashfold, and W. Domcke, Phys. Chem. Chem. Phys. **18**, 20007 (2016).
[5] D. A. Blank, S. W. North, and Y. T. Lee, Chem. Phys. **187**, 35 (1994).
[6] J. Wei, A. Kuczmann, J. Riedel, F. Renth, and F. Temps, Phys. Chem. Chem. Phys. **5**, 315 (2003).
[7] J. Wei, J. Riedel, A. Kuczmann, F. Renth, and F. Temps, Faraday Discuss. **127**, 267 (2004).
[8] H. Lippert, H.-H. Ritzel, I. V. Hertel, and W. Radloff, Chem. Phys. Chem. **5**, 1423 (2004).
[9] B. Cronin, M. G. D. Nix, R. H. Qadiri, and M. N. R. Ashfold, Phys. Chem. Chem. Phys. **6**, 5031 (2004).
[10] M. N. R. Ashfold, B. Cronin, A. L. Devine, R. N. Dixon, and M. G. D. Nix, Science **312**, 1637 (2006).
[11] B. Cronin, A. L. Devine, and M. N. R. Ashfold, Phys. Chem. Chem. Phys. **8**, 3440 (2006).
[12] V. Papadakis and T. N. Kitsopoulos, Rev. Sci. Instrum. **77**, 083101 (2006).
[13] V. Poterya, V. Profant, M. Fárník, P. Slavíček, and U. Buck, J. Chem. Phys. **127**, 064307 (2007).
[14] L. Rubio-Lago, D. Zaouris, Y. Sakellariou, D. Sofikitis, T. N. Kitsopoulos, F. Wang, X. Yang, B. Cronin, A. L. Devine, G. A. King *et al.*, J. Chem. Phys. **127**, 064306 (2007).
[15] M. Epshtein, A. Portnov, R. Kupfer, S. Rosenwaks, and I. Bar, J. Chem. Phys. **139**, 184201 (2013).
[16] G. M. Roberts, C. A. Williams, H. Yu, A. S. Chatterlay, J. D. Young, S. Ullrich, and V. G. Stavros, Faraday Discuss **163**, 95 (2013).
[17] G. Wu, S. P. Neville, O. Schalk, T. Sekikawa, M. N. R. Ashfold, G. A. Worth, and A. Stolow, J. Chem. Phys. **142**, 074302 (2015).
[18] V. Vallet, Z. Lan, S. Mahapatra, A. L. Sobolewski, and W. Domcke, J. Chem. Phys. **123**, 144307 (2005).

© Author(s) 2019

[19]M. Barbatti, M. Vazdar, A. J. A. Aquino, M. Eckert-Maksić, and H. Lischka, J. Chem. Phys. **125**, 164323 (2006).
[20]M. Vazdar, M. Eckert-Maksić, M. Barbatti, and H. Lischka, Mol. Phys. **107**, 845 (2009).
[21]K. Saita, M. G. D. Nix, and D. V. Shalashilin, Phys. Chem. Chem. Phys. **15**, 16227 (2013).
[22]D. Picconi and S. Y. Grebenshchikov, J. Chem. Phys. **148**, 104103 (2018).
[23]D. Picconi and S. Y. Grebenshchikov, J. Chem. Phys. **148**, 104104 (2018).
[24]W. Xie, W. Domcke, S. C. Farantos, and S. Y. Grebenshchikov, J. Chem. Phys. **144**, 104105 (2016).
[25]M. Palmer, I. Walker, and M. Guest, Chem. Phys. **238**, 179 (1998).
[26]Z. Lan, A. Dupays, V. Vallet, S. Mahapatra, and W. Domcke, J. Photochem. Photobiol. A Chem. **190**, 177 (2007).
[27]V. Vallet, Z. Lan, S. Mahapatra, A. Sobolewski, and W. Domcke, Faraday Discuss. **127**, 283 (2004).
[28]I. Frank and K. Damianos, J. Phys. Chem. **126**, 125105 (2007).
[29]S. Rosenwaks, *Vibrationally Mediated Predissociation* (RSC Publishing, Cambridge, 2009).
[30]A. Sinha, R. L. Vander Wal, and F. F. Crim, J. Chem. Phys. **91**, 2938 (1989).
[31]M. Brouard and R. Mabbs, Chem. Phys. Lett. **204**, 543 (1993).
[32]F. F. Crim, J. Phys. Chem. **100**, 12725 (1996).
[33]A. Bach, J. Hutchison, R. J. Holiday, and F. F. Crim, J. Phys. Chem. **107**, 10490 (2003).
[34]G. Dorfman, A. Melchior, I. Bar, and S. Rosenwaks, J. Phys. Chem. **106**, 8285 (2002).
[35]M. Epshtein, A. Portnov, S. Rosenwaks, and I. Bar, J. Chem. Phys. **134**, 201104 (2011).
[36]D. J. Nesbitt, in *Mode Sel. Chem.*, edited by J. Jortner, R. D. Levine, and B. Pullman (Springer Netherlands, Dordrecht, 1991), pp. 113–126, ISBN 978-94-011-2642-7.
[37]K. Grygoryeva, J. Rakovský, O. Votava, and M. Fárník, J. Chem. Phys. **147**, 013901 (2017).
[38]K. Grygoryeva, J. Rakovský, O. Votava, and M. Fárník, J. Chem. Phys. **149**, 094303 (2018).
[39]J. Fedor, J. Kočišek, V. Poterya, O. Votava, A. Pysanenko, L. Lipciuc, T. N. Kitsopoulos, and M. Fárník, J. Chem. Phys. **134**, 154303 (2011).
[40]A. T. J. B. Eppink and D. H. Parker, Rev. Sci. Instrum. **68**, 3477 (1997).
[41]S. Gibson, D. Hickstein, R. Yurchak, D. Das, and G. Shih, A python package for abel transformation, https://pypi.org/project/pyabel (2017).
[42]B. Whitaker, *Imaging in Molecular Dynamics* (Cambridge University Press, Cambridge, 2003).
[43]I. Dauster, C. A. Rice, P. Zielke, and M. A. Suhm, Phys. Chem. Chem. Phys. **10**, 2827 (2008).
[44]One exception in the data of Cronin et al.[9] was the $n_9 = 1$ vibration of pyrrolyl fragment with parallel transition.

© Author(s) 2019

B.2 Publication II

Title: **Different Dynamics of CH_3 and Cl Fragments from Photodissociation of CH_3Cl in Clusters**

Journal: *The Journal of Physical Chemistry A*
DOI: `https://doi.org/10.1021/acs.jpca.0c05926`

Supporting Information

Note: Reprinted (adapted) with permission from *J. Phys. Chem. A* 2020, **124**, 7633-7643. Copyright 2020 American Chemical Society.

THE JOURNAL OF PHYSICAL CHEMISTRY A

pubs.acs.org/JPCA Article

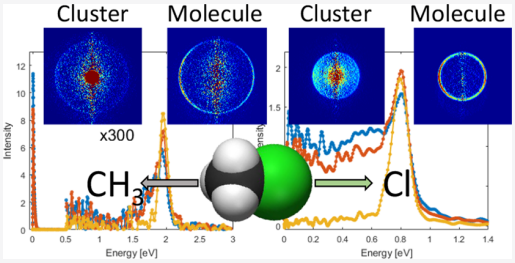
Different Dynamics of CH_3 and Cl Fragments from Photodissociation of CH_3Cl in Clusters

Ivo S. Vinklárek, Jozef Rakovský, Viktoriya Poterya, and Michal Fárník*

Cite This: J. Phys. Chem. A 2020, 124, 7633−7643 Read Online

ACCESS | Metrics & More | Article Recommendations | Supporting Information

ABSTRACT: We investigate the photodissociation of CH_3Cl at 193.3 nm using the velocity map imaging technique in $(CH_3Cl)_n$ clusters in comparison with isolated molecules. Our results for the isolated molecules are in excellent agreement with the previous study of Cl fragments, and we extend it by detecting also the $CH_3(\nu = 0)$ fragments. For the clusters, the Cl (and Cl*) and CH_3 fragment images are dominated by intense central isotropic features. The corresponding kinetic energy distributions (KEDs) reveal significant differences in the CH_3 and Cl fragment dynamics. While the CH_3 fragments exhibit a very narrow near-zero kinetic energy peak, pointing to almost complete *caging* of CH_3 fragments, the Cl (and Cl*) fragments show more structured KEDs extending all the way to the maximum available kinetic energy. The Cl KED spectra have a bimodal character with two broad peaks close to zero and around 0.6 eV. We observe a higher $I_{CH_3(\nu=0)}/I_{Cl}$ signal ratio from the clusters compared to the monomers. This is attributed to an efficient quenching of the higher vibrationally excited ν_2 states of the CH_3 fragments generated in the photodissociation. Collisional quenching of these excited states in clusters enhances the detected $CH_3(\nu = 0)$ state. Finally, we determine the [Cl*]/[Cl] branching ratio for the photodissociation pathways in the clusters as ≈0.55 ± 0.15 compared to 0.86 for the isolated molecules, which is also attributed to the collisional quenching of the excited state in the clusters. The clusters and photofragment dynamics are discussed.

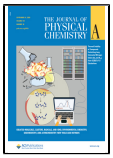


INTRODUCTION

The photodissociation of polyatomic molecules often involves different potential energy surfaces, which can be coupled, and the process can proceed along different pathways on these potentials. This represents one of the challenges in the investigation of photodissociation dynamics. Methyl halogenids CH_3X (X = Cl, F, I, Br) represent the benchmark systems to investigate the intersurface dynamics of the photodissociation pathways. Therefore, their photolysis after the Ã-band absorption was investigated by a number of experimental and theoretical studies.[1−24] The unique role of the C−X bonding in these molecules combines the simplicity of the diatomic photolysis with the complexity of multidimensional potential hypersurfaces of polyatomic molecules involving different vibronic states and conical intersections. Although a great effort was put into a detailed understanding of the dissociation pathways of isolated CH_3X monomers,[1−20] experimental studies investigating the influence of the cluster environment on the photodissociation pathways are rarer.[9,20,25−28] Here we address this issue by investigating the CH_3Cl photodissociation in clusters at 193.3 nm using the velocity map imaging (VMI), which is a well-established technique to study CH_3X photolysis.[1,7,18,29]

An excellent overview of CH_3X photodissociation and differences in the photolysis pathways among various halogenated analogues of CH_3X, with the focus on chloromethane CH_3Cl, can be found in ref 7. More recent works concentrated rather on CH_3Br,[15,18,30] and especially CH_3I.[9,12−14] Here, we provide only a brief overview of the photochemistry relevant to the present case of CH_3Cl. When excited in the Ã-band, from 165 to 230 nm, an electron localized in a nonbonding orbital of a chlorine atom is transferred to the antibonding σ^* orbital along the C−Cl coordinate.[31] In general, three essentially repulsive electronic states are involved in the C−Cl bond dissociation as depicted schematically in Figure 1, corresponding to the states traditionally denoted as $^3Q_1$, $^3Q_0$, and $^1Q_1$ ordered bottom-up by energy in the Franck−Condon region. The $^3Q_1$ and $^1Q_1$ excited states both correlate asymptotically with the ground $^1A_1$ state. Thus, they result in the $CH_3Cl \rightarrow CH_3 + Cl(^2P_{3/2})$ dissociation channel yielding the Cl fragment in the ground $^2P_{3/2}$ spin−orbit state, and the transitions to both these states have perpendicular character (the corresponding anisotropy recoil parameter $\beta = -1$). On the other hand, the dissociation

Received: June 29, 2020
Revised: August 29, 2020
Published: August 31, 2020



Downloaded via ACADEMY OF SCIENCES CZECH REPUBLIC on April 7, 2022 at 14:04:15 (UTC).
See https://pubs.acs.org/sharingguidelines for options on how to legitimately share published articles.

ACS Publications © 2020 American Chemical Society

https://dx.doi.org/10.1021/acs.jpca.0c05926
J. Phys. Chem. A 2020, 124, 7633−7643

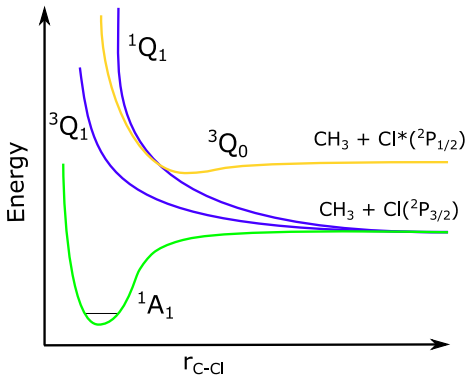


Figure 1. Schematic picture of the cut through the relevant potential energy hypersurfaces of CH_3Cl along the C−Cl coordinate drawn according to ref 7

along the $^3Q_0$ potential yields the spin−orbit excited state $Cl^*(^2P_{1/2})$.

Symmetry distortion enables intersystem crossing (ISC) between $^3Q_0$ and $^1Q_1$, which occurs out of the Franck−Condon region. The ISC probabilities of $P_{^3Q_0 \rightarrow {}^1Q_1} = 0.69$ and $P_{^1Q_1 \rightarrow {}^3Q_0} = 0.49$ were calculated by Townsend et al.[7] from the fragment ratio $[Cl^*]/[Cl] = 0.86$ and from their measured anisotropy recoil parameters $\beta = -0.46$ and $\beta^* = -0.74$ for populating the $Cl(^2P_{3/2})$ and $Cl^*(^2P_{1/2})$, respectively. The dissociation of CH_3Cl is assumed to be fast enough to exclude any significant changes of anisotropy parameters due to the molecule rotation.[32,33] The calculations were made under the assumption that the $^3Q_1$ state is not populated by the excitation at 193.3 nm, which resulted in 87% and 13% absorption probabilities to $^1Q_1$ and $^3Q_0$, respectively. The asymmetry in the ISC probabilities was proposed to be due to the steeper potential surface of the $^1Q_1$ state compared to the $^3Q_0$ state, which resulted in a more rapid dissociation on the $^1Q_1$ surface consequently sampling a smaller range of distorted geometries than in the $^3Q_0$ pathway.[34,35] Therefore, the ISC probability was smaller in the former case. The well-understood photolysis of the CH_3Cl monomer provides a good background for the investigation of the effect of cluster environment on its photodissociation dynamics.

Here, we extend the previous VMI investigations of CH_3Cl photolysis[7] by detecting also the $CH_3(\nu = 0)$ fragment in addition to the previously studied Cl and Cl* fragments. More importantly, we produce clusters of CH_3Cl molecules and investigate the dynamics of the Cl (and Cl*) and CH_3 fragments. They exhibit quite different behavior.

The paper is organized as follows: First, we provide some details of our VMI experiment. Then, we briefly compare our results for the isolated molecule with the previously published results.[7] In the following section we present our results for the clusters, and subsequently we discuss our clusters and the revealed different dynamical behavior of the CH_3 and Cl fragments. At the end we briefly summarize our experimental observations and conclusions.

EXPERIMENTAL SECTION

The experiments were performed on the Apparatus for IMaging (AIM) previously described in detail elsewhere.[36] A mixture of 7% of chloromethane CH_3Cl (Sigma-Aldrich, ≥99.5%) in a buffer gas (He or Ar) was supersonically expanded at a total stagnation pressure of 1.7 bar(a) into a vacuum chamber through a commercial pulsed valve (General Valves) with the nozzle diameter of 0.6 mm at a repetition rate of 10 Hz. Other expansion conditions (stagnation pressures and concentrations) were also exploited as outlined further in the text. The molecules passing through a skimmer formed a molecular beam entering the detection chamber with the VMI assembly of the original Parker and Eppink design.[37] Two counterpropagating UV lasers intercepted the molecular beam in the center of the VMI extraction region for photodissociation and resonant multiphoton ionization.

The photolysis laser pulses with wavelength at 193.3 nm were generated by an ArF excimer laser (Coherent ExciStar XS, 10 Hz, 0.55 mJ). The laser radiation was horizontally polarized by a thin film polarizer oriented at the Brewster angle, and the polarized beam was focused to the VMI center with a $f_0 = 50$ cm lens. The photodissociation fragments were ionized via a (2 + 1) resonance-enhanced multiphoton ionization (REMPI) scheme. The radiation was produced by a UV OPO laser (EKSPLA NT-230) focused with the system of two lenses (planoconvex and positive meniscus), producing an effective focal length $f_0 = 25$ cm. Both lasers were spatially overlapped, and a 10 ns delay between the photodissociation and ionization pulse was introduced to prevent any mixed-multiphoton effects. It ought to be stressed that laser intensity dependencies were carefully checked to avoid any multiphoton effects, which could be easily confused with clustering effects as mentioned below, and strictly single-photon photodissociation processes are reported here. The UV OPO laser was running at half the repetition rate (5 Hz) of the photolysis laser to record the background signal without the REMPI laser, which was subtracted from the velocity map images. Synchronization of the pulse valve and both the photodissociation and ionization lasers was driven by the delay generator (BNC 575).

The following (2 + 1) REMPI ionization schemes were exploited in our experiments: the CH_3 fragments in the vibrational $\nu = 0$ ground state were ionized at 333.5 nm (0.9 mJ),[38,39] and the Cl fragments were ionized at 235.31 nm (0.68 mJ) and 235.17 nm (0.65 mJ) in the ground $Cl(4p\ ^2P_{1/2} \leftarrow 3p\ ^2P_{3/2})$ and excited $Cl^*(4p\ ^2D_{3/2} \leftarrow 3p\ ^2P_{1/2})$ states, respectively.[40] The wavelengths for the REMPI schemes were found as maxima of the measured action spectra. The spectral width of the OPO UV laser was ≈4 cm^{-1}.

The detector assembly was perpendicular with respect to the plane defined by the molecular and laser beams. The ionized fragments were extracted from the interaction region by the VMI ion optics toward the detector. After a flight-path of about 45 cm, the ions arrived at the microchannel plate (MCP) detector in a chevron stack with a phosphor screen. The images were recorded by the CCD camera (Unibrain).

To reconstruct the original 3D velocity distribution, the images were further processed by inverse Abel transformation. In particular, we used the direct method of the Python package[41] and its implementation in Cython (other methods were tested and yielded essentially the same results). The inverse Abel transformation amplifies the noise near the symmetry axis, i.e., along the central vertical axis of our images as explained in ref 42 (on page 70). The kinetic energy distribution (KED) and angular distributions of the fragments were acquired by the standard integration methods,[41,42] and the energy scale was calibrated with the reference velocity map images of HBr.[36,43] The anisotropy recoil parameters β were

https://dx.doi.org/10.1021/acs.jpca.0c05926
J. Phys. Chem. A 2020, 124, 7633−7643

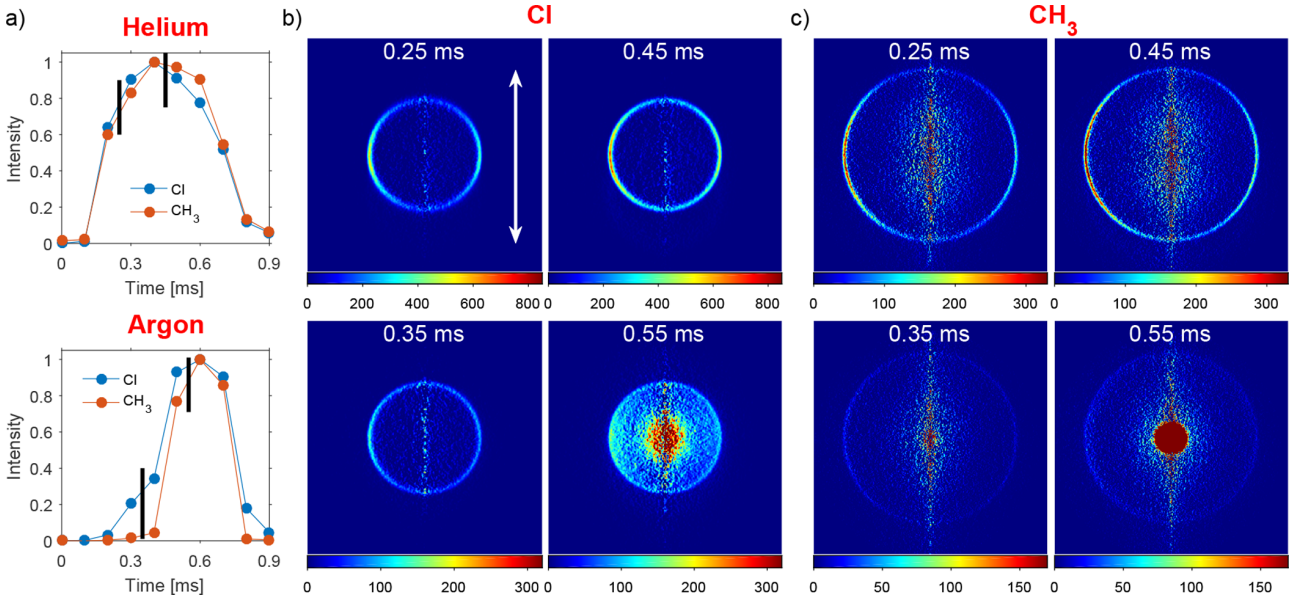


Figure 2. Photofragment images of CH_3Cl at 193.3 nm seeded in helium (top row) and argon (bottom row). Panel (a) shows the integrated image intensity verus the stage of the pulsed nozzle opening profile for both Cl and CH_3 fragments. The transformed images correspond to the $Cl(^2P_{3/2})$ (b) and $CH_3(\nu = 0)$ (c) fragments. The images were measured in early (0.25 ms in He, 0.35 ms in Ar) and middle (0.45 ms in He, 0.55 ms in Ar) stages of the valve-opening cycle as indicated by the black vertical lines in (a).

obtained using the same package[41] and fitting the angular distribution by the well-known formula[42]

$$I(\theta) \propto 1 + \beta P_2(\cos\theta) \quad (1)$$

where $P_2(x) = 3/2x^2 - 1/2$ is the second-order Legendre polynomial.

The CH_3Cl gas was seeded in argon to induce clustering, while nonclustering conditions were achieved in helium buffer gas, as demonstrated below. It is well-known that the conditions in pulsed expansions can change significantly in different stages of the gas pulse, and the rotational temperatures and clustering conditions can be very different.[36,44−46] For HBr/Ar coexpansion, we have demonstrated that the images recorded in the opening stage of the valve corresponded to isolated molecules, later on the valve was fully opened and strong clustering occurred, and at even later times the valve was closing and the images were dominated by isolated molecules again.[36] For the present case of CH_3Cl, the time profile of the gas pulse was scanned for the desired clustering conditions, and clear distinction between monomer and clustering conditions was found along the beam profile in the Ar expansion. The examples are shown and discussed in the next sections. We refer to these stages of the pulsed nozzle opening profile as early, middle, and late stage, locating them at about 0.3−0.4, 0.4−0.6, and 0.6−0.9 ms, respectively, after the trigger signal.

Using nonspecific multiphoton ionization of CH_3Cl and CH_3Cl^+ detection, the velocity profile of the primary beam could be obtained from the images, and the corresponding speed ratio could be evaluated. Using the standard textbook expression,[45] the translational temperature in the middle stage of the expansion could be estimated from the speed ratio as roughly 3 K in Ar and 1 K in He.

Special attention was paid to suppress any multiphoton processes since they could be confused with cluster effects resulting in central features. For example, in the case of CH_3Br a signal in the center of images originally assigned to the clusters[47] was later attributed to the multiphoton ionization and CH_3Br^+ ion dissociation by the same group[30] as confirmed also by other groups.[15] In the Supporting Information we show an example of the image arising from multiphoton processes, Figure S3. The cluster images generated in the Ar expansions below exhibit quite different patterns, and the multiphoton processes were carefully suppressed in our present cluster experiments.

RESULTS

Photodissociation of the CH_3Cl Molecule. The results of VMI of CH_3Cl seeded in helium and photolyzed at 193.3 nm are shown in the first row of Figure 2. The images were recorded at different stages of the nozzle valve opening cycle. The total $CH_3(\nu = 0)$ and Cl signals are plotted in Figure 2a versus the delay time from the trigger signal opening the valve. The vertical black lines indicate the image recording times at 0.25 and 0.45 ms. The corresponding images of $Cl(^2P_{3/2})$ and CH_3 are shown in Figure 2b and c, respectively. Additional images recorded at other delays along the gas pulse profile are shown in the Supporting Information. First, we produce a molecular beam composed of pure monomers. Since the clustering effects were reported for CH_3I molecules,[9,20] we are concerned about the cluster contamination in the pure monomer beam and check for clustering at different delays as outlined above. No qualitative change is observed between the images, as illustrated in Figure 2 and further images in the Supporting Information, and they are assigned to isolated CH_3Cl molecules in contrast to the clusters observed in the Ar expansion below.

The images in the top row of Figure 2 corresponding to the photodissociation of the isolated CH_3Cl molecules exhibit a single-ring structure. The inverse Abel transformation introduces some artificial noise near the image symmetry axis as outlined in the Experimental Section. This noise can be also

https://dx.doi.org/10.1021/acs.jpca.0c05926
J. Phys. Chem. A 2020, 124, 7633−7643

increased by an imperfect subtraction of the background signal. These effects yield the noise in images observed closer to the vertical axis going through the center in the present images. Both Cl and $CH_3(\nu = 0)$ fragment images exhibit a perpendicular character with respect to the polarization of the photolysis laser indicated by the white vertical arrow in the first image of Figure 2b. A similar single ring structure is measured for $Cl^*(^2P_{1/2})$ fragments; see Figure S4 in the Supporting Information.

In Figure 3, we extract the KED spectra and angular distributions of Cl and Cl* (a) and $CH_3(\nu = 0)$ (b) fragments

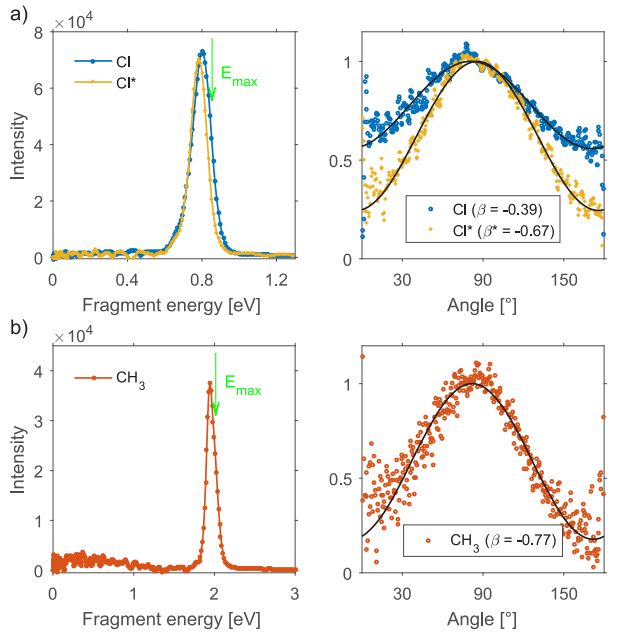


Figure 3. Kinetic energy distribution spectra and anisotropy profiles of (a) $Cl(^2P_{3/2})$ and $Cl^*(^2P_{1/2})$ and (b) $CH_3(\nu = 0)$ fragments from the photodissociation of isolated CH_3Cl molecules at 193.3 nm. To avoid the noise near the symmetry axis introduced by the inverse Abel transformation (see the text), the integration was done in the intervals 10°−170° and 190°−350° to obtain the KED spectra. Vertical arrows labeled E_{max} correspond to the maximum kinetic energy of the corresponding fragment. Angular distributions were fitted (black lines) to yield anisotropy parameters β.

integrating the images in Figure 2 (and Figure S4 in the Supporting Information) at the delay time of 0.45 ms. The KED spectra of Cl and Cl* fragments in Figure 3a exhibit single peaks with the maxima at 0.79 and 0.78 eV, respectively. In Figure 3a the spectra were normalized to the branching ratio [Cl*]/[Cl] of 0.86. This value was reported in ref 7 as derived by averaging values from earlier reports[5,6,48,49] with rescaling due to an incorrect line strength factor calibration. The $CH_3(\nu = 0)$ fragments in Figure 3b display a sharp peak at 1.95 eV. The low-intensity signal below ~1.5 eV originates from the central noise.

The maximum kinetic energy E_{max} of a given fragment is marked by the green vertical arrow in the corresponding KED spectrum (see the Supporting Information for details). It is $E_{max}^{Cl} = 0.86$ eV and $E_{max}^{CH_3} = 1.99$ eV for Cl and CH_3 fragments, respectively. For the excited Cl* fragment, $E_{max}^{Cl*} = 0.82$ eV. The KED peaks are quite narrow with high-energy tails not exceeding E_{max} significantly corresponding to little internal excitation of the parent CH_3Cl molecules. The observed maxima in KED spectra are shifted by 0.07 and 0.04 eV with respect to the calculated E_{max} for Cl and Cl*, respectively, and the corresponding energy is available for an internal excitation of CH_3 fragments.

Several CH_3 vibrational modes could be populated in the photodissociation process as observed, e.g., in the photodissociation of CH_3Br: C−H symmetric stretch ν_1 (3004 cm^{-1}), umbrella mode ν_2 (606 cm^{-1}), asymmetric stretch ν_3 (3161 cm^{-1}), and degenerate deformation ν_4 (1398 cm^{-1}). The observed KED maximum of the Cl fragment suggests $\nu_2 \approx 2-3$ vibrational excitation of the CH_3 umbrella mode in excellent agreement with the results of Townsend et al.[7] The Cl* KED maximum at 0.78 eV corresponds to $\nu_2 \approx 2$ excitation of CH_3 in this dissociation channel. Here, Townsend et al.[7] indicated a lower vibrational excitation $\nu_2 \approx 0$ in the perpendicular direction compared to $\nu_2 \approx 2$ in a nearly parallel direction for the excited Cl* channel. We do not evaluate perpendicular and parallel KEDs separately from our conventional VMI data due to the lower signal-to-noise ratio.[7] Nevertheless, our results for isolated molecules are in very good agreement with the previous work.[7]

We present images detecting the CH_3 fragment in its vibrational ground state $\nu = 0$. The slight shift between the maximum kinetic energy $E_{max}^{CH_3} = 1.99$ eV and the corresponding peak maximum at 1.95 eV would suggest some rotational excitation and/or a contribution to this fragment from the dissociation into the Cl* excited channel. In this channel, the maximum kinetic energy corresponds to $E_{max}^{CH_3} = 1.92$ eV due to the total available energy E_{avl} lowered by the spin−orbit splitting E_{SO}. We have searched for the CH_3 fragments in higher vibrationally excited states, recording the action spectra by scanning the ionization laser wavelength for the corresponding REMPI. Figure 4 shows the spectra with $\nu = 0$ and a broad peak corresponding to the $\nu_2 = 1$ state. The integrated intensity of this peak corresponds to about half of

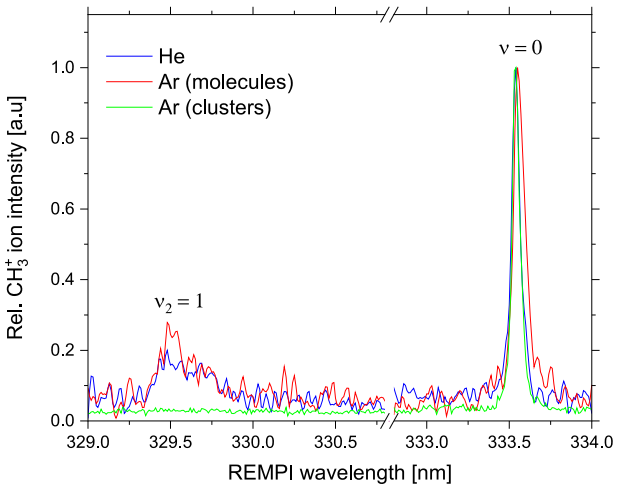


Figure 4. Action spectrum of CH_3Cl recorded with a 193.3 nm photodissociation laser by scanning the REMPI laser wavelength. The spectra were recorded for isolated molecules in He expansion (blue) and for clusters in Ar expansion (green). The spectrum in the clustering regime has also been recorded excluding the central (cluster) part of the image; i.e., this spectrum (red) corresponds to the free unclustered molecules in the cluster beam. All spectra were normalized on the main $\nu = 0$ peak.

https://dx.doi.org/10.1021/acs.jpca.0c05926
J. Phys. Chem. A 2020, 124, 7633−7643

the ground state peak; however, its width suggests a substantial rotational excitation, and only low-quality images could be recorded for the $\nu_2 = 1$ excited state.

Further information derived from the VMI experiments is the anisotropy of the photodissociation process. The angular distributions of both Cl and Cl* fragments in Figure 3a exhibit perpendicular character and similarly the angular distribution of $CH_3(\nu = 0)$ in Figure 3b. The plotted distributions were fitted, as outlined in the Experimental Section, to obtain the anisotropy recoil parameters β. The derived values $\beta = -0.39(0.07)$ for the Cl ground state and $\beta^* = -0.67(0.08)$ for the Cl* excited state exhibit somewhat less pronounced perpendicularity compared to the values of Townsend et al.,[7] $\beta = -0.46$ and $\beta^* = -0.74$, respectively. The small differences are within our experimental error and might be caused by the imperfect polarization of our 193.3 nm laser light. The angular distribution of $CH_3(\nu = 0)$ fragments yields $\beta = -0.77(0.10)$, which is higher than what we observe for the Cl fragments. It is worth noting that fitting the $CH_3(\nu_2 = 1)$ image (not shown) yields even more pronounced perpendicular character with $\beta = -0.95(0.19)$. This observation is consistent with the prediction from Cl measurements of Townsend et al.[7] that the vibrationally excited CH_3 fragments which correspond to the Cl fragments with lower kinetic energies would exhibit a higher anisotropy closer to the limiting value $\beta = -1$.

The photofragment angular distribution resulting from the CH_3Cl photodissociation at 193.3 nm was a subject of some discussion previously. The earlier studies[6,50] using Doppler time-of-flight measurements suggested a parallel character of the transition. On the other hand, the VMI study[7] clearly demonstrated the perpendicular transition. This observation agrees with the original prediction[51] that the role of the $^3Q_0$ and $^3Q_1$ states in the $\tilde{A}$-band excitation of CH_3X becomes less significant as the mass of X decreases due to the weaker spin–orbit mixing with the $^1Q_1$ state. Our data fully confirm the anisotropy recoil parameters obtained by Townsend et al.[7] as well as their energy distributions for Cl and Cl* fragments. In addition, the complementary measurements of CH_3 fragments further confirm the dynamics of the CH_3Cl molecule photodissociation outlined in ref 7.

Photodissociation of CH_3Cl in Clusters. Our main emphasis here is on the cluster dynamics. The bottom row in Figure 2 shows VMIs of CH_3Cl seeded in argon. Unlike in helium, the images depend on the stage of the pulsed nozzle opening profile, in which the beam is probed. We show two examples: images taken in the early stage of the valve opening at 0.35 ms, which agree well with the images in the top row of Figure 2 recorded in He and thus correspond to the isolated molecules. On the other hand, images of both fragments Cl and $CH_3(\nu = 0)$ recorded in the middle stage, when the valve is fully opened at 0.55 ms, exhibit strong central features in addition to the sharp molecular rings. The central features dominate the images and correspond to the cluster generation as will be argued below. Further images of Cl and CH_3, as well as Cl*, recorded at different stages of the pulsed nozzle opening profile demonstrating different clustering conditions along the gas pulse are shown in the Supporting Information.

The strong central features characteristic for photodissociation in clusters were observed in quite a few cases previously.[36,43,52−59] They result from the fragment *caging*, as the fragments lose their velocity by collisions with the surrounding environment. The central "blobs" have isotropic angular distributions contrary to the monomer rings as the fragment collisions reduce the anisotropy. Still, there is distinctive difference in the shape of the central feature between Cl (or Cl*) and CH_3 images. Whereas the Cl fragments cover the broad range of velocities up to the monomer ring, the CH_3 fragments distribution is narrow with a maximum close to the zero velocity.

This is illustrated in the KED spectra in Figure 5a and b for Cl and CH_3 fragments, respectively. The Cl and Cl* fragments

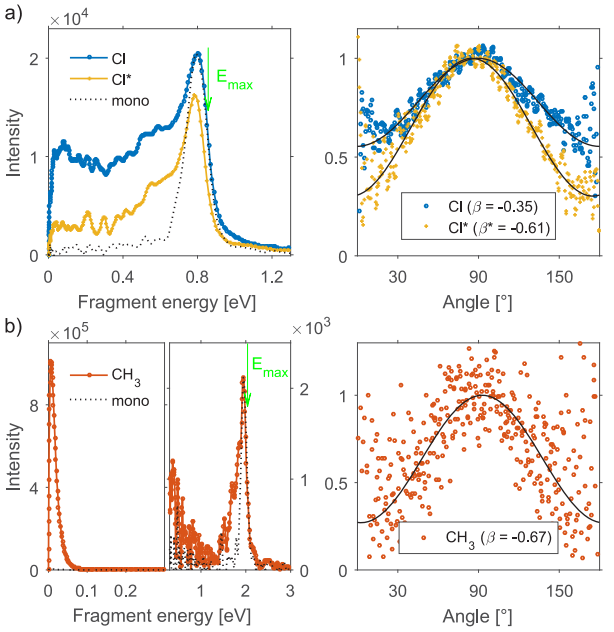


Figure 5. KED spectra and anisotropy profiles of (a) $Cl(^2P_{3/2})$ and $Cl^*(^2P_{1/2})$ and (b) $CH_3(\nu = 0)$ fragments in argon (7% CH_3Cl in Ar, stagnation pressure 1.7 bar). The KED spectra of monomer photolysis from Figure 3 are shown by dotted lines for comparison. The KED of CH_3 fragments is plotted in two graphs with different intensity scales to highlight the low monomer signal around 2 eV. Angular distributions were integrated between 0.60 and 0.98 eV for Cl and 1.65−2.25 eV for CH_3, and they were fitted (black lines) to yield the anisotropy parameters β.

in Figure 5a cover a broad range of translation energies from near-zero up to the maximum translation energy of the monomer photodissociation E_{max}. The blue and yellow spectra correspond to the ground Cl and excited Cl* state, respectively. Qualitatively, both spectra exhibit similar features: the sharp peak near E_{max} corresponding to the monomer KED discussed above and the broad feature extending to zero kinetic energy. The broad distribution has a bimodal structure with two broad maxima around 0.6 eV and close to zero.

The sharp peaks were assigned to the photodissociation of unclustered monomers in the molecular beam. The region of the sharp peaks was analyzed to extract the angular recoil distributions which are plotted in the right column of Figure 5a. Fitted anisotropy parameters $\beta = -0.35(0.04)$ and $\beta^* = -0.61(0.07)$ for Cl and Cl*, respectively, agree within the error bars with the anisotropy parameters obtained for isolated molecules above. They are somewhat lowered by the underlying isotropic signal from the clusters. There is also an energetic argument for the assignment of the sharp peak to the isolated molecules: if the Cl fragments were dissociated from the clusters, the mass of the whole remaining cluster would

https://dx.doi.org/10.1021/acs.jpca.0c05926
J. Phys. Chem. A 2020, 124, 7633−7643

replace the mass of the CH_3 fragment in the momentum conservation equation (assuming a diatomic-like dissociation). Subsequently, the corresponding kinetic energy imparted into the Cl fragment would be higher. This effect was observed previously for, e.g., ICl clusters.[54] However, there is no shift of the KED maximum position in Figure 6a. Therefore, the sharp

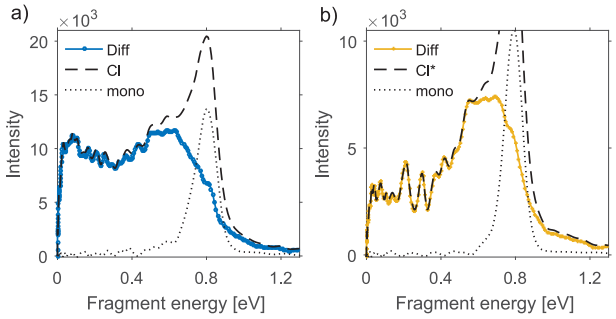


Figure 6. KED spectra of (a) Cl($^2P_{3/2}$) and (b) Cl*($^2P_{1/2}$) fragments taken from Figure 5 (here shown as the dashed lines) after subtraction of the corresponding monomer contribution (dotted lines). The difference is shown by the full colored line.

peaks in the cluster KEDs can be assigned unambiguously to the unclustered monomers, and the monomer contribution can be subtracted from the cluster KED spectra.

The KED spectra of Cl and Cl* fragments from clusters with the subtracted monomer contribution are plotted in Figure 6a and b, respectively. The dashed and dotted lines show the original spectra before the subtraction and the monomer spectra, respectively. In the final subtracted spectra, the bimodal character becomes clear.

Panel b in Figure 5 shows the KED spectrum of CH_3 fragments from the Ar expansion. The graph is split into two parts with different intensity scales for clarity (note the difference of more than 2 orders of magnitude). The majority of the CH_3 signal from the clusters comes from the narrow central peak with kinetic energy below 0.1 eV, which is illustrated in the first part of the graph. Nevertheless, there is still a low sharp peak around 2 eV. The anisotropy parameter corresponding to this peak could be obtained from fitting the angular distribution shown in the right panel, yielding $\beta = -0.67(0.18)$. This is in reasonably good agreement with the monomer photodissociation. Following the same line of arguments as above for Cl fragments, the sharp peak in CH_3 KED was assigned to the monomers in the molecular beam. The corresponding KED spectrum from isolated molecules is shown as the dotted line in the KED for comparison. Its subtraction leaves essentially only the strong zero kinetic energy peak.

The character of the CH_3 fragment KED spectra is quite different from the above-discussed Cl and Cl* fragments. The strong zero kinetic energy peak suggests that the CH_3 fragments are stopped almost completely in the clusters. On the other hand, the Cl and Cl* fragments are slowed down so that their kinetic energies fill the entire range between zero and E_{max}; see Figure 6. Here, we refer to the corresponding processes as *caging* and *delayed exit*, respectively, as termed by Buck for photodissociation of hydrogen halides in rare gas clusters.[60] It ought to be mentioned that even the caged fragments with zero kinetic energy must escape the cluster in order to be detected; i.e., the clusters decay in the photodissociation and subsequent fragment-slowing processes. It is also worth noting that after subtracting the monomer contribution, there remains a tail of Cl and Cl* fragments in the KEDs exceeding E_{max}. This is consistent with the effect mentioned above that a Cl fragment can be accelerated to a higher velocity when dissociating from a cluster rather than from a single CH_3Cl molecule.

Another surprising experimental observation concerns a large difference in signal intensity ratio between $CH_3(\nu = 0)$ and Cl fragments from the clusters when compared to the isolated molecules. The integrated signal of the monomers yields the ratio $I_{CH_3}/I_{Cl} \approx 0.25 \pm 0.02$, while the corresponding ratio in the clusters is about 10 times larger, $I_{CH_3}/I_{Cl} \approx 2.15 \pm 0.15$. The signal ratio is evaluated from integrated raw images, which eliminates uncertainty factors introduced in the intensities by the mathematical procedure of transformation. The images for both the isolated molecules and clusters are recorded in the Ar expansion. The molecular regime corresponds to the early stage (delay 0.35 ms), and the cluster images are recorded at the middle stage (delay 0.55 ms), as shown in Figure 2b. Using the same expansion should eliminate any ambiguities in the intensity due to the differences between He and Ar expansions.

We also evaluate the branching ratio between Cl* and Cl by integrating the areas of the KED spectra and taking their ratio. For the monomer photodissociation, the corresponding integrated signal ratio is $I_{Cl^*}/I_{Cl} \approx 0.93 \pm 0.15$, which was scaled to the [Cl*]/[Cl] branching ratio of 0.86 given in the literature.[5−7,48,49] For the clusters, we integrate the spectra in Figure 6 with the monomer contribution already subtracted. The corresponding signal ratio from the cluster experiments is $I_{Cl^*}/I_{Cl} \approx 0.60 \pm 0.15$, which was scaled according to the monomer to the branching ratio [Cl*]/[Cl] ≈ 0.55 ± 0.15 for the photodissociation in clusters.

DISCUSSION OF THE PHOTODISSOCIATION DYNAMICS IN CLUSTERS

The cluster environment can change the simple diatomic-like dissociation picture presented in Figure 1 significantly. Even the presence of a single rare gas atom can modify the potential barriers along the dissociation pathways, cause disappearances of conical intersections, and close some dissociation channels or even open new ones.[52,53,61−64] However, investigation of the involved potential energy hypersurfaces requires high-level *ab initio* calculations, which go beyond our present experimental work. Therefore, we analyze the environmental effects qualitatively in terms of the above-mentioned mechanistic approach of photofragment caging,[60] which was successfully implemented in cluster studies previously.[36,55,57,65−67]

First, we discuss what kind of clusters can be generated in our experiment. Since the expansion proceeds with 7% CH_3Cl in Ar, the clusters could contain CH_3Cl molecules as well as Ar atoms. Hydrogen halide molecules HX and small $(HX)_n$ clusters inside large Ar clusters were prepared by HX/Ar coexpansions previously.[36,60,65,66] However, these studies demonstrated that the HX molecules were embedded in argon clusters only when very diluted HX/Ar mixtures were used with HX concentrations below 1%. Already at concentrations of a few percent, only pure HX clusters without Ar were generated. The analogy with the previous HX/Ar studies would suggest pure $(CH_3Cl)_n$ clusters in our present case. We have attempted to generate Ar-covered CH_3Cl

https://dx.doi.org/10.1021/acs.jpca.0c05926
J. Phys. Chem. A 2020, 124, 7633−7643

clusters by diluting the expanding mixture. However, no qualitative changes in the images could be observed until the signal disappeared with dilution. On the other hand, we have used pure CH_3Cl expansions without Ar to confirm the pure $(CH_3Cl)_n$ clusters. The VMI images for the clusters generated in the pure CH_3Cl expansions were qualitatively identical with the results obtained for CH_3Cl seeded in Ar. Therefore, we conclude that the pure $(CH_3Cl)_n$ clusters are generated in our experiments with Ar.

The literature on $(CH_3Cl)_n$ clusters is relatively scarce. The calculations of $(CH_3X)_2$ dimers reported structures corresponding to the parallel arrangement of the molecules with head-to-tail orientation, i.e., the antiparallel orientation of the dipole moments.[68] Two similar structures were identified—hydrogen-bonded C−H···X and C···X bonded—with the interaction energies of about 8.5 kJ/mol (88 meV) and differences of only 5−10% between these structures. The photodissociation of clusters dominated by such $(CH_3Cl)_2$ dimers would result in Cl and CH_3 fragments dissociating freely from the clusters without any caging. Since our KEDs exhibit the strong caging for CH_3 and delayed exit for Cl fragments, our mean cluster size goes undoubtedly far beyond the dimers. It is worth noting that for matrix-isolated dimers also head-to-head isomers were tentatively proposed to be generated in supersonic expansions.[69]

Larger clusters were investigated by X-ray photoelectron spectroscopy in the bulk together with molecular dynamics simulations of the clusters of 208 CH_3Cl molecules.[70] These investigations established the $(CH_3Cl)_4$ as the cluster core with a pyramidal tetrameric structure. In this tetramer structure, there is also no preference for Cl nor for CH_3 to point in or out of the cluster to justify the observed caging and delayed exit. Therefore, we conclude that our cluster sizes go even far beyond the tetramer, possibly to clusters composed of tens or even hundreds of molecules.

We have attempted to obtain different cluster sizes by changing the expansion conditions, namely, the stagnation pressure of the CH_3Cl/Ar mixture (at the 7% mixing ratio), as shown in Figure 7. Apparently, the expansion pressure did not have any significant influence on the generated clusters. Further expansion conditions including different concentrations were exploited as well, as outlined above. Nevertheless,

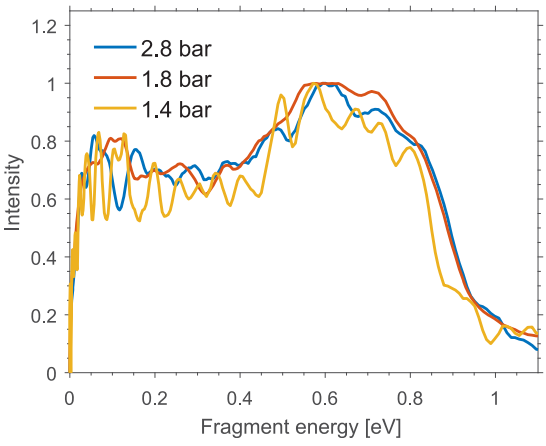


Figure 7. $Cl(^2P_{3/2})$ fragment KED spectra recorded with 7% CH_3Cl in argon at different stagnation pressures between 1.4 and 2.8 bar as indicated. The spectra were normalized to maximum value.

the obtained VMIs and KEDs were qualitatively the same. This suggests that within the range of experimental conditions exploited here, relatively large pure $(CH_3Cl)_n$ clusters were generated in the range of sizes where the differences in the cluster size distributions caused by different expansion conditions are not reflected qualitatively in the photodissociation fragment dynamics in these clusters.

Photodissociation of a CH_3Cl molecule inside the large cluster could lead to some caging for both CH_3 and Cl fragments. On the other hand, the photodissociation of a molecule in the surface layer can yield fast fragments depending on the surface layer structure. The molecular dynamics simulations[70] of the CH_3Cl clusters composed of 208 molecules revealed almost spherical shape with the surface layer composed of antiparallel side-by-side dimer structures. In such configuration, fast free CH_3 as well as Cl fragments should be produced by the photodissociation of the surface CH_3Cl molecules without preferential caging of one of the photoproducts. Our photodissociation results would rather suggest clusters with some surface layer corresponding to the CH_3Cl molecules oriented by their CH_3 end into the cluster interior. In this structure photodissociation of the surface molecules would then lead to the CH_3 fragment caging, since it pointed into the cluster, while the Cl fragment would dissociate unhindered from the clusters yielding the faster Cl even beyond E_{max}. This type of arrangement of the surface layer was suggested as one of the possible structures (branched structure) for large HCl clusters.[71] However, the analogy between CH_3Cl and HCl clusters is limited. Clearly, further theoretical insight into the cluster structure and dissociation dynamics would be required to resolve these issues.

The Cl and Cl* fragments exhibit the bimodal KED shape in Figures 6 and 7 with a broad maximum at ≈0.6 eV and a low-energy distribution starting near zero. The Cl kinetic energy of 0.6 eV would correspond to about 0.85 eV of the internal excitation energy in the CH_3 fragment if the fragments originated from a two-body CH_3Cl dissociation. Such high CH_3 excitation seems unrealistic. However, the Cl fragment can lose its energy gradually in inelastic collisions with other cluster constituents. The peak at 0.6 eV is shifted by about 0.2 eV from the maximum of the monomer dissociation. Thus, the Cl fragment, which was generated with the kinetic energy of 0.8 eV in the photodissociation process, has to deposit 0.2 eV into the cluster internal degrees of freedom in some inelastic processes to contribute to the maximum at 0.6 eV. There are many intra- and intermolecular modes where the escaping Cl fragment can deposit the 0.2 eV energy in the cluster, and the large width of the peak reflects the many possibilites where the energy can be stored in the cluster. Nevertheless, this does not explain the bimodal character of the KED distribution.

We have considered the possibility of the lower energy Cl fragments originating from the photodissociation of molecules in the cluster interior, for which the fragment caging is more likely than for the (near-)surface molecules. The surface molecules would then yield the faster ≈0.6 eV peak including the fragments with energies beyond E_{max}. To test this hypothesis experimentally, we exploit different expansion conditions yielding different cluster sizes. The larger clusters with smaller surface-to-volume ratio should have a smaller relative contribution of the faster ≈0.6 eV peak in KED; i.e., this peak should decrease with the cluster size relative to the near-zero energy peak. The cluster size should increase with the expansion pressure (at a constant CH_3Cl/Ar concen-

https://dx.doi.org/10.1021/acs.jpca.0c05926
J. Phys. Chem. A 2020, 124, 7633−7643

tration). Therefore, we have performed the experiment for several stagnation pressures between 1 and 3 bar as shown in Figure 7. However, the KEDs do not exhibit any significant differences. In addition, the spectrum recorded in pure CH_3Cl expansion looked also essentially the same. It is possible that the cluster size change achieved by the different expansion conditions might not be sufficient to induce an observable change in the surface-to-volume ratio. Although this seems unlikely, based on our experience with the cluster generation, we cannot disprove this possibility. In any case, the above proposed explanation of the bimodal character of the Cl fragment KED remains speculative, and theoretical calculations of the clusters and potential energy perturbations would be highly desirable.

Another interesting experimental observation is the 10 times increase in the signal intensity ratio of CH_3 to Cl fragments I_{CH_3}/I_{Cl} in clusters compared to isolated molecules. First, we have to check that this cannot be an experimental artifact resulting from the delay between the photodissociation and ionization laser pulses. The CH_3 fragments are faster than the Cl fragments and could escape the ionization volume during the 10 ns delay time in the experiments with isolated molecules. More CH_3 fragments would then be detected in the cluster experiment, where they are efficiently slowed down. We performed simple simulations estimating how the fragments escape the ionization volume. They suggested that the majority of the CH_3 fragments should be still confined within the ionization volume after the 10 ns delay. We have performed an experimental check as well, measuring the I_{CH_3}/I_{Cl} ratio for different delay times between −5 and +15 ns. There seems to be a slight decrease of the I_{CH_3}/I_{Cl} ratio (about 20% between 0 and 15 ns); however, this could not by far explain the 10-fold increase of the ratio observed in the clusters. Therefore, we seek other interpretations in the cluster photodissociation dynamics.

In our experiments, we detect the CH_3 fragments in the vibrational ground $\nu = 0$ state. As already mentioned above, our REMPI signal from the higher ν_2 states was too low to record reliable images. The Cl KED spectra of the monomer dissociation suggest a preferential population of $\nu_2 = 2-3$ states. The $CH_3(\nu = 0)$ fragment relative intensity could be increased in the clusters by quenching the higher ν_2 vibrational states and funneling the population into the $\nu = 0$ state. To check this hypothesis, we record the action spectra for isolated molecules (in He expansion) and for clusters (in Ar); see Figure 4. For isolated molecules, the integrated intensity of the $\nu_2 = 1$ resonance peak corresponds to roughly half of the ground state peak as already mentioned above. However, in clusters we do not observe any significant peak at the $\nu_2 = 1$ resonance position within our sensitivity better than 3×10^{-2}. Thus, the quenching of the higher vibrational states of CH_3 fragments populated in clusters can explain qualitatively the observed $CH_3(\nu = 0)$ intensity increase. Indeed, since we could not detect the higher ν_2 states in our experiment, the proposed cluster quenching cannot provide quantitative agreement, and other possible mechanisms could contribute to the observed I_{CH_3}/I_{Cl} ratio increase in clusters.

There is another possible explanation of the observed I_{CH_3}/I_{Cl} ratio increase, namely, a decrease of the detection probability of the Cl fragments in clusters. In the investigation of the photodissociation of CH_3I in clusters by Syage,[26] generating of I_2 molecules was proposed by reactions of I fragments with another CH_3I molecule. The generation of I_2 in the $(CH_3I)_2$ dimers was also discussed by Vidma et al.[20] Analogous reactions of Cl fragments within CH_3Cl clusters can be proposed to yield Cl_2. This process would lead to a loss of the detected Cl fragments from CH_3Cl in the clusters and correspondingly to the increase of the I_{CH_3}/I_{Cl} ratio.

Finally, we have also evaluated the branching ratio between the Cl* and Cl channel for the photodissociation in clusters, which was ≈0.55 ± 0.15 compared to 0.86 given in the literature for the isolated molecule.[5−7,48,49] Thus, the cluster environment enhances the reaction pathways leading to the $Cl(^2P_{3/2})$ ground state in comparison with the $Cl^*(^2P_{1/2})$ output channel. Similar enhancement of the $^2P_{3/2}$ ground state with respect to the $^2P_{1/2}$ state was observed already for the photodissociation of CH_3I in clusters.[26] The above-mentioned intracluster reactions generating I_2 were mentioned as a possible explanation since the excited state may react preferentially to give I_2. Analogous reactions of the $Cl^*(^2P_{1/2})$ would deplete the excited state channel in our case. Also the $^2P_{1/2}$ state could be collisionally relaxed to the ground state $^2P_{3/2}$, as was also proposed in the case of CH_3I clusters,[26] and the probabilities for electronically nonadibatic quenching of Cl* in collisions with D_2 and He were measured.[72] Indeed, there is also the possibility that the branching ratio changes due to the change in the potential energy surface near the crossing due to the solvent effects, and the dissociation channel along the $^1Q_1$ potential leading to the $Cl(^2P_{3/2})$ ground state is enhanced in the clusters. However, we cannot use our measured [Cl*]/[Cl] branching ratio and β parameters to estimate the ISC probabilities of $P^3{}_{Q_0} \rightarrow {}^1Q_1$ and $P^1{}_{Q_1} \rightarrow {}^3Q_0$ as done by Townsend et al.[7] For the photodissociation in the clusters, the observed isotropic distibution $\beta \approx 0$ stems from the postdissociation fragment scattering in the clusters rather than from the genuine dynamics at the intersystem crossing; therefore, it cannot be used to evaluate the ISC probability. Even if the surface-crossing probabilities are not affected relative to the monomer, a shift in the band origins and/or absorption cross sections of the involved states in the cluster environment would still change the observed product branching. Clearly some theory is required here.

CONCLUSIONS

We have investigated the photodissociation of CH_3Cl at 193.3 nm using the velocity map imaging technique. For the isolated molecules, we find our results in an excellent agreement with the previous experiments of Townsend et al.,[7] and we have extended the previous study of Cl fragments by measuring also the CH_3 fragments in the vibrational ground state. The CH_3 fragments exhibited angular distribution corresponding to the anisotropy recoil parametr $\beta = -0.77(0.10)$, and for $\nu_2 = 1$ we tentatively observe an even higher anisotropy of $\beta = -0.95(0.19)$ corresponding to a process of perpendicular character. These observations fully confirm conclusions of the previous work.[7]

Our main focus is on the photodissociation of CH_3Cl in the cluster environments. Using Ar as the buffer gas, we produce relatively large pure $(CH_3Cl)_n$ clusters composed of tens or possibly even hundreds of molecules. We can see clear signatures of cluster photodissociation in both Cl (and Cl*) and CH_3 fragment images: the intense central isotropic features. The corresponding KEDs evaluated from these

https://dx.doi.org/10.1021/acs.jpca.0c05926
J. Phys. Chem. A 2020, 124, 7633−7643

central features reveal significant differences in the CH_3 and Cl fragment behavior. While the CH_3 fragments exhibit a strong caging resulting in a very narrow near-zero kinetic energy peak, the Cl (and Cl*) fragments show a more structured KED extending all the way to the maximum available kinetic energy. A small fraction of the Cl fragments exhibits even energies larger than the maximum available energy. This corresponds to the kinematic effect, when the Cl fragment dissociates against the cluster rather than just against the CH_3 fragment in a two-body-like process. The observed Cl KED spectra have a bimodal character with a broad near-zero distribution and a broad peak near 0.6 eV. We discuss the differences between the CH_3 and Cl fragment dynamics as well as the bimodal character of Cl KED in terms of the cluster structure and mechanical fragment caging and delayed exit. However, theoretical investigations of cluster structure, dynamics, and solvent effects on the potential hypersurfaces are needed to elucidate the observed effects.

Another intriguing experimental observation is a higher propensity for detecting the CH_3 fragments from clusters compared to the CH_3 fragments from monomers. The ratio of integrated signals of CH_3 to Cl fragments I_{CH_3}/I_{Cl} is about 10 times higher from the cluster images than from the monomer images. We suggest that the higher vibrationally excited ν_2 states of the CH_3 fragments generated in the CH_3Cl molecule photodissociation (Cl KED maximum corresponds to $\nu_2 \approx 2-3$) are quenched to the ground state $CH_3(\nu = 0)$ in the clusters. For the above I_{CH_3}/I_{Cl} ratio, we detect the $CH_3(\nu = 0)$ only; thus, its relative population increases for the photodissociation in the clusters. This observation is also supported by the action spectra, where we see depopulation of the $\nu_2 = 1$ peak in the clusters. Another explanation of the observed I_{CH_3}/I_{Cl} ratio increase can involve Cl fragment loss by reactions in the clusters generating Cl_2, in analogy with CH_3I experiments.[20,26]

Finally, we determine the [Cl*]/[Cl] branching ratio for photodissociation pathways in the clusters as $\approx 0.55 \pm 0.15$, compared to 0.86 determined for isolated molecules.[5−7,48,49] Thus, the cluster environment enhances the reaction pathways leading to the Cl ground state in comparison with the Cl* output channel; i.e., the dissociation channel along the $^1Q_1$ potential is enhanced in the clusters. Several scenarios are proposed to explain the observed change in the branching ratio qualitatively.

Our experimental observations are unambiguous; however, they call for theoretical explanations. The cluster structure calculations, and especially the calculations of the effects of the environment on the potential energy hypersurfaces, on which the photodissociation dynamics proceeds would be highly desirable.

■ ASSOCIATED CONTENT

Supporting Information

The Supporting Information is available free of charge at https://pubs.acs.org/doi/10.1021/acs.jpca.0c05926.

Additional experimental data; VMI images in the molecular and clustering regime; multiphoton effect and pressure dependence of the cluster images (PDF)

■ AUTHOR INFORMATION

Corresponding Author

Michal Fárník − *J. Heyrovský Institute of Physical Chemistry, Czech Academy of Sciences, 182 23 Prague 8, Czech Republic;* orcid.org/0000-0002-7106-0719; Phone: +420 2 66053206; Email: michal.farnik@jh-inst.cas.cz

Authors

Ivo S. Vinklárek − *J. Heyrovský Institute of Physical Chemistry, Czech Academy of Sciences, 182 23 Prague 8, Czech Republic; Faculty of Mathematics and Physics, Charles University, 121 16 Prague 2, Czech Republic*

Jozef Rakovský − *J. Heyrovský Institute of Physical Chemistry, Czech Academy of Sciences, 182 23 Prague 8, Czech Republic*

Viktoriya Poterya − *J. Heyrovský Institute of Physical Chemistry, Czech Academy of Sciences, 182 23 Prague 8, Czech Republic*

Complete contact information is available at: https://pubs.acs.org/10.1021/acs.jpca.0c05926

Notes

The authors declare no competing financial interest.

■ ACKNOWLEDGMENTS

The authors acknowledge the support of the Czech Science Foundation (GAČR) project No. 19-14105S and also the Praemium Academiae of the Czech Academy of Sciences.

■ REFERENCES

(1) Chandler, D. W.; Houston, P. L. Two-Dimensional Imaging of State-Selected Photodissociation Products Detected by Multiphoton Ionization. *J. Chem. Phys.* **1987**, *87*, 1445−1447.

(2) Monce, M. N.; Edwards, A. K.; Wood, R. M.; Steuer, M. F.; Shah, A. V. Coincidence Detection of Dissociative Fragments from CH_3Cl. *J. Chem. Phys.* **1983**, *78*, 597−598.

(3) Kawasaki, M.; Kasatani, K.; Sato, H.; Shinohara, H.; Nishi, N. Photodissociation of Molecular Beams of Halogenated Hydrocarbons at 193 nm. *Chem. Phys.* **1984**, *88*, 135−142.

(4) Tiemann, E.; Kanamori, H.; Hirota, E. Diode Laser Spectroscopy for Monitoring the Yield of Metastable Cl from Photodissociation of Simple Molecules. *J. Chem. Phys.* **1988**, *88*, 2457−2468.

(5) Matsumi, Y.; Das, P. K.; Kawasaki, M. *Erratum*: Doppler Spectroscopy of Chlorine Atoms Generated from Photodissociation of Hydrogen Chloride and Methyl Chloride at 157 and 193 nm [J. Chem. Phys. 92, 1696 (1990)]. *J. Chem. Phys.* **1992**, *97*, 5261−5261.

(6) Melchior, A.; Lambert, H. M.; Dagdigian, P. J.; Bar, I.; Rosenwaks, S. The Photodissociation of Ground and Vibrationally Excited Halogenated Alkanes. *Isr. J. Chem.* **1997**, *37*, 455−465.

(7) Townsend, D.; Lee, S. K.; Suits, A. G. DC Slice Imaging of CH_3Cl Photolysis at 193.3 nm. *J. Phys. Chem. A* **2004**, *108*, 8106−8114.

(8) Kato, H.; Masui, H.; Hoshino, M.; Cho, H.; Ingólfsson, O.; Brunger, M. J.; Limão-Vieira, P.; Tanaka, H. A-Band Methyl Halide Dissociation via Electronic Curve Crossing as Studied by Electron Energy Loss Spectroscopy. *J. Chem. Phys.* **2010**, *133*, 054304.

(9) Kartakoullis, A.; Samartzis, P. C.; Kitsopoulos, T. N.; Parker, D. H. Photodissociation of Methyl Iodide and Methyl Iodide Clusters at 193 nm. *J. Phys. Chem. C* **2013**, *117*, 22383−22390.

(10) Eppink, A. T. J. B.; Parker, D. H. Energy Partitioning Following Photodissociation of Methyl Iodide in the A-Band: A Velocity Mapping Study. *J. Chem. Phys.* **1999**, *110*, 832−844.

(11) de Nalda, R.; Izquierdo, J. G.; Durá, J.; Bañares, L. Femtosecond Multichannel Photodissociation Dynamics of CH_3I from the A-Band by Velocity Map Imaging. *J. Chem. Phys.* **2007**, *126*, 021101.

(12) Durá, J.; de Nalda, R.; Amaral, G. A.; Bañares, L. Imaging Transient Species in the Femtosecond A-Band Photodissociation of CH_3I. *J. Chem. Phys.* **2009**, *131*, 134311.
(13) Rubio-Lago, L.; García-Vela, A.; Arregui, A.; Amaral, G. A.; Bañares, L. The Photodissociation of CH_3I in The Red Edge of the A-Band: Comparison Between Slice Imaging Experiments and Multi-surface Wave Packet Calculations. *J. Chem. Phys.* **2009**, *131*, 174309.
(14) Murillo-Sánchez, M. L.; González-Vázquez, J.; Corrales, M. E.; de Nalda, R.; Martínez-Nuñez, E.; García-Vela, A.; Bañares, L. Femtochemistry Under Scrutiny: Clocking State-Resolved Channels in the Photodissociation of CH_3I in the A-Band. *J. Chem. Phys.* **2020**, *152*, 014304.
(15) Blanchet, V.; Samartzis, P. C.; Wodtke, A. M. UV Photodissociation of Methyl Bromide and Methyl Bromide Cation Studied by Velocity Map Imaging. *J. Chem. Phys.* **2009**, *130*, 034304.
(16) Corrales, M. E.; de Nalda, R.; Bañares, L. Strong Laser Field Control of Fragment Spatial Distributions from a Photodissociation Reaction. *Nat. Commun.* **2017**, *8*, 1−7.
(17) Lipciuc, M. L.; Janssen, M. H. M. High-Resolution Slice Imaging of Quantum State-to-State Photodissociation of Methyl Bromide. *J. Chem. Phys.* **2007**, *127*, 224310.
(18) Wang, F.; Lipciuc, M. L.; Kartakoullis, A.; Glodic, P.; Samartzis, P. C.; Yang, X.; Kitsopoulos, T. N. Slice Imaging of Methyl Bromide Photofragmentation at 193 nm. *Phys. Chem. Chem. Phys.* **2014**, *16*, 599−606.
(19) Lambert, H. M.; Dagdigian, P. J. Photodissociation of Vibrationally Excited CH_3Cl: Modification of the Dissociation Dynamics. *Chem. Phys. Lett.* **1997**, *275*, 499−505.
(20) Vidma, K. V.; Baklanov, A. V.; Khvorostov, E. B.; Ishchenko, V. N.; Kochubei, S. A.; Eppink, A. T. J. B.; Chestakov, D. A.; Parker, D. H. UV Photodissociation of the van der Waals Dimer $(CH_3I)_2$ Revisited: Pathways Giving Rise to Ionic Features. *J. Chem. Phys.* **2005**, *122*, 204301.
(21) Solà, M.; Carbonell, E.; Lledós, A.; Duran, M.; Bertran, J. *Ab Initio* Study of the Effect of External Perturbations in the Dissociation of CH_3Cl. *J. Mol. Struct.: THEOCHEM* **1992**, *255*, 283−296.
(22) Escure, C.; Leininger, T.; Lepetit, B. *Ab Initio* Study of Methyl-Bromide Photodissociation in the A-Band. *J. Chem. Phys.* **2009**, *130*, 244305.
(23) Granucci, G.; Medders, G.; Velasco, A. M. Potential Energy Surfaces of the First Three Singlet States of CH_3Cl. *Chem. Phys. Lett.* **2010**, *500*, 202−206.
(24) De Medeiros, V. C.; De Andrade, R. B.; Leitão, E. F.; Ventura, E.; Bauerfeldt, G. F.; Barbatti, M.; Do Monte, S. A. Photochemistry of CH_3Cl: Dissociation and CH···Cl Hydrogen Bond Formation. *J. Am. Chem. Soc.* **2016**, *138*, 272−280.
(25) Syage, J. A. Angle-Velocity-Resolved Measurements of $I(^2P_{(3/2,1/2)})$ from $(CH_3I)_n$ Cluster Photodissociation at 266 and 304 nm. *Chem. Phys. Lett.* **1995**, *245*, 605−614.
(26) Syage, J. A. State Specific, Angle Velocity Resolved Measurements of Photodissociation in Clusters: I Atom Escape from $(CH_3I)_n$ (n= 1,2,3). *Chem. Phys.* **1996**, *207*, 411−426.
(27) Tanaka, Y.; Kawasaki, M.; Matsumi, Y. Ion Fragment Imaging of the Photodissociation of Methyl Iodide Small Clusters at 266 nm. *Bull. Chem. Soc. Jpn.* **1998**, *71*, 2539−2545.
(28) Das, S.; Sharma, P.; Vatsa, R. K. Tracing Photoionisation Behaviour of Methyl Iodide in Gas Phase: From Isolated Molecule to Molecular Aggregate. *J. Photochem. Photobiol., C* **2017**, *33*, 27−53.
(29) Suits, A. G. Photofragment Imaging. *Rev. Sci. Instrum.* **2018**, *89*, 111101.
(30) Wang, F.; Lipciuc, M. L.; Yang, X.; Kitsopoulos, T. N. Multiphoton Dissociation Dynamics of CH_3Br. *Phys. Chem. Chem. Phys.* **2009**, *11*, 2234−2240.
(31) Mulliken, R. S. Halogen Molecule Spectra. II. Interval Relations and Relative Intensities in the Long Wave-Length Spectra. *Phys. Rev.* **1940**, *57*, 500.
(32) Zhong, D.; Cheng, P. Y.; Zewail, A. H. Bimolecular Reactions Observed by Femtosecond Detachment to Aligned Transition States: Inelastic and Reactive Dynamics. *J. Chem. Phys.* **1996**, *105*, 7864−7867.
(33) Dzvonik, M.; Yang, S.; Bersohn, R. Photodissociation of Molecular Beams of Aryl Halides. *J. Chem. Phys.* **1974**, *61*, 4408−4421.
(34) Amatatsu, Y.; Morokuma, K.; Yabushita, S. *Ab Initio* Potential Energy Surfaces and Trajectory Studies of A-Band Photodissociation Dynamics: $CH_3I^* \rightarrow CH_3 + I$ and $CH_3 + I^*$. *J. Chem. Phys.* **1991**, *94*, 4858−4876.
(35) Amatatsu, Y.; Yabushita, S.; Morokuma, K. Full Nine-Dimensional *Ab Initio* Potential Energy Surfaces and Trajectory Studies of A-Band Photodissociation Dynamics: $CH_3I^* \rightarrow CH_3$+I, CH_3+I^*, and $CD_3I^* \rightarrow CD_3$+I, CD_3+I^*. *J. Chem. Phys.* **1996**, *104*, 9783−9794.
(36) Fedor, J.; Kočišek, J.; Poterya, V.; Votava, O.; Pysanenko, A.; Lipciuc, L.; Kitsopoulos, T. N.; Fárník, M. Velocity Map Imaging of HBr Photodissociation in Large Rare Gas Clusters. *J. Chem. Phys.* **2011**, *134*, 154303.
(37) Eppink, A. T. J. B.; Parker, D. H. Velocity Map Imaging of Ions and Electrons Using Electrostatic Lenses: Application in Photoelectron and Photofragment Ion Imaging of Molecular Oxygen. *Rev. Sci. Instrum.* **1997**, *68*, 3477−3484.
(38) Hudgens, J. W.; DiGiuseppe, T. G.; Lin, M. C. Two Photon Resonance Enhanced Multiphoton Ionization Spectroscopy and State Assignments of the Methyl Radical. *J. Chem. Phys.* **1983**, *79*, 571−582.
(39) Eppink, A. T.; Parker, D. H. Methyl Iodide A-band Decomposition Study by Photofragment Velocity Imaging. *J. Chem. Phys.* **1998**, *109*, 4758−4767.
(40) Arepalli, S.; Presser, N.; Robie, D.; Gordon, R. J. Detection of Cl Atoms and HCl Molecules by REMPI. *Chem. Phys. Lett.* **1985**, *118*, 88−92.
(41) Hickstein, D. D.; Gibson, S. T.; Yurchak, R.; Das, D. D.; Ryazanov, M. A Direct Comparison of High-Speed Methods for the Numerical Abel Transform. *Rev. Sci. Instrum.* **2019**, *90*, 065115.
(42) Whitaker, B. *Imaging in Molecular Dynamics*; Cambridge University Press: Cambridge, U.K., 2003.
(43) Grygoryeva, K.; Rakovský, J.; Vinklárek, I. S.; Votava, O.; Fárník, M.; Poterya, V. Vibrationally Mediated Photodissociation Dynamics of Pyrrole. *AIP Adv.* **2019**, *9*, 035151.
(44) Lülf, H.-W.; Andresen, P. In *Rarefied Gas Dynamics 13*; Belotserkovskii, O. M., Kogan, M. N., Kutateladse, S. S., Rebrov, A. K., Eds.; Plenum Press: New York, 1985; Vol. 2, p 911.
(45) Pauly, H. *Atom, Molecule and Cluster Beams*; Springer: Berlin, 2000.
(46) Irimia, D.; Kortekaas, R.; Janssen, M. H. M. *In situ* Characterization of a Cold and Short Pulsed Molecular Beam by Femtosecond Ion Imaging. *Phys. Chem. Chem. Phys.* **2009**, *11*, 3958−3966.
(47) Gougousi, T.; Samartzis, P. C.; Kitsopoulos, T. N. Photodissociation Study of CH_3Br in the First Continuum. *J. Chem. Phys.* **1998**, *108*, 5742.
(48) Zhang, J.; Dulligan, M.; Wittig, C. Photodissociation of HCl at 193.3 nm: Spin−Orbit Branching Ratio. *J. Chem. Phys.* **1997**, *107*, 1403.
(49) Regan, P. M.; Langford, S. R.; Ascenzi, D.; Cook, P. A.; Orr-Ewing, A. J.; Ashfold, M. N. R. Spin−Orbit Branching in $Cl(^2P)$ Atoms Produced by Ultraviolet Photodissociation of HCl. *Phys. Chem. Chem. Phys.* **1999**, *1*, 3247−3251.
(50) Matsumi, Y.; Das, P. K.; Kawasaki, M. Doppler Spectroscopy of Chlorine Atoms Generated from Photodissociation of Hydrogen Chloride and Methyl Chloride at 157 and 193 nm. *J. Chem. Phys.* **1990**, *92*, 1696−1701.
(51) Mulliken, R. S. Intensities in Molecular Electronic Spectra X. Calculations on Mixed-Halogen, Hydrogen Halide, Alkyl Halide, and Hydroxyl Spectra. *J. Chem. Phys.* **1940**, *8*, 382−395.
(52) Rubio-Lago, L.; Zaouris, D.; Sakellariou, Y.; Sofikitis, D.; Kitsopoulos, T. N.; Wang, F.; Yang, X.; Cronin, B.; Devine, A. L.; King, G. A.; et al. Photofragment Slice Imaging Studies of Pyrrole and the Xe···Pyrrole Cluster. *J. Chem. Phys.* **2007**, *127*, 064306.

https://dx.doi.org/10.1021/acs.jpca.0c05926
J. Phys. Chem. A 2020, 124, 7633−7643

(53) Lipciuc, M. L.; Wang, F.; Yang, X.; Kitsopoulos, T. N.; Fanourgakis, G. S.; Xantheas, S. S. Cluster-Controlled Photofragmentation: The Case of the Xe-Pyrrole Cluster. *ChemPhysChem* **2008**, *9*, 1838−1841.
(54) Glodic, P.; Kartakoullis, A.; Fárník, M.; Samartzis, P. C.; Kitsopoulos, T. N. Driving Photochemistry by Clustering: The ICl-Xe Case. *J. Chem. Phys.* **2012**, *137*, 154306.
(55) Poterya, V.; Kočišek, J.; Pysanenko, A.; Fárník, M. Caging of Cl atoms from Photodissociation of CF_2Cl_2 in Clusters. *Phys. Chem. Chem. Phys.* **2014**, *16*, 421−429.
(56) Poterya, V.; Kočišek, J.; Lengyel, J.; Svrčková, P.; Pysanenko, A.; Hollas, D.; Slavíček, P.; Fárník, M. Clustering and Photochemistry of Freon CF_2Cl_2 on Argon and Ice Nanoparticles. *J. Phys. Chem. A* **2014**, *118*, 4740−4749.
(57) Poterya, V.; Lengyel, J.; Pysanenko, A.; Svrčková, P.; Fárník, M. Imaging of Hydrogen Halides Photochemistry on Argon and Ice Nanoparticles. *J. Chem. Phys.* **2014**, *141*, 074309.
(58) Poterya, V.; Nachtigallová, D.; Fárník, J. L. M.; Lengyel, J. Photodissociation of Aniline N−H Bond in Clusters of Different Nature. *Phys. Chem. Chem. Phys.* **2015**, *17*, 25004−25013.
(59) Svrčková, P.; Pysanenko, A.; Lengyel, J.; Rubovič, P.; Kočišek, J.; Poterya, V.; Slavíček, P.; Fárník, M. Photodissociation Dynamics of Ethanethiol in Clusters: Complementary Information from Velocity Map Imaging, Mass Spectrometry and Calculations. *Phys. Chem. Chem. Phys.* **2015**, *17*, 25734−25741.
(60) Buck, U. Photodissociation of Hydrogen Halide Molecules in Different Cluster Environment. *J. Phys. Chem. A* **2002**, *106*, 10049−10062.
(61) Poterya, V.; Profant, V.; Fárník, M.; Slavíček, P.; Buck, U. Experimental and Theoretical Study of the Pyrrole Clusters Photochemistry: Closing the $\pi\sigma^*$ Dissociation Pathway by Complexation. *J. Chem. Phys.* **2007**, *127*, 064307.
(62) Fárník, M.; Poterya, V.; Votava, O.; Ončák, M.; Slavíček, P.; Dauster, I.; Buck, U. Solvent Induced Photostability of Acetylene Molecules in Clusters Probed by Multi-Photon Dissociation. *J. Phys. Chem. A* **2009**, *113*, 7322−7330.
(63) Poterya, V.; Profant, V.; Fárník, M.; Šištík, L.; Slavíček, P.; Buck, U. Photoinduced Processes in Hydrogen Bonded System: Photodissociation of Imidazole Clusters. *J. Phys. Chem. A* **2009**, *113*, 14583−14590.
(64) Slavíček, P.; Fárník, M. Photochemistry of Hydrogen Bonded Heterocycles Probed by Photodissociation Experiments and *Ab Initio* Methods. *Phys. Chem. Chem. Phys.* **2011**, *13*, 12123−12137.
(65) Nahler, N. H.; Baumfalk, R.; Buck, U.; Vach, H.; Slavíček, P.; Jungwirth, P. Photodissociation of HBr in and on Ar_n Clusters: The Role of the Position of the Molecule. *Phys. Chem. Chem. Phys.* **2003**, *5*, 3394−3401.
(66) Nahler, N. H.; Fárník, M.; Buck, U.; Vach, H.; Gerber, R. B. Photodissociation of HCl and Small $(HCl)_m$ Complexes in and on Large Ar_n Clusters. *J. Chem. Phys.* **2004**, *121*, 1293−1302.
(67) Poterya, V.; Fárník, M.; Slavíček, P.; Buck, U.; Kresin, V. V. Photodissociation of Hydrogen Halide Molecules on Free Ice Nanoparticles. *J. Chem. Phys.* **2007**, *126*, 071101.
(68) Ramasami, P.; Ford, T. A. The Structures and Vibrational Spectra of the Methyl Halide Dimers. An *Ab Initio* Study. *J. Mol. Struct.* **2016**, *1126*, 2−10.
(69) Futami, Y.; Kudoh, S.; Ito, F.; Nakanaga, T.; Nakata, M. Structure of Methyl Halide Dimers in Supersonic Jets by Matrix-Isolation Infrared Spectroscopy and Quantum Chemical Calculations. *J. Mol. Struct.* **2004**, *690*, 9−16.
(70) Harnes, J.; Abu-samha, M.; Winkler, M.; Bergersen, H.; Sæthre, L.; Børve, K. Neutral CH_3Cl and CH_3Br Clusters Studied by X-ray Photoelectron Spectroscopy and Modeling: Insight to Intermolecular Interactions and Structure. *J. Electron Spectrosc. Relat. Phenom.* **2008**, *166*, 53−64.
(71) Skvortsov, D.; Choi, M. Y.; Vilesov, A. F. Study of HCl Clusters in Helium Nanodroplets: Experiments and *Ab Initio* Calculations as Stepping Stones from Gas Phase to Bulk. *J. Phys. Chem. A* **2007**, *111*, 12711−12716.
(72) Parsons, B. F.; Chandler, D. W. An Investigation of Nonadiabatic Interactions in $Cl(^2P_j)+D_2$ via Crossed-Molecular-Beam Scattering. *J. Chem. Phys.* **2005**, *122*, 174306.

https://dx.doi.org/10.1021/acs.jpca.0c05926
J. Phys. Chem. A 2020, 124, 7633−7643

B.3 Publication III

Title: **Clustering and multiphoton effects in velocity map imaging of methyl chloride**

Journal: *Molecular Physics*
DOI: https://doi.org/10.1080/00268976.2020.1823507

Note: Drafted version.

Clustering and multiphoton effects in velocity map imaging of methyl chloride

I. S. Vinklárek[a], J. Rakovský, V. Poterya and M. Fárník

J. Heyrovský Institute of Physical Chemistry, Czech Academy of Sciences, Dolejškova 2155/3, 182 23 Prague 8, Czech republic;
[a] *also affiliated at:* Charles University, Faculty of Mathematics and Physics, Ke Karlovu 3, 121 16, Prague 2, Czech Republic

ARTICLE HISTORY
Compiled April 7, 2022

ABSTRACT
We have investigated different effects caused by clustering and multiphoton processes in the photodissociation of CH_3Cl using velocity map imaging (VMI). Single-photon dissociation of CH_3Cl at 193.3 nm yields CH_3 and Cl fragments probed subsequently by resonance enhanced multiphoton ionization (REMPI) at 333.52 nm and 235.31 nm, respectively. In the clusters, the CH_3 fragments are strongly "caged" losing most of their kinetic energy. Consequently, the VMI is dominated by a sharp central peak. On the other hand, the Cl fragments lose a broad range of energies in the cluster, yielding a blurred isotropic "central blob" in VMI. At an increased 193 nm photon flux, another central feature appears in the CH_3 images for isolated CH_3Cl molecules. This "hour-glass" shaped image corresponds to the CH_3Cl multiphoton ionization at 193 nm and subsequent CH_3Cl^+ ion photodissociation at 333 nm. The ion photodissociation is a parallel process with the anisotropy β-parameter values between +1.3 and +2.0. The total kinetic energy release (TKER) distribution suggests a high CH_3^+ vibrational excitation. The CH_3Cl^+ ion photodissociation is discussed and compared to the photodissociation of similar CH_3Br^+ ion.

KEYWORDS
photodissociation, molecular clusters, solvent effects, multiphoton ionization, energy transfer

1. Introduction

The introduction of the imaging technique for photodissociation products by Chandler and Houston [1] followed ten years later by velocity map imaging (VMI) by Eppink and Parker [2] opened new horizons in investigation of photodissociation dynamics. Many innovative and sophisticated modifications of the VMI technique have been developed since then, which have been outlined in quite a few books and reviews [3–8] and covered by topical journal issues [9, 10]. With this brilliant technique, the photodissociation dynamics of numerous molecules has been unveiled in unprecedented level of details. Nevertheless, extending this detailed knowledge from the individual molecules in the gas phase to the photodissociation in a solvent environment relevant

CONTACT M. Fárník, E-mail: michal.farnik@jh-inst.cas.cz

to the bulk chemistry still remains challenging. Cluster studies can help to bridge the gap between the isolated molecules and bulk.

Despite the huge progress in the imaging techniques, VMI of the photodissociation of molecules in clusters remains an uneasy task. One of the major problems represents the fact that the photodissociation fragments often collide with the cluster constituents and are slowed down to near-zero velocities (*caging*), resulting in structureless features at the center of the image often referred to as a "central blob". There are several problems with these central features. First, in the classical VMI using inverse Abel transformation, the mathematical procedure introduces a large noise close to the symmetry axis, which interferes with the central features. Second, the near-zero energy features and their errors are enhanced in the kinetic energy distributions due to the velocity→energy transformation, since the distribution is divided by the velocity. Finally, some molecules exhibit slow, near-zero energy fragments, e.g. from a statistical dissociation of individual molecules, and they overlap with the central features due to the clusters. Thus the cluster and molecular contributions are often difficult to disentangle.

Yet another problem in VMI of clusters is represented by molecular contribution in cluster beams. A certain cluster size distribution is always produced in a supersonic expansion. If small clusters are generated, usually the distribution has an exponential character. Thus, for example, if the mean cluster size corresponds to trimers, there are still more than twice as many monomers than the trimers in the beam [11]. Consequently, the VMI from the photodissociation of such a molecular beam might still be dominated by monomer features, despite a substantial cluster contribution.

When sharp rings corresponding to the photodissociation of isolated molecules persist in the cluster image, they can still have different origins, which are often difficult to disentangle. The rings can originate from the unclustered fraction of molecules in the beam, but they can also correspond to the fragments from the clusters that escaped without collisions with the cluster constituents. Indeed, the fragments photodissociated from clusters might be accelerated due to the larger momentum transfer from the heavier clusters [12], the rings can be blurred due to the energy transfer into the cluster modes etc. Nevertheless, assigning features observed in VMI experiments with clusters can be challenging.

Quite often in the literature, if the images from isolated molecules exhibited only sharp rings, the appearance of a central feature in the images was automatically associated with cluster effects [13–18]. Unambiguous cluster effects could be observed in experiments, where beams of relatively large clusters were generated and individual molecules were deposited on the clusters later on in a pickup cell before the photodissociation [19–21]. However, in other than pickup experiments the assignment of blurred central features might be more ambiguous, especially in VMI experiments without the capability of mass spectrometry with a sufficient mass range, resolution and sensitivity. Other effects, such as multiphoton processes, may generate central features in the images as well. We presented an example of ethanethiol [22], where we combined the VMI with reflectron time-of-flight mass spectrometry to demonstrate that a broad central blob in images resulted from multiphoton processes while the photodissociation in clusters yielded very sharp zero-kinetic-energy peak.

Here we present an example where distinct central features are observed, corresponding to different origins in the photodissociation of CH_3Cl. We demonstrate a clear difference between cluster effects and features which originate from multiphoton processes in isolated CH_3Cl molecules, namely multiphoton ionization and subsequent photodissociation of the nascent CH_3Cl^+ ion. Similar multiphoton ionization and ion

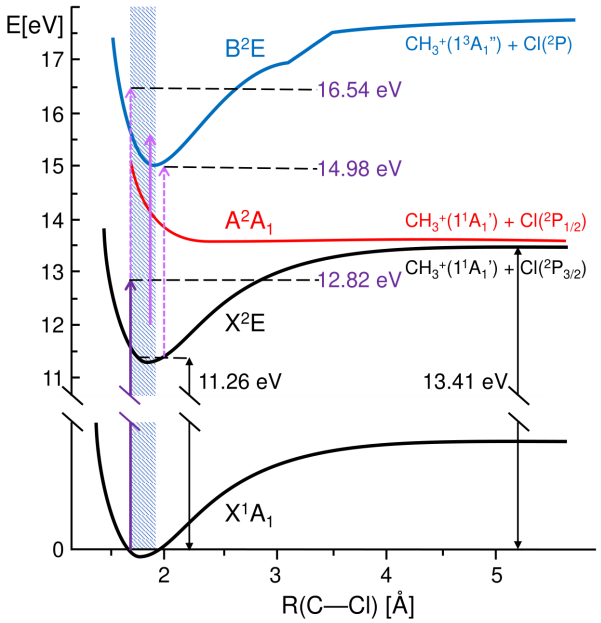


Figure 1. Schematic illustration of the cut through the potential energy surfaces of CH_3Cl molecule and CH_3Cl^+ ion along the C–Cl coordinate (based on [37]). Dashed area shows the Franck-Condon region, the violet vertical arrows indicate the possible UV excitations in our present experiment.

photodissociation was observed for CH_3Br previously [23, 24]. However, the confusion between the cluster and multiphoton effects resulting in the central features in images can be also illustrated on the CH_3Br example. The signal in the center of CH_3 images from CH_3Br observed earlier by Gougousi *et al.* [25] was originally attributed to the cluster photodissociation. Later on, the same group suggested that this signal should result from the photodissociation of CH_3Br^+ ion instead, see Wang *et al.* [24].

The photodissociation of CH_3Cl^+ ion has been studied since 1970s using the ion cyclotron resonance spectrometer [26–28], and other ion dissociation techniques[29–33]. More recently, also the photoelectron–photoion coincidence (PEPICO) spectrometry [34] and the mass-analyzed ion kinetic energy (MIKE) spectrometry [35] were implemented. In the later study the anisotropy parameters and kinetic energy release distributions of the CH_3^+ fragments were determined at several dissociation wavelengths. Accompanied quantum chemical calculations suggested excitation to the first excited electronic state A^2A_1 of a repulsive character, however, this transition should have a perpendicular character (anisotropy parameter $\beta = -1$), while the experimental results pointed a more parallel transition with $\beta = +1.2$. The parallel character of the CH_3Cl^+ dissociation was also observed in the earlier experiments [28]. Parallel transition would be consistent with the excitation of the next excited B^2E state. The dissociation was proposed to proceed via internal conversion (IC) from B to A followed by the dissociation on the A surface [32]. However, this pathway was disputed by a later theoretical study [36]. A recent experiments combining synchrotron radiation with double imaging photoelectron photoion coincidences (i^2PEPICO) shed more light onto the photodissociation dynamics of this ion [37].

Figure 1 shows a schematic sketch of the potentials along the C–Cl dissociation coordinate based on [37]. The X^2E ground state of the CH_3Cl^+ molecular ion adiabatically correlates to the $CH_3^+(1^1A_1') + Cl(^2P_{3/2})$ ground state. The A^2A_1 electronic state is repulsive and directly dissociates to produce $CH_3^+(1^1A_1')$ and $Cl(^2P_{1/2})$ in the

spin-orbit excited state. A large kinetic energy release and vibrational excitation of the ν_2 umbrella mode of the CH_3^+ fragment ion have been experimentally measured for the dissociation of the A^2A_1 state [37]. The B^2E electronic state is a bound state and it undergoes IC to the high vibrational states of the X^2E ground state of the ion and then statistically dissociates into $CH_3^+(1^1A_1')$ and $Cl(^2P_{3/2})$ fragments.

The purpose of our present work is twofold. First, we demonstrate a clear distinction between the cluster and multiphoton effects in the VMI of CH_3Cl molecules. Although similar examples of clustering or multiphoton effects (namely with CH_3I and CH_3Br molecules) can be found in the literature, here we provide a direct comparison for the single system, CH_3Cl. Second, we deliver further experimental data investigating the photodissociation of the CH_3Cl^+ ion. Despite the significant experimental and theoretical effort cited above, some issues still remain unresolved.

2. Experiment

The velocity map images (VMIs) were acquired with our Apparatus for IMaging (AIM) previously described in [16]. Briefly, the sample gas mixture of 7% of CH_3Cl seeded in Ar or He buffer gas was supersonically expanded through a pulsed valve nozzle with repetition rate of 10 Hz and skimmed to enter the vacuum chamber with VMI optics mounted perpendicularly to the molecular beam. The molecular beam was intersected by two laser beams. First, the molecules were irradiated at 193.3 nm (6.41 eV) by excimer laser (Coherent ExciStar XS) focused with $f_0 = 50$ cm lens. The laser beam was horizontally polarized with thin film polarizer (TFP) oriented at the Brewster angle. The second laser pulse from tunable UV-OPO laser (EKSPLA) followed the 193.3 nm pulse with the 10 ns delay. The UV-OPO laser was triggered at 5 Hz, half the 193.3 nm laser repetition rate, to enable shot-to-shot background signal measurement with the 193.3 nm only. Focusing of the UV-OPO laser beam was achieved by two lenses (plano-convex and positive meniscus) with effective focal length $f_0 = 25$ cm.

In the photodissociation experiment with CH_3Cl molecules and clusters, the molecules were photolyzed by the 193.3 nm photons and the fragments were ionized by the UV-OPO laser via resonance enhanced multiphoton ionization (REMPI) process in (2+1) excitation scheme. The CH_3 fragments in their vibrational ground state were efficiently ionized at 333.52 nm (3.72 eV), while the Cl fragments in the spin-orbit ground state $^2P_{3/2}$ were ionized at 235.31 nm (5.27 eV) [38]. Already here, we can reveal that in the multiphoton experiments discussed below the CH_3Cl molecule was ionized by two 193.3 nm photons and the CH_3Cl^+ molecular ion was dissociated by the ∼333 nm photon to yield the CH_3^+ ion fragments.

The generated ions were extracted from the focus area by ion optics according to the original design of Eppink and Parker [2] in the direction of gated microchannel plate (MCP) detector combined with phosphor screen recorded by the CCD camera (Unibrain). The timing of the gas and laser pulses and the MCP detector gating was synchronized by a delay generator (BNC 575).

The acquired images were processed by inverse Abel transformation to restore central cut through the original 3D velocity distribution, and further integrated according to the standard procedures [3, 39] to retrieve the total kinetic energy release (TKER) distribution and angular profiles. The TKER-axis was calibrated by measurements of H-fragments from the photodissociation of HBr molecules [16].

3. Results

3.1. Cluster effect

Recently, we have investigated the effects of the photodissociation of CH_3Cl in clusters in detail [38]. Using different buffer gas He or Ar in the expansion and/or probing different phases of the gas pulse in different delay times after the valve opening, we have clearly identified cluster-related features in the images. Figure 2 shows examples of the CH_3 (a) and Cl (b) fragment images. The images are split in half, the left hand side (labeled M) shows the isolated molecule results while the right hand side (labeled C) exhibits the image obtained from the clusters. The photodissociation of isolated molecules yields a single sharp ring with an anisotropy of a perpendicular character for each fragment. On the other hand, the cluster images are strongly dominated by an isotropic feature in the center. Panel (c) shows the corresponding TKER distributions of the two fragments. The TKER of CH_3 and Cl fragments from isolated molecules are shown by the black dashed-dotted and dotted lines, respectively. The blue and red full lines correspond to the TKER of the same fragments from the clusters. The monomer contributions obtained in the molecular regime have been subtracted from these distributions. Note that there is a difference of about two orders of magnitude in the intensity scales corresponding to the two fragments.

The two fragments exhibit a distinctly different behavior: while the CH_3 fragments are slowed down in the clusters to the kinetic energies peaking sharply close to zero (*caging*), the Cl fragments can loose different amount of their energy in the cluster and leave with different kinetic energies between zero and the maximum available energy $E_{max} = E_{avl} = 2.85$ eV. Their TKER distribution exhibits a bimodal distribution with maximum around 2 eV. Some of the Cl fragments even exceed E_{max}, which reflects the fact that the TKER axis assumes momentum and energy conservation in a direct two-body dissociation of an isolated CH_3Cl molecule. Partitioning of the excess energy between the CH_3 and Cl fragments and considering the momentum conservation would yield the maximum kinetic energies $E_{max}(CH_3) = E_{avl} \times \frac{m(Cl)}{M_{iso}} = E_{avl} \times f_{CH_3}$ and $E_{max}(Cl) = E_{avl} \times \frac{m(CH_3)}{M_{iso}} = E_{avl} \times f_{Cl}$ for the CH_3 and Cl fragments, respectively ($m(Cl)$, $m(CH_3)$ and M_{iso} are the masses of Cl, CH_3 and CH_3Cl, in this order). However, if the Cl fragment dissociate from the whole cluster rather than the isolated CH_3Cl molecule, $E_{max}(Cl)$ could be substantially larger assuming the same energy and momentum conservation due to the increase of the f_{Cl} factor, where M_{iso} would be replaced by the mass of the whole cluster M_{clu}, and $m(CH_3)$ by M_{clu} minus $m(Cl)$ mass. For large clusters, this factor converges to 1, $f_{Cl} \to 1$, and thus the Cl fragment from the cluster could eventually carry more of the available energy in kinetic energy than the Cl fragment from the isolated molecule. Thus, strictly speaking, the TKER axis is valid only for the CH_3 and Cl fragments from isolated molecules. Nevertheless, we plot the cluster results on the same energy scale for a direct comparison. Further details discussing the different behavior of CH_3 and Cl fragments after the photodissociation of CH_3Cl in the clusters can be found in our recent publication [38]. Here, the important point is that the cluster effects result in different central features in images, which can be anything between the sharp zero-energy peak (CH_3) and the quite blurred broad distribution (Cl).

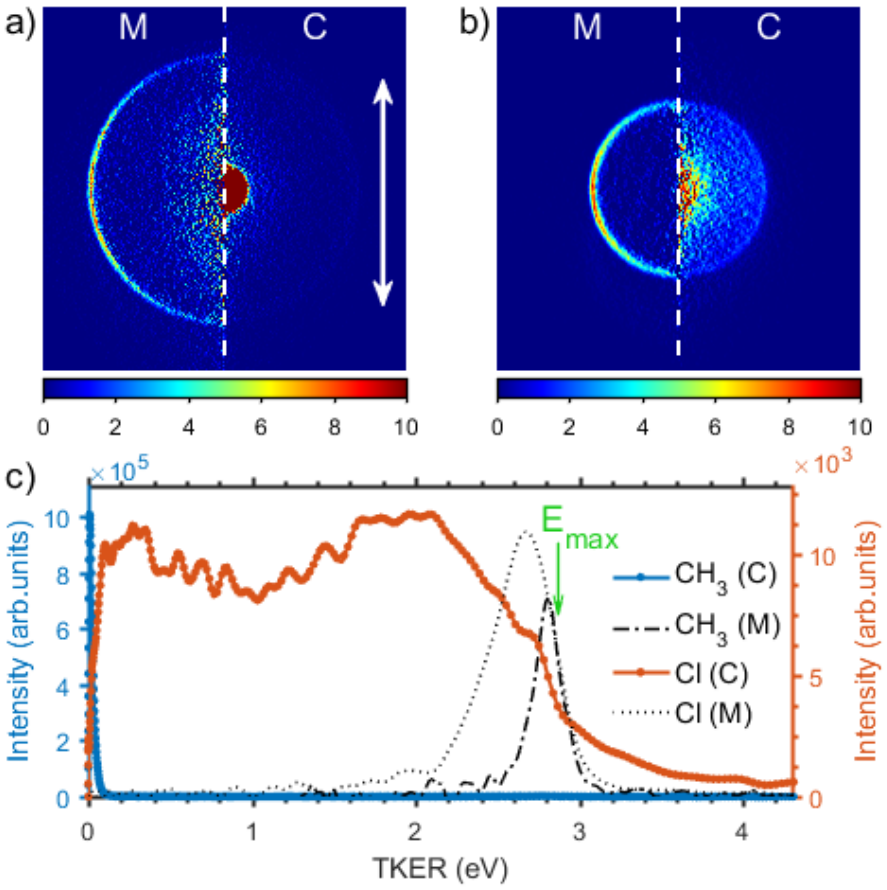


Figure 2. Photofragment images of CH_3 (a) and Cl (b) fragments after the photodissociation of CH_3Cl at 193 nm. The left hand side of the images corresponds to the molecular regime (M), the right hand side corresponds to the clusters (C). The bottom panel (c) shows the total kinetic energy release (TKER) distributions of the two fragments obtained from the clusters. The left intensity scale corresponds to the CH_3 fragment TKER (blue), the right one corresponds to the Cl distribution (red). The TKER distributions from isolated molecules are shown for comparison by black dashed-dotted and dotted lines, respectively (intensity was scaled arbitrarily for visual presentation). E_{max} denotes the maximum TKER available in the photodissociation of an isolated CH_3Cl molecule.

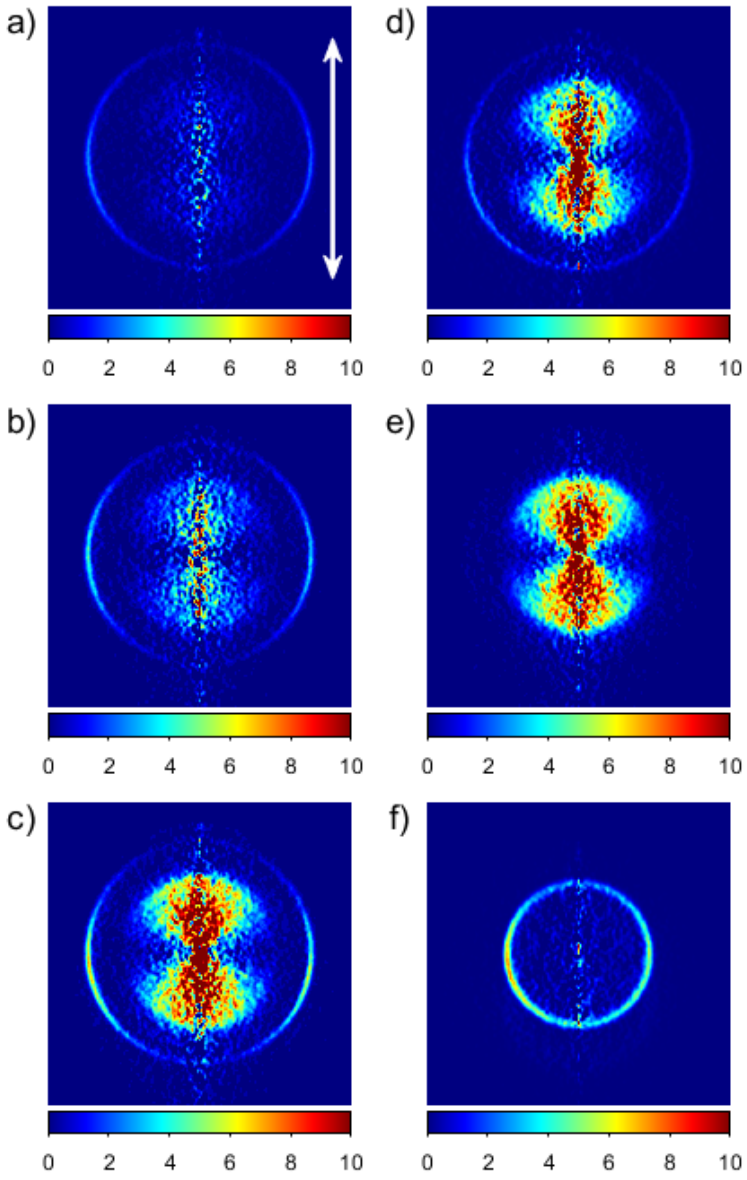


Figure 3. Photofragment images after the irradiation of isolated CH_3Cl molecules by 193.3 nm laser followed by UV-OPO pulse. Left column shows the images recorded at the UV-OPO wavelength of 333.52 nm corresponding to the CH_3 fragment REMPI. The 193.3 nm photon flux increased from (a) 4 to (b) 8 and to (c) 16×10^{25} photons·cm^{-2}s^{-1}. Both 193.3 nm and 333.52 nm lasers were polarized as indicated by the white arrow in panel (a). Image (d) corresponds to the same conditions as image (c), but the 193.3 nm laser was not polarized (TFP was removed from the laser beam). Image (e) corresponds again to the conditions of image (c), but the UV-OPO laser was tuned out-off resonance to 333.00 nm. Image (f) shows the Cl fragment image recorded under the conditions of image (c) with the UV-OPO laser tuned to the REMPI of Cl($^2P_{2/3}$) at 235.31 nm.

3.2. Multiphoton effect

Now, we focus on the expansion regime, where the molecular beam is composed of isolated molecules, and we investigate the effects of increased photon flux on the images. It yielded a central feature as well, however, of a different character. Figure 3, left column, shows the dependence of the images on the 193.3 nm laser intensity. Pannels (a)-(c) correspond to the increasing laser intensity resulting in the photon flux 4, 8 and 16×10^{25} photons$\cdot$cm^{-2}s^{-1}, respectively. The probe laser intensity was kept constant at the resonant wavelength of CH_3 REMPI of 333.52 nm. Besides the single sharp ring corresponding to the photodissociation of isolated CH_3Cl molecules and REMPI ionization of the CH_3 fragments, as discussed above in Figure 2, there appears a central "hour-glass" shaped feature increasing with the laser intensity. This image exhibits anisotropy parallel to the probe laser polarization, which is indicated by the white double-headed arrow in Figure 3 (a). The pump 193.3 nm laser was polarized in the same direction, however, the image was independent of the pump laser polarization, as indicated by image (d) recorded with unpolarized 193.3 nm laser. The image disappears when either of the two laser beams is blocked, thus it requires both the pump and the probe photons, however, the central feature is almost independent of the probe wavelength in a broad range $310 - 400$ nm. This is in agreement with previous measurements of CH_3Cl^+ ion photodissociation [26, 29]. The image recorded at 333.00 nm just off-resonance (333.52 nm) is shown in panel (e): the sharp ring disappears, nevertheless the hour-glass pattern remains essentially the same as in panel (c). Finally, panel (e) shows the Cl image corresponding to panel (c) recorded at the maximum 193 nm laser power. The REMPI laser for Cl was tuned to 235.31 nm corresponding to the ground state Cl($^2P_{3/2}$) ionization. This image is almost identical to the one presented in Figure 2 (b) showing that the Cl fragment image does not depend on the 193.3 nm photon flux.

Indeed, all the above evidence in Figure 3 points to a multiphoton origin of the hour-glass feature. A more quantitative picture can be gained by integrating the images to obtain the total signal intensity dependence on the 193.3 nm photon flux. This dependence is shown in Figure 4 (a). The measurements were done with unpolarized beam, therefore there are larger photon fluxes than in Figure 3. The images recorded at the REMPI wavelength 333.52 nm (blue circles) and off-resonance at 333.00 nm (red circles) are compared. In the off-resonance images, the single ring molecular image is missing, i.e. subtracting the off-resonance images from the REMPI ones results in the pure molecular ring deleting the central structure. The integral of the difference images is then plotted in panel (b). The dependencies of the total integrated signal both in and out of REMPI in panel (a) are clearly non-linear (fitted with a second order polynomial), while their difference in panel (b) depends linearly on the laser intensity. This suggests that a single photon process – namely the 193.3 nm CH_3Cl photodissociation – is responsible for the ring structure, while the hour-glass feature in the images is generated by processes involving more than one 193.3 nm photon.

Finally, turning the REMPI laser off at the high 193.3 nm photon flux resulted in two-photon ionization of CH_3Cl at 12.82 eV. The image of the parent CH_3Cl^+ ion is shown in detailed Figure 5 (a) corresponding to a tiny dot displaced from the image center as expected for CH_3Cl^+ travelling with the velocity of the molecular beam. Subtracting this primary beam image from the image with the REMPI laser on, results in an apparent hole in the image in place of the parent CH_3Cl^+ ions, Figure 5 (b). This suggests that the 333 nm (3.72 eV) photons dissociate the CH_3Cl^+ ions yielding the CH_3^+ fragments, which generate the observed hour-glass pattern in

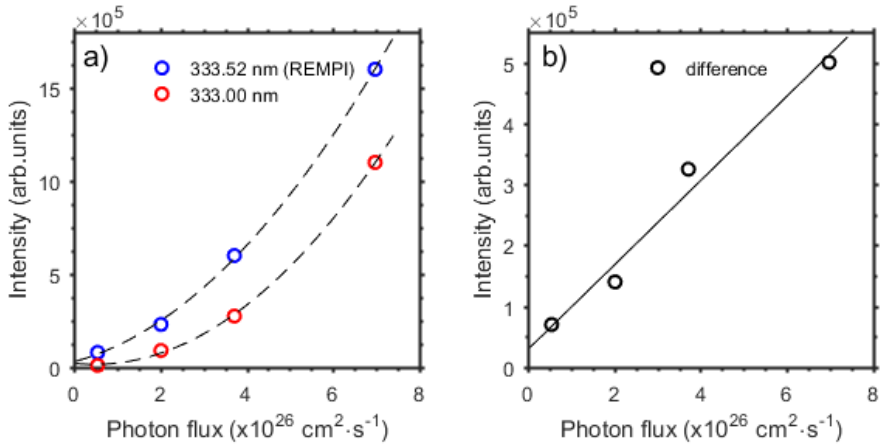


Figure 4. (a) Intensity dependence of CH_3 signal on 193.3 nm photon flux for OV-OPO laser tuned at the CH_3 REMPI wavelength (333.52 nm), blue circles, and just out-off resonance (333.00 nm), red circles. The difference between the signal in and out off resonance shows the linear dependence (b). These measurements were done with unpolarized 193.3 nm light without the TFP, therefore higher photon fluxes were achieved than in Figure 3.

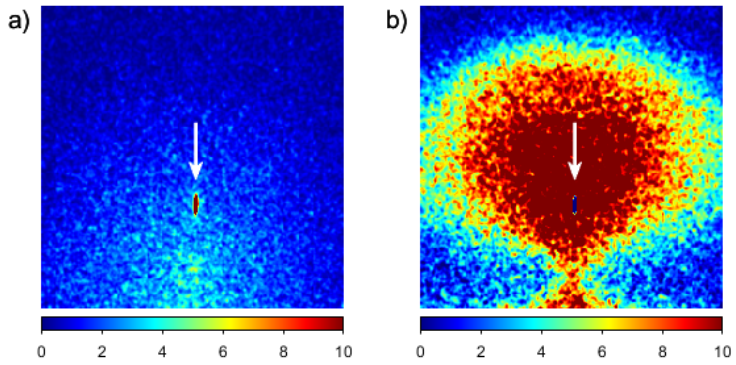


Figure 5. Raw image with 193.3 nm laser only (a). The image corresponds to the ionization of the beam to CH_3Cl^+ ions. The raw CH_3^+ fragment image recorded with UV-OPO laser at 333.52 nm (b), where the primary beam image (a) was subtracted.

the image. Increasing the time-delay of the probe laser resulted in essentially the same images as long as the CH_3Cl^+ ions did not escape the focus volume of the probe laser at the time delays well beyond the 10 ns.

To confirm the above proposed scenario, we record also the time-of-flight mass spectra with our VMI spectrometer. The spectra are shown in Figure 6. Panel (a) shows the spectrum recorded with the 193.3 nm laser only, and panel (b) the spectrum with the UV-OPO laser at 333.52 nm turned on as well. The bottom panel (c) shows the difference. Most of the peaks in the two spectra subtract completely, since they correspond to a non-specific 193.3 nm multiphoton ionization of the background molecules (mostly oil hydrocarbons from vacuum pumps). The subtraction of the C^+ and CH^+ peaks at $m/z = 12$ and 13 is not perfect, since these peaks are too large in the background saturating the detector. However, there are clear negative peaks in the difference spectrum at $m/z = 50$ and 52 corresponding to the CH_3Cl^+ parent ions (due to the ^{35}Cl and ^{37}Cl isotopes), and an intense positive peak at $m/z = 15$ corresponding to CH_3^+. This confirms that the CH_3Cl^+ parent ions are dissociated to

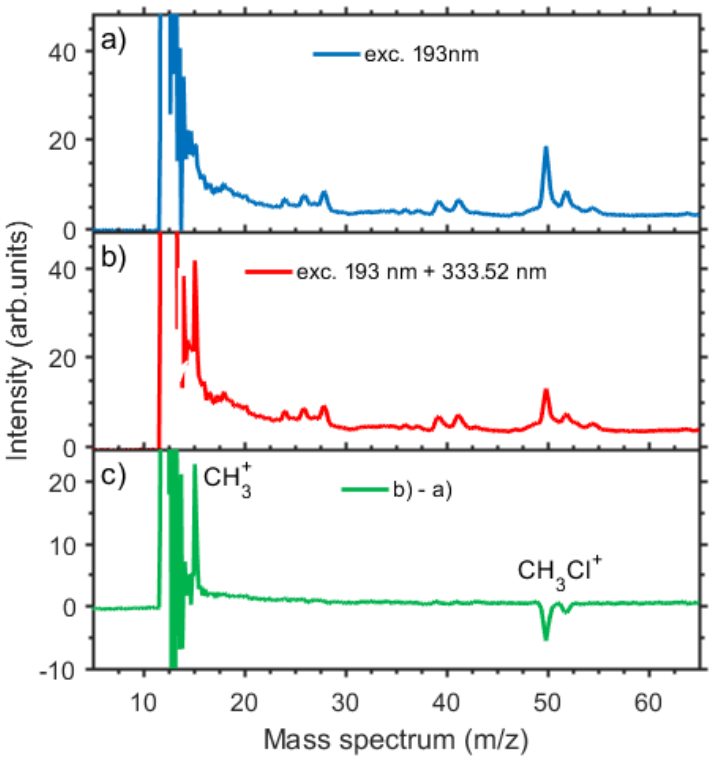


Figure 6. Time-of-flight mass spectra: (a) 193.3 nm laser only, (b) 193.3 nm and 333.52 nm, and (c) difference.

CH_3^+ by the 333 nm photons. It ought to be mentioned that the CH_3^+ images were recorded with gating the detector for the mass 15 amu, therefore there cannot be any interference from the ions below $m/z = 15$ in the images.

3.3. CH_3Cl^+ ion photodissociation

We have shown that the observed hour-glass shape pattern in the images corresponds to the photodissociation of CH_3Cl^+ ion, which was generated by two-photon ionization of CH_3Cl at 193.3 nm. To analyze the ion photodissociation process, we extract the CH_3^+ fragment TKER distribution in Figure 7. The distribution measured at the REMPI wavelength 333.52 nm exhibits the relatively narrow strong peak at 2.85 eV corresponding the 193 nm photodissociation of CH_3Cl and subsequent REMPI of the CH_3 fragment, which was observed and discussed previously [38, 40]. The CH_3Cl^+ ion photodissociation yields a broad distribution extending from zero to about 2 eV with a peak around 1.1 eV. When the VMI is recored off-resonance at 333.00 nm the sharp peak corresponding to the dissociation of CH_3Cl molecule disappears and only the broad distribution from the photodissociation of CH_3Cl^+ ion persists.

The hour-glass pattern in the VMI exhibits a parallel character. The angular distributions and corresponding anisotropy parameters β have been evaluated from the images and plotted as a function of the kinetic energy release in Figure 8. The angular distributions were evaluated in energy intervals of 0.14 eV. The β-parameter was obtained by fitting the angular distribution with the well-known formula [3] $I(\theta) \propto 1 + \beta P_2(\cos\theta)$, where $P_2(x) = \frac{3}{2}x^2 - \frac{1}{2}$ is the second order Legendre polynomial. An example of the angular distribution and the corresponding fit is shown

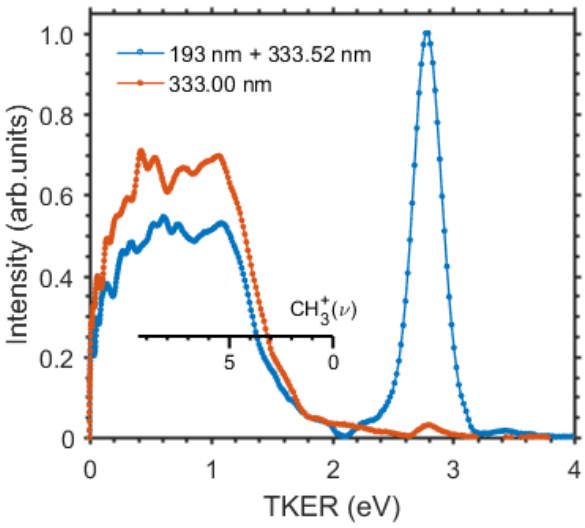


Figure 7. TKER spectra acquired at the CH_3 REMPI wavelength of 333.52 nm (blue) and off-resonance at 333.00 nm (red). The corresponding images are in Figure 3 (c) and (e), respectively.

in the inset of Figure 8 for the energy interval 1.00-1.14 eV. The graph confirms the prevailing perpendicular character of the photodissociation transition in the CH_3Cl^+ ion with β between +1.3 and +2.0.

4. Discussion

Figure 1 shows schematically the potentials along the C–Cl dissociating bond and the excitation processes involved in our experiment. CH_3Cl is ionized at 12.82 eV (i.e. via two 193.3 nm photon absorption), as indicated by the violet vertical arrow. The CH_3Cl^+ molecular ion is subsequently dissociated by a ∼333 nm (3.72 eV) photon. The ionization threshold of CH_3Cl into the $CH_3Cl^+(X^2E)$ ion ground state corresponds to 11.26 eV [41], i.e. the two-photon ionization proceeds about 1.5 eV above this threshold and the excess energy is partly carried away by the departing electron and the rest is distributed between the internal degrees of freedom of the CH_3Cl^+ ion. The X^2E ground state correlates with the $CH_3^+(1^1A_1)$ + $Cl(^2P_{3/2})$ dissociation. Based on the C–Cl bond dissociation energy $D_0(CH_3-Cl) = 3.565$ eV in CH_3Cl molecule [40, 42] and the adiabatic ionization energy of CH_3 $AIE(CH_3) = 9.843$ eV [43], the $CH_3Cl^+(X^2E)$ dissociation limit corresponds to 13.41 eV, as indicated in Figure 1 [37].

Further above the X^2E ground state, the dissociative A^2A_1 state can be found, which correlates to the $CH_3^+(1^1A_1)$ + $Cl(^2P_{1/2})$ dissociation. The difference between these two states in the asymptotic limit corresponds to the $Cl(^2P_{3/2})$-$(^2P_{1/2})$ spin-orbit splitting of 0.109 eV. Finally, above 15 eV, B^2E excited state of the ion is located, which is bound along the C–Cl coordinate.

The angular analysis of the hour-glass pattern in the images pointed to the prevailing parallel character of the corresponding photodissociation transition. This suggests that the excitation proceeds to the B^2E state. The $X^2E \rightarrow A^2A_1$ transition would have a perpendicular character, and a very low oscillator strength was calculated for this transition into the A^2A_1 state [35], since it is forbidden for the ground state ion of C_{3v} symmetry.

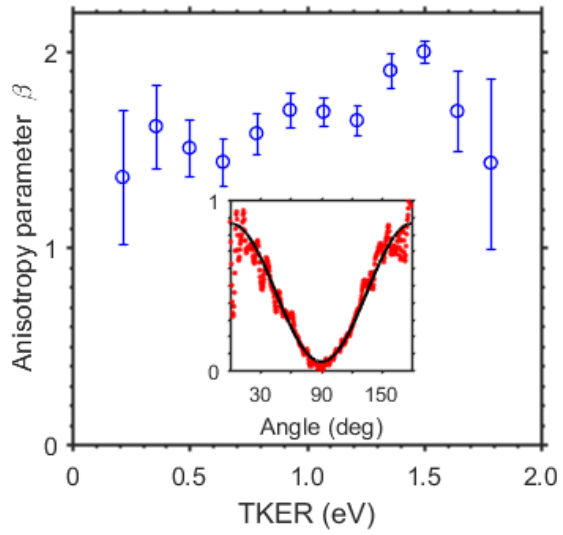


Figure 8. Fitted anisotropy parameter β as a function of the TKER obtained from image (c) in Figure 3. The inset shows an example of the angular distribution integrated for energy $E = 1.00 - 1.14$ eV together with the corresponding fit (see text).

Adding the photodissociation photon energy of 3.72 eV directly to the ionization energy of 12.82 eV, the total excitation energy would correspond to 16.54 eV and a relatively high vibrational level of the B^2E state could be excited, Figure 1. However, such process assumes a zero kinetic energy electron after the ionization, which is unrealistic. On the other hand, an electron with 1.56 eV kinetic energy would leave the CH_3Cl^+ ion in the X^2E state vibrational ground state $\nu = 0$ after the ionization. In such case, the total excitation energy with the dissociating photon would correspond to 14.98 eV just below the B^2E state. This is also an unlikely process, since we exclude the excitation directly into the A^2A_1 state based on the observed anisotropy of VMI and the low oscillator strength. Thus, the ion populates some $CH_3Cl^+(X^2E,\nu)$ energy levels between 11.26 eV and 12.82 eV, and the 333 nm photodissociation proceeds from a distribution of these levels, as indicated by the light purple arrows in Figure 1. The absorption of 333 nm photon promotes the ion into the B^2E state.

The dissociation of the B^2E state was proposed to proceed *via* the internal conversion to highly vibrationally excited (X^2E,ν) states, and further along the $CH_3^+(1^1A_1)$ + $Cl(^2P_{3/2})$ dissociation pathway [37]. The vibrationally excited $CH_3^+(\nu \geq 0)$ fragments can be produced. Thus the observed TKER distribution reflects a convolution of the distribution of the populated vibrational states of the parent CH_3Cl^+ ion, and the distribution of the CH_3^+ fragment vibrational states. From the unresolved TKER distribution in Figure 7, we cannot determine the populated vibrational states unambiguously, nevertheless, we attempt some reasonable estimates below.

The TKER distribution does not exhibit any sharp threshold, which is probably due to the distribution of the initial populated parent ion $CH_3Cl^+(\nu \geq 0)$ states. Nevertheless, the TKER suggests that the maximum released kinetic energy corresponds roughly to 2 eV indicated in Figure 7 by $CH_3^+(\nu = 0)$. This would imply that the highest excited state accessed by the photodissociation excitation of the ion would lie around 15.4 eV (i.e. the $CH_3^+(1^1A_1)$ + $Cl(^2P_{3/2})$ dissociation limit of 13.41 eV plus the 2 eV). Subtracting the 333 nm photon energy from the 15.4 eV, we obtain the highest populated $CH_3Cl^+(X^2E,\nu)$ ion level at 11.7 eV. This level lies about 0.4 eV above the

$CH_3Cl^+(X^2E,\nu = 0)$ ground state, and would be populated, if the ionizing photons would release an electron with 1.1 eV of the kinetic energy, which seems reasonable.

Assuming the threshold of TKER distribution at about 2 eV, the maximum of the distribution around 1.1 eV would correspond the excitation of about 5-6 vibrational quanta as indicated in Figure 7. We assume either umbrella mode ($\nu_2 = 168$ meV) or in-plane bend ($\nu_4 = 170$ meV) [44] excitation, based on the analogy with the CH_3Br^+ ion photodissociation [23, 24]. Blanchet *et al.* [23] observed excitation of high vibrational states of CH_3^+ fragments in the CH_3Br^+ photodissociation at around 330 nm. Vibrational states $\nu = 3 - 7$ or $5 - 9$ were observed, depending on alternative assignments of the Br fragment to the spin-orbit excited $^2P_{1/2}$ or ground $^2P_{3/2}$ state, respectively. Both ν_2 and ν_4 progressions fitted their spectra, and were mentioned as possible interpretations. Wang et al. [24] observed the CH_3Br^+ ion photodissociation in multiphoton one-color experiment. They dissociated the CH_3Br^+ ion also around 330 nm, and they assigned the CH_3^+ vibrational excitation to the ν_2 umbrella mode with the maximum occurring around $\nu_2 = 3 - 5$ for the dissociation channel where the Br fragment populated the spin-orbit excited level $Br(^2P_{1/2})$. Both CH_3Br experiments [23, 24] exhibit hour-glass shaped images for the CH_3Br^+ ion photodissociation with parallel character quite similar to the present CH_3Cl^+ photodissociation images. However, for the CH_3Br^+ ion, the resolution of vibrational structure was possible. Nevertheless, our TKER distribution also suggests the propensity for the channeling of the available energy into the CH_3^+ vibrations rather than to the fragment translation after the CH_3Cl^+ photodissociation in agreement with the CH_3Br^+ investigations [23, 24].

We can also compare our results to the earlier work of Won *at al.* [35], whose MIKES experiment provided the kinetic energy release spectra and anisotropy parameters β for the CH_3Cl^+ ion photodissociation. At the wavelength of 357 nm (3.47 eV), they obtained $\beta \approx +1.2$ and a broad Gaussian shaped energy spectrum peaking around 0.9 eV. These results are roughly similar to our present results, however, it ought to be mentioned that they produced the parent CH_3Cl^+ ions by electron ionization, and in the view of the current energy scheme in Figure 1, their dissociation energy of 3.47 eV would not be sufficient to reach the B^2E state from the ground vibrational state of the ion.

5. Conclusion

We have investigated the clustering and multiphoton effects in the photodissociation of CH_3Cl at 193.3 nm using VMI. Both these effects result in "central blobs" in the images, however, they can be clearly distinguished.

First, we analyze the clustering effects in the single-photon photodissociation of CH_3Cl at 193.3 nm yielding CH_3 and Cl fragments. They exhibit a distinctly different behavior: while the CH_3 fragments are slowed down in the clusters to the kinetic energies peaking sharply close to zero (*caging*), the Cl fragments can loose different amount of energy in the cluster and leave with kinetic energies between zero and the maximum available energy. Thus the clusters can exhibit images with any features between the sharp intense central peak (CH_3) and quite blurred isotropic "central blob" (Cl).

Multiphoton effects lead to two-photon 193.3 nm CH_3Cl ionization, and subsequently the CH_3Cl^+ ion is photolyzed at 333 nm yielding CH_3^+ fragment ion. This process produces an "hour-glass" shaped image of CH_3^+ from which the anisotropy

parameter β and TKER distribution are evaluated. The excitation is of parallel character with β ranging from +1.3 to +2.0 in dependence on the fragment kinetic energy. The TKER exhibits a broad distribution between zero and ≈2 eV suggesting high CH_3^+ vibrational excitation with maximum around $\nu \approx 5-6$ in ν_2 (umbrella) or ν_4 (in-plane bend) mode.

The two-photon ionization proceeds to the X^2E ion state subsequently excited by the photodissociation photon into the B^2E state. The internal conversion to highly vibrationally excited X^2E states then leads to the dissociation along the $CH_3^+(1^1A_1)$ + $Cl(^2P_{3/2})$ pathway.

Acknowledgement(s)

We acknowledge the support of the Czech Science Foundation (GAČR) project No.: 19-14105S and also Praemium Academiae of the Czech Academy of Sciences. We are also very grateful to Dave Parker, thanks to whom we have been invited to join the VMI community in 2009 within a European ITN network. We really enjoyed being part of this group of very nice people and excellent scientists, and we have benefited from that in many respects: notably, we have learned and introduced the VMI technique in our experiments in Prague. We really appreciate that Dave has always been very friendly and supportive to our group.

6. References

References

[1] D.W. Chandler and P.L. Houston, J. Chem. Phys. **87**, 1445 (1987).
[2] A.T.J.B. Eppink and D.H. Parker, Rev. Sci. Instrum. **68**, 3477 (1997).
[3] B. Whitaker, *Imaging in Molecular Dynamics* (Cambridge University Press, Cambridge, 2003).
[4] M.N.R. Ashfold, N.H. Nahler, A.J. Orr-Ewing, O.P.J. Vieuxmaire, R.L. Toomes, T.N. Kitsopoulos, I.A. Garcia, D.A. Chestakov, S.M. Wu, and D.H. Parker, Phys. Chem. Chem. Phys. **8**, 26 – 53 (2006).
[5] H. Reisler, Annu. Rev. Phys. Chem. **60**, 39 – 59 (2009).
[6] C. Vallance, Phil. Trans. R. Soc. Lond. A **96**, 2591 – 2609 (2014).
[7] D.W. Chandler, P.L. Houston and D.H. Parker, J. Chem. Phys. **147**, 013601 (2017).
[8] A.G. Suits, Rev. Sci. Instrum. **89**, 111101 (2018).
[9] A.G. Suits, M. Kawasaki and W. Lawrance, PCCP **8**, 2905–3036 (2006).
[10] D.W. Chandler, P.L. Houston and D.H.P. (editors), J. Chem. Phys. **147** (2017).
[11] V. Profant, V. Poterya, M. Fárník, P. Slavíček and U. Buck, J. Phys. Chem. A **111**, 12477 – 12486 (2007).
[12] P. Glodic, A. Kartakoullis, M. Fárník, P.C. Samartzis and T.N. Kitsopoulos, J. Chem. Phys. **137**, 154306 (2012).
[13] Y. Tanaka, M. Kawasaki and Y. Matsumi, Bull. Chem. Soc. Jpn **71**, 2539 – 2545 (1998).
[14] K.V. Vidma, A.V. Baklanov, E.B. Khvorostov, V.N. Ishchenko, S.A. Kochubei, A.T.J.B. Eppink, D.A. Chestakov and D.H. Parker, J. Chem. Phys. **122**, 204301 (2005).
[15] K.V. Vidma, D.H. Parker, G.A. Bogdanchikov, A.V. Baklanov and S.A. Kochubei, J. Phys. Chem. A **114**, 3067 (2010).
[16] J. Fedor, J. Kočišek, V. Poterya, O. Votava, A. Pysanenko, L. Lipciuc, T.N. Kitsopoulos and M. Fárník, J. Chem. Phys. **134**, 154303 (2011).
[17] A. Kartakoullis, P.C. Samartzis, T.N. Kitsopoulos and D.H. Parker, J. Phys. Chem. C **117**, 22383–22390 (2013).
[18] V. Poterya, J. Kočišek, A. Pysanenko and M. Fárník, Phys. Chem. Chem. Phys. **16**, 421 – 429 (2014).
[19] V. Poterya, J. Kočišek, J. Lengyel, P. Svrčková, A. Pysanenko, D. Hollas, P. Slavíček and M. Fárník, J. Phys. Chem. A **118**, 4740 – 4749 (2014).
[20] V. Poterya, J. Lengyel, A. Pysanenko, P. Svrčková and M. Fárník, J. Chem. Phys. **141**, 074309 (2014).
[21] V. Poterya, D. Nachtigallová, J. Lengyel and M. Fárník, Phys. Chem. Chem. Phys. **17**, 25004 – 25013 (2015).
[22] P. Svrčková, A. Pysanenko, J. Lengyel, P. Rubovič, J. Kočišek, V. Poterya, P. Slavíček and M. Fárník, Phys. Chem. Chem. Phys. **17**, 25734 – 25741 (2015).
[23] V. Blanchet, P.C. Samartzis and A.M. Wodtke, J. Chem. Phys. **130**, 034304 (2009).

[24] F. Wang, M.L. Lipciuc, X. Yang and T.N. Kitsopoulos, Phys. Chem. Chem. Phys. **11**, 2234–2240 (2009).
[25] T. Gougousi, P.C. Samartzis and T.N. Kitsopoulos, J. Chem. Phys. **5742**, 108 (1998).
[26] R.C. Dunbar, J. Am. Chem. Soc. **93**, 4354–4358 (1971).
[27] R.C. Dunbar and J.M. Kramer, J. Chem. Phys. **58**, 1266–1267 (1973).
[28] R.G. Orth and R.C. Dunbar, J. Chem. Phys. **68**, 3254–3259 (1978).
[29] M.L. Vestal and J.H. Futrell, Chem. Phys. Lett. **28**, 559–561 (1974).
[30] A.S. Werner, B.P. Tsai and T. Baer, J. Chem. Phys. **60**, 3650 (1974).
[31] T. Baer, A.S. Werner, B.P. Tsai and F.L. Stephen, J. Chem. Phys. **61**, 5468 (1974).
[32] J.H.D. Eland, R. Frey, A. Kuestler and H. Schulte, Int. J. Mass Spectrom. Ion Phys. **22**, 155 (1976).
[33] A. Carrington, D.R.J. Milverton and P.J. Sarre, Mol. Phys. **32**, 297 (1976).
[34] C. Lane and I. Powis, J. Phys. Chem. **97**, 5803 (1993).
[35] D.S. Won, M.S. Kima, J.C. Choe and T.K. Ha, J. Phys. Chem. **115**, 5454–5460 (2001).
[36] H.W. Xi, M.B. Huang, B.Z. Chen and W.Z. Li, J. Phys. Chem. A **109**, 4381–4387 (2005).
[37] X. Tang, X. Lin, W. Zhang, G.A. Garcia and L. Nahon, Phys. Chem. Chem. Phys. **18**, 23923–23931 (2016).
[38] I.S. Vinklárek, J. Rakovský, V. Poterya and M. Fárník, J. Phys. Chem. A **submitted** (2020).
[39] D.D. Hickstein, S.T. Gibson, R. Yurchak, D.D. Das and M. Ryazanov, Rev. Sci. Instrum. **90**, 065115 (2019).
[40] D. Townsend, S.K. Lee and A.G. Suits, J. Phys. Chem. A **108**, 8106–8114 (2004).
[41] S.E. Stein, in *NIST Mass Spec Data Center, "Mass Spectra" in NIST Chemistry WebBook, NIST Standard Reference Database Number 69*, edited by P. J. Linstrom and W. G. Mallard (National Institute of standards and Technology, Gaithersburg MD, 20899 (http://webbook.nist.gov), June 2005).
[42] V.C. De Medeiros, R.B. De Andrade, E.F. Leitão, E. Ventura, G.F. Bauerfeldt, M. Barbatti and S.A. Do Monte, J. Am. Chem. Soc. **138**, 272–280 (2016).
[43] B.K.C. de Miranda, C. Alcazar, M. Elhanine, B. Noller, P. Hemberger, I. Fischer, G.A. Garcia, H. Soldi-Lose, J. Žabka and P. Botschwina, J. Phys. Chem. A **114**, 4818–4830 (2010).
[44] X.H. Liu, R.L. Gross and A.G. Suits, Science **294**, 2527–2529 (2001).

B.4 Publication IV

Title: **Energy partitioning and spin–orbit effects in the photodissociation of higher chloroalkanes**

Journal: *Physical Chemistry Chemical Physics*
DOI: https://doi.org/10.1039/D1CP01371H

Supporting Information

Note: Use in submissions of dissertations is granted by Royal Society of Chemistry.

PCCP

ARTICLE TYPE

Cite this: DOI: 00.0000/xxxxxxxxxx

Energy Partitioning and Spin-orbit Effects in the Photodissociation of Higher Chloroalkanes

Ivo S. Vinklárek,[a‡] Jiří Suchan,[b] Jozef Rakovský,[a] Kamila Moriová,[a‡] Viktoriya Poterya,[a] Petr Slavíček,[*b] and Michal Fárník[*a]

Received Date
Accepted Date

DOI: 00.0000/xxxxxxxxxx

We investigate the photodissociation dynamics of C–Cl bond in chloroalkanes CH_3Cl, n-C_3H_7Cl, i-C_3H_7Cl, n-$C_5H_{11}Cl$, combining velocity map imaging (VMI) experiment and direct *ab initio* dynamical simulations. The Cl fragment kinetic energy distributions (KEDs) from the VMI experiment exhibit a single peak with maximum close to 0.8 eV, irrespective of the alkyl chain length and C–Cl bond position. In contrary to CH_3Cl, where less than 10% of the available energy is deposited into the internal excitation of the CH_3 fragment, for all higher chloroalkanes around 40% to 60% of the available energy goes into the alkyl fragment excitation. We apply the classical hard spheres and spectator model to explain the energy partitioning, and compare the classical approach with direct *ab initio* dynamics simulations. The alkyl chain appears to be a soft, energy absorbing unit. We further investigate the role of the spin-orbit effects on the excitation and dynamics. Combining our experimental data with theory allows us to derive the probability of the direct absorption into the triplet electronic state as well as the probabilities for intersystem crossing. The results indicate an increasing direct absorption into the triplet state with the increasing alkyl chain length.

1 Introduction

Photodissociation of halogenoalkanes is a prototypical polyatomic process, where one can directly investigate the energy transfer between modes and non-adiabatic transition between electronic states. These systems have, therefore, been largely studied by laser experiments and theory.[1–34] The majority of these investigations focused on the photodissociation of the smallest alkanes halo-methanes CH_3X (X = F, Cl, Br, I).[2–24,26–28,32] Due to the presence of the heavy halogen atom, the photodissociation dynamics is controlled by spin-orbit effects. Relatively large spin-orbit interaction opens up a possibility of a direct singlet-triplet absorption yielding various initial dissociative conditions[6,15,26,29,30] and subsequent mixing through intersystem crossing (ISC) on the dissociation pathway. The different reaction channels are reflected in the properties of the outgoing fragments, e.g. change in kinetic energy release, vibrational and rotational excitation and angular distribution. By far, the most extensively studied system was iodomethane CH_3I.[2,3,7–14,16,20,24] The chlorinated species received less attention[3–7,19,21,23,27,28] due to the expected weaker role of the spin-orbit interaction in the molecule with the lighter Cl atom. Nevertheless, we demonstrate here that the spin-orbit effects can play a non-negligible role in chlorinated species especially for longer alkyl chain molecules.

Previous studies have indicated that the generated fragment properties strongly depend on the alkyl chain length and halogen group position.[1,3,13,14,25,29,30,32] One of the important questions is the distribution of the available energy among the various degrees of freedom of the dissociating molecules. The photodissociation of halomethanes can often be treated by pseudo-diatomics approach, which maximizes the released kinetic energy of the halogen fragment.[6,8,15,27] On the other hand, higher alkyl-chain molecules[1,3,29,30,32] offer the possibility to deposit a significant fraction of the available energy into the fragment internal excitation.

The dissociation dynamics can be analyzed with classical models of energy partitioning,[1,3,35] which predict the excess energy disposal into the vibrational and rotational modes of polyatomic fragments.[1,3,29,30] This energy partitioning was first illustrated in detail by Riley and Wilson[1] for higher iodoalkanes dissociation, which was described as quasi-diatomic C–I dissociation followed by recoil of a semi-rigid radical. Similar approach was implemented later in the analysis of experiments with bromo- alkanes and alkenes.[3,29,30,34] In our present investigation, we apply

[a] *J. Heyrovský Institute of Physical Chemistry, v.v.i., The Czech Academy of Sciences; Dolejškova 2155/3, 182 23 Prague 8, Czech Republic. Fax: +420 2 8658 2307; Tel: +420 2 6605 3206; E-mail: michal.farnik@jh-inst.cas.cz*

[b] *University of Chemistry and Technology, 166 28 Prague 6, Czech Republic. E-mail: petr.slavicek@vscht.cz*

† Electronic Supplementary Information (ESI) available: Semiempirical intersystem crossing model, simulation Cartesian coordinates and orbitals. See DOI: 10.1039/cXCP00000x/

‡ Also affiliated at: Faculty of Mathematics and Physics, Charles University, 121 16 Prague 2, Czech Republic

the above simple classical mechanics approaches to a series of Cl-alkanes of different chain-length, and compare them with our direct *ab initio* non-adiabatic simulations.

The studied chloroalkanes are excited into $\tilde{A}$-band through the transfer of an electron localized in a non-bonding orbital of chlorine to the antibonding σ^* orbital along the C–Cl coordinate.[36] At the laser wavelength of 193 nm (6.41eV), three optically active repulsive states can be reached, denoted traditionally following the Mulliken[36] notation as $^3Q_1$, $^3Q_0$ and $^1Q_1$ ordered bottom-up by energy in the Franck-Condon region (see figure 1 in Ref. 6). The first triplet state $^3Q_1$ will not be further considered, as its oscillator strength from ground state is several orders of magnitude lower than for the other two states.[6,8] Considering a linear alkyl chain, the singlet $^1Q_1$ state has perpendicular orientation of the transition moment with respect to the C–Cl bond (anisotropy paramater $\beta = -1$) and is asymptotically correlated with the chlorine fragment in the ground state Cl ($^2P_{3/2}$). On the contrary, the triplet $^3Q_0$ state crosses the $^1Q_1$ state at the extended C–Cl bond distances and asymptotically correlates with a spin-orbit excited chlorine radical Cl*($^2P_{1/2}$). The triplet state can, in principle, be populated directly from the singlet ground state with the transition mediated by the spin-orbit coupling. Previous theoretical[24,36] and experimental work[6,8,15,26,33] on halomethanes suggested close to parallel character of the absorption transition (anisotropy parameter $\beta = +2$). However, the orientation of the transition dipole moment cannot be assumed *a priori*, and we can obtain it from our *ab initio* calculations for the present molecules. The anisotropy of absorption for both excited states $^1Q_1$ and $^3Q_0$ can be perturbed by halogen position within the molecule, distortion of linear frame and prolongation of alkyl chain resulting in reducing the dependence of transition moment on C–Cl bond orientation. It ought to be stressed that the anisotropy character of the initial absorption is preserved in the anisotropy of the fragment angular distribution, since the dissociation process is fast and proceeds on femtosecond scale preventing any significant blurring by the molecular rotation.[37,38] Due to the strong spin-orbit coupling caused by molecular frame distortion from C_{3v} symmetry the relaxation pathway can undergo ISC among the $^1Q_1$ and $^3Q_0$ excited states yielding the anisotropy of each Cl and Cl* fragment as linear combination of initial absorption characters.[39,40]

Based on the above considerations, models were proposed to analyze the fragment angular distributions and spin-orbit state populations in order to reveal the absorption ratios and ISC probabilities into the different dissociation channels. The model was firstly proposed by Frey and Felder[41] and similar models were applied to CH_3I,[31,33] CH_3Cl,[6] CH_3Br,[15,26] 2-bromobutane,[29] 2-bromopropyl,[30] and tert-butyl bromide and iso-butyl bromide.[32] The most extensively studied bromoalkanes show an increasing role of spin-orbit effect with increasing alkyl chain length, although a direct comparison is rather difficult as different photodissociation wavelengths were involved.[15,26,29,30,32] The photodissociation of CH_3Cl was analysed by Townsend *et al.*[6] however, their model assumed extreme anisotropy values for the absorption to the $^1Q_1$ ($\beta = -1$) and $^3Q_0$ ($\beta = +2$) excited states. Here, we modify the model by implementing our *ab initio* calculated β values to analyze our experimental results, and we determine the absorption and ISC probabilities into the different dissociation channels for higher chloroalkenes.

We have investigated the photodissociation of CH_3Cl at 193 nm by velocity map imaging (VMI) experiment previously, both as isolated molecule[27,28] as well as molecule in clusters.[27] The three selected higher chloroalkanes studied here, i.e. n-propyl chloride n-C_3H_7Cl, n-pentyl chloride n-$C_5H_{11}Cl$ and i-propyl chloride i-C_3H_7Cl, allow us to investigate the impact of the alkyl chain prolongation and chlorine group position on the inter-surface dynamics of the photodissociation. We focus on the energy transfer between different modes for the different chloroalkanes and the role of the spin-orbit effects. The energy transfer derived from the accompanying *ab initio* non-adiabatic calculations is compared with simple classical models. In addition, using our calculated β parameters we obtain absorption transition probabilities into the different dissociation states.

Our present study is analogous and complementary to the work of Corrales et al.,[42] where the correlation between chemical structure and the photodissociation dynamics of C–I bond was investigated in series of linear and branched alkyl iodides from CH_3I to n-C_4H_9I and t-C_4H_9I. Femtosecond time-resolved VMI spectroscopy together with dynamical calculations revealed the reaction specificity due to the interplay between C–I bond and the other degrees of freedom of the molecules. While the femtosecond experiment provides the dynamical information directly, in the present nanosecond experiment the dynamics of the reaction has to be inferred from the energy distribution. On the other hand, in our experiment the spectral resolution of the nanosecond laser allows the investigation of the spin-orbit effects.

The paper is organized as follows. Brief description of the VMI experiment and dynamical simulation approach is followed by calculations of potential surfaces for studied systems. Then, the measured kinetic energy distributions are discussed from the point of view of the classical mechanics models and *ab initio* simulations. The next sections are dedicated to the measured angular distributions and detailed insight into spin-orbit effects. Finally, we summarize the observations.

2 Methods

2.1 Experiment

The velocity map images (VMI) were recorded with our Apparatus for IMaging (AIM).[43] The buffer gas helium passed through an external reservoir containing the sample of commercially available alkyl chlorides (Sigma-Aldrich) and carried the evaporated molecules towards the nozzle. The reservoir was kept at a constant temperature T_R in the bath of the temperature regulator (Julabo CORIO CP-1000F). The vapor pressure of the sample molecules p_v was derived from the temperature T_R. A gas mixture of the sample molecules with helium was expanded at the total stagnation pressure p_0 through the pulsed nozzle (General Valves) with the diameter of 0.6 mm at the repetition frequency of 10 Hz. The expansion conditions are summarized in Table 1.

The molecular beam passed through a 1 mm skimmer into the VMI vacuum chamber. In the extraction region of a perpendic-

Table 1 The expansion conditions of the molecules seeded in He buffer gas: T_R is temperature of sample reservoir, p_v is vapour pressure of the sample at T_R, and p_0 is the total stagnation pressure of the expanding mixture. The expansion conditions for CH_3Cl correspond to Ref. 27, where a gas mixture of 7% CH_3Cl in He was used.

Molecule	T_R (°C)	p_v (bar)	p_0 (bar)
CH_3Cl [27]	22	0.12 (7%)	1.7
n-C_3H_7Cl	3	0.12	1.8
n-$C_5H_{11}Cl$	22	0.04	1.8
i-C_3H_7Cl	-24.5	0.08	1.8

ularly mounted VMI setup,[44] two counter-propagating UV lasers photolyzed the molecules and subsequently ionized the Cl fragments with the 2+1 resonance-enhanced multiphoton ionization process (REMPI). The photodissociation laser pulse at 193.3 nm (6.41 eV) was generated by ArF excimer laser (Coherent ExciStar XS, 10 Hz, 0.55 mJ). Its radiation was horizontally polarized by a thin film polarizer oriented at Brewster angle, and focused with $f_0 = 50$ cm lens to the interaction region. The second ionizing pulse generated by UV OPO laser (EKSPLA NT-230, spectral width ≈ 4 cm^{-1}) arrived with 10-20 ns delay to prevent any mix-multiphoton effects. To record simultaneously the background images with the excimer laser only, the OPO laser ran at the half-repetition rate (5 Hz). The background image was subtracted from the signal in the evaluation procedure. The OPO laser was set to the wavelengths 235.305 nm and 235.173 nm for the REMPI of the ground Cl ($4p^2P_{1/2} \leftarrow 3p^2P_{3/2}$) and excited ($4p^2D_{3/2} \leftarrow 3p^2P_{1/2}$) Cl* fragments, respectively.[45] To spatially overlap ionization pulse with the dissociation region, we used two lenses (plano-convex and positive meniscus) with effective focal length $f_0 = 25$ cm.

The ionized Cl fragments were extracted by VMI assembly perpendicularly with respect to the molecular beam and laser polarization towards the detector. After the flight through the 45 cm long field-free region, the ions were detected by a gated microchannel plate detector (MCP) in chevron stack combined with a phosphor screen. The image was recorded by the CCD camera (Unibrain) and simultaneously processed with centroiding algorithm. The synchronization of the whole VMI experiment (nozzle valve, lasers and MCP gate) was driven by the delay generator (BNC 575).

The collected images were further transformed by the inverse Abel transformation (Python module abel) to reconstruct original 3D velocity distribution.[46] We used the standard integration methods[46,47] to acquire the kinetic energy distribution (KED) and angular distribution from the measured images. The energy scale calibration was provided by the reference velocity map imaging of HBr.[43,48] We have also determined the [Cl*]/[Cl] population ratio for each molecule. For the CH_3Cl case, the ratio of [Cl*]/[Cl] = 0.86 was reported in Ref. 6. It was derived by averaging values from earlier measurements with rescaling due to an incorrect line strength factor calibration.[5,25,49,50] Thus we refer to this value, and we find a calibration factor to scale our measured [Cl*]/[Cl] ratio from CH_3Cl to the same value of 0.86 (this was reported also in our previous work[27]). Subsequently, we applied the same calibration factor to the ratios, which we have obtained experimentally for the other molecules investigated here. This procedure required that the laser intensities, REMPI probabilities and detection probabilities were all kept constant throughout the experiments, which was carefully checked and possible fluctuations were incorporated in the corresponding experimental error bars.

2.2 Theory

Most of the calculations were done with the state averaged complete active space (SA-CASSCF) method with 12 electrons in 7 orbitals (12/7) and 6-31+G* basis set. The active space was selected to accommodate for all relevant excited states both in the Franck-Condon (FC) region and the dissociated structure. We usually averaged over the first three singlet states (further denoted as SA(3S)), including the ground state and first two excited states, which are degenerate in the FC geometry. If needed, we also incorporated three triplet states (the SA(3S+3T) scheme). The CASSCF method was used for all the dynamical simulations, with the same active space for all of the molecules. The CASSCF calculatiosn were performed with the MOLPRO 2012 package.[51]

Dynamical calculations in the excited states were performed in our in-house-code ABIN,[52] using the adiabatic Landau-Zener surface hopping approach.[53,54] For each molecule, 1000 trajectories were simulated for 300 steps with a time step of 0.24 fs. At the end of the simulation, the chlorine atom was always fully separated from the rest of the molecule. The equations of motion were integrated with a Verlet algorithm. The ground state was sampled via the Wigner sampling, providing us with a set of initial positions and momenta. We used the implementation of the Wigner sampling from the SHARC code.[55] The initial vibrational wavefunction was obtained with vibrational frequencies calculated at the SA(3S)-CASSCF level. The experiment with a nanosecond 193 nm laser pulse required a filtering of initial geometries, fulfilling initial resonance condition[56,57]

$$\rho(\vec{R},\vec{P},E_{ph}) = W(\vec{R},\vec{P})\delta(E_f(\vec{R}) - E_i(\vec{R}) - E_{ph}). \quad (1)$$

i.e. the Wigner function $W(\vec{R},\vec{P})$ at coordinates $\vec{R}$ and momenta $\vec{P}$ space is filtered by a delta function with condition that the difference between energy of final $E_f(\vec{R})$ and initial $E_i(\vec{R})$ state is equal to the photon energy E_{ph}.

This was done by calculating 100 thousand excited states calculations on geometries of initial vibrational wavefunction and selecting those in the 192-194 nm interval. The CASSCF method suffers from the lack of the dynamical correlation. To benchmark the energetics, we have further calculated the dissociation energies of the C–Cl bond with the CCSD(T) and aug-cc-pVTZ basis set for all the molecules. These calculations were performed in the Gaussian09 package (revision D.01).[58]

The absorption spectrum was calculated with the nuclear ensemble model, called also the reflection principle method.[59–61] The excitation energies and transition dipole moments are evaluated from a set of geometries sampling the ground state nuclear density and the smooth absorption spectrum is then calculated as

$$\sigma_H(E_{ph}) = \frac{\pi}{3\hbar\varepsilon_0 c}\frac{1}{nH\sqrt{2\pi}}\sum_{i=1}^{n}\sum_{b}E_{ab}(\vec{R}_i)|\vec{\mu}_{ab}(\vec{R}_i)|^2 \times$$
$$\times \exp\left(-\frac{1}{2}\left(\frac{E-E_{ab}(\vec{R}_i)}{H}\right)^2\right) \qquad (2)$$

where $\sigma_H(E_{ph})$ is the absorption cross section at the photon energy E_{ph} corresponding to the transition from the initial state a to final state b. The energy difference E_{ab} is evaluated for the i-th of n single points sampled and $\vec{\mu}_{ab}(\vec{R}_i)$ is the corresponding transition dipole moment in nuclear geometry $\vec{R}$, $\hbar$ is the reduced Planck constant, ε_0 is the vacuum permittivity, c is the speed of light. The bandwidth parameter H was set to a value of 0.1 eV. The electronic parameters were calculated with the time-dependent density functional theory within the Tamm-Dancoff approximation. We used the BHandHLYP functional with a high fraction of exact exchange and the aug-cc-pVTZ basis set. As one of the critical questions raised in the present work was the fraction of molecules excited directly into the triplet electronic state, we have included also the spin-orbit Hamiltonian into the calculations. This allowed us to separate the singlet-singlet and singlet-triplet spectrum by using the k-dimensional tree statistical approach.[62] We were able to sort out singlet and triplet states from the adiabatic manifold formed after the spin-orbit calculation based on the similarity of excitation energy and transition electric dipole moment values with those of the minimal structure. The Breit-Pauli spin-orbit Hamiltonian was used. It was treated at the mean field level. The TDDFT/TDA calculations were performed in the ORCA 4.2.0 code.[63]

The angular distributions for computation of anisotropy parameter were evaluated as histograms of the angles between the C–Cl bond vector and the transition electronic dipole moment vector for resonance condition fulfilling geometries. We further assumed a conservation of adiabatic state characteristics or their consistent ordering between all the sampled geometries, see 3.3.1.

3 Results and Discussion

3.1 Calculated states and dissociation energies

Photodissociation of chloroalkanes upon the excitation into the first absorption band is an archetypal example of a direct photodissociation. The electronic transitions corresponding to the first absorption band are mostly connected to the promotion of the electrons from the non-bonding p orbitals of the chlorine atoms into the σ^* orbital of the C–Cl bond (for more information, see the orbitals in the Electronic Supplementary Material ESI†). In a pseudo-diatomic notation, these excitations would correspond to the Σ and Π states, and traditionally, these states have been denoted as $^3Q_0$ and $^1Q_1$, as outlined in the introduction. The singlet and triplet states are relatively close in energy. Table 2 shows the excitation energies and corresponding oscillatory strengths for all the molecules studied in the present work. We observe that the excitation energies are rather similar for the different species which is in accord with the localized character of the excitation. The calculated energy strongly depends on the electronic structure method used. This is due to the extremely steep potential energy surface along the C–Cl bond so that even a modest change in geometry significantly modifies the excitation energy.

Table 3 shows also the calculated bond dissociation energies. The values are again very similar for all the molecules and the calculated energies are close to the experiment whenever the data are available. The bond dissociation energy of 3.6 eV leads to the excess energy of about 2.8 eV released during the photodissociation. We also present the "unrelaxed" dissociation energies, neglecting the reorganization of the alkyl fragment. This energy is in fact the most relevant for the discussion of the energetics of the chlorine fragment due to the very fast nature of the process; the available excess energy is then reduced by some 0.2 eV. Note that the calculated dissociation energy is almost 1 eV smaller for the CASSCF method used for the subsequent simulations which will lead to a larger excess energy available.

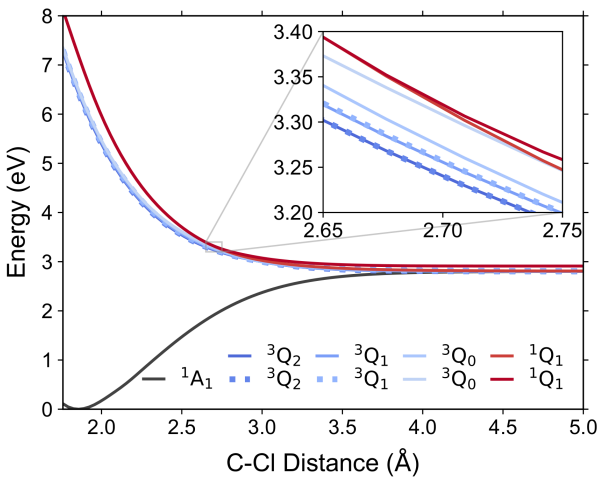


Fig. 1 Potential energy curves along the C-Cl coordinate for the CH_3Cl molecule. The adiabatic potential energy curves are calculated at the SA(3S+3T)CASSCF/6-31+G* level with the spin-orbit terms included.

Figure 1 displays adiabatic excited states for CH_3Cl dissociation computed using the SA(3S+3T)CASSCF method. In the inset, we observe crossing of states which results in two possible final states of chlorine, $Cl(^2P_{3/2})$ and $Cl^*(^2P_{1/2})$. Dissociation curves for other chloralkane analogues look qualitatively similar and differ mainly in the final dissociation energy.

3.2 Kinetic energy distribution

Figure 2 shows the KEDs of Cl and Cl* fragments for all the measured molecules. Their corresponding Abel transformed images are shown in the insets. All the images exhibit a single ring. The only exception is the case of i-C_3H_7Cl with an appreciable intensity closer to the image center, which will be discussed later. We show also CH_3Cl case discussed previously[6,27] in panel (a) for direct comparison. The KED spectra intensities have been normalized as outlined in Sec. 2.1 and scaled to the Cl fragment intensity maximum for each panel.

The narrow peaks in KED spectra could be fitted by a sin-

Table 2 Calculated excitation energies (eV) and respective oscillator strengths (f) for the doubly degenerate lowest singlet (EE-S) and triplet (EE-T) states. Molecules were re-optimized at the respective levels of theory.

	CH_3Cl				n-C_3H_7Cl				n-$C_5H_{11}Cl$				i-C_3H_7Cl			
method / base	EE-S	f	EE-T	f	EE-S	f	EE-T	f	EE-S	f	EE-T	f	EE-S	f	EE-T	f
CASSCF[i]	7.25	0.0031	6.44	-	7.46	0.0047	6.72	-	7.47	0.0047	6.72	-	7.35	0.0058	6.64	-
	7.25	0.0031	6.44	-	7.54	0.0046	6.79	-	7.55	0.0046	6.79	-	7.40	0.0050	6.68	-
BHandHLYP[ii]	7.44	0.0019	6.73	-	7.54	0.0002	6.82	-	7.56	0.0003	6.82	-	7.55	0.0005	6.79	-
	7.44	0.0020	6.73	-	7.55	0.0005	6.85	-	7.57	0.0005	6.85	-	7.57	0.0001	6.81	-
EOM-CCSD[iii]	7.44	0.0036	6.84	-	7.53	0.0012	6.93	-	7.37	0.0015	6.77	-	7.51	0.0004	6.91	-
	7.44	0.0036	6.84	-	7.53	0.0020	6.95	-	7.39	0.0034	6.80	-	7.52	0.0002	6.92	-

[i]SA(3S+3T)-CASSCF/6-31+G*, [ii]BHandHLYP/aug-cc-pVTZ, [iii]EOM-CCSD/aug-cc-pVTZ

Table 3 Calculated dissociation energies of the studied chloroalkanes (eV). The experimental D_0 values taken from the corresponding references are shown for comparison: CH_3Cl,[6,64] i-C_3H_7Cl,[3,65] and n-$C_5H_{11}Cl$.[66]

molecule	CASSCF[i]	CCSD(T)[ii]	CCSD(T)[ii] relax.	experiment
CH_3Cl	2.89	3.88	3.69	3.565
n-C_3H_7Cl	2.91	3.96	3.77	-
n-$C_5H_{11}Cl$	2.95	3.96	3.77	3.653
i-C_3H_7Cl	2.95	3.96	3.77	3.635

[i]SA(3S+3T)-CASSCF/6-31+G*, [ii]CCSD(T)/aug-cc-pVTZ

gle Gaussian function (fits not shown for clarity of the figure), and the fitted peak positions E_k together with the full width at half maximum (FWHM) ΔE_k are summarized in Table 4. The total available energy that can be stored into the translational and internal (vibrations and rotations) degrees of freedom of the fragments after the photodissociation is equal to $E_{tot} = E_{UV} - D_0$ ($E_{UV} = 6.41$ eV, D_0 is the experimental value of C–Cl dissociation energy outlined in the last column of Table 3; value for n-C_3H_7Cl has not been reported, to the best of our knowledge, thus, in the view of similarity of the calculated C–Cl bond dissociation energies, we take it equal to the i-C_3H_7Cl value). For the excited Cl* fragment, also the spin-orbit splitting $E_{SO} = 0.109$ eV[6] has to be subtracted to obtain E_{tot}.

As the energy analysis below suggests, we can assume two-body R–Cl dissociation for the present molecules without any further fragmentation of the R-fragment. Under this assumption, we can calculate the total translational energy E_T from the measured Cl fragment kinetic energy E_k simply applying the momentum conservation, which yields $E_T = \frac{M}{m_R} E_k$, where M is the mass of the whole molecule, and m_R is the mass of the R-fragment. From the total available energy E_{tot}, the part corresponding to E_T goes into the translation of both fragments, and the rest goes into the internal excitation of the R-fragment. Thus, we can evaluate the ratio $f_I^{exp} = 1 - \frac{E_T}{E_{tot}}$, which corresponds to the fraction of the available energy going into the R-fragment internal excitation. The E_T and f_I^{exp} values are summarized in Table 4. It ought to be stressed that these values have been calculated from the maximum position E_k of the Gaussian peak fitted into the measured KEDs. Thus, they reflect the mean values except for i-C_3H_7Cl, where, strictly speaking, E_k corresponds to the most probable value. The f_I^{exp} values suggest that about half of the available energy is deposited into the internal excitation of the R-fragments and the rest is released into the fragment kinetic energy. The exception represents CH_3Cl where less than 10% of the available energy goes into the CH_3 fragment excitation. It might be noted that the f_I^{exp} values are somewhat smaller when evaluated from the Cl* compared to the values evaluated from the Cl KEDs.

Table 4 The peak maximum positions E_k and the FWHM values ΔE_k (eV) from the Gaussian fit to the KEDs representing the measured mean kinetic energy of the Cl fragments . The total translation energy E_T, and the fraction f_I^{exp} of the total available energy deposited in the R-fragment internal degrees of freedom were calculated as outlined in the text.

Molecule	Fragment	$E_k/\Delta E_k$	E_T	f_I^{exp}
CH_3Cl	Cl	0.79/0.12	2.63	0.08
	Cl*	0.78/0.11	2.60	0.05
n-C_3H_7Cl	Cl	0.82/0.26	1.48	0.47
	Cl*	0.83/0.22	1.51	0.44
n-$C_5H_{11}Cl$	Cl	0.81/0.26	1.21	0.56
	Cl*	0.82/0.22	1.23	0.54
i-C_3H_7Cl	Cl	0.87/0.35	1.58	0.43
	Cl*	0.90/0.28	1.64	0.39

3.2.1 Classical mechanics models

We can discuss the energetics in terms of simple classical mechanics models. First, the hard spheres approach gives us the maximum possible kinetic energy of the Cl fragment assuming no internal excitation of the R-fragment. We treat the process as the photodissociation of a diatomic molecule R–Cl. Thus, the above outlined total available energy E_{tot} goes just into the fragment kinetic energy, and the Cl fragment kinetic energy can be calculated as $E_{HS} = E_{tot} \frac{m_R}{M}$. The calculated E_{HS} values are outlined in Table 5. Except for CH_3Cl, this simple approach hugely overestimates the observed Cl fragments kinetic energies.

The opposite extreme case is represented by the spectator model implemented previously for the photodissociation of alkyl iodides [1,35] and other halogenated hydrocarbons.[3] This approach assumes that Cl initially dissociates just against the carbon atom, to which it is directly bound, and the other atoms in the dissociating molecule act only as spectators. Considering the momentum conservation in the C–Cl dissociation, the fraction of the total available energy E_{tot}, which can be converted to the Cl fragment kinetic energy corresponds to $E_{sp} = E_{tot} \frac{m_C}{m_C + m_{Cl}}$ (m_C and m_{Cl} are the masses of C and Cl atom, respectively), see Table 5. The rest of the total available energy goes into the R-fragment: a part goes into its translation, since the momentum conservation is independent of the model and must be fulfilled for the whole molecule, and the remaining part is distributed among internal degrees of freedom, as no further fragmentation is energetically accessible.

The green arrows in Figure 2 indicate the calculated Cl frag-

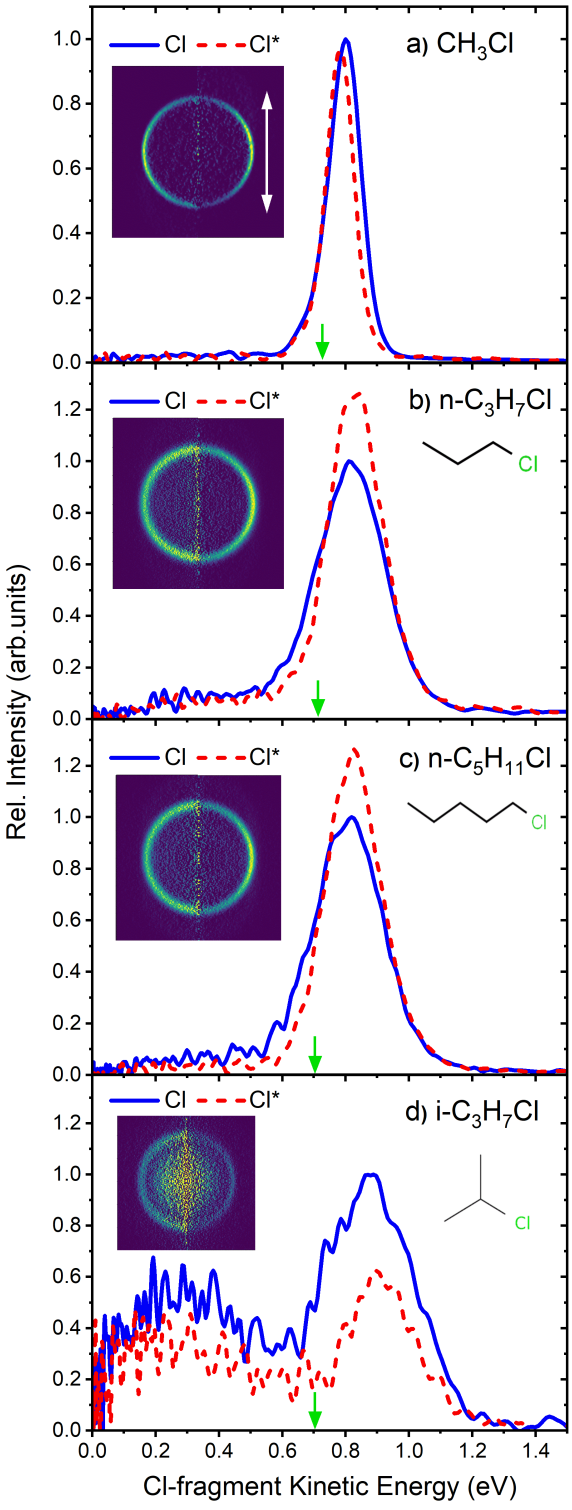


Fig. 2 The Cl fragment kinetic energy distributions (KEDs) from the 193 nm photodissociation of the investigated molecules; the solid blue and dashed red lines correspond to the Cl and Cl* KEDs, respectively. The insets show the Abel transformed images split in left and right half corresponding to Cl and Cl*, respectively. The laser polarization is indicated by the white arrow in the top image.

Table 5 Cl fragment kinetic energies E_{HS} and E_{sp} (eV) calculated from the hard spheres approach and spectator model, respectively. The fraction of the total available energy deposited into the R-fragment internal degrees of freedom according to the spectator model f_I^{sp}.

Molecule	Fragment	E_{HS}	E_{sp}	f_I^{sp}
CH_3Cl	Cl	0.86	0.73	0.15
	Cl*	0.82	0.70	
n-C_3H_7Cl	Cl	1.53	0.71	0.54
	Cl*	1.47	0.68	
n-$C_5H_{11}Cl$	Cl	1.85	0.71	0.62
	Cl*	1.78	0.68	
i-C_3H_7Cl	Cl	1.53	0.71	0.54
	Cl*	1.47	0.68	

ment kinetic energy E_{sp}. For all the molecules, they are close to the observed KED peak values E_k. However, it ought to be noted that the calculated E_{sp} values correspond to the maximum Cl fragment kinetic energy possible within the spectator model, while the experimental KEDs extend significantly beyond the E_k values for all the molecules except for CH_3Cl. Thus the spectator model clearly underestimates the Cl fragment kinetic energy.

Within this model, we can evaluate the ratio of internal energy excitation after the photodissociation as $f_I^{sp} = 1 - \frac{\mu_C}{\mu_R}$, where $\mu_C = \frac{m_C \cdot m_{Cl}}{m_C + m_{Cl}}$ and $\mu_R = \frac{m_R \cdot m_{Cl}}{m_R + m_{Cl}}$ are the reduced masses of the C–Cl and R–Cl systems, respectively. It is independent of the Cl spin-orbit state. The f_I^{sp} seems to be in good agreement with the experimental values f_I^{exp} in Table 4. However, it ought to be stressed again that f_I^{exp} has been evaluated from the *mean* Cl fragment kinetic energy E_k, while f_I^{sp} corresponds to the *maximum* kinetic energy of the Cl fragment possible within the spectator model.

In summary, the hard spheres approach and spectator model give us the upper (E_{HS}) and lower (E_{sp}) limits, respectively, for the *maximum* translation energy of the Cl fragment after the photodissociation. Our experimental outcomes are within these limits, closer to the spectator model, where roughly half of the available energy E_{tot} is dissipated into the internal excitation of the R-fragment.

Yet another way to present the photodissociation dynamics of these molecules from the perspective of the above models is to introduce an *effective fragment mass*. We can treat the photodissociation as an an X–Cl diatomics (hard sphere approach) with fragment X of effective mass m_X different from the real fragment R mass m_R. The measured kinetic energy of Cl fragment E_k allows us to simply evaluate m_X, which turns out to be equal to 13.7 u for CH_3Cl, 15.2 u for n-C_3H_7Cl, 17.0 u for i-C_3H_7Cl, and 15.1 u for $C_5H_{11}Cl$ (slightly different m_X values obtained from E_k measured for Cl and Cl* were averaged here to report just one number for each molecule). This shows that the effective mass is close to the CH_3 group for all the molecules rather than to the whole R-fragment mass. The overall mass of the molecule, i.e. the chain length, does not play any significant role. In the case of i-C_3H_7Cl the fragment is apparently "heavier"; clearly the C atom against which the Cl dissociates is bound more strongly to the remaining atoms.

The above models discuss the energy partitioning between the translation and internal modes of the fragments. The partition-

ing of the internal excitation between vibrational and rotational degrees of freedom of the alkyl fragment is more subtle. Previous study of iodoalkanes reported that the channeling between rotational and vibrational energy differs for linear and branched structures.[42] In a linear structure, the bond dissociation associated with the rotation of the alkyl fragment can be treated by a classical rigid rotor model.[1,3,35] Within this model, the rotational energy increases with the alkyl chain length and is larger for the linear versus branched structure. However, from our experimental spectra, we can only infer the internal excitation without distinguishing vibrations and rotations. Similarly, our theoretical simulations below suggest that a strict distinction between vibrations and rotations of highly energized molecule is somewhat ambiguous. Therefore, we discuss only the internal excitation without further distinguishing vibrations and rotations of the alkyl fragment.

As the final remark, the KEDs from i-C_3H_7Cl in Figure 2d) exhibit additional fragments with low kinetic energies below 0.6 eV. The signal-to-noise is relatively low, and these results have to be considered cautiously. The central low intensity feature in the images could originate from a background signal, which is usually subtracted (see Sec. 2.1). However, for the weak signals of i-C_3H_7Cl the background subtraction was difficult and residual background signal could not be ruled out. The central features in the images can also result from clusters or multiphoton processes. It has been demonstrated in numerous studies, most relevant to the present study is our recent work on CH_3Cl,[28] where we have discussed this point in detail. Based on this experience, we could exclude multiphoton effects, nevertheless, we could not exclude clustering unambiguously. Distinct conditions for clustering and single-molecule regime were found for all the investigated molecules except for i-C_3H_7Cl. Despite all effort, the recorded images exhibit some central intensity, and the mass spectra of i-C_3H_7Cl recorded under the present conditions still indicate a peak beyond the monomer mass, i.e., most likely a cluster fragment. All attempts to lower the stagnation pressure, change the buffer gas (He, Ar), and/or dilute the expansion mixture even further led to the loss of the VMI signal. Nevertheless, the peak of the fast fragments in Figure 2d) is unambiguous, and its position and width fits well the discussion of the whole series of molecules investigated here, thus we assign it to the monomer photodissociation.

3.2.2 *Ab initio* simulations

We have simulated the dissociation processes by means of *ab initio* on-the-fly non-adiabatic dynamics, with a particular focus on the kinetic energy of the outgoing chlorine photo-fragment and the energy transfer between the different normal modes. All the simulations are performed for the 193 nm photon, i.e. we do not perform a vertical excitation. The simulations take place on the CASSCF potential energy surface, lacking the dynamical correlation. As a result, the bond dissociation energy of the C–Cl bond is lower than in the experiment and, conversely, the excess energy available upon the excitation with the 193 nm photon is larger. The numerical value of the calculated kinetic energy cannot be, therefore, directly compared with the experiment. However, the dissociation energies are approximately the same for all of the studied molecules (see Table 2) and we can therefore investigate the influence of the length and position of the alkyl chain.

Upon the promotion of the system into the $^1Q_1$ state, we observe an immediate and very fast photodissociation. The dissociation is essentially complete in 25 fs and this time does not differ too much for the 4 species investigated in the present study. This is not surprising in the view of the classical photodissociation model of Liu and Zewail,[67] since the potential energy surface, excitation energy, and effective reduced mass are very similar for all 4 systems. The dynamics can be visualized, e.g., by recording the average kinetic energy. Figure 3 shows the time evolution of the kinetic energy of the alkyl fragment averaged over 1000 trajectories. Upon the initial ballistic period, we see some further oscillations for the larger molecules, while there are almost no changes for CH_3Cl. We can also see the significant energy transfer for the molecules with an extended alkyl chain.

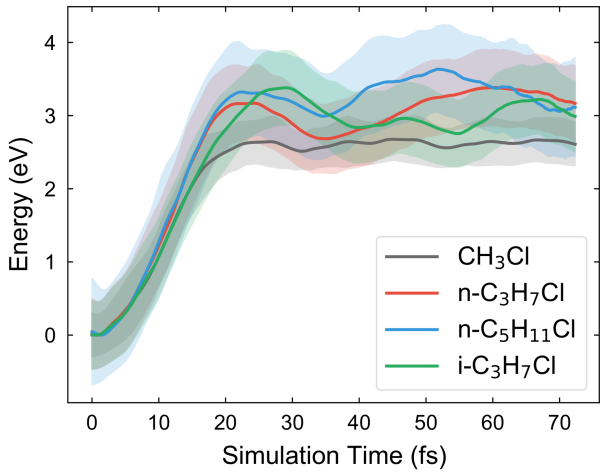


Fig. 3 Time evolution of the potential energy for different chloroalkanes. Line represents the mean value at a given step, error bars represent the standard deviation. Average over 1000 trajectories.

The experimentally observable quantity is the kinetic energy of the outgoing Cl fragment. The calculated KEDs are presented in Figure 4. The kinetic energy of the Cl fragment for CH_3Cl peaks at 1.1 eV. The fraction of energy deposited in the internal degrees of freedom is close to zero and the effective mass is evaluated to be 15.6 u. The distribution of the kinetic energies is relatively narrow. We conclude the methyl fragment behaves almost as an atom since the energy of 1.1 eV is an upper energy limit for this case. Out of 6.42 eV, 2.89 eV is consumed by dissociation, remaining 3.53 eV (plus relaxation energy, assuming 0.19 eV) must be redistributed between Cl and methyl fragment. In hard spheres approach this leads to ratio of 35:15, which based on the momentum conservation yields a maximum of 1.12 eV available to the Cl fragment. Except this higher value of the fragment kinetic energy, all the simulation results are consistent with the experiment.

The distribution of kinetic energy of the outgoing chlorine fragment is very similar for n-C_3H_7Cl, i-C_3H_7Cl and n-$C_5H_{11}Cl$ molecules, peaking at around 1.3 eV (see Figure 4). The constant

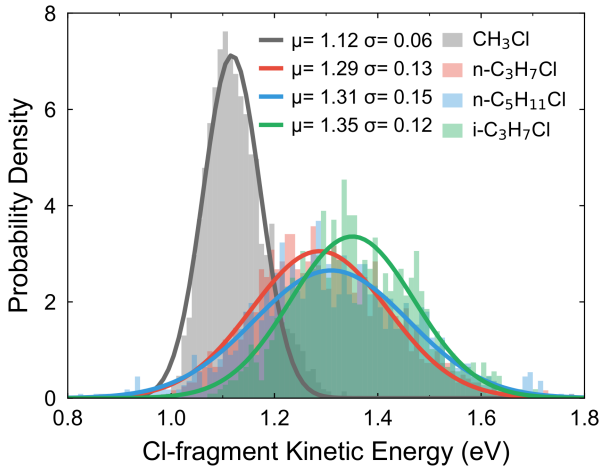


Fig. 4 Histogram of the Cl fragment kinetic energies for studied molecules obtained with the direct *ab initio* calculations together with the parameters (mean value μ, standard deviation σ) of the fitted Gaussian function.

chlorine kinetic energy confirms the view that the alkyl group cannot be considered as a pseudo-atom with a mass equal to the total mass of the fragment. Energy analysis indicates that the fraction of energy deposited in the internal degrees of freedom f_I^{casscf} is 0.36 for n-C_3H_7Cl, 0.47 for n-$C_5H_{11}Cl$ and 0.33 for i-C_3H_7Cl in the simulations. We calculate the effective mass of the fragment m_X, which is equal to 19.5 u for n-C_3H_7Cl and n-$C_5H_{11}Cl$, and 21.0 u for i-C_3H_7Cl. It is worth noting that the calculated kinetic energy of the Cl fragments from i-C_3H_7Cl is slightly but unambiguously higher than that from n-C_3H_7Cl and n-$C_5H_{11}Cl$, which is in nice qualitative agreement with the experiment and simply reflects the position of the C–Cl bond within the molecule.

Unlike in the experiment, the calculated energies are somewhat higher for the higher chloroalkanes than for the CH_3Cl. As mentioned above, the discrepancy between CH_3Cl and larger chloroalkanes in our calculations stems from the inadequacy of the CASSCF approach. The general trend is the same in the simulated data and in the experiment. The fraction of the energy deposited into the internal energy of the fragment is approximately constant for the heavier chloroalkanes while it is essentially zero for CH_3Cl. The observed amount of the internal energy deposited in the fragment is higher than in the theoretical simulations. In other words, the "theoretical" fragment is stiffer than the real fragment. In fact, this is in agreement with the known scaling factors for the calculations of vibrational frequencies.[68] This factor amounts to about 0.9 for the Hartree-Fock method so that the force constant should be corrected by a factor of 0.8 (proportional to the square the scaling factor). It seems that even this minor difference controls the energy transfer on the ultrafast time-scale of the photodissociation process.

3.3 Angular distribution

Further information delivered by the VMI experiment is the anisotropy of the photodisociation process. To obtain the angular distributions, the images were integrated over the region of the monomer peak using the standard procedures described in Sec. 2.1. The resulting angular distributions are shown in Figure 5 together with the fits according to the usual formula[47] $I(\theta) \propto 1 + \beta P_2(\cos\theta)$, where P_2 is second Legendre polynomial. The fitted anisotropy β-parameters are summarized in Table 6.

From comparison with the PES schematics in Figure 1, we can see symmetry exchange between $^1Q_1$ and Cl fragments on one side, and $^3Q_0$ and Cl* fragments on the other. Whereas the absorption to $^3Q_0$ state has parallel character, the angular symmetry of the diabatically correlating Cl* fragments has a perpendicular character. In the case of CH_3Cl it has even more perpendicular character than the Cl fragments, which correlate diabatically with $^1Q_1$ state, to which the absorption is expected to be perpendicular. On the other hand, the angular distributions of the ground state Cl fragments for all the other molecules except of CH_3Cl exhibit rather parallel character with $\beta > 0$. Such a strong mixing of symmetry is possible by intersystem crossing (ISC) between $^1Q_1$ and $^3Q_0$ states due to significant spin-orbit coupling. Below, we present a simple model based on previous literature,[6,9,15,26,29,30,41] which allows for evaluation of the spin-orbit coupling.

Table 6 The ratio of [Cl*]/[Cl] quantum yields from Figure 2 and anisotropy β-parameters from Figure 5. The estimated experimental uncertainty in parenthesis.

Molecule	[Cl*]/[Cl]	β(Cl)	β(Cl*)
CH_3Cl	0.86	-0.39(0.07)	-0.67(0.08)
n-C_3H_7Cl	1.09(0.35)	0.13(0.08)	-0.38(0.08)
n-$C_5H_{11}Cl$	1.04(0.35)	0.17(0.08)	-0.30(0.08)
i-C_3H_7Cl	0.55(0.25)	0.25(0.12)	-0.18(0.12)

3.3.1 Anisotropy and intersystem crossing

For CH_3Cl, Townsend et al.[6] estimated the relative probabilities of absorption to $^1Q_1$ and $^3Q_0$ states and significance of their spin-orbit coupling using β-parameters and quantum yields of Cl fragment in each state. Essentially, they compared their experimental fitted β-parameters with their theoretical values for absorption from the ground state ($^1A_1$).

Townsend et al.[6] assumed theoretical values $\beta = -1$ for the transition to the $^1Q_1$ state, and $\beta = +2$ transition to the $^3Q_0$ state. In reality, these extremal values of β-parameters are diminished by non-linear geometry of molecule in the time of absorption. This is mainly pronounced for n-C_3H_7Cl and n-$C_5H_{11}Cl$, where the orientation of transition dipole moment is less strictly connected to chlorine bond orientation and is significantly influenced by alkyl chain orientation. Therefore, the extended hydrocarbon chain can disrupt the parallel and perpendicular absorption symmetry to more isotropic one or shift the angle of maximal absorption to a new value. We calculate the corrected absorption β-parameters from sampling of an angle distribution between transition dipole moment and C–Cl bond orientation within absorption transition to each excited state (Table S1 in ESI†). We assume no anisotropy blurring by the rotation of the molecule as the dissociation proceeds fast on a fs scale. The calculated β-parameters together with our experimental values are implemented to obtain the direct absorption and transition probabilities using the model

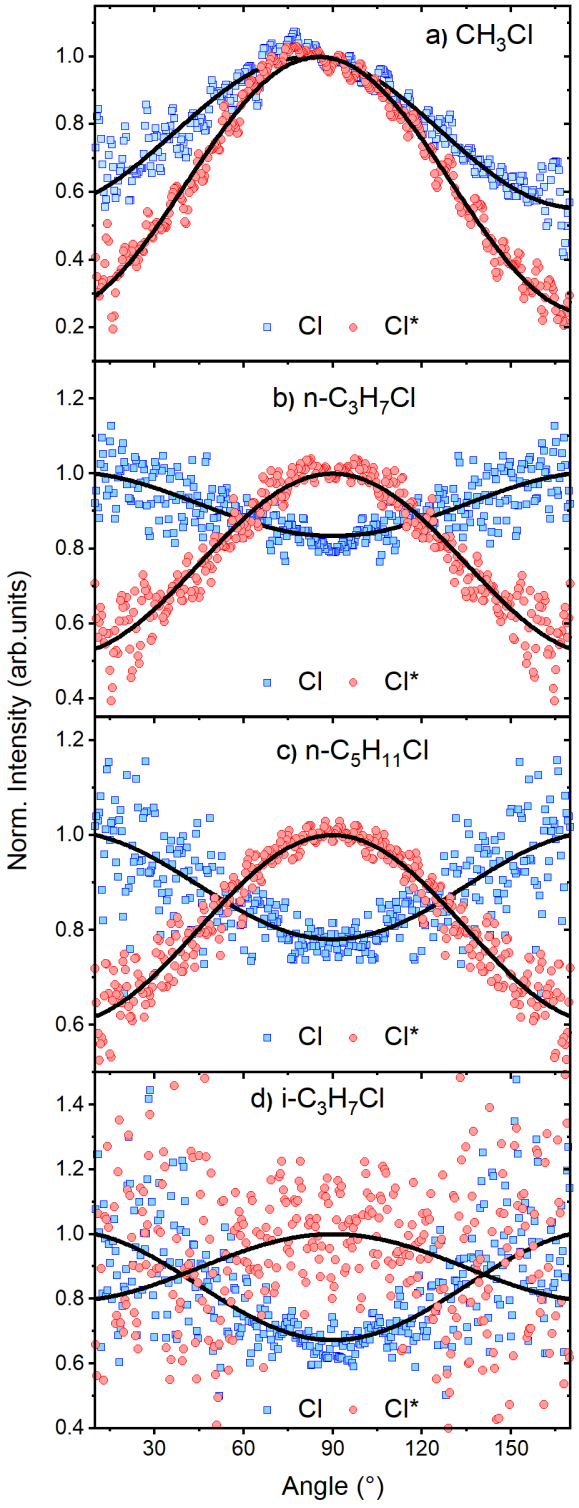


Fig. 5 The angular distributions corresponding to the images in Figure 2.

analogical to Townsend et al.[6] outlined in ESI†.

The calculated probabilities of absorption transitions and ISC are shown in Table 7. For comparison we also present the values calculated from the extremal values of β-parameters -1 and +2 in ESI,† (Table S2). Generally, most of the Cl fragments in both states come from absorption to $^1Q_1$ as the absorption probability to singlet state $^1A_1 \rightarrow {}^1Q_1$ is above 0.8 and further probability of ISC to the triplet state $^1Q_1 \rightarrow {}^3Q_0$ is between 0.4 and 0.6 for all the investigated molecules. Whereas the alkyl chain prolongation yields only slight increase of the absorption probability to the triplet, the position of chlorine group seems to have larger impact with almost twice as much absorption to $^3Q_0$ in case of i-C_3H_7Cl compared to n-C_3H_7Cl. From the perspective of the excited state spin-orbit coupling, the position of chlorine group on second carbon in the case of chloropropyl has an opposite effect reducing the $^3Q_0 \rightarrow {}^1Q_1$ probability of ISC transition from 0.96 to 0.84 and $^1Q_1 \rightarrow {}^3Q_0$ ISC transition probability from 0.58 to 0.41. This value is even lower than 0.49 for CH_3Cl. The alkyl chain prolongation from n-C_3H_7Cl to n-$C_5H_{11}Cl$ shows no further impact on calculated probabilities although the differences in the VMI images are significant. This seems to be reasonable as the C–Cl bond cannot be affected by the distant carbons.

Table 7 The probabilities of absorption to $^1Q_1$ ($^1A_1 \rightarrow {}^1Q_1$) and $^3Q_0$ ($^1A_1 \rightarrow {}^3Q_0$) states and the ISC probabilities of $^1Q_1 \rightarrow {}^3Q_0$ and vice versa calculated with the corrected β-values. Model description shown in ESI†.

Molecule	CH_3Cl	n-C_3H_7Cl	n-$C_5H_{11}Cl$	i-C_3H_7Cl
$^1A_1 \rightarrow {}^1Q_1$	0.91(0.05)	0.88(0.11)	0.88(0.11)	0.78(0.13)
$^1A_1 \rightarrow {}^3Q_0$	0.09(0.04)	0.12(0.05)	0.12(0.05)	0.22(0.05)
$^1Q_1 \rightarrow {}^3Q_0$	0.49(0.05)	0.59(0.12)	0.58(0.13)	0.41(0.14)
$^3Q_0 \rightarrow {}^1Q_1$	0.81(0.45)	0.96(0.49)	0.96(0.53)	0.84(0.31)

3.3.2 Singlet-triplet absorption: *ab initio* simulations

The model presented above predicts a relatively large probability of the direct excitation into the triplet state. Furthermore, the fraction of population transferred directly into the triplet state increases with the length of the alkyl chain. At the first sight, the high probability of the singlet-triplet absorption seems to be improbable, since the relativistic effects are not expected to be large for an organic molecule with chlorine. However, the excitation wavelength of 193 nm acts at the very red edge of the singlet spectrum, i.e., the probability of the absorption into the singlet state is low and the direct singlet-triplet absorption can become competitive. In fact, direct singlet-triplet absorptions are recently increasingly discussed as a viable route in photochemical reactions.[69,70]

We have tested the hypothesis of direct singlet-triplet absorption by simulations of the triplet contributions into the absorption spectra. Figure 6 shows the calculated absorption spectra (in logarithmic scale) of the investigated molecules together with the available experimental data and the triplet contribution. The theory somewhat deviates from the experiment both in the intensity and position of the main peak, as expected for the time dependent density functional theory calculations. However, the overall shape and magnitude of the intensity is well captured. We generally observe that the absorption cross section (near the first maximum) is around 10^{-18} cm^2 (at 180 nm) while the maximum of the singlet-triplet absorption cross section is only 10^{-20} cm^2 (at 193 nm). However, the cross section sharply decreases for an increasing wavelength and the contribution of the singlet-triplet ab-

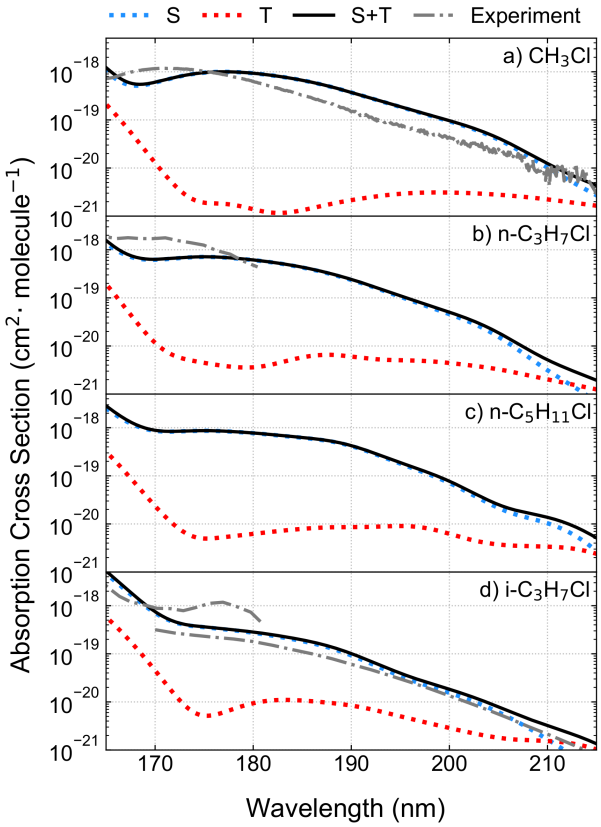


Fig. 6 Simulated absorption cross sections for different chloroalkanes. Contributions to absorption to singlet (S, dotted blue) and triplet (T, dotted red) states, and complete calculated absorption spectrum (S+T, black line); experimental data for a) Ref. 71, b) Ref. 72 and d) Ref. 72,73 (dash-dotted gray). The simulated data were calculated at the BHandHLYP/aug-cc-pVTZ level using reflection principle approach.

sorption becomes non-negligible above 190 nm for all molecules. Using the curve at 193 nm, we get a contribution of 1% for the direct triplet population for CH_3Cl, 3.5% for n-C_3H_7Cl, 3.4% for n-$C_5H_{11}Cl$ and 11.6% for i-C_3H_7Cl. The absolute values are smaller than the outcome of the above model, however, the trends are in qualitative agreement with the experiment.

4 Conclusions

We combine the VMI experiment and direct *ab initio* simulations to investigate the photodissociation of the C–Cl bond in chloroalkanes of increasing length of the alkyl chain (CH_3Cl, n-C_3H_7Cl, i-C_3H_7Cl, n-$C_5H_{11}Cl$). The reaction is an example of a direct dissociation on a steep slope - the photodissociation comes to a completion in 25 fs. However, the dynamics is inherently multidimensional and the energy transfer between the modes controls the course of the reaction. Furthermore, the spin-orbit interaction plays a non-negligible role in the reaction which is getting more important with the increasing size of the alkyl chain.

Energy transfer: The kinetic energy distributions of the Cl (Cl*) atoms exhibit a single peak with maximum close to 0.8 eV. For all the molecules except for CH_3Cl, this energy is way below the limit calculated within the classical hard spheres approach treating the process as a quasi-diatomic R–Cl photodissociation. Another classical approach assumes C–Cl photodissociation with the rest of the molecule acting as a spectator in the process. This spectator model yields the lower limit, which is, however, closer to the observed Cl fragment energy. The classical approach allows evaluation of an effective mass of the fragment, against which the Cl fragment dissociates in the diatomic-like picture. The effective masses range between 13 u and 18 u for all the molecules, close to the CH_3 mass irrespective of the actual R-fragment mass. The alkyl chain acts as a relatively soft, energy absorbing unit.

Direct *ab initio* simulations tailored for simulating dynamics upon the excitation with a fixed wavelength support the above picture. The dissociation of the chlorine fragment occurs against a "soft wall" due to the very fast dissociation taking place on the order of tens of femtoseconds. The energy of the nearest carbon atom then dissipates into the internal modes of the alkyl chain. The numerical values of the energies are not fully in agreement with the experiment due to the electronic structure used. More importantly, the *ab initio* alkyl fragments are too rigid and their effective masses are, therefore, slightly higher (19-21 u) compared to the experiment. Nevertheless, the qualitative picture confirms the experimental observations.

In summary, both experiment and theory show that for all the studied molecules a significant portion of the available energy, 40-60%, is deposited into the internal excitation (rotations and vibrations) of the R-fragment, except for CH_3Cl, where less than 10% goes into the internal energy.

Anisotropy and Spin-orbit effects: The experimentally measured anisotropy of the fragments was analyzed in terms of excitation probability into a particular state and the intersystem crossing probability. We have implemented a model used previously,[6,15,26,29,30,41] however, we have used modified β-parameters obtained from our quantum mechanical calculations considering a mismatch between the C–Cl bond direction and the transition moment vector. Our analysis yields a relatively high contribution of the direct excitation into the “forbidden” triplet state (9-22%) and intersystem crossing probabilities $^1Q_1 \rightarrow {}^3Q_0$ (40-60%) and $^3Q_0 \rightarrow {}^1Q_1$ (80-100%). The increasing role of a direct singlet-triplet excitation is confirmed by the simulated UV absorption spectra.

Authors contribution

M.F.: conceptualization, methodology, writing – original draft, review and editing; I.S.V.: investigation, formal analysis, visualization, writing – review and editing; J.R.: software, investigation; K.M.: investigation; V.P.: writing – review and editing; J.S.: software, formal analysis, visualization, writing – review and editing; P.S.: methodology, writing – review and editing.

Conflicts of interest

There are no conflicts to declare.

Acknowledgements

M.F., V.P., J.R. and K.M. appreciate the support of the Czech Science Foundation grant No.: 19-14105S. I.S.V. and K.M. were supported by Grant Agency of Charles University, grant No.: 374721.

J.S. and P.S. were supported by Czech Science foundation, grant number GA20-15825S and by The Ministry of Education, Youth and Sports from the Large Infrastructures for Research, Experimental Development and Innovations project „e-Infrastructure CZ – LM2018140“.

Notes and references

1 S. J. Riley and K. R. Wilson, *Faraday Discuss.*, 1972, **53**, 132–146.

2 D. W. Chandler and P. L. Houston, *J. Chem. Phys.*, 1987, **87**, 1445–1447.

3 M.Kawasaki, K. Kasatani and H. Sato, *Chem. Phys.*, 1984, **88**, 135–142.

4 E. Tiemann, H. Kanamori and E. Hirota, *J. Chem. Phys.*, 1988, **88**, 2457–2468.

5 Y. Matsumi, K. D. Puspendu and M. Kawasaki, *J. Chem. Phys.*, 1992, **97**, 5261–5261.

6 D. Townsend, S. K. Lee and A. G. Suits, *J. Phys. Chem. A*, 2004, **108**, 8106–8114.

7 H. Kato, H. Masui, M. Hoshino, H. Cho, O. Ingólfsson, M. J. Brunger, P. Limão-Vieira and H. Tanaka, *J. Chem. Phys.*, 2010, **133**, 054304.

8 A. Kartakoullis, P. C. Samartzis, T. N. Kitsopoulos and D. H. Parker, *J. Phys. Chem. C*, 2013, **117**, 22383–22390.

9 A. T. J. B. Eppink and D. H. Parker, *J. Chem. Phys.*, 1999, **110**, 832–844.

10 R. de Nalda, J. G. Izquierdo, J. Durá and L. Bañares, *J. Chem. Phys.*, 2007, **126**, 021101.

11 J. Durá, R. de Nalda, G. A. Amaral and L. Bañares, *J. Chem. Phys.*, 2009, **131**, 134311.

12 L. Rubio-Lago, A. García-Vela, A. Arregui, G. A. Amaral and L. Bañares, *J. Chem. Phys.*, 2009, **131**, 174309.

13 M. L. Murillo-Sánchez, J. González-Vázquez, M. E. Corrales, R. de Nalda, E. Martínez-Nuñez, A. García-Vela and L. Bañares, *J. Chem. Phys.*, 2020, **152**, 014304.

14 M. L. Murillo-Sánchez, A. Zanchet, S. M. Poullain, J. González-Vázquez and L. Bañares, *Sci. Rep.*, 2020, **10**, 1–11.

15 V. Blanchet, P. C. Samartzis and A. M. Wodtke, *J. Chem. Phys.*, 2009, **130**, 034304.

16 M. E. Corrales, R. de Nalda and L. Bañares, *Nat. Commun.*, 2017, **8**, 1–7.

17 M. L. Lipciuc and M. H. M. Janssen, *J. Chem. Phys.*, 2007, **127**, 224310.

18 F. Wang, M. L. Lipciuc, A. Kartakoullis, P. Glodic, P. C. Samartzis, X. Yang and T. N. Kitsopoulos, *Phys. Chem. Chem. Phys.*, 2014, **16**, 599–606.

19 H. M. Lambert and P. J. Dagdigian, *Chem. Phys. Lett.*, 1997, **275**, 499–505.

20 K. V. Vidma, A. V. Baklanov, E. B. Khvorostov, V. N. Ishchenko, S. A. Kochubei, A. T. J. B. Eppink, D. A. Chestakov and D. H. Parker, *J. Chem. Phys.*, 2005, **122**, 204301.

21 M. Solà, E. Carbonell, A. Lledós, M. Duran and J. Bertran, *J. Mol. Struct.-Theochem*, 1992, **87**, 283–296.

22 C. Escure, T. Leininger and B. Lepetit, *J. Chem. Phys.*, 2009, **130**, 244305.

23 G. Granucci, G. Medders and A. M. Velasco, *Chem. Phys. Lett.*, 2010, **500**, 202–206.

24 V. C. De Medeiros, R. B. De Andrade, E. F. Leitão, E. Ventura, G. F. Bauerfeldt, M. Barbatti and S. A. Do Monte, *J. Am. Chem. Soc.*, 2016, **138**, 272–280.

25 A. Melchior, H. M. Lambert, P. J. Dagdigian, I. Bar and S. Rosenwaks, *Isr. J. Chem.*, 1997, **37**, 455–465.

26 T. Gougousi, P. C. Samartzis and T. N. Kitsopoulos, *J. Chem. Phys.*, 1998, **108**, 5742–5746.

27 I. S. Vinklárek, J. Rakovský, V. Poterya and M. Fárník, *J. Phys. Chem. A*, 2020, **124**, 7633–7643.

28 I. S. Vinklárek, J. Rakovský, V. Poterya and M. Fárník, *Mol. Phys.*, 2021, **119**, e1823507.

29 R. Zhu, B. Tang, X. Zhang and B. Zhang, *J. Phys. Chem. A*, 2010, **114**, 6188–6193.

30 D.-N. Zhou, R. Mao, L.-M. Zhang, Q. Zhang and Y. Chen, *Chin. J. Chem. Phys.*, 2013, **24**, 647.

31 R. A. Hertz and J. A. Syage, *J. Chem. Phys.*, 1994, **100**, 9265–9268.

32 Y. Wang, S. Zhang, Z. Wei, Q. Zheng and B. Zhang, *J. Chem. Phys.*, 2006, **125**, 184307.

33 A. T. Eppink and D. H. Parker, *J. Chem. Phys.*, 1998, **109**, 4758–4767.

34 A. Müller, F. Talbot and S. Leutwyler, *J. Chem. Phys.*, 2001, **115**, 5192 – 5202.

35 G. E. Busch and K. R. Wilson, *J. Chem. Phys.*, 1972, **56**, 3626–3638.

36 R. S. Mulliken, *Phys. Rev.*, 1940, **57**, 500.

37 D. Zhong, P. Y. Cheng and A. H. Zewail, *J. Chem. Phys.*, 1996, **105**, 7864–7867.

38 M. Dzvonik, S. Yang and R. Bersohn, *J. Chem. Phys.*, 1974, **61**, 4408–4421.

39 Y. Amatatsu, K. Morokuma and S. Yabushita, *J. Chem. Phys.*, 1991, **94**, 4858–4876.

40 Y. Amatatsu, S. Yabushita and K. Morokuma, *J. Chem. Phys.*, 1996, **104**, 9783–9794.

41 J. G. Frey and P. Felder, *Chem. Phys.*, 1996, **202**, 397–406.

42 M. E. Corrales, V. Loriot, G. Balerdi, J. Gonzáles-Vázques, R. de Nalda, L. Bañares and A. Zewail, *Phys. Chem. Chem. Phys.*, 2014, **16**, 8812–8818.

43 J. Fedor, J. Kočišek, V. Poterya, O. Votava, A. Pysanenko, L. Lipciuc, T. N. Kitsopoulos and M. Fárník, *J. Chem. Phys.*, 2011, **134**, 154303.

44 A. T. J. B. Eppink and D. H. Parker, *Rev. Sci. Instrum.*, 1997, **68**, 3477–3484.

45 S. Arepalli, *Chem. Phys. Lett.*, 1985, **118**, 88–92.

46 D. D. Hickstein, S. T. Gibson, R. Yurchak, D. D. Das and M. Ryazanov, *Rev. Sci. Instrum.*, 2019, **90**, 065115.

47 B. Whitaker, *Imaging in Molecular Dynamics*, Cambridge University Press, Cambridge, 2003.

48 K. Grygoryeva, J. Rakovský, I. S. Vinklárek, O. Votava, M. Fárník and V. Poterya, *AIP Advances*, 2019, **9**, 035151.

49 J. Zhang, M. Dulligan and C. Wittig, *J. Chem. Phys.*, 1997, **107**, 1403–1405.

50 P. M. Regan, S. R. Langford, A. J. Orr-Ewing and M. N. R. Ashfold, *J. Chem. Phys.*, 1999, **110**, 281–288.

51 H.-J. Werner, P. J. Knowles, G. Knizia, F. R. Manby and M. Schütz, *Wiley Interdiscip. Rev. Comput. Mol. Sci.*, 2012, **2**, 242–253.

52 D. Hollas, J. Suchan, O. Svoboda, M. Ončák and P. Slavíček, *ABIN*, 2018, https://doi.org/10.5281/zenodo.1228462.

53 J. Suchan, J. Janoš and P. Slavíček, *J. Chem. Theory Comput.*, 2020, **16**, 5809–5820.

54 A. K. Belyaev, C. Lasser and G. Trigila, *J. Chem. Phys.*, 2014, **140**, 224108.

55 S. Mai, M. Richter, M. Heindl, M. F. S. J. Menger, A. Atkins, M. Ruckenbauer, F. Plasser, L. M. Ibele, S. Kropf, M. Oppel, P. Marquetand and L. González, *SHARC2.1: Surface Hopping Including Arbitrary Couplings — Program Package for Non-Adiabatic Dynamics*, sharc-md.org, 2019.

56 J. Suchan, D. Hollas, B. F. E. Curchod and P. Slavíček, *Faraday Discuss.*, 2018, **212**, 307–330.

57 A. Martínez-Mesa and P. Saalfrank, *J. Chem. Phys.*, 2015, **142**, 194107.

58 M. J. Frisch, G. W. Trucks, H. B. Schlegel, G. E. Scuseria, M. A. Robb, J. R. Cheeseman, G. Scalmani, V. Barone, B. Mennucci, G. A. Petersson, H. Nakatsuji, M. Caricato, X. Li, H. P. Hratchian, A. F. Izmaylov, J. Bloino, G. Zheng, J. L. Sonnenberg, M. Hada, M. Ehara, K. Toyota, R. Fukuda, J. Hasegawa, M. Ishida, T. Nakajima, Y. Honda, O. Kitao, H. Nakai, T. Vreven, J. A. Montgomery, Jr., J. E. Peralta, F. Ogliaro, M. Bearpark, J. J. Heyd, E. Brothers, K. N. Kudin, V. N. Staroverov, R. Kobayashi, J. Normand, K. Raghavachari, A. Rendell, J. C. Burant, S. S. Iyengar, J. Tomasi, M. Cossi, N. Rega, J. M. Millam, M. Klene, J. E. Knox, J. B. Cross, V. Bakken, C. Adamo, J. Jaramillo, R. Gomperts, R. E. Stratmann, O. Yazyev, A. J. Austin, R. Cammi, C. Pomelli, J. W. Ochterski, R. L. Martin, K. Morokuma, V. G. Zakrzewski, G. A. Voth, P. Salvador, J. J. Dannenberg, S. Dapprich, A. D. Daniels, Ö. Farkas, J. B. Foresman, J. V. Ortiz, J. Cioslowski and D. J. Fox, *Gaussian 09 Revision D.01*, Gaussian Inc. Wallingford CT 2009.

59 S. Sršeň, J. Sita, P. Slavíček, V. Ladányi and D. Heger, *J. Chem. Theory Comput.*, 2020, **16**, 6428–6438.

60 M. Ončák, L. Šištík and P. Slavíček, *J. Chem. Phys.*, 2010, **133**, 174303.

61 M. Barbatti, A. J. Aquino and H. Lischka, *Phys. Chem. Chem. Phys.*, 2010, **12**, 4959–4967.

62 J. L. Bentley, *Commun. ACM*, 1975, **18**, 509–517.

63 F. Neese, *Wiley Interdiscip. Rev. Comput. Mol. Sci.*, 2012, **2**, 73–78.

64 S. J. Blanksby and G. B. Ellison, *Acc. Chem. Res*, 2003, **36**, 255–263.

65 W. R. Stevens, A. Bodi and T. Baer, *J. Phys. Chem. A*, 2010, **114**, 11285–11291.

66 J. P. Leal, N. Marques and J. Takats, *J. Organomet. Chem.*, 2001, **632**, 209–214.

67 Q. Liu and A. H. Zewail, *J. Phys. Chem.*, 1993, **97**, 2209–2220.

68 *CCCBDB Vibrational frequency scaling factors*, `https://cccbdb.nist.gov/vibnotes.asp`, (accessed March 2021).

69 M. Nakajima, S. Nagasawa, K. Matsumoto, T. Kuribara, A. Muranaka, M. Uchiyama and T. Nemoto, *Angew. Chem.*, 2020, **132**, 6914–6919.

70 O. Svoboda and P. Slavíček, *J. Phys. Chem. Lett.*, 2014, **5**, 1958–1962.

71 S. Eden, P. Limão-Vieira, S. Hoffmann and N. Mason, *Chem. Phys.*, 2007, **331**, 232–244.

72 J. W. Raymonda, L. O. Edwards and B. R. Russell, *J. Am. Chem. Soc.*, 1974, **96**, 1708–1712.

73 D. Gillotay and P. C. Simon, *Ultraviolet absorption cross-sections of photoactive species of stratospheric interest. Part 1: The Halocarbons*, `http://satellite.mpic.de/spectral_atlas/cross_sections/Halogeno-alkanes+radicals/Chloroalkanes/i-C3H7Cl,(CH3)2CHCl_GillotaySimon(1990)_295K_170-230nm.txt`, (accessed March 2021).

B.5 Publication V

Title: **Uptake of Hydrogen Bonding Molecules by Benzene Nanoparticles**

Journal: *Journal of Physical Chemistry Letters*
DOI: `https://doi.org/10.1021/acs.jpclett.2c00835`

Note: Drafted version, accepted on 12^{th} of April, 2022 in *Journal of Physical Chemistry Letters* with supporting info.

Uptake of Hydrogen Bonding Molecules by Benzene Nanoparticles

Ivo S. Vinklárek,[†,‡] Andriy Pysanenko,[†] Eva Pluhařová,[*,†] and Michal Fárník[*,†]

[†]*Department of Dynamics of Molecules and Clusters, J. Heyrovský Institute of Physical Chemistry, v.v.i., The Czech Academy of Sciences, Dolejškova 2155/3, 182 23 Prague, Czech Republic*

[‡]*Department of Chemical Physics and Optics, Faculty of Mathematics and Physics, Charles University, Ke Karlovu 3, 121 16 Prague, Czech Republic*

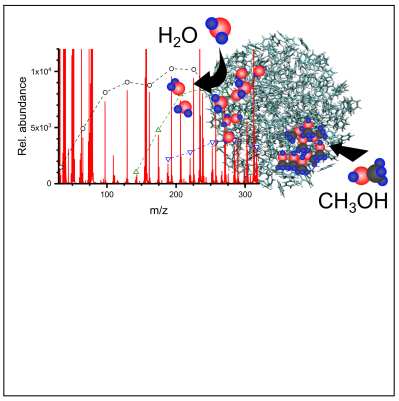
E-mail: eva.pluharova@jh-inst.cas.cz; michal.farnik@jh-inst.cas.cz

Phone: +420 2 6605 3206. Fax: +420 2 6605 3910

Abstract

The uptake of molecules on nanometer-size clusters of polyaromatic hydrocarbons (PAHs) is important for water condensation on PAH aerosols in the atmosphere, as well as for the ice mantel growth on nanoparticles in the interstellar medium. We generate benzene clusters Bz_N of the mean size $\bar{N} \approx 300$ (radius $\bar{R} \approx 2.2$ Å) as a model system for the PAH nanoparticles. Using molecular beams and mass spectrometry detection, we investigate the uptake of water, methanol and ethanol by these clusters. All picked up molecules are highly mobile on Bz_N and generate clusters within a time shorter than 3 milliseconds. The relative uptake for the different investigated molecules can be directly compared and quantified. Water molecules exhibit the lowest relative pickup probability by about 30% lower than the one for methanol or ethanol, which are approximately the same.

TOC Graphic



Aromatic carbonaceous compounds, such as benzene and polyaromatic hydrocarbon (PAH) molecules are omnipresent in our Earth atmosphere as well as in many regions of interstellar space. They can become part of atmospheric aerosols, which have a huge impact on the Earth's radiation balance.[1] PAHs and products of their atmospheric degradation contribute to positive radiative forcing by absorption of light, as a part of the so-called atmospheric brown carbon.[2] The aerosol particles, in general, play a pivotal role in atmospheric chemistry, since they act as surface catalysts for heterogeneous reactions.[3,4] In addition, the impact of aerosols on the air quality and human health, namely the carcinogenicity of PAHs, has been long recognized.[5]

From another point of view, astronomical observations reveal that various aromatic carbonaceous compounds, namely benzene and PAHs are present in different galaxies.[6–10] Carbonaceous grains and gaseous PAHs are believed to constitute the majority of carbon available in diffuse clouds.[11,12] Icy mantles and PAHs are involved in photochemical pathways to complex organic molecules in the interstellar medium (ISM).[13] The life cycle of large PAHs in the interstellar medium involves their breaking down by UV radiation to small PAHs and the generation of fragment clusters.[14,15] The recently launched James Webb Space Telescope should provide further insight into the PAH life cycle,[10] which adds on topicality to our present investigation.

Here, we investigate the uptake of molecules by nanometer-size benzene clusters. As species that get picked up by the Bz_N clusters we choose the following hydrogen bonding molecules with increasing complexity: water H_2O, methanol CH_3OH and ethanol CH_3CH_2OH. Their uptake can mimic the hydration of PAH soot particles in the atmosphere. Since water and methanol belong to the main molecular species observed in the interstellar ice mantles,[16] it can also represent the laboratory analogue to the ice mantles that grow on PAH nanoparticles.

From the fundamental point of view, the mixed benzene-water clusters serve as model systems for studying PAH-water interactions.[17,18] Their IR spectroscopy revealed their struc-

ture and the microscopic hydrophobicity of the aromatic ring.[19] The hydration and proton transfer in benzene-water cation clusters was studied with ion-mobility experiments and calculations.[20] Recently, clusters of the more complex PAHs, namely naphthalene, with water were investigated.[21,22] In most of the experimental studies so far, the clusters were prepared by coexpansion of benzene (or other PAHs) with water vapor. In contrast to that, here we generate pure nanometer-size benzene clusters and deposit several molecules on them as they pass through a pickup chamber. Such uptake processes can mimic the initial steps in the ice mantel growth. In addition, it allows molecular level investigations of the pickup, coagulation and reactions after the electron ionization in the benzene-molecule clusters.

In our experiment, the benzene clusters Bz_N were produced by a continuous supersonic expansion of benzene vapor with argon, resulting in the mean size $\bar{N} \approx 300$ and radius of 2.2 nm as determined below. As they fly through a vacuum chamber where the molecules can be introduced, they can pick up several molecules. Then, the clusters enter a time-of-flight mass spectrometer (TOF), where the mass spectra after the electron ionization are recorded. The experimental setup is described elsewhere[23,24] and more details are given in the attached Supporting Information (SI). It ought to be mentioned that due to the cluster fragmentation and limited discrimination-free mass range of our TOF spectrometer, the mean cluster size has been derived from the Poisson distribution of the adsorbed molecular clusters rather than from the mass spectra, as is detailed in SI.

Figure 1 shows examples of the mass spectra of the benzene clusters after the uptake of the molecules. The mass spectra in extended mass and intensity range are shown in SI. Panel 1a) corresponds to the uptake of water. The blue trace at the bottom shows the mass spectrum of pure benzene clusters without any pickup. This spectrum is shown and discussed in detail in the SI. When the water molecules are evaporated into the pickup cell, water clusters appear in the mass spectrum, as demonstrated by the upper trace (red). The new ion series after the pickup are indicated by the following symbols: protonated water clusters $(H_2O)_kH^+$ (black circles) and water clusters with benzene $Bz_n{\cdot}(H_2O)_k^+$ (triangles). It is interesting to note

that the pure water clusters are protonated, while the major series of benzene containing cluster ions correspond to non-protonated species, although the dominating peaks of the first three members of the single Bz containing series are even deprotonated, i.e., $Bz{\cdot}(H_2O)_kOH^+$, $k = 0-2$. Figure 1b) shows a part of the spectrum after the methanol pickup. The spectrum is very similar to the previous one in terms of the generated species: protonated methanol clusters $(CH_3OH)_kH^+$ (black circles) and methanol clusters with benzene $(Bz)_n{\cdot}(CH_3OH)_k^+$ (triangles). Finally, the pickup of ethanol (EtOH) in Figure 1c) exhibits the same features: protonated ethanol clusters $(EtOH)_kH^+$ and ethanol clusters with benzene $(Bz)_n{\cdot}(EtOH)_k^+$.

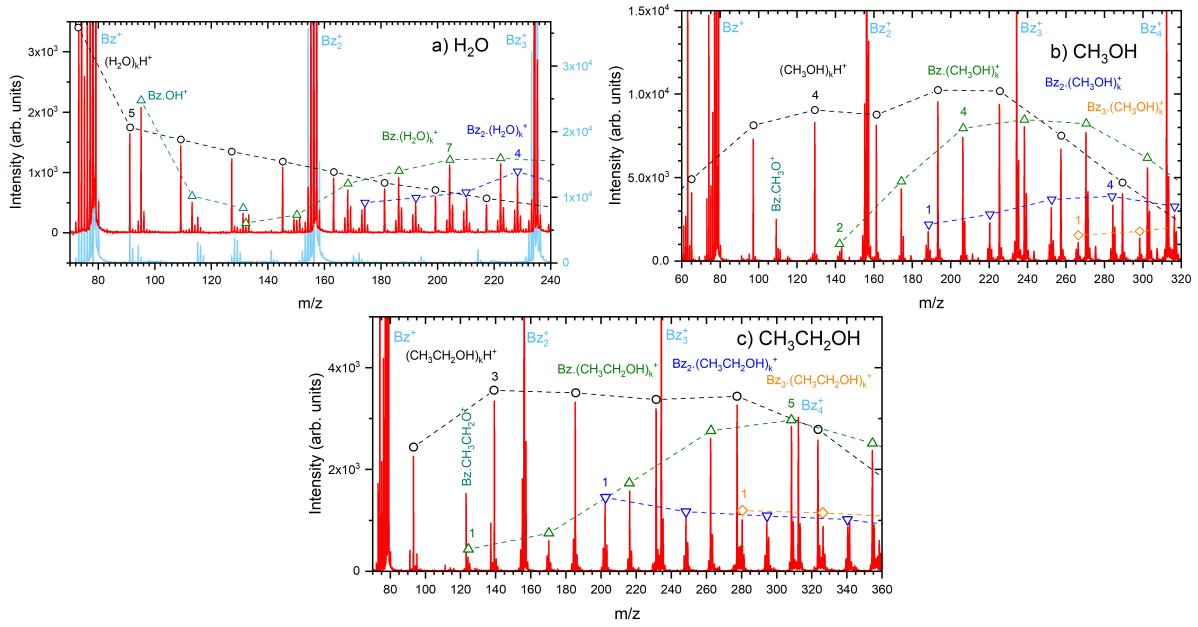


Figure 1: Mass spectra of the benzene clusters after the pickup of molecules a) water H_2O (blue bottom spectrum shows the pure Bz cluster spectrum without the pickup), b) methanol CH_3OH, and c) ethanol CH_3CH_2OH. The symbols and dashed lines indicate series of the cluster ion fragments of the adsorbed molecules (see text for details).

Interestingly, the mass peaks corresponding to the protonated, non-protonated and dehydrogenated species are present in all series in different abundances for different adsorbed molecules. The details of the cluster ionization and ion-molecule reactions, which can yield the observed cluster ion fragments, will be the subject of future investigations. Here, we

concentrate on the overall pickup of different molecules on benzene clusters demonstrated by the ions containing the adsorbed molecules and their fragments independently of their actual composition and structure. Finally, it ought to be mentioned that more spectra (3 for EtOH, 5 for MeOH, and 7 for H_2O) have been recorded and evaluated under different experimental conditions (see SI) and the results below represent an average of all the measurements.

The molecules are picked up one by one, but the spectra contain quite large molecular clusters. Thus, the presence of the molecular cluster ions in the spectra shows that the molecules coagulate efficiently on/in benzene nanoparticles during their flight-time from the pickup to the ionization region, which is about 3 ms (1.8 m over the measured cluster velocity of 540 m/s). Note that observed molecular cluster ions cannot be generated from individual molecules after the cluster ionization leading to the cluster fragmentation.

In order to assess differences of the pickup of the three hydrogen bonding molecules by the benzene nanoparticles, we integrate the intensities of all mass peaks containing the molecule M and its fragments. We assume that this integrated intensity I_{M} is proportional to the number of Bz_N clusters which picked up at least one molecule M in the pickup cell. It should be noted that a benzene nanoparticle that picked up molecules M contributes the same amount to the signal integrated in I_{M} independently of how many molecules M were embedded in the nanoparticle and whether the molecules coagulated or not. Analogically, we integrate all the *clean* Bz_n^+ peaks (including the corresponding peaks displaced by $m/z = \pm 1, \pm 2$, etc., as outlined in SI). This integral, I_{C}, corresponds to the clusters, which passed through the pickup cell without adsorbing any molecule M. The ratio $R_{\mathrm{up}} = \frac{I_{\mathrm{M}}}{I_{\mathrm{C}}+I_{\mathrm{M}}}$ then reflects the relative probability of the uptake for the given molecules M by the Bz_N nanoparticles (see SI for more details). These ratios are summarized in Table 1.

Table 1: Relative uptake ratios R_{up} of different molecules M by the Bz_N clusters.

Molecule M	R_{up}
water H_2O	0.21±0.10
methanol CH_3OH	0.30±0.08
ethanol CH_3CH_2OH	0.29±0.08

We need to discuss several assumptions of the mass spectrometry analysis justifying the comparison of R_{up} factor for different molecules as a relative measure of their uptake probability. The mass peak intensity depends on the following factors: (1) the ionization probability of the cluster, (2) the fragmentation after the ionization, and (3) the detection probability of the ion fragment. (1) For large clusters, the ionization cross section can be approximated by the geometrical cluster cross section of Bz_N. The number of molecules picked up by the clusters is significantly smaller than the cluster size N. Thus, the cross section does not change significantly by the uptake of the molecules and the ionization cross section of the cluster after the pickup can be assumed proportional to the Bz_N geometrical cross section independently of the adsorbed molecules. (2) According to the mass spectra, the fragmentation pattern is similar for all the adsorbed molecules. In addition, the fragmentation is not critical as long as all the ions containing the molecules (H_2O, MeOH and EtOH) and their fragments are accounted for in the signal integration. In this respect, also mass coincidences between fragments containing the molecules do not represent any problem. On the other hand, the mass coincidences between the ions containing the molecules $\mathrm{Bz}_n\mathrm{M}_k^+$ and the *clean* Bz_m^+ ions can introduce errors. There are such coincidences, e.g., 3 Bz molecules correspond to 13 H_2O molecules (see SI). Thus, we have included possible uncertainties in the error bars. (3) Finally, it is reasonable to assume that the detection probability of a $\mathrm{Bz}_n\mathrm{M}_k^+$ ion does not depend significantly on the kind of molecule M.

In addition, we have to consider the possibility that the molecules M can evaporate from the cluster upon ionization yielding the *clean* Bz_n^+ peaks and contributing to I_{C} rather than to I_{M}. Nevertheless, even this process would not change the fact that the ratio R_{up} for the different molecules reflects their relative pickup probabilities, provided that the molecule evaporation is similar for all the species, which is a reasonable assumption in view of their similar binding energies with benzene discussed below.

First, we discuss the uptake of different molecules quantified in Tab. 1. Within the relatively large error bars, given especially by the uncertainties in the pickup pressure de-

termination and the mass coincidences, the uptake probabilities for different molecules are similar. Nevertheless, the observed trend in $R_{\rm up}$ suggests that the uptake probability for water is by 30% smaller than that for MeOH and EtOH, which are almost the same.

The first reasoning could be that the pickup probability reflects the sticking of the molecule to the cluster in the uptake process and thus it would correlate with the binding energy of the molecule to benzene. Indeed, the binding energy of $H_2O\cdots Bz$ is smaller than the one between MeOH and EtOH and Bz (see Tab. 2 discussed below). However, the differences are smaller than the uncertainty of the theoretical estimates, therefore we consider other factors discussed below.

The ratio $R_{\rm up}$ is proportional to the cluster cross section. The actual size of the molecule factors into the evaluation of the cross section via $\sigma = \pi(R_{\rm C} + r_{\rm M})^2$, where $R_{\rm C}$ is the cluster radius and $r_{\rm M}$ is the van der Waals radius of the molecule. Further below, we evaluate the mean cluster radius $\bar{R} \approx 2.2$ nm from the Poisson distribution of the picked up molecules. The cluster radius is the dominant term, however, the radius of the molecule can make a small difference in the cross section. Considering $r_{\rm M} = 0.19$ nm, 0.25 nm and 0.28 nm for H_2O, MeOH and EtOH, respectively, and $R_{\rm C} = \bar{R}$, the ratio of the cross sections for the three molecules would be 0.93:0.98:1. Thus, this correction points in the right direction with the cluster collision cross section for water being the smallest, though not by ∼30% compared to MeOH and EtOH. Thus, none of the above considered factors could account for the 30% lower value of $R_{\rm up}$ for water with respect to MeOH and EtOH quantitatively, nevertheless, they follow the observed qualitative trend.

The pickup of molecules enables us to determine the actual size of the large cluster. The uptake is supposed to follow Poisson statistics.[25] Thus, information about the pickup cross sections of the clusters can be evaluated from the mass spectra.[26,27] Let us represent the cluster by a sphere with the cross section σ. As it flies through the pickup cell of the length $L = 17$ cm filled with gas at the pressure p and temperature T, it collides with the molecules, which can stick to the cluster. According to the Poisson distribution, the probability that

the cluster collides with k molecules equals to

$$P_k = \frac{(\alpha p)^k}{k!} \cdot e^{-\alpha p},\ \alpha = \frac{\sigma L}{k_B T}\,. \tag{1}$$

The cluster ion intensities of M_k^+ will follow the Poisson distribution P_k assuming that all k molecules stick to Bz_N upon collisions and coagulate to a cluster M_k on it and that the ionization does not result in any fragmentation of M_k. Thus, we could plot the adsorbed molecular clusters ion intensities as a function of their size k and fit them with Eq. (1) to derive the pickup cross section σ. A good agreement of these fits provides support for the stringent assumptions above. It should be noted that the above approach assumes that all the clusters can be represented by the mean pickup cross section corresponding to the mean size $\bar{N}$. Large clusters have log-normal size distributions and thus, in principle, a convolution of the log-normal and Poisson distributions should be used in the analysis.[28] Nevertheless, for practical purposes the Poisson distribution has been mostly considered in the literature.[25–27,29–33] Therefore, we find the use of the Poisson fits in the present case justified.

Figure 2 shows the dependencies of the M_kH^+ and $Bz{\cdot}M_k^+$ ion intensities on k for the pickup of methanol (a,b) and ethanol (c,d) on benzene nanoparticles. Note that for the protonated pure clusters, i.e., $(MeOH)_kH^+$, $(EtOH)_kH^+$, and $(H_2O)_kH^+$, panel (a), (c), and (d), respectively, the abscissa represents $k+1$ rather than k, since we assume that the protonated fragment originated from the neutral cluster that was larger by one molecule, i.e., $(MeOH)_{k+1} \rightarrow (MeOH)_kH^+$. In the right column, we show also the distribution of the Bz-containing fragments $Bz{\cdot}M_k^+$. Here we plot the distribution as a function of k, since we assume that the fragmentation after ionization proceeds through benzene evaporation. Similar distributions could also be found for series with more than one Bz molecule, see SI.

The $(MeOH)_kH^+$ and $(EtOH)_kH^+$ and the corresponding Bz containing series follow the Poisson distributions, and we can evaluate the pickup cross sections σ from the fits. Assuming

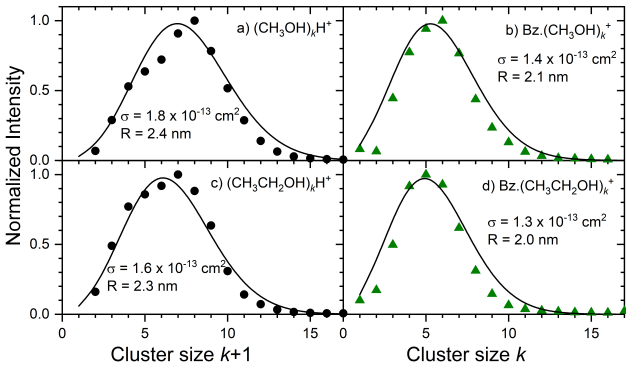


Figure 2: Cluster ion fragment abundances (symbols) fitted with Poisson distributions (lines). The left column shows the protonated cluster ions of the adsorbed molecules a) MeOH and c) EtOH. The right column shows the analogical series with one Bz molecule $Bz{\cdot}M_k^+$.

the spherical cluster shape, the corresponding nanoparticle radius R can be evaluated from $\sigma = \pi R^2$. In the case of water, the $(H_2O)_kH^+$ ions do not quite follow the Poisson distribution (see SI). Clearly, the stringent assumptions are not fulfilled here. Nevertheless, for MeOH, EtOH ions (and even for $Bz{\cdot}(H_2O)_k^+$, see SI) the fits provide consistent σ values yielding a mean cluster radius around $\bar{R} \approx 2.2 \pm 0.2$ nm. Since the same cluster beam was used in all experiments, we assume that this represents the mean cluster radius of the Bz_N clusters implemented in these pickup experiments.

Assuming the benzene density $\rho = 876$ kg·m^{-3}, the sphere of the estimated radius of 2.2 nm would contain about 300 Bz molecules. We can compare this value to the estimate from classical molecular dynamics simulations of clusters containing 200 and 300 Bz molecules. We perform the simulations at 150 K (the cluster temperature is discussed below) employing the OPLS-AA force field,[34,35] which is recommended for condensed phase benzene.[36] Figure 3 shows a normalized distribution of carbon and hydrogen atoms as a function of the distance from the cluster center of mass. The shape of the curves corresponding to the C and H atom is similar, which indicates the preference of a flat or just slightly tilted orientation of the benzene molecules on the cluster surface. The curves drop to the half of the cluster density at 1.8 nm for 200 molecules and 2.1 nm for 300 molecules. The latter value is in a good agreement with the mean cluster radius derived from the experiment, thus

we can conclude that our neutral clusters are composed of about 300 Bz molecules.

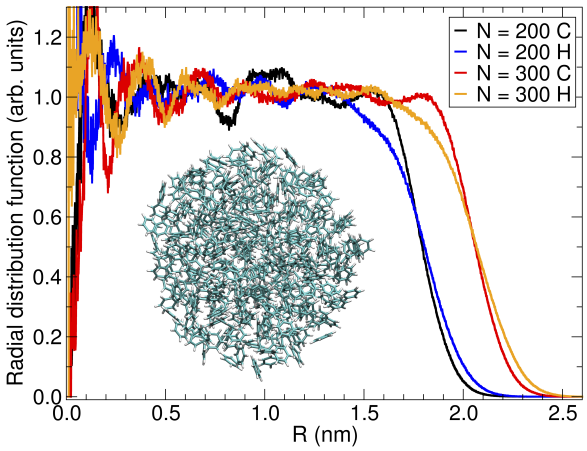


Figure 3: Radial distributions of C and H atoms from the center of mass of Bz_N clusters with $N = 200$ and 300 Bz molecules. The distributions were normalized on R^2.

It ought to be mentioned that the cluster pickup cross section does not necessarily coincide with the geometrical cross section of the sphere representing the cluster. This has been discussed in detail in our previous work on water clusters, where the measured pickup cross sections were larger than the geometrical cross sections due to the attractive interactions between polar and polarizable molecules and clusters.[37,38] In the present case, the clusters are composed of non-polar benzene molecules, therefore we do not expect the polarization forces to play such an important role.

The measured pickup cross section involves the probability of the cluster collision with the molecule as well as the probability of the molecule sticking to the cluster. To evaluate the pickup cross section from the Poisson distribution, we have assumed that the sticking probability equals one. If this is not the case, the evaluation procedure is still valid, but the evaluated quantity is the product of the pickup cross section with the sticking coefficient.

The complete coagulation of the adsorbed molecules on Bz clusters is assumed to justify the observed Poisson distribution. This requires the molecules to be highly mobile on Bz_N and coagulate to clusters within the 3 ms flight-time from the pickup chamber to the ionization region. This is interesting to compare with the pickup of different molecules on

other clusters, e.g., Ar_N and $(H_2O)_N$.[39–41] We observed coagulation of different adsorbed molecules on Ar_N, while the same molecules adsorbed on ice $(H_2O)_N$ nanoparticles were less mobile and did not coagulate. Most recently, these observations have also been supported by a combined experimental and theoretical investigation of H_2O_2 molecules on Ar_N and $(H_2O)_N$.[42] Nevertheless, we have observed coagulation of some molecules on ice nanoparticles as well.[43,44]

In this respect, the benzene clusters are similar to argon rather than water ice nanoparticles; the embedded molecules coagulate on benzene readily as they do on argon clusters. This can be justified by different binding strengths of the picked-up molecule with the cluster constituents and between the picked-up molecules M$\cdots$M. The binding energies are summarized in Tab. 2. The M$\cdots$Ar interaction is much weaker than between the hydrogen bonding molecules themselves. Thus, the hydrogen bonding molecules move on the Ar cluster surface until they encounter another hydrogen bonding partner. On the contrary, the alcohols picked up by water clusters are stabilized by 2-3 hydrogen bonds[45–47] which corresponds to $\sim$40 kJ$\cdot$mol^{-1}.[48] Therefore, they are not likely to move and find other alcohol molecules, even though the dissociation energies of (MeOH$\cdots$H$_2$O) and (EtOH$\cdots$H$_2$O) heterodimers are slightly lower than those of the corresponding alcohol homodimers.[49]

Table 2: Binding strengths (dissociation energies) of dimers in kJ$\cdot$mol^{-1}. The first column of each series compiles data from the literature, the second column is the theoretical estimate obtained by the same procedure for all systems.

Molecule	Ar	Bz		H_2O		MeOH		EtOH	
H_2O	1.7[a]	13.8[d]	10.6 [g]	22.8[h]	12.2-20.8[i]	18.5[j]	19.4–23.6[k]	21.0[j]	22.4[j]	22.4[j]
MeOH	1.5[b]	17.0[e]	12.9[g]	19.4–23.6[k]		21.0[j]	15.0–22.8	21.4[j]	-	-
EtOH	[c]	4.8[f]	13.1[g]	22.4[j]		22.4[j]	-	-	15.1–23.3[j,l]	23.5[j]

[a] Ref. 50; [b] Ref. 51; [c] not found; [d] Ref. 52; [e] Ref. 53; [f]Ref. 54; [g] this work, the same procedure as in [j]; [h] exp.; [i] Ref. 55; [j] Ref. 49; [k] Ref. 48; [l] Ref. 56

The differences in binding strengths of the (M$\cdots$Bz) dimers and (M$\cdots$M) dimers are not as pronounced as for the (M$\cdots$Ar) case. When comparing the available theoretical estimates, it is important to take into account the method, the size of the basis set and whether

thermal effects were included or not.[55] Therefore, we have calculated all the (M$\cdots$Bz) binding strengths in the third column of Table 2 by the same method as used in Ref. 49. The selected values (10.6, 12.9 and 13.1 kJ$\cdot$mol^{-1}) show that the binding strength of (M$\cdots$Bz) is similar for all molecules M and it grows in the following order H_2O<MeOH <EtOH . The binding of the heterodimer is by 8–9 kJ$\cdot$mol^{-1} weaker than that of (M$\cdots$M).

The coagulation of the molecules M on Bz clusters is also supported by the tendency of M to form hydrogen bonded chains or cycles attached to the aromatic ring.[53,57,58] In these structures, each of the M molecules forms two hydrogen bonds, not just one as in the dimer case.

From the point of view of the uptake process, the important question is the state of the benzene clusters - are they liquid or solid? This is indeed dependent on their temperature. In general, clusters in molecular beams generated by supersonic expansions attain low temperatures, e.g., in extreme 0.37 K for large superfluid He-nanodroplets,[59] about 40 K for large Ar clusters,[60,61] 50-180 K for water ice nanoparticles,[62] 90-135 K for methanol clusters,[63] etc. However, the cluster temperature is difficult to determine experimentally and various models were proposed. A simple estimate is outlined in SI. Earlier electron diffraction studies of benzene clusters in supersonic jets revealed the cluster vibrational temperature on the order of 100-150 K.[64] Electron diffraction experiments of Heenan et al. suggest that the benzene molecules in the clusters are not organized into regular arrays and the local order is similar but not identical to that in the solid, resembling that expected for a supercooled liquid. Stace et al. addressed the question of the cluster state by infra-red spectroscopy of relatively small clusters ($n < 15$) and concluded that these clusters are best described in terms of a liquid-like rather than a solid-like state.

Our present simulations shown in Fig. 3 have been performed at 150 K and agree with a non-crystalline disordered benzene cluster structure. We could speculate, if the maxima in the radial distribution of atoms might correspond to certain crystalline-like layers or shell closures as known, e.g., for argon clusters. However, the molecules at the cluster surface are

not organized into regular arrays. Many clusters, e.g., water, have a crystalline core covered by a quasiliquid layer (QLL).[66,67] Recent simulations together with our pickup experiments[42] have demonstrated that the adsorbed molecules on large argon clusters can submerge into the surface layer but remain very mobile finding each other quickly and forming clusters in less than a microsecond. In this respect, the present experiments suggest that the molecules behave similarly on benzene cluster, i.e., the benzene clusters are liquid like or posses a QLL, and the embedded molecules are highly mobile and coagulate to the hydrogen bonded molecular clusters.

Several conclusions can be drawn from the present experiments and calculations:

- The cluster ion fragment abundance follows the theoretical Poisson distribution, which allows us to evaluate the nanoparticle radius of $R \approx 2.2$ Å. This radius is consistent with the Bz_N clusters composed of about $\bar{N} \approx 300$ benzene molecules according to our theoretical simulations.

- All adsorbed molecules, water H_2O, methanol CH_3OH, and ethanol CH_3CH_2OH, are highly mobile on Bz_N and generate clusters within a time shorter than 3 milliseconds.

- The relative uptake for water, methanol and ethanol can be directly compared using the ratios R_{up} evaluated from the mass spectra: $R_{\mathrm{up}} = 0.21$, 0.30 and 0.29 for H_2O, MeOH and EtOH, respectively. They are discussed in terms of different binding energies and radii of the molecules, and the qualitative trend can be substantiated with water exhibiting the lowest relative pickup probability.

The present measurements of the relative uptake probability for different molecules on benzene clusters represent the very first experimental estimates of this quantity. The investigated pickup and coagulation processes might be important for water condensation on PAH aerosols in the atmosphere. Additionally, it can be related to the initial steps in the ice mantel growth on PAH particles in the interstellar medium. The water molecules exhibit a lower probability for uptake compared to methanol. Thus, methanol ice mantles can be gener-

ated in some regions despite the lower abundance of methanol compared to water molecules. The present experiments pave the road to future investigations with nanoparticles of more complex PAHs and pickup of other atmospherically and astrochemically relevant molecules.

Acknowledgement

The authors acknowledge the support of the Czech Science Foundation GAČR project number 21-07062S. Also, ISV thanks the project "Grant Schemes at CU" (reg. no. CZ.02.2.69/0.0/0.0/19-073/0016935).

Supporting Information Available

Details of the experimental and theoretical methods, additional mass spectra, discussion of the pickup probabilities, estimate of the cluster temperature.

References

(1) Seinfeld, J. H.; Pandis, S. N. *Atmospheric Chemistry and Physics: From Air Pollution to Climate Change*; John Wiley & Sons Inc.: Hoboken, NJ, 2016.

(2) Laskin, A.; Laskin, J.; Nizkorodov, S. Chemistry of Atmospheric Brown Carbon. *Chem. Rev.* **2015**, *115*, 4335–4382.

(3) Ravishankara, A. R. Heterogeneous and Multiphase Chemistry in the Troposphere. *Science* **1997**, *276*, 1058–1065.

(4) George, C.; Ammann, M.; D'Anna, B.; Donaldson, D. J.; Nizkorodov, S. A. Heterogeneous Photochemistry in the Atmosphere. *Chem. Rev.* **2015**, *115*, 4218–4258.

(5) Finlayson-Pitts, B. J.; Pitts, J. N. Tropospheric Air Pollution: Ozone, Airborne Toxics, Polycyclic Aromatic Hydrocarbons, and Particles. *Science* **1997**, *276*, 1045–1052.

(6) Ehrenfreund, P.; Rasmussen, S.; Cleaves, J. H. Experimentally Tracing the Key Steps in the Origin of Life: The Aromatic World. *Astrobiology* **2006**, *6*, 490–520.

(7) Peeters, E.; Spoon, H. W. W.; Tielens, A. G. G. M. Polycyclic Aromatic Hydrocarbons as a Tracer of Star Formation? *Astrophysical J.* **2004**, *613*, 986–1003.

(8) Smith, J. D. T.; Draine, B. T.; Dale, D. A.; Moustakas, J.; Kennicutt, R. C. J.; Helou, G.; Armus, L.; Roussel, H.; Sheth, K.; Bendo, G. J. The Mid-Infrared Spectrum of Star-Forming Galaxies: Global Properties of Polycyclic Aromatic Hydrocarbon Emission. *Astrophysical J.* **2007**, *656*, 770–791.

(9) Tielens, A. G. G. M. Interstellar Polycyclic Aromatic Hydrocarbon Molecules. *Annu. Rev. Astron. Astrophys.* **2008**, *46*, 289–337.

(10) Candian, A.; Zhen, J.; Tielens, A. G. G. M. Aromatic Universe. *Phys. Today* **2018**, *71*, 38–43.

(11) Pendleton, Y. J.; Allamandola, L. J. The Organic Refractory Material in the Diffuse Interstellar Medium: Mid-Infrared Spectroscopic Constraints. *Astrophysical J. Supp.* **2002**, *138*, 75–98.

(12) Snow, T. P.; McCall, B. J. Diffuse Atomic and Molecular Clouds. *Annu. Rev. Astron. Astrophys.* **2006**, *44*, 367–414.

(13) Öberg, K. I. Photochemistry and Astrochemistry: Photochemical Pathways to Interstellar Complex Organic Molecules. *Chem. Rev.* **2016**, *116*, 9631–9663.

(14) Rapacioli, M.; Calvo, F.; Joblin, C.; Parneix, P.; Toublanc, D.; Spiegelman, F. Formation and Destruction of Polycyclic Aromatic Hydrocarbon Clusters in the Interstellar Medium. *A&A* **2006**, *460*, 519–531.

(15) Lange, K.; Dominik, C.; Tielens, A. G. G. M. Stability of Polycyclic Aromatic Hydrocarbon Clusters in Protoplanetary Disks. *A&A* **2021**, *653*, 1–12.

(16) Gibb, E.; Whittet, D.; Boogert, A.; Tielens, A. G. G. M. Interstellar ice: The Infrared Space Observatory Legacy. *Astrophysical J. Supp.* **2004**, *151*, 35–73.

(17) Mons, M.; Dimicoli, I.; Piuzzi, F. Gas Phase Hydrogen-Bonded Complexes of Aromatic Molecules: Photoionization and Energetics. *Int. Rev. Phys. Chem.* **2010**, *21*, 101–135.

(18) Prakash, M.; Samy, K. G.; Subramanian, V. Benzene-Water (BZW_n ($n = 1 - 10$)) Clusters. *J. Phys. Chem. A* **2009**, *113*, 13845–13852.

(19) Miyazaki, M.; Fujii, A.; Ebata, T.; Mikami, N. Infrared Spectroscopy of Size-Selected Benzene-Water Cluster Cations $[C_6H_6\text{-}(H_2O)_n]^+$ ($n = 1-23$): Hydrogen Bond Network Evolution and Microscopic Hydrophobicity. *J. Phys. Chem. A* **2004**, *108*, 10656–10660.

(20) Ibrahim, Y. M.; Mautner, M. M. N.; Alshraeh, E. H.; El-Shall, M. S.; Scheiner, S. Stepwise Hydration of Ionized Aromatics. Energies, Structures of the Hydrated Benzene Cation, and the Mechanism of Deprotonation Reactions. *J. Am. Chem. Soc.* **2005**, *127*, 7053–7064.

(21) Chatterjee, K.; Dopfer, O. Infrared Spectroscopy of Hydrated Polycyclic Aromatic Hydrocarbon Cations: Naphthalene$^+$–Water. *Phys. Chem. Chem. Phys.* **2017**, *19*, 32262–32271.

(22) Xu, B.; Stein, T.; Ablikim, U.; Jiang, L.; Hendri, J.; Head-Gordon, M.; Ahmed, M. Probing Solvation and Reactivity in Ionized Polycyclic Aromatic Hydrocarbon–Water Clusters with Photoionization Mass Spectrometry and Electronic Structure Calculations. *Faraday Discuss.* **2019**, *217*, 414–433.

(23) Fárník, M.; Lengyel, J. Mass Spectrometry of Aerosol Particle Analogues in Molecular Beam Experiments. *Mass Spec Rev.* **2018**, *37*, 630 – 651.

(24) Fárník, M.; Fedor, J.; Kočišek, J.; Lengyel, J.; Pluhařová, E.; Poterya, V.; Pysa-

nenko, A. Pickup and Reactions of Molecules on Clusters Relevant for Atmospheric and Interstellar Processes. *Phys. Chem. Chem. Phys.* **2021**, *23*, 3195 – 3213.

(25) Lewerenz, M.; Schilling, B.; Toennies, J. P. Successive Capture and Coagulation of Atoms and Molecules to Small Clusters in Large Liquid Helium Clusters. *J. Chem. Phys.* **1995**, *102*, 8191.

(26) Macler, M.; Bae, Y. K. Determination of Mean Cluster Size by Water Capture. *J. Phys. Chem. A* **1997**, *101*, 145–148.

(27) Fedor, J.; Poterya, V.; Pysanenko, A.; Fárník, M. Cluster Cross Sections from Pickup Measurements: Are the Established Methods Consistent? *J. Chem. Phys.* **2011**, *135*, 104305.

(28) Vongehr, S.; Shao-Chun, T.; Xiang-Kang, M. Collision Statistics of Clusters: From Poisson Model to Poisson mixtures. *Chinese Phys. B* **2010**, *19*, 023602.

(29) Mestdagh, J. M.; Gaveau, M. A.; Gée, C.; Sublemontier, O.; Visticot, J. P. Cluster Isolated Chemical Reactions. *Int. Rev. Phys. Chem.* **1997**, *16*, 215–247.

(30) Behrens, M.; Fröchtenicht, R.; Hartmann, M.; Siebers, J. G.; Buck, U. Vibrational Spectroscopy of Methanol and Acetonitrile Clusters in Cold Helium Droplets. *J. Chem. Phys.* **1999**, *111*, 2436–2443.

(31) Gaveau, M.-A.; Glogauen, E.; Fournier, P.-R.; Mestdagh, J.-M. Transition State Spectroscopy of the Photoinduced Ca + CH_3F Reaction. 1. A Cluster Isolated Chemical Reaction Study. *J. Phys. Chem. A* **2005**, *109*, 9494–9498.

(32) Stienkemeier, F.; Lehmann, K. K. Spectroscopy and Dynamics in Helium Nanodroplets. *J. Phys. B* **2006**, *39*, R127–R166.

(33) Pelimanni, E.; Hautala, L.; Hans, A.; Kivimäki, A.; Kook, M.; Küstner-Wetekam, C.;

Marder, L.; Patanen, M.; Huttula, M. Core and Valence Level Photoelectron Spectroscopy of Nanosolvated KCl. *J. Phys. Chem. A* **2021**, *125*, 4750–4759.

(34) Jorgensen, W. L.; Tirado-Rives, J. The OPLS Potential Functions for Proteins. Energy Minimizations for Crystals of Cyclic Peptides and Crambin. *J. Am. Chem. Soc.* **1988**, *110*, 1657–1666.

(35) Jorgensen, W. L.; Severance, D. L. Aromatic-Aromatic Interactions: Free Energy Profiles for the Benzene Dimer in Water, Chloroform, and Liquid Benzene. *J. Am. Chem. Soc.* **1990**, *112*, 4768–4774.

(36) Fu, C. F.; Tian, S. X. A Comparative Study for Molecular Dynamics Simulations of Liquid Benzene. *J. Chem. Theory Comput.* **2011**, *7*, 2240–2252.

(37) Lengyel, J.; Kočišek, J.; Poterya, V.; Pysanenko, A.; Svrčková, P.; Fárník, M.; Zaouris, D.; Fedor, J. Uptake of Atmospheric Molecules by Ice Nanoparticles: Pickup Cross Sections. *J. Chem. Phys.* **2012**, *137*, 034304.

(38) Lengyel, J.; Pysanenko, A.; Poterya, V.; Slavíček, P.; Fárník, M.; Kočišek, J.; Fedor, J. Irregular Shapes of Water Clusters Generated in Supersonic Expansions. *Phys. Rev. Lett.* **2014**, *112*, 113401.

(39) Pysanenko, A.; Habartová, A.; Svrčková, P.; Lengyel, J.; Poterya, V.; Roeselová, M.; Fedor, J.; Fárník, M. Lack of Aggregation of Molecules on Ice Nanoparticles. *J. Phys. Chem. A* **2015**, *119*, 8991 – 8999.

(40) Pysanenko, A.; Pluhařová, E.; Vinklárek, I. S.; Rakovský, J.; Poterya, V.; Kočišek, J.; Fárník, M. Ion and radical chemistry in $(H_2O_2)_N$ clusters. *Phys. Chem. Chem. Phys.* **2020**, *22*, 15312–15320.

(41) Pysanenko, A.; Vinklárek, I. S.; Fárník, M.; Poterya, V. Generation of $(H_2O_2)_N$ Clusters on Argon and Ice Nanoparticles. *Int. J. Mass Spectrom.* **2020**, *461*, 116514.

(42) Poštulka, J.; Slavíček, P.; Pysanenko, A.; Poterya, V.; Fárník, M. Bimolecular Reactions on Sticky and Slippery Clusters: Electron-Induced Reactions of Hydrogen Peroxide. *J. Chem. Phys.* **2022**, *156*, 054306.

(43) Rubovič, P.; Pysanenko, A.; Lengyel, J.; Nachtigallová, D.; Fárník, M. Biomolecule Analogues 2-Hydroxypyridine and 2-Pyridone Base Pairing on Ice Nanoparticles. *J. Phys. Chem. A* **2016**, *120*, 4720 – 4730.

(44) Pysanenko, A.; Kočišek, J.; Poterya, V.; Fárník, M. Clustering of Uracil Molecules on Ice Nanoparticles. *J. Phys. Chem. A* **2017**, *121*, 1069 – 1077.

(45) Lengyel, J.; Pysanenko, A.; Fárníková, K.; Pluhařová, E.; Fárník, M. Oxidation Enhances Aerosol Nucleation: Measurement of Kinetic Pickup Probability of Organic Molecules on Hydrated Acid Clusters. *J. Phys. Chem. Lett.* **2020**, *11*, 2101 – 2105.

(46) Han, G.; Ding, Y.; Qian, P.; Zhang, C.; Song, W. Theoretical Investigation of Gas Phase Ethanol-$(Water)_n$ (n = 1-5) Clusters and Comparison with Gas Phase Pure Water Clusters $(Water)_n$ (n = 2-6). *Int. J. Quant. Chem.* **2013**, *113*, 1511–1521.

(47) Mandal, A.; Prakash, M.; Kumar, R. M.; Parthasarathi, R.; Subramanian, V. Ab Initio and DFT Studies on Methanol-Water Clusters. *J. Phys. Chem. A* **2010**, *114*, 2250–2258.

(48) Albertí, M.; Amat, A.; Aguilar, A.; Pirani, F. Methanol–Methanol and Methanol–Water Systems: the Intermolecular Interactions Controlling the Transition from Small Clusters to the Liquid Phase. *Phys. Chem. Chem. Phys.* **2017**, *19*, 16765–16774.

(49) Fileti, E. E.; Chaudhuri, P.; Canuto, S. Relative Strength of Hydrogen Bond Interaction in Alcohol–Water Complexes. *Chem. Phys. Lett.* **2004**, *400*, 494–499.

(50) Cohen, R. C.; Saykally, R. J. Determination of an Improved Intermolecular Global Po-

tential Energy Surface for Ar–H_2O from Vibration–Rotation–Tunneling Spectroscopy. *J. Chem. Phys.* **1993**, *98*, 6007–6030.

(51) Carvalho, F. M.; Kiametis, A. S.; de Araújo Oliveira, A. L.; Pirani, F.; Gargano, R. Spectroscopy, Lifetime, and Charge-Displacement of the Methanol-Noble Gas Complexes: An Integrated Experimental-Theoretical Investigation. *Spectrochim. Acta A Mol. Biomol. Spectrosc.* **2021**, *246*, 119049.

(52) Hobza, P. Calculations on Noncovalent Interactions and Databases of Benchmark Interaction Energies. *Acc. Chem. Res.* **2012**, *45*, 663–672.

(53) Matisz, G.; Kelterer, A. M.; Fabian, W. M.; Kunsági-Máté, S. Coordination of Methanol Clusters to Benzene: A Computational Study. *J. Phys. Chem. A* **2011**, *115*, 10556–10564.

(54) Hema,; Bhatt, T.; Pant, T.; Dhondiyal, C. C.; Rana, M.; Chowdhury, P.; Joshi, G. C.; Arya, P.; Tiwari, H. Computational Study of the Intermolecular Interactions and Their Effect on the UV-Visible Spectra of the Ternary Liquid Mixture of Benzene, Ethanol and Propylene Glycol. *J. Mol. Model* **2020**, *26*, 268.

(55) Kim, K. S.; Tarakeshwar, P.; Lee, J. Y. Molecular Clusters of Π-Systems: Theoretical Studies of Structures, Spectra, and Origin of Interaction Energies. *Chem. Rev.* **2000**, *100*, 4145–4186.

(56) González, L.; Mó, O.; Yáñez, M. Density Functional Theory Study on Ethanol Dimers and Cyclic Ethanol Trimers. *J. Chem. Phys.* **1999**, *111*, 3855–3861.

(57) Slipchenko, L. V.; Gordon, M. S. Water-Benzene Interactions: An Effective Fragment Potential and Correlated Quantum Chemistry Study. *J. Phys. Chem. A* **2009**, *113*, 2092–2102.

(58) Müller-Dethlefs, K.; Hobza, P. Noncovalent Interactions: A Challenge for Experiment and Theory. *Chem. Rev.* **2000**, *100*, 143–168.

(59) Hartmann, M.; Miller, R. E.; Toennies, J. P.; Vilesov, A. F. Rotationally Resolved Spectroscopy of SF_6 in Liquid Helium Clusters: A Molecular Probe of Cluster Temperature. *Phys. Rev. Lett.* **1995**, *75*, 1566.

(60) Farges, J.; de Feraudy, M. F.; Raoult, B.; Torchet, G. Structure and Temperature of Rare Gas Clusters in a Supersonic Expansion. *Sur. Sci.* **1981**, *106*, 95–100.

(61) Farges, J.; de Feraudy, M. F.; Raoult, B.; Torchet, G. Noncrystalline Structure of Argon Clusters. II. Multilayer Icosahedral Structure of Ar_N Clusters $50 \leq N \leq 750$. *J. Chem. Phys.* **1986**, *84*, 3491–3501.

(62) Becker, D.; Dierking, C. W.; Suchan, J.; Zurheide, F.; Lengyel, J.; Fárník, M.; Slavíček, P.; Buck, U.; Zeuch, T. Temperature Evolution in IR Action Spectroscopy Experiments with Sodium Doped Water Clusters. *Phys. Chem. Chem. Phys.* **2021**, *23*, 7682–7695.

(63) Steinbach, C.; Fárník, M.; Ettischer, I.; Siebers, J.; Buck, U. Isomeric Transitions in Size-Selected Methanol Hexamers Probed by OH-Stretch Spectroscopy. *Phys. Chem. Chem. Phys.* **2006**, *8*, 2752–2758.

(64) Heenan, R. K.; Valente, E. J.; Bartell, L. S. Electron Diffraction Studies of Supersonic Jets. II. Formation of Benzene Clusters. *J. Chem. Phys.* **1983**, *78*, 243–248.

(65) Stace, A.; Bernard, D.; Crooks, J.; Reid, K. Benzene Clusters: Liquid or Solid State? *Mol. Phys.* **1987**, *60*, 671–679.

(66) Cheng, H.-P.; Berry, R. S. Surface Melting of Clusters and Implications for Bulk Matter. *Phys. Rev.* **1992**, *45*, 7969–7980.

(67) Pradzynski, C. C.; Forck, R. M.; Zeuch, T.; Slavíček, P.; Buck, U. A Fully Size-Resolved Perspective on the Crystallization of Water Clusters. *Science* **2012**, *337*, 1529–1532.